Sensitivity of Next-Generation Water-based Neutrino Detectors for Reactor Antineutrino Detection

Stephen Wilson

Supervisor: Dr. Patrick Stowell

Department of Physics & Astronomy

University of Sheffield

A thesis submitted in partial fulfilment of the requirements for the degree of

Doctor of Philosophy

January 2024

Abstract

Nuclear fission reactors are a key source of power generation in many countries worldwide, but come with the potential for nuclear weapons proliferation. Safeguarding of current reactors through item accountancy is seen as sufficient to prevent this, but new developments in reactor technology pose new risks. Using the unshieldable antineutrino signal emitted by reactors during the fission process to monitor core operations offers a potential solution.

A test bed facility has been developed to characterise and test new equipment for a large neutrino detector that could be used for non-proliferation. A programme of testing for Photo-Multiplier Tubes (PMTs) has been undertaken, resulting in a thorough understanding of the inherent dark rate background.

The PMT characterisation was used to inform the design of a mid- to far-field antineutrino monitoring prototype located in Boulby Mine, with its sensitivity to real reactor antineutrino signals in a complex landscape evaluated using Monte Carlo simulations. A novel event reconstruction-data reduction-analysis chain has been developed to harness the inverse beta decay signal of a positron and neutron pair to extract reactor signals from backgrounds.

This analysis pathway has been compared to an independent pathway, with significant improvements found. The detector is found to have sensitivity to power reactors over 150 km away, with the use for future non-proliferation applications of neutrino detectors showing potential. Consideration of a viable path toward the inclusion and application of antineutrino monitoring of reactors for non-proliferation determines that neutrino detectors may have future utility.

Declaration

I, the author, confirm that this thesis is my own work except as noted here or cited. I am aware of the University's Guidance on the Use of Unfair Means[1]. This work has not been previously been presented for an award at this, or any other, university.

In chapter 3, where the development of a water tank and test bed facility for neutrino detectors is discussed, I took all data and performed all analyses presented. The construction of the tank and first filtration system were undertaken by Matt Thiesse. I made several modifications to the circulation system, and installed measures to restrict external light from the system. General development and maintenance was performed by Matt Thiesse, Sam Fargher, Andrew Scarff, Rob Foster and me. This work has been published in [1].

The work in chapter 4 surrounds the characterisation of photomultiplier tubes. I performed all work in section 4.6, including both hardware operation and software development for control and analysis. Support for the installation and operation of hardware was provided by Sam Fargher, Rob Foster and Andrew Scarff. They are acknowledged as authors in the publication of this work in [2]. The work in section 4.5 was a large collaborative effort, which I contributed to significantly through the development of control software and measurement procedure. The overall testing programme was led by Matt Needham and Gary Smith at the University of Edinburgh. This work in published in [3]. The gadolinium soak tests of photomultiplier tubes in subsubsection 4.7.1.3 were performed by Chris Toth at Boulby Underground Laboratory. I selected the tubes to be soaked as described in subsubsection 4.7.1.1, with Max Calle supporting my work.

The design and simulation of a large neutrino detector are described in chapter 5, which constituted a large group effort by the WATCHMAN collaboration. All detector geometries and calculations of signal and backgrounds, as well as all implementations of the simulation package, described here are my own. Direct support was obtained from Liz Kneale on the validation of the implemented models and designs.

In chapter 6 and chapter 7, I developed the entirety of the data reduction and analysis from subsection 6.1.2 onward. Some support was obtained from Liz Kneale during the validation stage, and with the calculation of radionuclide rates and development of work in subsection 6.2.5. Support was also obtained by James Armitage and Chris Cotsford for the work in section 7.2, with this work available in [4]. However, the

[1] www.sheffield.ac.uk/ssid/unfair-means

majority of the work in these chapters is my own. My contributions to the work in chapter 5, chapter 6 and chapter 7 are published in [5].

Acknowledgments

In some ways, the acknowledgments section has been the hardest one to write because there are so many people who have been supportive.

Firstly my supervisor, Patrick Stowell, deserves recognition for the support he has provided, and for the number of fires he has had to put out. Patrick was not my original supervisor, yet despite not working on the same projects, he was able to guide me to the end of my PhD in a better manner than I could have asked for. He has always found time to provide help and useful advice, and his in depth comments on my thesis drafts were vital.

I could not mention academic support without mentioning Susan Cartwright. I am not sure I, or anyone for that matter, has ever known anyone quite like Susan. She is without doubt the most well-read, knowledgable and thorough person I know. It is well known in the department that what Susan says, goes. After all, if she was not correct, she would not say it. On countless occasions, she has provided support when I have run out of ideas and needed advice, and her encyclopaedic knowledge has been such an important resource.

Finally, Lee Thompson's no nonsense approach has saved me so much time over the last few years. His experience, ability to find solutions and his attitude have left a lasting impression on all who have been fortunate enough to work with him.

From academic supervisors to the person who has given more supervision and support than anyone ever should. Liz Kneale completed her PhD around two years before me, and as such has had to put up with being the target for my near constant questions. She is a wonderful person and physicist, and her contribution to my work has been so important that I could list her as an author for this work. I have learned so much from Liz, and she has been such an inspiration.

To the other three people who have been stuck with my questions: Sam, Andrew and Matt, thank you for dealing with me. Sam taught me everything I know about experimental physics, and how to fix any problem with black tape. Andrew provided constant support and was a perfect person to bounce ideas from, and is responsible in no small part for the ounce of sanity I have left. Despite no longer being in the field, both Sam and Andrew have continued to provide advice. Matt has been the adult of the office, dealing with myself and the rest of the PhD students with great patience but still cracking the occasional unexpected joke. He has also taught me much more than

I think he realises.

I have received support for my work from many people within the WATCHMAN collaboration. In particular, Gary Smith and Matt Needham in Edinburgh, Jon Coleman in Liverpool, and the team at Boulby Underground Laboratory. Marc Bergevin at Lawrence Livermore National Laboratory deserves a special acknowledgment. Marc always had an hour to spare to help me with code and analysis, even when he did not have a spare hour in his day. I am one of many people who worked in WATCHMAN who owes Marc a lot of gratitude.

Doing, and particularly finishing, a PhD would have been nearly impossible without the other equally stressed PhD students in the office. Talking absolute nonsense to the point that we have a board of out-of-context quotes has provided the required break from work, and sinking German children on the high seas will never fail to amuse. My time has been filled with memories that make no sense at all, and many random pints. So, to Commodore Foster, Jimothy, the man who thinks abroad means leaving South Yorkshire, and Hank: thank you.

To my wonderful family, without their support I would never have come this far. They have always pushed me to be the best I can, and have always been there for anything I need. Surviving as a student is never easy, and it would have been nearly impossible without them. I am so grateful to have them in my life.

Finally, the biggest thank you must go to my amazing fiancée, Mi-Ye. Words really do not do what she has done for me justice. She has been there through everything: the times I had motivation and would work constantly, and the times I did not want to get out of bed. She has dealt with late-night meetings and detector shifts, being away for conferences or in train tunnels, and my general tired and grumpy demeanour. She has been my rock, and is without doubt the most wonderful and caring person I know. I am so lucky to have her, and I hope to be able to provide her as much love and support as she has to me.

Contents

1 Introduction **1**

1.1 The Early History of Neutrinos 1

1.1.1 Postulation 1

1.1.2 Discovery 3

1.1.3 Flavours 8

1.1.4 Bruno Pontecorvo 10

1.2 Neutrino Propagation 14

1.2.1 Postulation of Oscillation 14

1.2.2 Missing Neutrinos and the Solution 14

1.2.3 Current Theories 17

1.2.4 Current Measurements 21

1.3 Nuclear Reactors and the Role of the Antineutrino 23

1.3.1 Reactors for Power Generation 23

1.3.2 Nuclear Proliferation 26

1.3.3 Safeguards 27

1.3.4 Reactor Antineutrinos 28

1.4 Thesis Aims and Structure 33

2 Antineutrino Interactions and Detection **35**

2.1 Interactions with Matter 35

2.2 Light Production in Matter 39

2.2.1 Cherenkov Radiation 39

2.2.2 Scintillation 41

2.2.3 Neutron Capture 43

2.2.4 Light Loss Mechanisms 43

2.3 Detector Fill Media 45

2.3.1 Gadolinium doping . . . 45
2.3.2 Water-based Liquid Scintillator . . . 46
2.4 Summary . . . 48

3 PocketWATCH Water Cherenkov Detector Test Bed 51
3.1 Facility Description . . . 51
3.1.1 PocketWATCH Tank . . . 51
3.1.2 Water Filtration . . . 53
3.1.3 Water Temperature . . . 54
3.1.4 Maintenance . . . 55
3.2 Performance . . . 55
3.2.1 Light Tightness . . . 55
3.2.2 Water Temperature . . . 56
3.2.3 Water Quality . . . 58
3.3 Summary . . . 65

4 Photomultiplier Tubes and their Characterisation 71
4.1 Background on PMTs . . . 72
4.1.1 Window and Photocathode . . . 73
4.1.2 Charge and Gain . . . 74
4.1.3 Timing . . . 75
4.1.4 Undesired Pulses . . . 77
4.1.5 Dark Noise . . . 78
4.2 PMT Requirements for Reactor Antineutrino Detection . . . 78
4.3 Hamamatsu R7081-100 Photomultiplier Tube . . . 79
4.4 Electronics Used for Testing of Hamamatsu R7081 PMTs . . . 81
4.5 Quality Assurance and Acceptance Testing . . . 82
4.5.1 Setup . . . 83
4.5.2 Data Taking, Processing and Quality . . . 83
4.5.3 Gain . . . 85
4.5.4 Peak to Valley . . . 88
4.5.5 Dark Counts . . . 89
4.6 Temperature-dependent Measurements in Water . . . 91
4.6.1 Measurement Procedure . . . 92
4.6.2 Analysis . . . 95

4.6.3 Results . . . 97
4.6.4 Discussion . . . 99
4.6.5 Conclusion of Temperature-dependent Dark Rate Characterisation 102
4.7 Pressure Testing . . . 104
4.7.1 PMT Soak Testing in Gadolinium-doped Water . . . 104
4.7.2 Acrylic Vessels . . . 112
4.8 Summary . . . 114

5 Neutrino Experiment One: A Remote Reactor Antineutrino Monitor 117
5.1 Requirements for Reactor Antineutrino Monitor . . . 117
5.2 Location and Facility . . . 118
5.2.1 Underground Facility . . . 118
5.2.2 Reactor Landscape at Boulby . . . 120
5.3 Detector . . . 125
5.3.1 Cavern . . . 125
5.3.2 Rejected Designs . . . 126
5.3.3 Neutrino Experiment One . . . 127
5.4 Simulations . . . 129
5.4.1 Detector . . . 130
5.4.2 Reactor Modelling and Signals . . . 132
5.4.3 Backgrounds . . . 134
5.4.4 Systematic Uncertainties on Signal and Background . . . 147
5.5 Summary . . . 147

6 Event Reconstruction and Data Reduction 149
6.1 Event Reconstruction . . . 150
6.1.1 Vertex Reconstruction . . . 150
6.1.2 Energy Reconstruction . . . 154
6.1.3 Energy Analogues in NEO . . . 160
6.2 Data Reduction using LEARN . . . 161
6.2.1 Neutron Multiplicity . . . 161
6.2.2 Rejection of Radioactive Singles . . . 162
6.2.3 Fast Neutron Rejection . . . 167
6.2.4 Energy Cuts . . . 168
6.2.5 Analytical Post-Muon Veto . . . 171

6.3 Summary 172

7 Sensitivity of Neutrino Experiment One 175

7.1 Required Observation Time 176

7.1.1 Anomaly Detection Metric 176

7.1.2 Reactor Measurement Metric 178

7.1.3 Sensitivity Results 178

7.2 Remote Reactor Ranging 189

7.2.1 Background Inclusion 191

7.2.2 Minimum Chi-Squared Analysis 192

7.2.3 Fourier Transform Analysis 193

7.2.4 Ranging Results 195

7.2.5 Discussion 199

7.3 Conclusions 201

8 Future Work and Conclusions 209

8.1 Current Status of WATCHMAN and AIT-NEO 210

8.2 Boulby Underground Laboratory Development 210

8.3 Conclusion 210

List of Acronyms

AC Alternating Current

ADC Analogue-to-Digital Conversion

AGR Advanced Gas-cooled Reactor

AGS Alternating Gradient Synchrotron

AIT the Advanced Instrumentation Testbed

ANTARES the Astronomy with a Neutrino Telescope and Abyss environmental RESearch project

AWE the Atomic Weapons Establishment

BONSAI Branch Optimization Navigating Successive Annealing Iterations

BUGS Boulby UnderGround Screening

BUTTON the Boulby Underground Test Tank for Observing Neutrinos

CHESS Cherenkov/Scintillation Separation

CLHEP Class Library for High Energy Physics

CNO Carbon-Nitrogen-Oxygen

Cobraa Coincident-Background Reactor Antineutrino Analysis

CoRe Combined Reconstruction

CT Computerised Tomography

DAQ Data Acquisition

DC Direct Current

DIN di-isopropylnaphthalene

DNN the Office of Defense Nuclear Nonproliferation

DONUT Direct Observation of the NU Tau

DT Deuterium-Tritium

DUNE Deep Underground Neutrino Experiment

EGADS Evaluating Gadolinium's Action on Detector Systems

EM Electromagnetic

ES Elastic Scattering

FCT Fourier Cosine Transform

FRET Förster Resonant Energy Transfer

FST Fourier Sine Transform

FT Fourier Transform

GALLEX the Gallium Experiment

GCR Gas-Cooled Reactor

Geant4 GEometry ANd Tracking 4

GLG4sim Generic Liquid-scintillator Anti-Neutrino Detector or *GenericLAND*

HEU Highly Enriched Uranium

HK Hyper-Kamiokande

HV High Voltage

IAEA International Atomic Energy Agency

IBD Inverse Beta Decay

ICL Israel Chemicals Ltd

ID Inner Detector

IMB Irvine-Michigan-Brookhaven

JUNO Jiangmen Underground Neutrino Observatory

KamLAND Kamioka Liquid Scintillator Antineutrino Detector

KM3NeT Cubic Kilometre Neutrino Telescope

LAB Linear Alkyl Benzene

LAPPD™ Large Area Picosecond PhotoDetector™

LEARN Likelihood Event Analysis of Reactor Neutrinos

LEP the Large Electron Positron Collider

LINAC Linear Accelerator

lpm Litres Per Minute

LWR Light Water Reactor

LZ LUX-ZEPLIN

MC Monte Carlo

MCP Micro-Channel Plate

MSW Mikheyev-Smirnov-Wolfenstein

m.w.e Metres Water Equivalent

NDT Non-Destructive Testing

NEO Neutrino Experiment One

NIU Neutrino Interaction Units

NOνA NuMI Off-Axis ν_e Appearance

NPT Treaty on the Non-Proliferation of Nuclear Weapons

OD Outer Detector

PDF Probability Density Function

PID Particle Identification

PINGU Precision IceCube Next Generation Upgrade

PMNS Pontecorvo–Maki–Nakagawa–Sakata

PMT Photo-Multiplier Tube

PPO 2,5-diphenyloxazole

PSUP PMT Support Structure

PWR Pressurised Water Reactor

QA Quality Assurance

RAT-PAC Reactor Analysis Tool - Plus Additional Codes

RENO Reactor Experiment for Neutrino Oscillation

RF Radio-Frequency

SAGE the Soviet-American Gallium Experiment

SETR Single-Electron Time Response

SHV Safe High Voltage

SK Super-Kamiokande

SLAC the Stanford Linear Accelerator Center

SLD the SLAC Large Detector

SMR Small Modular Reactor

SNO the Sudbury Neutrino Observatory

SNU Solar Neutrino Units

SONGS San Onofre Nuclear Generating Station

SPE Single Photo-Electron

STFC Science & Technology Facilities Council

T2K Tokai to Kamioka

TTS Transit Time Spread

UDEAL Underground Device Evaluating Attenuation Length

UV Ultra-Violet

WbLS Water-based Liquid Scintillator

Chapter 1

Introduction

The neutrino is the lightest and most abundant known particle in the Universe. It has very little mass and interacts very rarely, via the weak force, giving them a ghostly nature. Despite this, they contain important information about the nature of the Universe; among other things they carry information about lepton number conservation through their flavour oscillation, about nuclear interactions and decays, and about supernovae. As such, studying the neutrino has been the goal of many physicists around the world since the 1950s.

1.1 The Early History of Neutrinos

1.1.1 Postulation

The neutrino was postulated as a remedy to a problem discovered in 1914 by James Chadwick [6], where the energy spectrum of electrons emitted during β decay did not match the theoretical expectations at the time. The theory at the time suggested β decay would result only in an electron and a change in chemical element. It was expected that, due to the conservation of energy, this electron would be monoenergetic. This became an issue when James Chadwick showed that the electron had a continuous energy spectrum that ended at the expected energy monoenergetic electrons should be emitted at. Figure 1.1 shows an example arbitrary β decay spectrum compared to the expected monoenergetic emission. If energy was conserved, Chadwick's discovery would suggest there is some missing energy. However, there was no consensus on whether this was the case. Niels Bohr suggested that energy may not be conserved during this decay

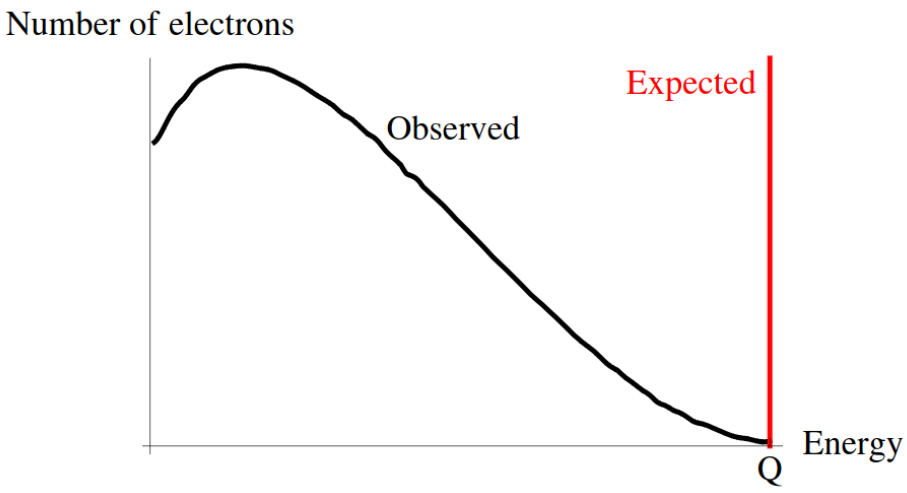

Figure 1.1: Example β decay spectrum. Reprinted from [7].

[8], but is conserved on average.

It would not be until 1930 that a good solution would be proposed. In his letter to a meeting of physicists[1] in Tübingen, addressed "Liebe Radioaktive Damen und Herren"[2], Wolfgang Pauli proposed a "desperate remedy" [9, 10]. His remedy was a new particle. Specifically, he proposed that alongside the electron emitted during β decay, a spin 1/2 neutral fermion that was very weakly interacting was also emitted. This particle would conserve energy and angular momentum. This was a contentious proposal, given only the electron [11] and proton [12] had been discovered at this point. Even Pauli was uncomfortable with the situation; he had proposed a particle he thought impossible to detect.

Despite this, Enrico Fermi adopted a three-body beta decay formalism [13, 14], the first theory of weak interactions. This was originally rejected by Nature for containing "speculations too remote" [15]. Experiments showing the upper energy limit of the emitted electron [16], and James Chadwick's discovery of the neutron in 1932 [17], made the idea of a new neutral particle to carry away excess energy seem more plausible than the idea that energy is not conserved. Fermi proposed that the neutron within a nucleus would decay to a proton, with an electron and the new neutral particle emitted:

$$n \rightarrow p + e^{-} + \bar{\nu}_e.$$

[1] Lise Meitner and Hans Geiger in particular

[2] "Dear radioactive ladies and gentlemen"

He suggested that this new particle could be detected via Inverse Beta Decay (IBD)

$$\bar{\nu}_e + p \rightarrow e^+ + n.$$

The discovery of the neutron did cause one small issue. The new, weakly interacting particle had been called a "neutron" by Pauli due to its neutral nature. However, the neutron discovered by Chadwick was not the same particle, so Pauli's particle needed a new name. Fermi adopted the Italian diminutive "neutrino", coined jokingly by Edoardo Amaldi to mean "little neutral one" [18]. Bethe and Peierls estimated the neutrino cross section to be $\sigma < 10^{-44}\,\mathrm{cm}^2$, concluding there was "no practically possible way of observing the neutrino" [19].

1.1.2 Discovery

1.1.2.1 An Explosive Solution

In 1951, Frederick Reines, then a group leader at Los Alamos laboratory, decided the goal of detecting the "elusive neutrino" was worth striving for [20]. The neutrino was believed to be undetectable, due to it being very weakly interacting. Reines needed a large number of neutrinos to observe them, so naturally he decided an atomic bomb was his best option. Whilst seeming like a radical option, Reines had been involved in the Manhattan Project and later directed a series of nuclear weapons tests. The choice of a bomb was to yield an intense pulse of particles above background. However, neither he nor Fermi, who alongside Bethe agreed an atomic bomb would be the best source of neutrinos, knew how to build a large enough detector to detect the resulting neutrinos. It was not until Reines discussed the idea of neutrino detection with Clyde Cowan Jr. that the concept of a large liquid scintillator detector[3] was discussed as part of Project Poltergeist [21].

Under the plan by Reines and Cowan (Figure 1.2), a large liquid scintillator detector would be suspended half way down a 150 ft shaft, 40 m horizontally from the location the bomb would be detonated at. The area below the detector would be a vacuum tank, and above the detector would be back filled. When the bomb was detonated, the detector would be released and allowed to free-fall. This allows the shock-wave of the blast to pass by without disturbing the detector and should allow the detector

[3]Until then, the largest detectors were a litre or so in volume. Reines and Cowan needed a tonne-scale detector.

to observe neutrinos. Foam rubber and feathers would be piled at the bottom of the shaft for the detector to land on. The detector would then be extracted once the surface radioactivity had died down. This plan was approved by the then director

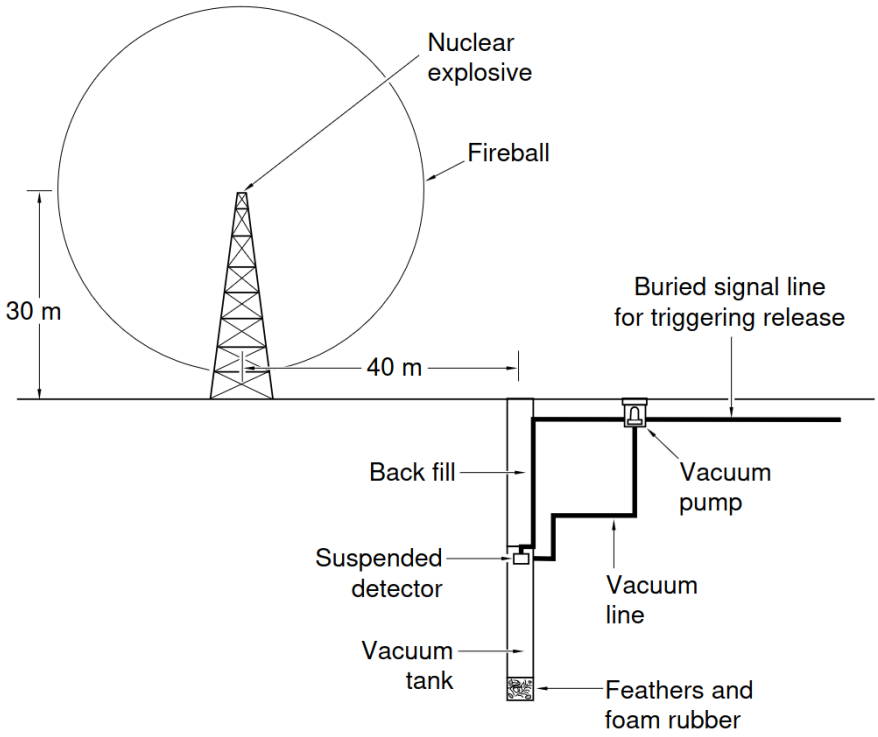

Figure 1.2: The original Reines and Cowan proposal to use a nuclear explosive as a source of neutrinos and detect them by dropping a liquid scintillator detector down a nearby shaft. Reprinted from [21].

of Los Alamos, Norris Bradbury, possibly due to the support of Fermi and Bethe, and possibly due to the success of previous nuclear weapons operations carried out by Reines. Bradbury was also known to be impressed by the 3 orders of magnitude reduction in neutrino interaction cross section the detector could achieve. The previous upper limit was $10^{-37}\,\mathrm{cm}^2$ [22], but Reines and Cowan expected to achieve sensitivity to $10^{-40}\,\mathrm{cm}^2$, although the theoretical value at the time was $10^{-44}\,\mathrm{cm}^2$.

1.1.2.2 A More Sensible Alternative - Hanford Experiment

Work to build a detector and dig a shaft for this experiment was underway as soon as approval was granted. In Autumn 1952, after the work was presented to the Physics

Division at Los Alamos, J. M. B. Kellogg urged Reines and Cowan to review the use of an explosive and instead consider a fission reactor [20, 21]. The neutrino flux from an explosion would be several thousand times that of a reactor, but the gamma and neutron background would be the same. This was the reason the bomb was initially chosen. If the background could be suppressed, the reactor would be a more viable option.

Initially, the intention was to observe the positron produced by IBD first through scintillation and then through annihilation γs. The realisation that identifying the neutron as well as the positron gave Reines and Cowan the mechanism by which to reduce backgrounds. This is what was needed to allow a fission reactor to be used as a source of neutrinos.

The design proposed for their first attempt was a cylindrical, liquid scintillator-filled detector doped with a neutron capture agent, either boron or cadmium[4] [23, 24]. The design consisted of 90 Photo-Multiplier Tubes (PMTs), and was shielded by alternating layers of lead and paraffin to attenuate external γs and neutrons. An umbrella of Geiger-Mueller tubes to veto muons was used to further reduce background rates.

This detector was placed near the face of the Hanford reactor, as seen in Figure 1.3. Energy calibration was performed using ^{60}Co and ^{16}N, and positron-neutron pairs were analysed. Once all backgrounds were considered, the difference in coincident pair rates between the reactor pile being on and off was 0.41 ± 0.20 delayed counts per minute. This gave the first "probable" detection of the neutrino [25].

1.1.2.3 Confirmation - Savannah River

The large reactor-independent background at Hanford, due to the location of the detector on the surface causing it to be exposed to cosmic ray muons, was a major drawback. Cosmic rays and the production of neutron secondaries in the shielding were much more abundant than the neutrino signal. To make a conclusive first detection of the neutrino, a new detector was designed and the Savannah River reactor was used. The Savannah River reactor was much more powerful than Hanford, and had a shielded location 11 m from the core and 12 m underground.

The redesign of the detector was to discriminate neutrinos from the reactor and cosmic ray-produced particles. Two tanks of water with cadmium chloride dissolved in them were sandwiched between three tanks containing liquid scintillators. The protons

[4]Cadmium was used in the final detector.

Figure 1.3: The liquid scintillator detector used at Hanford. Reprinted from [20].

in the water were the targets for IBD, and the scintillator tanks were instrumented with 110 PMTs. If IBD occured in a water tank, the positron annihilation would be visible in the scintillator tank above and below that water tank. A neutron capture event would then follow to create a delayed-coincidence signal. No signal would originate from the scintillation tank furthest from the water tank in which the event occurred. This allowed the location of the event to be determined and false-coincident events to be discriminated. For false-coincident events, there would be no clear relation between the location of the signals. The layout of the detector can be seen in Figure 1.4.

The experiment took over 1371 hours of data [26], including both reactor on and off time, with an initial aim to determine whether there was an increase of neutrino-like signals when the reactor was on. The rate observed with the reactor on was over a factor of 5 greater than with the reactor off, at 2.88 $\pm$ 0.22 counts per hour and 0.56

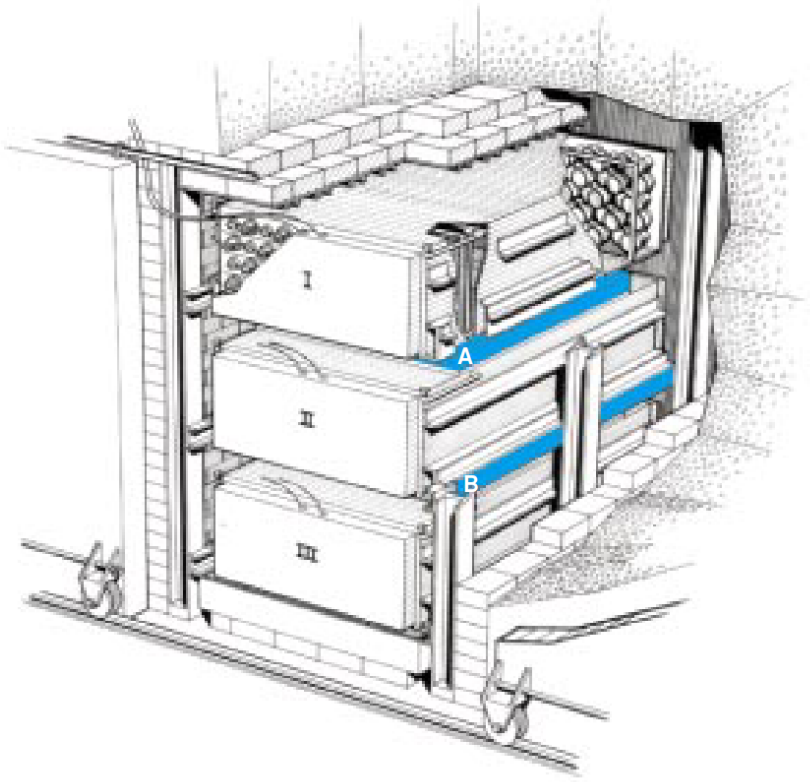

Figure 1.4: Schematic of the Savannah River Neutrino Detector. Reprinted from [21].

$\pm$ 0 06 counts per hour respectively.

To confirm this observation was due to neutrinos, several studies of the system and backgrounds were performed. Changes to the shielding were tested to confirm that γs and neutrons are not entering the detector, and that the neutrino-like rate does not change. Confirmation that the first signal in the pair was a positron came by changing the lead shielding between the water and scintillation tanks to reduce the positron detection efficiency as annihilation γs are shielded. Varying the cadmium concentration caused the neutron capture efficiency to change, and the coincident signal rate dropped to nearly 0 when the cadmium was removed. Heavy water was added to the water tanks to reduce the proton density, and showed a significant drop in the antineutrino detection efficiency but only a slight drop for background events [20].

These tests, alongside the significant signal increase with the reactor on and the signal to background ratio of 4:1 for accidental and 5:1 for correlated reactor-independent backgrounds, confirmed the first detection of the neutrino had been made [20, 21, 26]. This news was sent to Pauli via telegram; he supposedly interrupted his meeting to

read this and celebrated with champagne.

The expriment at Savannah River was updated and improved to measure a more accurate interaction cross section, with a result consistent with theory [27].

1.1.3 Flavours

After the detection of the neutrino, evidence of parity violation was found in beta decay by Wu [28] after being proposed by Lee and Yang [29], and explained by several people as the theory of weak decay was developed [30–32]. The neutrino was also shown to be left-handed[5] shortly afterward [33]. Cowan and Reines considered the idea of using the neutrino to probe the weak interaction in energy ranges beyond ordinary β decay using accelerators [20]. They also considered the question of was the "neutretto", the neutral particle produced when a pion decays into a muon, the same as the neutrino from β decay.

The muon had been discovered in 1937 [34] and was expected to decay to an electron. However, the electron showed a continuous energy distribution much like in β decay. Searches for

$$\mu \rightarrow e + \gamma$$

showed an absence of the γ energy emission [35]. Treating the decay of muons in the same way as β decay seemed sensible.

The idea of using an accelerator was conceived independently by Bruno Pontecorvo [36] and Melvin Schwartz [37]. The suggestion was a proton beam could be directed at a target to produce pions and kaons, which decay to muons and neutrinos that travel approximately in the direction of the original proton beam.

In 1962, Schwartz alongside Lederman and Steinberger led a team to investigate the neutrino produced alongside a muon [38]. Using the Alternating Gradient Synchrotron (AGS) at Brookhaven, they investigated the

$$\pi^{\pm} \rightarrow \mu^{\pm} + (\nu/\bar{\nu})$$

interaction with the expectation that if the neutrino here is the same as β decay, electrons and muons would be produced in equal abundance by neutrino interactions.

To do this, pulses of protons from the AGS were diverted to a beryllium target to produce pions and kaons. The π and K were produced in the general direction of the

[5]Its direction of motion is opposite to its direction of spin.

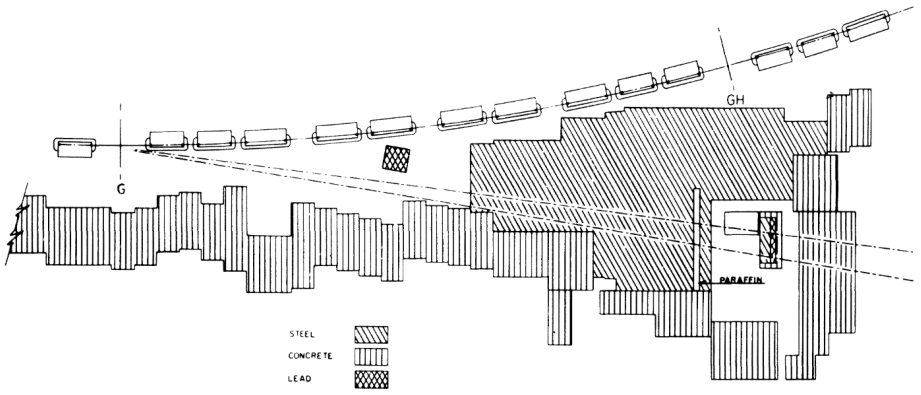

Figure 1.5: Plan view of the AGS neutrino experiment. Reprinted from [38].

protons, and directed at an iron shield. Neutrinos are produced during the pion decay and the shield stops all but the neutrinos. An array of spark chamber modules was used to detect charged particles produced by neutrinos interacting. A plan of the whole setup is shown in Figure 1.5.

The pulses of protons were used to create 30 ns gates with a Cherenkov counter on the pion beam in coincidence with triggering panels in the detector. Tracks in the spark chamber were used to identify events, with muons leaving single tracks and those produced by neutrinos having tracks originating within the detector. Electrons produce showers in a spark chamber, so muons and electrons can be distinguished. The electron shower signal was calibrated by taking two of the modules from the detector to the Cosmotron electron beam.

Out of the events observed, 34 were single tracks produced in the detector and therefore deemed to be muons. Of these, 29 were expected to be due to neutrinos after cosmic ray analysis with the AGS switched off. If the neutrinos associated with β decay and muons were the same, around 29 electrons showers would be observed. However, only 6 were seen and they were of different appearance to those seen at the Cosmotron. The conclusion was therefore

$$\nu_e \neq \nu_\mu$$

when lepton universality is considered. This was the first confirmation that there are multiple types of neutrino, and won the Nobel Prize in 1988[6].

In 1975, the discovery of anomalous lepton production in electron-positron anni-

[6]This won the Nobel Prize before Frederick Reines did for the first detection of the neutrino, which was in 1995

hilation at the Stanford Linear Accelerator Center (SLAC) led to the discovery of a new lepton with a mass of 1.6 - 2.0 GeV [39][7]. This was the tau, which has a mass of 1.77686 GeV [40]. A new lepton flavour indicated a new neutrino flavour to go with it. Due to the high mass, tau production and measurements proved difficult. However, the total number of lepton flavours could be constrained via the number of particles that couple to the Z^0 boson. It is assumed that the "invisible" component of the Z^0 decay width is due to neutrinos, and can be determined by subtracting all observed decays from the total Z^0 decay width. Measurements at the Large Electron Positron Collider (LEP) [41–44] and in the SLAC Large Detector (SLD) [45] (Figure 1.6) gave indirect evidence of the tau neutrino from this, and combined analysis of all data gave a constraint on the number of active light neutrinos with $2m_\nu < m_Z$ of [46]

$$N_\nu = 2.9840 \pm 0.0082.$$

The first direct observation came from Direct Observation of the NU Tau (DONUT) in 2000 [47], when they used the decay of charmed mesons produced by 800 GeV protons from the Tevatron at Fermilab hitting a tungsten target to produce tau leptons in

$$D_S \rightarrow \bar{\nu}_\tau + \tau \text{ and}$$

$$\tau \rightarrow \nu_\tau + X.$$

The neutrino underwent charged-current interactions in the nuclear emulsion detector to produce τ leptons. The τ has a short lifetime and so decayed quickly to a single charged daughter with a branching ratio of 0.86 and a short $\sim$2 mm track. The decay leaves a "kink" in the track with allows the τ to be identified. Four of these tracks were seen by DONUT, with an estimated background of 0.34 ± 0.05 events and a probability of 4×10^{-4} of the tau tracks being background. This gave the first direct measurement of ν_τ, and completed the set of active light neutrinos.

1.1.4 Bruno Pontecorvo

The key moments in the history of our understanding of neutrinos cannot be discussed without mentioning the Italian-born Soviet physicist Bruno Pontecorvo. Bruno Pontecorvo started in experimental physics at Rome University where, as part of Fermi's Via Panisperna boys, he was involved in the experiment that led to the discovery of

[7] This won Martin Perl the Nobel Prize alongside Frederick Reines in 1995

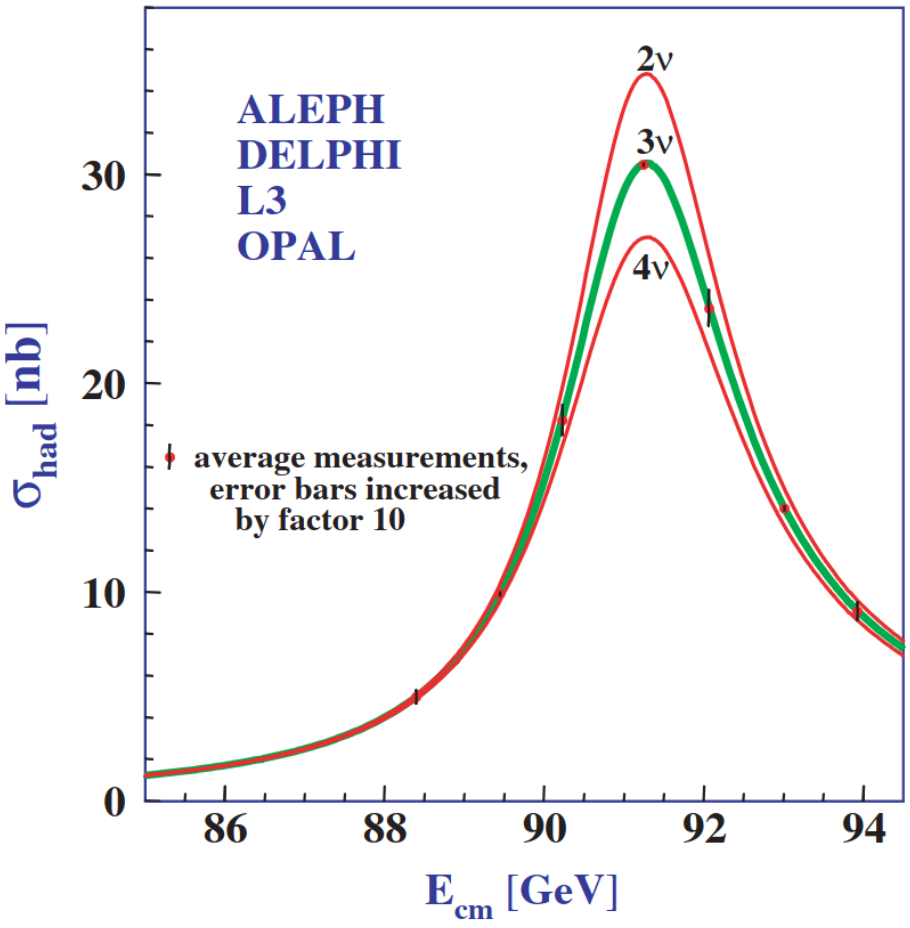

Figure 1.6: The hadron production cross section near the resonance of the Z^0 boson from combined measurements. The coupling predictions of the Standard Models for two, three and four neutrino species are shown under the assumption they account for the invisible decay width. Reprinted from [46].

slow neutrons in hydrogenous materials and neutron activation [48, 49]. This discovery led to the discovery of nuclear fission.

He then moved to Paris to join the Curie-Joliot group, where he studied nuclear isomerism. Here, he studied the excitation of protons and neutrons via interaction with γs followed by subsequent energy emission, noting that there was no chemical change [50]. During his time in France, Pontecorvo joined the French Communist Party.

In 1940, as Paris was under the threat of German occupation and Pontecorvo being of Jewish descent, he fled with his family by bicycle [51]. After initial rejection by the British, he moved to Oklahoma to work on oil well logging using neutrons [52–56]. He

developed a method that saw the first practical use of slow neutrons.

Following this period, he worked in the British Tube Alloys team on the development of nuclear weapons in Montreal [51], which became part of the Manhattan Project. In particular, he was involved in the development of the ZEEP nuclear reactor at Chalk River and the commissioning of the NRX reactor, the most powerful research reactor in the world that the time [51, 57].

In Canada, Pontecorvo started his research into elementary particle physics, taking an interest in cosmic rays and neutrinos. In 1946, he proposed the radiochemical method for neutrino detection [58]

$$\nu + (A, Z) \rightarrow e^- + (A, Z + 1).$$

The decay of the secondary nucleus could be used to observe the interaction. Pontecorvo suggested

$$^{37}\mathrm{Cl} + \nu_e \rightarrow {}^{37}\mathrm{Ar} + e^- \tag{1.1}$$

as

- C_2Cl_4 is a cheap, non-flammable liquid;
- ^{37}Ar is unstable with a 34.8 day half-life;
- ^{37}Ar is a rare gas and can be extracted from a large detector.

This mechanism was later used by Ray Davis to show that the antineutrino and neutrino are different particles [59] and at Homestake for solar neutrino detection [60], which also used Pontecorvo and his team's low-background proportional counter invented in 1948 [57, 61].

Once the muon had been shown to be weakly interacting [62], Pontecorvo, alongside Hincks, set about investigating the decay [35, 63]. An upper limit on the probability of the

$$\mu \rightarrow e + \gamma$$

decay was set, before Pontecorvo drew an analogy between electron and muon weak interactions [64]. He suggested that the weak interaction has an $e - \nu$ pair and a $\mu - \nu$ pair, and that the weak interaction is universal to $e - \mu$. He also suggested that the muon is a spin 1/2 particle and a neutrino is emitted when a muon captures on a nucleus. His investigation of

$$\mu^- + (A, Z) \rightarrow \nu + (A, Z - 1) \text{ and } e^- + (A, Z) \rightarrow \nu + (A, Z - 1)$$

showed that they are both characterised by the same Fermi constant G_F, leading him to conclude there is a "fundamental analogy" between β-processes and muon absorption.

He continued his work on nuclear reactor design and slow neutrons, and moved to Harwell in the UK. The FBI had suspected Pontecorvo and his wife of being communist, and had already identified his siblings as communists. Colleagues of Pontecorvo who had worked on the Manhattan project and other nuclear development, such as Klaus Fuchs, were confirmed as Soviet spies which raised concern over Pontecorvo. In September 1950, when on holiday in Rome, he and his family abruptly flew to Stockholm. He was helped by Soviet agents to enter Finland and then the Soviet Union, where he was welcomed and given significant honours and privileges, thus defecting from his Italian and British citizenship. His defection caused major concerns in the West over the potential transfer of nuclear secrets.

Once in the Soviet Union, he joined what is now the Joint Institute for Nuclear Research (JINR) in Dubna. From the late 1950s, he started considering the use of an accelerator for neutrino experiments via pion and kaon production and decay [36]. He also started considering the role of the neutrino, and whether the neutrinos associated with electrons and muons are the same. Over the decade from 1957, he started working on the idea that neutrinos were different types and could oscillate between the types. This was inspired by the

$$K^0 \rightleftarrows \bar{K}^0$$

strangeness oscillations [65]. Starting with the idea that neutrinos and antineutrinos could oscillate between each other [66, 67], he eventually developed the idea that

$$\nu_\mu \rightleftarrows \nu_e$$

could occur [68] after the discovery that

$$\nu_e \neq \nu_\mu,$$

something he suspected to be the case since his time in Canada in the 1940s [57]. He was also able to predict that neutrinos would be produced in intense bursts by supernovae.

Bruno Pontecorvo's theories are especially impressive when it is realised that he developed many of them before the prerequisite theories and measurements existed. He developed ideas surrounding the interaction of particles before they had been discovered, and proposed several ideas that would later be used in significant breakthrough measurements.

1.2 Neutrino Propagation

Whilst neutrinos are unusual in their interaction properties, they are even more unusual in their propagation. The quantum mechanical process of neutrino oscillation, in which the probability of observing a neutrino in a weak lepton flavour (e, μ, τ) state changes as it travels, gives rise to unique properties.

1.2.1 Postulation of Oscillation

As stated, the concept of neutrinos oscillating between states was proposed by Pontecorvo in 1957 based on the idea that neutrinos and antineutrinos were different states. This allowed the theory of neutrino flavour oscillations by Maki, Nakagawa and Sakata to be developed in 1962 [69], with Pontecorvo himself significantly adapting his theory over time. Despite the concept of neutrino flavour oscillations being around for some time, there was little evidence and consensus that the theory was correct for a long period.

1.2.2 Missing Neutrinos and the Solution

Since their first detection, neutrinos have been studied in many different ways. In the 1950s, Ray Davis attempted to apply Pontecorvo's proposed radiochemical method (Equation 1.1) [59] to reactor neutrinos but saw no clear detection. He did, however, show neutrinos and antineutrinos are not the same particle. He then proposed this method for a solar neutrino detector in the Homestake mine alongside John Bahcall [60, 70]. Bahcall produced a model of the solar neutrino flux [71] based on Bethe's mechanisms of solar energy production in the *pp* and Carbon-Nitrogen-Oxygen (CNO) chains [72], and attempted to measure this flux with the proposed detector.

The first version of the detector saw no result, so a second version was developed. This detector was filled with 390,000 L of C_2Cl_4, and had an overburden of 4,400 Metres Water Equivalent (m.w.e). As neutrinos interact, gaseous Ar is produced. It is extracted by flushing the detector with helium and a known quantity of ^{36}Ar to measure the extraction efficiency, and the ^{37}Ar decays are counted using a proportional counter. The threshold of 814 keV meant only a sample of the solar flux could be measured, demonstrated by the solar neutrino spectra in Figure 1.7.

The initial measurements created an upper limit to the observed flux, but this limit was significantly below the expected value. Over the 20 year of data-taking life of the

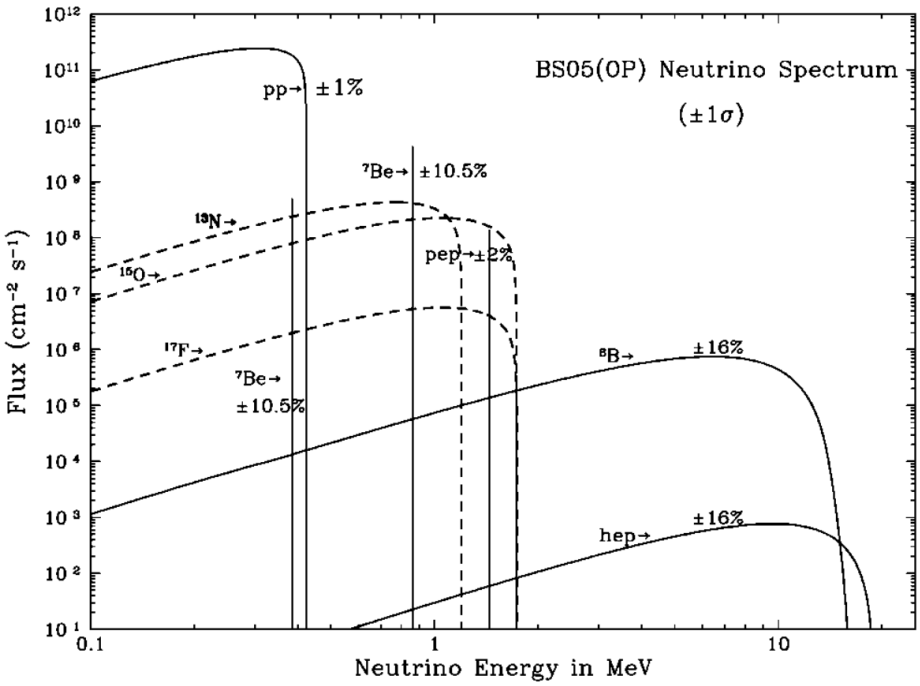

Figure 1.7: Standard solar model neutrino spectra. The dotted lines are from the CNO fusion chain. Reprinted from [73].

experiment, a flux of 2.56 ± 0.16 (stat.) ± 0.16 (sys.) Solar Neutrino Units (SNU), where 1 SNU equals 10^{-36} captures per target atom per second, was measured [74]. This flux was significantly below the expected value, which Bahcall placed at 9.3 ± 1.3 SNU [75].

This created the "Solar Neutrino Problem", and there was debate as to why two thirds of the expected neutrinos were not observed. Experimental uncertainties were ruled out and the theoretical models checked, but the problem persisted.

Tension between theory and data increased as several experiments saw deficits. An alternative radiochemical method using gallium was proposed [76, 77], where the interaction

$$^{71}\mathrm{Ga} + \nu_e \rightarrow {}^{71}\mathrm{Ge} + e^- \tag{1.2}$$

is used. This has a threshold of 233 keV and could detect neutrinos from the *pp* interaction. This was a criticism of the Homestake experiment, and so gallium could resolve some disputes.

This method was applied in two concurrent experiments in the 1990s, the Gallium Experiment (GALLEX) and the Soviet-American Gallium Experiment (SAGE).

GALLEX, at Gran Sasso, used liquid $GaCl_3$ as the target; SAGE used liquid gallium metal just above its melting point. Both removed the germanium chemically and used proportional counters to observe the decays. GALLEX observed only 55 % of the predicted solar neutrino flux [78], with SAGE only seeing 55 - 60 % [79]. This provided support for the observations made by Homestake.

Radiochemical detectors were not the only ones to see a deficit. Kamiokande, a water Cherenkov detector, used neutrino-electron scattering to observe solar neutrinos. The outgoing electron direction strongly correlates to the neutrino direction in this process, and allows the direction of origin of the signal to be confirmed. Energy reconstruction of the event allowed the fusion process within the Sun that produced the neutrino to be identified. Despite using an entirely different detection method, Kamiokande still saw a deficit in the solar neutrino flux of around half the expected value [80]. Although this elastic scattering process is sensitive to all neutrino flavours, is it most sensitive to electron neutrinos as they are able to interact via both the neutral and charged current; the other flavours can only interact via the neutral current. Even if all interactions in Kamiokande are attributed to ν_e, the rate still falls below the predictions.

Many sources for the deficit were postulated, including astrophysical causes. However, a second anomaly in the neutrino sector appeared to rule this out. Atmospheric neutrinos, produced by pions and muons decaying in the atmosphere as a result of cosmic ray collisions, are expected to be a mix of electron and muon flavours. The expected ratio $N_{\nu_\mu}/N_{\nu_e} = 2$ is due to the decays

$$\pi^+ \rightarrow \mu^+ + \nu_\mu,$$

$$\mu^+ \rightarrow e^+ + \bar{\nu}_\mu + \nu_e.$$

Both Irvine-Michigan-Brookhaven (IMB) and Kamiokande saw reductions in the muon neutrino rate, resulting in a smaller than expected ratio [81, 82]. Searches at higher energies (multi-GeV) by Kamiokande, where the angular correlation between the neutrino and the charged lepton produced in the detector is better and neutrinos are more likely to be able to pass through the Earth, showed a large correlation between the reduced muon neutrino flux and the zenith-angle [83]. The lower energy (sub-GeV) neutrinos were isotropic in the detector.

This effect was confirmed by Super-Kamiokande (SK) with high statistics measurements of the asymmetry between upward- and downward-going neutrinos, with no asymmetry seen for electron neutrinos. This was strong evidence that neutrinos change

flavour as they travel. The upward-going neutrinos travel significantly further and hence have more opportunity to change flavour. This creates the reduction in muon flavour neutrinos. Furthermore, SK observed a result consistent with the oscillation of ν_μ to ν_τ, with the largest disappearance corresponding to the largest distance of travel [84].

Neutrino oscillations were confirmed, and the deficits resolved, when the Sudbury Neutrino Observatory (SNO) made measurements of the solar neutrino flux using heavy water (D_2O) [85]. Like previous water-based experiments, SNO was sensitive to charged current interactions,

$$\nu_e + {}^2\mathrm{H} \rightarrow p + p + e^-.$$

However, owing to its heavy water SNO was also sensitive to the neutral current,

$$\nu_x + {}^2\mathrm{H} \rightarrow p + n + \nu_x.$$

The neutral current interaction here has a 2.2 MeV threshold and so only sampled ^{8}B neutrinos, but is sensitive to all neutrino flavours. By observing a deficit in the charged current consistent with previous measurements, but showing a flux matching the expected solar flux in the neutral current, SNO conclusively confirmed that neutrinos oscillate in flavour as they propagate [86, 87]. The final cross-check on the measurement came from the elastic scattering process used in Kamiokande. As this is sensitive to all flavours but with a preference for electron flavour neutrinos, the flux should be higher than the charged current. By comparing their charged current interaction rates with SK's high statistics elastic scattering rate [88], SNO was able to show that the flux measured by elastic scattering was higher than that measured via the charged current as expected.

1.2.3 Current Theories

1.2.3.1 Vacuum Oscillations

The oscillation of flavour is unique to neutrinos as far as is currently known, and occurs due to the weak and mass eigenstates not being aligned. Neutrinos are produced at the vertex of the weak interaction, and are in a flavour state defined by the charged leptons in the interaction. However, each time a neutrino is produced in flavour state α, there is a probability that mass state i is created. Currently, there are three known flavour and mass states neutrinos can exist in, with the flavour state being a coherent

superposition of the mass states;

$$|\nu_\alpha\rangle = \sum_{i=1}^{3} U^*_{\alpha i}|\nu_i\rangle \quad \text{and} \quad |\nu_i\rangle = \sum_{\alpha=e,\mu,\tau} U_{\alpha i}|\nu_\alpha\rangle. \tag{1.3}$$

Here, $U_{\alpha i}$ is the Pontecorvo–Maki–Nakagawa–Sakata (PMNS) mixing matrix [69]. The PMNS matrix is unitary under the assumption neutrinos are Dirac fermions, and has dimensions 3×3 describing all possible rotations between mass and flavour states.

$$\begin{aligned} U = & \begin{pmatrix} U_{e1} & U_{e2} & U_{e3} \\ U_{\mu 1} & U_{\mu 2} & U_{\mu 3} \\ U_{\tau 1} & U_{\tau 2} & U_{\tau 3} \end{pmatrix} \\ & \underbrace{\begin{pmatrix} c_{12} & s_{12} & 0 \\ -s_{12} & c_{12} & 0 \\ 0 & 0 & 1 \end{pmatrix}}_{\text{solar}} \underbrace{\begin{pmatrix} c_{13} & 0 & s_{13}e^{-i\delta_{\text{CP}}} \\ 0 & 1 & 0 \\ -s_{13}e^{i\delta_{\text{CP}}} & 0 & c_{13} \end{pmatrix}}_{\text{accelerator}} \underbrace{\begin{pmatrix} 1 & 0 & 0 \\ 0 & c_{23} & s_{23} \\ 0 & -s_{23} & c_{23} \end{pmatrix}}_{\text{atmospheric}}, \end{aligned} \tag{1.4}$$

where $c_{ij} = \cos\theta_{ij}$ and $s_{ij} = \sin\theta_{ij}$ are the mixing angles between states i and j, and δ_{cp} is the CP violating phase. The CP violating phase is a complex phase that introduces difference between neutrino and antineutrino oscillations, and is placed onto θ_{13} by convention; each rotation will contribute a complex phase however. A fourth matrix is required if neutrinos are Majorana particles, with the form diag(1, $e^{i\phi_1}$,$e^{i\phi_2+\delta}$) [89].

Neutrinos propagate in their mass state $|\nu_i\rangle$, as only these are eigenstates of the Hamiltonian, and have eigenvalues of $E_i = \sqrt{m_i^2 + \mathbf{p}_i^2}$. The states evolve according to the time-dependent Schrödinger equation with no potential assuming a vacuum, and have a plane wave solution of the form

$$|\nu_i(x,t)\rangle = e^{-i(E_i t - \mathbf{p}_i \mathbf{x})}|\nu_i\rangle. \tag{1.5}$$

The flavour states are then expressed as

$$|\nu_\alpha(x,t)\rangle = \sum_{i=1}^{3} U^*_{\alpha i} e^{-i(E_i t - \mathbf{p}_i \mathbf{x})}|\nu_i\rangle. \tag{1.6}$$

Combining this with Equation 1.3 gives

$$|\nu_\alpha(x,t)\rangle = \sum_{\beta=e,\mu,\tau} \sum_{i=1}^{3} U^*_{\alpha i} e^{-i(E_i t - \mathbf{p}_i \mathbf{x})} U_{\beta i}|\nu_i\rangle, \tag{1.7}$$

which shows that the mass state is a superposition of all three flavour states for $t > 0$. Flavour state $|\nu_\alpha\rangle$ can be detected in flavour state $\langle\nu_\beta|$ some time later, with a probability given by the square of the transition amplitude

$$P(\nu_\alpha \to \nu_\beta) = |\langle\nu_\beta|\nu_\alpha(x,t)\rangle|^2 \tag{1.8}$$

$$\sum_i \sum_j U^*_{\alpha i} U_{\beta i} U_{\alpha j} U^*_{\beta j} e^{-i((E_i - E_j)t - (\mathbf{p}_i - \mathbf{p}_j)\mathbf{x})}. \tag{1.9}$$

The orthogonality of flavour states dictates that $\langle\nu_\beta|\nu_\alpha\rangle = \delta_{\beta\alpha}$. As neutrinos are highly relativistic, the plane-wave term is approximated to

$$E_i t - \mathbf{p}_i \mathbf{x} \approx \frac{m_i^2 L}{2E} \tag{1.10}$$

for a distance of travel L. The total oscillation probability is then given as

$$P_{\nu_\alpha \to \nu_\beta}(L, E) = \sum_i \sum_j U^*_{\alpha i} U_{\beta i} U_{\alpha j} U^*_{\beta j} \exp\left(- i \frac{\Delta m^2_{ij} L}{2E} \right), \tag{1.11}$$

where $\Delta m^2_{ij} = m^2_j - m^2_i$ is the mass-squared difference. The transition probability requires two non-zero neutrino masses as it is sensitive to the mass difference between states. This is in disagreement with the Standard Model, which requires neutrinos to be massless.

Vacuum oscillations explain the atmospheric neutrino anomaly, with the measurements made by SK matching these theoretical expectations. For reactor neutrinos, vacuum oscillations are similarly of relevance, with the survival probability of electron antineutrinos being of importance. The survival probability is given by

$$\begin{aligned} P_{\bar{\nu}_e \to \bar{\nu}_e} = 1 &- \cos^4(\theta_{13}) \sin^2(2\theta_{12}) \sin^2\left(\frac{1.27 \Delta m^2_{21} L}{E_{\bar{\nu}}} \right) \\ &- \cos^2(\theta_{12}) \sin^2(2\theta_{13}) \sin^2\left(\frac{1.27 \Delta m^2_{31} L}{E_{\bar{\nu}}} \right) \\ &- \sin^2(\theta_{12}) \sin^2(2\theta_{13}) \sin^2\left(\frac{1.27 \Delta m^2_{32} L}{E_{\bar{\nu}}} \right). \end{aligned} \tag{1.12}$$

1.2.3.2 Matter Oscillations

Although the atmospheric neutrino problem is solved by neutrino oscillations in a vacuum potential, the solar neutrino problem is not. The oscillation frequency, as shown in Equation 1.11, depends on L/E. As solar neutrinos do not all have the same energy,

different frequencies are expected. However, if L/E is very large, as is the case for solar neutrinos, the neutrinos should oscillate many times. This should form a detailed sinusoidal structure which will average out to a probability of each flavour of 1/3 for all energies. The results for solar neutrino measurements do not show this. Instead, the energy range each experiment is sensitive to has an effect on the electron neutrino flux observed. This suggests that very few flavour changes are happening before the neutrinos are observed, so that small changes to E create a large change in the survival probability. Furthermore, the distance to the Sun from Earth (L) changes seasonally, so the observed flux should also change seasonally but this is not the case.

This occurs due to the fact solar neutrinos are produced in the ultra-dense solar core and not in the near vacuum like atmospheric neutrinos are. Here, there are many free electrons in the dense plasma which ν_e can interact with, but there are no muons or taus for the other flavours to be affected by. This creates a potential in the Hamiltonian which will then change the oscillation parameters. This is the Mikheyev-Smirnov-Wolfenstein (MSW) effect [90, 91].

The MSW effect is resonant, so under certain conditions all electron-neutrinos are efficiently converted to another flavour. The lower energy *pp* chain neutrinos are mostly unaffected, but the higher energy neutrinos are. This creates the observed energy dependence on the solar ν_e flux on Earth, and accounts for the near disappearance of ^{7}Be neutrinos. This resonance only occurs if the mass that mostly consists of electron neutrinos (ν_1) is not the heaviest of the three masses (i.e., $\nu_1 < \nu_2$), which gives some information on the ordering of the masses[8].

The effect of changing density as a neutrino propagates through the medium to the near-vacuum as it leaves the Sun changes the mass state. In the high density limit of the solar core, the matter mixing angle tends to $\pi/2$. The neutrino mass states in matter, represented as

$$|\nu_{1m}\rangle = \cos\theta_m|\nu_e\rangle + \sin\theta_m|\nu_\alpha\rangle, \tag{1.13}$$

$$|\nu_{2m}\rangle = -\sin\theta_m|\nu_e\rangle + \cos\theta_m|\nu_\alpha\rangle, \tag{1.14}$$

reduce to

$$|\nu_{1m}\rangle \approx |\nu_\alpha\rangle, \tag{1.15}$$

$$|\nu_{2m}\rangle \approx -|\nu_e\rangle, \tag{1.16}$$

[8]It is unknown whether ν_3 is the heaviest or lightest mass state. This is the mass hierarchy problem.

so the electron neutrinos are mostly in the second mass state. Due to the change in density being slow enough to be considered adiabatic, transitions between ν_{1m} and ν_{2m} are neglected. Once the neutrinos escape the Sun, they revert to the vacuum potential. A near perfect match to the expected flux under the assumption of the MSW effect occurring was seen by SNO, with the difference being due to matter effects in the Earth causing a small ν_e regeneration.

1.2.4 Current Measurements

Since the confirmation that neutrinos do indeed oscillate in flavour, several experiments have been measuring the parameters of oscillation. The parameter space that an experiment is sensitive to is determined by its setup. The labels on Equation 1.4 give an indication of the type of experiment needed to measure a particular oscillation. Most experiments will analyse in a two-flavour mixing assumption and focus on the relevant parameters to simplify the relationship between oscillation parameters.

The constraints on θ_{12} and Δm^2_{21} are dominated by the long baseline reactor experiment Kamioka Liquid Scintillator Antineutrino Detector (KamLAND) and solar experiments. KamLAND [92] is particularly sensitive to Δm^2_{21} [93], and dominates the global fits, but there is tension [94] with the solar experiments [74, 95–101]. Recent SK data reduces this tension [102]. The solar experiments deduce $m_2 > m_1$ due to the MSW effect.

There are several short baseline reactor experiments setup for measuring θ_{13}. These experiments look for $\bar{\nu}_e$ disappearance over a short distance, with Daya Bay [103] and Reactor Experiment for Neutrino Oscillation (RENO) [104] having consistent results. This is the most recently determined mixing angle, and the smallest. Double Chooz first indicated that this mixing angle was non-zero [105], before Daya Bay confirmed it [106]. The importance of this angle being non-zero comes from its coupling to δ_{CP}; CP violation could not occur in the neutrino sector if this mixing angle was zero. Reactor experiments are sensitive to an effective mass which includes Δm^2_{32} as well as Δm^2_{31} [107], so the tightest constraints on Δm^2_{31} come from long baseline accelerator experiments.

Atmospheric neutrinos are used to measure θ_{23} and Δm^2_{32} through ν_μ disappearance. Experiments such as SK [108], IceCube DeepCore [109, 110] and the Astronomy with a Neutrino Telescope and Abyss environmental RESearch project (ANTARES) [111, 112] have all made measurements of Δm^2_{32} comparable with each other, although there

is some tension in the θ_{23} measurements between SK and DeepCore. Both SK and IceCube have observed ν_τ appearance in atmospherics [113, 114], which is experimental proof of neutrino oscillations.

Accelerator experiments, such as Tokai to Kamioka (T2K) [115] and NuMI Off-Axis ν_e Appearance (NOνA) [116], use meson decays to produce neutrino beams. By tuning the L/E properties of the beam-to-detector setup, different oscillation parameters can be achieved. These experiments are sensitive to the θ_{23} and Δm^2_{32} parameters through ν_μ disappearance, and θ_{13} through ν_e appearance. They also have some sensitivity to δ_{CP}, with T2K finding evidence to 3σ that δ_{CP} is non-zero in 2020 [117]. This result initially had a large tension with NOνA in normal ordering[9], but reanalysis gave results consistent to a 1.7σ level [118].

The current oscillation parameter measurements from a global fit are given in Table 1.1.

Parameter	Mass Hierarchy	
	Normal	Inverted
$\sin^2\theta_{12}$	$0.303^{+0.012}_{-0.012}$	$0.303^{+0.012}_{-0.011}$
θ_{12} (°)	$33.41^{+0.75}_{-0.72}$	$33.41^{+0.75}_{-0.72}$
$\sin^2\theta_{23}$	$0.451^{+0.019}_{-0.016}$	$0.569^{+0.016}_{-0.021}$
θ_{23} (°)	$42.2^{+1.1}_{-0.9}$	$49.0^{+1.0}_{-1.2}$
$\sin^2\theta_{13}$	$0.02225^{+0.00056}_{-0.00059}$	$0.02223^{+0.00058}_{-0.00058}$
θ_{13} (°)	$8.58^{+0.11}_{-0.11}$	$8.57^{+0.11}_{-0.11}$
δ_{CP}	232^{+36}_{-26}	276^{+22}_{-29}
$\frac{\Delta m^2_{21}}{10^{-5}\text{eV}^2}$	$7.41^{+0.21}_{-0.20}$	$7.41^{+0.21}_{-0.20}$
$\frac{\Delta m^2_{3l}}{10^{-3}\text{eV}^2}$	$+2.507^{+0.026}_{-0.027}$	$-2.486^{+0.025}_{-0.028}$

Table 1.1: Three-flavour oscillation parameters from a global fit to data including SK atmospheric data [108] and using χ^2 mapping for relevant neutrino parameters. Data taken from NuFIT 5.2 [118].

Future experiments aim to determine the octant of θ_{23} ($< \pi/2$ or $> \pi/2$), the mass hierarchy and δ_{CP}. Atmospheric experiments such as Precision IceCube Next Generation Upgrade (PINGU) [119] and Cubic Kilometre Neutrino Telescope (KM3NeT) [120] aim to determine the octant of θ_{23}, and new accelerator experiments such as

[9] $\nu_1 < \nu_2 < \nu_3$. Inverted ordering is defined as $\nu_3 < \nu_1 < \nu_2$.

Hyper-Kamiokande (HK) [121] and Deep Underground Neutrino Experiment (DUNE) [122] will look at δ_{CP}. DUNE should be sensitive to the mass hierarchy with its 1300 km baseline and larger matter effects. The Jiangmen Underground Neutrino Observatory (JUNO) [123, 124] reactor experiment aims to resolve the mass hierarchy in a model independent way.

1.3 Nuclear Reactors and the Role of the Antineutrino

Nuclear fission reactors have been a source of power generation since the 1950s [125], and continue to be used extensively across the world as a clean[10] energy source. In 2020, the International Atomic Energy Agency (IAEA) predicted an increase in global nuclear capacity of 80 % by 2050 [126].

However, nuclear fission has been used in weapons since the Second World War. Plutonium, a key material for nuclear weapons, is a by-product of nuclear power generation due to the irradiation of ^{238}U [127]. Chemical reprocessing can allow this plutonium to be extracted and used. This creates a scenario whereby power generation can be weaponised without careful constraints and monitoring.

1.3.1 Reactors for Power Generation

Nuclear reactors produce energy through the fission of ^{235}U, ^{238}U, ^{239}Pu and ^{241}Pu, where neutrons are captured and cause the isotope to split (fission) into neutron-rich daughter isotopes. The fission process releases neutrons, 2.5 on average [128], and gammas. The neutrons can cause further fission, continuing the process, and the gammas carry energy that can be used for power generation. The fission process requires an injection of neutrons to start, but can be self-sustaining once going. As multiple neutrons are emitted per fission, the rate of fission will increase with each reaction. This creates a chain reaction which is controlled via neutron-absorbing control rods, made out of materials such as boron or graphite, which stop the rate of reaction running away and becoming out of control. The controlled chain reactions produce a large amount of energy, which is transferred to a coolant and used for generating electricity. Not all neutrons will cause fission reactions. To cause a fission, neutrons generally need to be

[10]The environmental impact is debated.

slowed to thermal energies (thermalise) to allow them to be captured on a fissionable nucleus. To do this, a moderator is used to slow the neutrons down until they are at the right energy. The choice of moderator, and coolant, depends on the reactor design.

The most common reactor design in the UK is the Advanced Gas-cooled Reactor (AGR), which is a form of Gas-Cooled Reactor (GCR). AGRs use graphite as a neutron moderator and gaseous carbon dioxide as a coolant. The graphite contains channels that hold the fuel rods and allows the CO_2 flow through. The channels also act as the neutron moderator. The CO_2 is heated to $\sim$650 °C as it circulates the core, before exchanging its heat to create steam. The steam turns turbines to generate electricity, before condensing and being recirculated. A schematic of an AGR is shown in Figure 1.8.

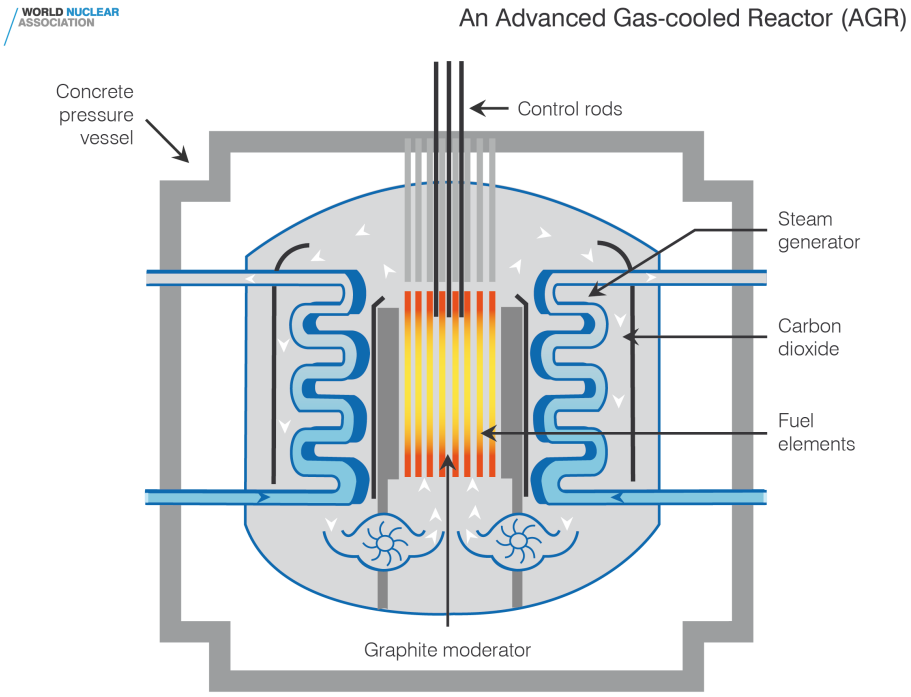

Figure 1.8: Design of an AGR. Reprinted from [129].

The most common reactor design in general is the Pressurised Water Reactor (PWR), a form of Light Water Reactor (LWR). PWRs use water at very high pressure, $\sim$150 atm, as the coolant and moderator; the high pressure ensures the water remains a liquid as it heats to $\sim$300 °C. The fuel is immersed in this water. The high pressure coolant water exchanges heat with a lower pressure water flow that is boiled and used to generate electricity in the same way as an AGR. A schematic of a PWR is shown in

Figure 1.9.

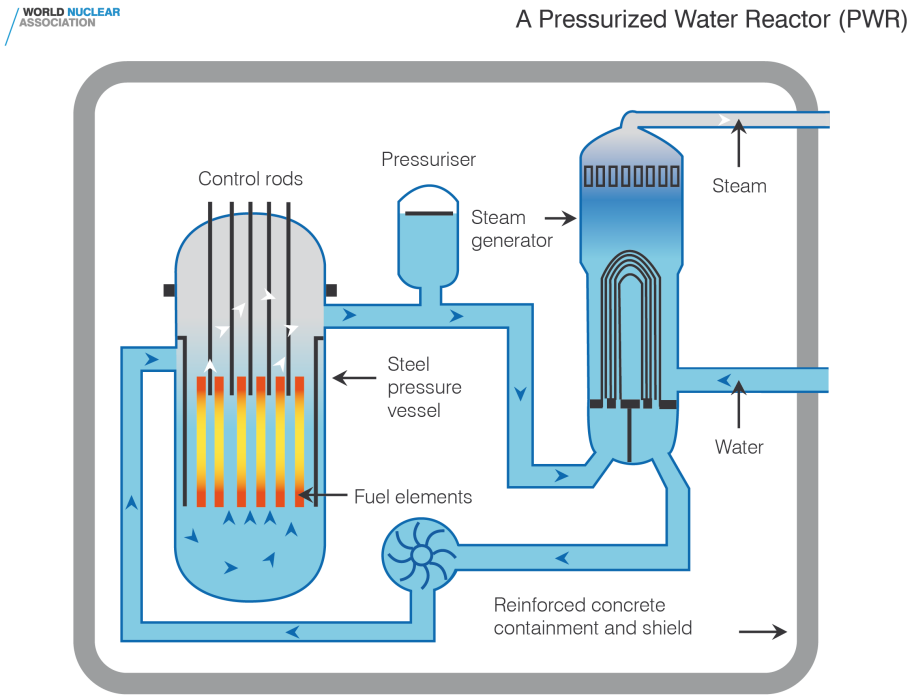

Figure 1.9: Design of a PWR. Reprinted from [129].

Both AGRs and PWRs use the same fuel, ^{235}U, in the form of hollow, sintered[11] pellets of enriched uranium oxide. The pellets are strung together in sealed metal tubes (fuel pins or rods), which are grouped together in fuel assemblies. The abundance of ^{235}U in natural uranium is 0.7 %, so it is enriched to 3 - 5 % [130]. The mass of uranium oxide fuel in the core dictates the power output of the reactor.

The ^{235}U contribution to the fission rate is 70 % in an AGR and 55 % in a PWR at the mid-point in the fuel cycle [131]. The other three fissioning isotopes (^{238}U, ^{239}Pu and ^{241}Pu) contribute the rest. Despite being dominant in uranium at > 99 % abundance, and still dominant in enriched uranium, ^{238}U contributes < 10 % of the total fissions. At the mid-point of the fuel cycle, ∼one third of the power generation comes from ^{239}Pu fissions in a PWR, with ∼20 % in an AGR. ^{239}Pu is produced in a neutron-rich core via

$$^{238}_{92}\mathrm{U} + \mathrm{n} \rightarrow {}^{239}_{92}\mathrm{U} \xrightarrow{\beta^-} {}^{239}_{93}\mathrm{Np} \xrightarrow{\beta^-} {}^{239}_{94}\mathrm{Pu}.$$

The capture of two successive neutrons on ^{239}Pu forms ^{241}Pu.

[11] Sintering is process to compress powder into pellets by pressure or heat without liquefaction.

The refuelling cycle of a reactor is a compromise between safety, optimal fuel usage and minimising downtime. AGRs are refuelled by small amounts regularly, every ∼4 months [131], as the fuel pins are spaced far enough apart to allow the quick replacement of individual fuel channels. This is possible as the neutron capture rate on the graphite moderator is minimal, allowing the channels to be spaced apart. As refuelling is relatively quick, the AGR refuelling cycle is designed to optimise fuel usage.

By contrast, the refuelling of PWRs is a slow and complex process. The neutron capture rate on the water moderator is significant, so the fuel pins are placed close together to reduce this effect. As such, all fuel assemblies need to be removed to refuel and replace depleted assemblies. This creates a suboptimal fuel usage, which causes the power output of the reactor to noticeably reduce over the fuel cycle as the ^{235}U is depleted (*burnup*).

1.3.2 Nuclear Proliferation

Nuclear fission was weaponised even before its use in power generation. Since the detonation of the first weapons in the Second World War nuclear weapons have proliferated rapidly, reaching a peak stockpile of ∼63,000 warheads in 1986 at the height of the Cold War [132], with more and more nations developing nuclear warheads [133]. Despite both the US and Russia, the dominant nuclear states with 90 % of the world's warheads and 99 % at the peak, decommissioning many of their weapons, the current stockpile is still ∼15,000 weapons [133].

It is clear that, with the increasing number of countries developing weapons and the existing stockpile, the proliferation of nuclear weapons is a concern. This concern has been significantly heightened in recent years due to rising global tensions, especially between nuclear states.

With the concern surrounding nuclear proliferation, there is also concern surrounding nuclear reactors. Nuclear reactors can be used a source of ^{239}Pu, a highly fissile[12] isotope, which is commonly used in nuclear fission weapons. This is because it is easier and cheaper to produce highly pure ^{239}Pu than highly enriched weapons-grade uranium. It also has the smallest critical mass, the smallest mass needed to sustain chain reactions, of the common nuclear fuels [134]. The nuclear properties of plutonium are

[12]Fissile materials can sustain a fission chain reaction with the capture of thermal neutrons. They are a subset of fissionable materials that can be fissioned by neutron capture, but sometimes require more energy than thermal neutrons provide.

given in [135]. This means only a few kilograms is sufficient to create a warhead, but the use of ^{239}Pu as reactor fuel requires tonnes, so diverting reactor fuel cycles to ^{239}Pu production for weapons is a quick process [136]. Furthermore, power reactors have moved to higher average burnups over time, increasing the concentration of plutonium in the spent fuel [127]. The first generation of GCRs in the UK, Magnox reactors, were optimised to produce ^{239}Pu [137].

In an attempt to curb the proliferation and testing of weapons, several international treaties and agreements have been formed. Notably, the Treaty on the Non-Proliferation of Nuclear Weapons (NPT) came into force in 1970 [138]. These treaties require methods for the verification of nuclear materials and reactors.

1.3.3 Safeguards

The IAEA has safeguards in place to verify compliance of signatories with the relevant treaties [139]. The current safeguards are designed to prevent the diversion of a specific minimum quantity of fissile material, 8 kg Pu and 25 kg Highly Enriched Uranium (HEU)[140][13]. Power reactors are designed to have a small number of well-defined operational tasks; they receive and store fresh fuel, load fuel into the core, transfer spent fuel to wet storage, and then transfer to dry storage. These tasks allow most safeguarding to be done through accountancy of fuel assembly components. Diversion of fuel is addressed via a continuity of knowledge using cameras, seals and other monitoring systems. Monitoring of core burnup would in principle add information to this safeguarding.

These safeguarding methods all require cooperation from the host state, and intrusive access. This access can come with no notice, as the IAEA will perform unannounced checks [141].

Research reactors are a particular case with special challenges for safeguarding [141]. Research reactors with a thermal power $< 10\,\mathrm{MW_{th}}$ are not a concern for safeguarding as they are unable to produce a sufficient quantity of weapons-grade material. There are 222 IAEA-classified research reactors, 40 with a power output $> 10\,\mathrm{MW_{th}}$ [142]. These reactors can be difficult to safeguard due to their flexibility of operation. They are not set up for single, predesignated tasks in the same way power reactors are. To verify declared operation, their power is monitored [143]. This occurs alongside

[13] Uranium enriched to contain 20 % or more ^{235}U [130]

other inspections and the standard inventory checks. Despite these checks, there are documented cases of misuse that were not detected by the IAEA [144].

Whilst it is generally agreed that the current safeguards are sufficient, particularly when cost is considered, new developments may lead to gaps in the methods [145]. The development of advanced reactor types, new nuclear deals and the requirement for non-cooperative monitoring may necessitate new monitoring techniques.

1.3.4 Reactor Antineutrinos

The potential for gaps in the future safeguarding against nuclear proliferation and misuse of nuclear reactors suggests new approaches should be considered. One such approach is to make use of the particle emission during nuclear fission, in particular antineutrinos. Neutrinos have a very low interaction cross section which means they are impossible to shield, and they will escape from their location of emission. The approach of applying the detection of antineutrinos to reactor observation was first proposed by Soviet scientists in the 1970s [146, 147], before being demonstrated at Rovno Nuclear Power Plant [148–150].

The proposed role of antineutrinos in non-proliferation is as part of the bulk accountancy of nuclear materials. By monitoring the operations of the core, and determining core composition, any discrepancies in the bulk fuel can be identified. The main goal of this is to identify the early shutdown of reactor cores. The build up of ^{239}Pu, the key material of concern for weapons production, during a reactor cycle is usually mitigated by it fissioning or through its conversion to ^{240}Pu. However, stopping a reactor cycle early can allow the extraction of ^{239}Pu from the core and the production of weapons-grade material. Monitoring the antineutrino flux from a reactor has the potential to identify both the change in core composition through a fuel cycle, and any shutdowns that occur, thus identifying potential production of weapons-grade material.

1.3.4.1 Emission

During the fission process, the isotopes produced by neutron capture and nuclear fission are neutron-rich. This makes them unstable and causes them to decay through beta decay. As well as the emission of a β particle, an electron antineutrino is also emitted. The flux of emission is not dependent on external conditions, depending only on the reactor core.

The antineutrino flux depends primarily on the power output of the reactor, and in particular the rate of fissions. There is a subdominant dependence on the composition of the reactor core too, i.e. the isotopes that are present in the fuel assemblies. The core composition and burnup depend on the reactor type. The antineutrino spectrum of a fissioning isotope is given by

$$\Phi_{\bar{\nu}_e,i}(E_{\bar{\nu}_e}) = P_{\text{th}} \frac{p_i \lambda_i(E_{\bar{\nu}_e})}{Q_i}, \tag{1.17}$$

where P_{th} is the thermal power of the core, p_i is the fraction of the thermal power resulting from the fission of isotope i, Q_i is the average thermal energy emitted per fission and $\lambda_i(E_{\bar{\nu}_e})$ is the antineutrino emission energy spectrum normalised to one fission for fissioning isotope i as a function of antineutrino energy $E_{\bar{\nu}_e}$. $\lambda_i(E_{\bar{\nu}_e})$ is given by

$$\lambda_i(E_{\bar{\nu}_e}) = \exp\left(\sum_{j=1}^{6} a_j E_{\bar{\nu}_e}^{j-1}\right), \tag{1.18}$$

where the coefficients a_j are fit parameters from the Huber-Mueller predictions [151, 152], which are derived from measurements of the β spectra from nuclear fission. The total antineutrino flux for a reactor is the summation of the contributions from individual isotopes.

The flux is sensitive to the fission fractions[14], particularly the proportion of ^{235}U, in the reactor core. As the core burnup progresses, ^{239}Pu is produced via neutrons from ^{235}U being captured on ^{238}U, which decays via two β decays to ^{239}Pu. This allows ^{239}Pu to accumulate. It is able to decay through α emission to ^{235}U or fission. When it undergoes fission, it will emit $\sim$65 % of the antineutrino flux of ^{235}U for the same power output [153, 154]. This creates a change in the antineutrino flux without a power output change and allows the increasing amount of ^{239}Pu, and burnup of ^{235}U, to be visible in the antineutrino spectrum. The time-evolution of the spectrum depends on the initial core composition, reactor type and power output, and burnup.

This evolution of the reactor antineutrino spectrum has been observed in the SONGS1 detector, along with the reactor power. The San Onofre Nuclear Generating Station (SONGS) reactor complex consists of three PWRs, and therefore has long refuelling periods. The reduction in antineutrino flux as burnup occurs can be seen in the SONGS1 data in Figure 1.10. A large drop in the antineutrino flux due to refuelling is also clearly visible in the data.

[14]The relative fraction of each fissioning isotope in the core.

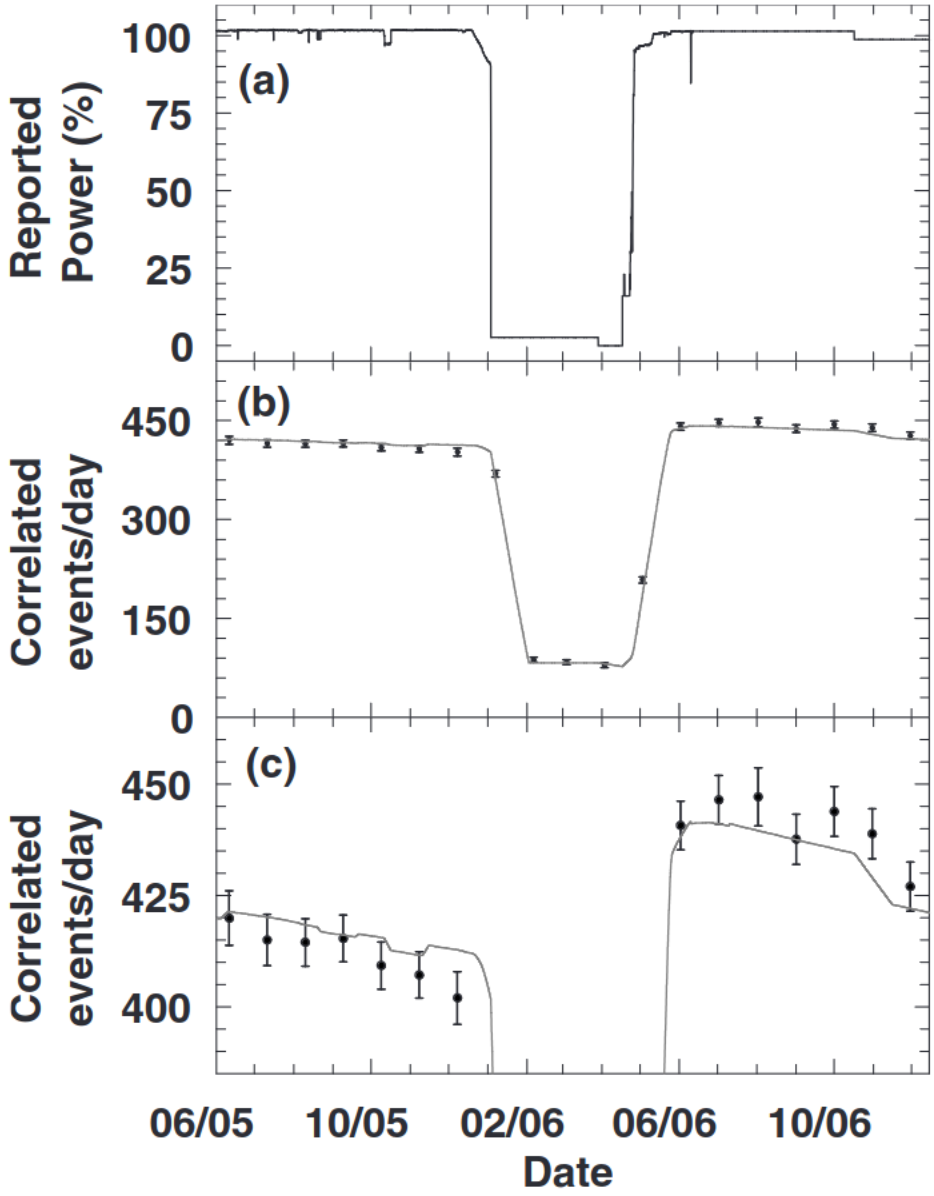

Figure 1.10: Power outage of the SONGS reactor and its effect on the neutrino flux observed in SONGS1. a) reported power of reactor, b) observed event rate and c) close up of b) to show decreasing event rate with fuel evolution. Reprinted from [155].

As antineutrino emission is isotropic, the flux drops off proportionally to the distance from the reactor squared.

1.3.4.2 Reactor Antineutrino Anomaly

The models of reactor antineutrino spectra for fissioning isotopes were modified by the Huber-Mueller predictions in 2011 [151, 152] using β spectra of the fissioning isotopes [156–159]. This modification resulted in a deficit of $5.7 \pm 2.3\,\%$ in the detected antineutrino flux [160]. This deficit was confirmed by STEREO [161]. Beyond the flux deficit, an excess at 5 MeV was observed in Daya Bay, RENO, Double Chooz and NEOS [162–165]. The deficit and shoulder at 5 MeV are seen in Figure 1.11. This

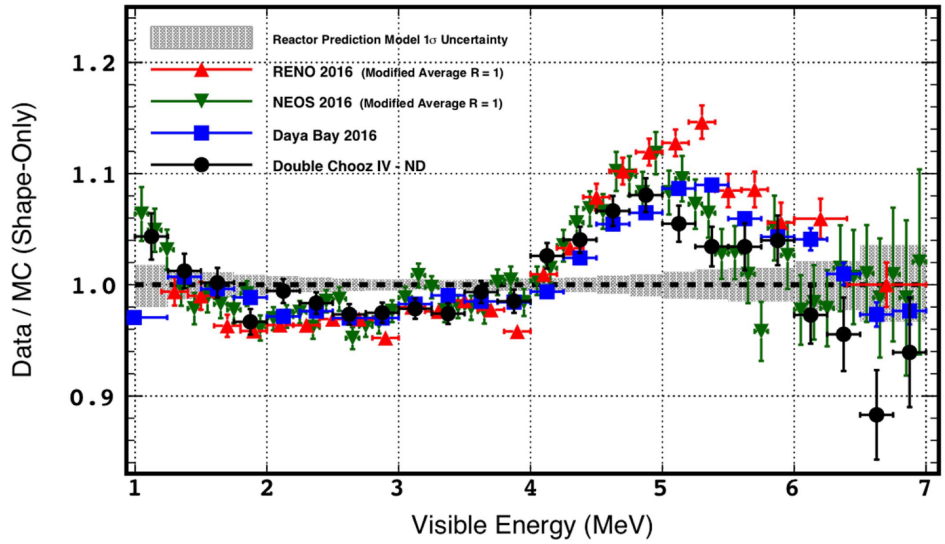

Figure 1.11: The Huber-Mueller model compared to data from several reactor experiments, showing a general deficit in the observed reactor antineutrino rate and an excess at 5 MeV. Reprinted from [164].

created the reactor neutrino anomaly, in which the antineutrino flux predictions based on the β spectra of the fissioning isotopes did not match the measured flux in several independent experiments.

Daya Bay and RENO both saw evidence correlating the emission from ^{235}U and the flux deficit [162, 163], with RENO suggesting there is also a dependence on ^{235}U for the 5 MeV bump [163]. *Ab initio* calculations from fission and β yields, and a re-evaluation of the Huber-Mueller model using updated predictions, produced a better agreement with data and suggest that ^{235}U was the cause of the flux deficit [166].

Measurements of β spectra used in the Huber-Mueller model predictions come from using thin foils of uranium or plutonium oxide between nickel foils to capture thermal neutrons. The measurements of three of the fissioning isotopes were taken in the 1980s,

with ^{238}U in 2013. A re-evaulation of the ^{235}U and ^{239}Pu β spectra showed there was previously a 5 % overestimation in the ^{235}U cumulative β spectrum [167]. This is the expected source of the reactor antineutrino flux deficit after recalculation of the spectra with the Huber-Mueller model [168]. Alternative models, such as in [169], show improvements in part of the antineutrino flux compared to the Huber-Mueller predictions, but still can not explain the 5 MeV bump.

The excess at 5 MeV is as yet unresolved, but attempts at new models and understanding of interactions have suggested possible ways to account for it. One suggestion is biases on the reference spectra of fission electrons could cause the anomalies [170], with forbidden transitions another explanation [171].

The simulations in chapter 5, and subsequent data reduction and analyses, did not include the resolution to the reactor antineutrino anomaly as spectra calculated prior to 2021 were used. As such, the deficit and the 5 MeV bump are accounted for in the systematic uncertainties on reactor IBD rates.

1.3.4.3 Previous Detection and Experiments

Reactor antineutrinos have been detected in many experiments since their first observation by Cowan and Reines, and first proof of application at Rovno. Until 2022, all detections had been using scintillators. Detectors are generally doped with a neutron capture agent to take advantage of the IBD signal (see subsection 2.3.1). Detectors such as Daya Bay [172], Double Chooz [173] and RENO [174] are able to probe the mixing angle θ_{13}, as well as look for sterile neutrinos. The JUNO detector will attempt to use reactor antineutrinos to resolve the mass hierarchy of neutrino states [123]. The choice of scintillator instead of water is because the energy spectrum of reactor antineutrinos is in the region 0 to 10 MeV, and generally peaks around 3 to 4 MeV depending on their distance of travel. For water-filled detectors, such as SK, the energy threshold is generally too low when light yield and backgrounds are accounted for. However, SNO+ was able to successfully observe reactor antineutrinos in 2022 by lowering its threshold to 1.4 MeV, allowing it to observe 50 % of the 2.2 MeV γs from neutron capture on hydrogen [175, 176]. More detail on antienutrino interactions is given in section 2.1 and detection mechanisms is given in section 2.2.

1.4 Thesis Aims and Structure

The work in this thesis presents the development and characterisation of detector technologies for the purpose of reactor antineutrino detection and monitoring. An analysis of detector performance and sensitivity to real reactors in a realistic environment has been performed to understand the requirements of far-field reactor antineutrino monitoring for non-proliferation purposes.

This chapter has introduced the early history of the neutrino, and its relevance to nuclear reactor safeguarding. The rest of the thesis is structured as follows:

- Chapter 2 explains the general detection principles for reactor antineutrinos, including their interaction and the observable signal produced.
- Chapter 3 presents a test bed facility developed for characterising hardware for a water-based neutrino detector.
- Chapter 4 details the characterisation of photomultiplier tubes for use in a detector, with a particular focus on the first characterisation of photomultiplier tubes in the purpose-built water tank described in chapter 3.
- Chapter 5 describes Neutrino Experiment One, a proposed detector for mid- to far-field reactor neutrino monitoring, alongside the simulation of signal and background sources in the detector.
- Chapter 6 presents the event reconstruction and data reduction algorithms developed for the analysis of detector designs.
- Chapter 7 presents three analyses, a rate-only sensitivity analysis for various detector designs to reactors in a realistic environment and two spectral analyses using neutrino oscillations to determine the distance to an observed reactor.
- Chapter 8 gives concluding remarks to the work presented throughout.

Chapter 2

Antineutrino Interactions and Detection

Due to their neutral charge and the fact they only interact via the weak interaction, neutrinos are not directly observable. Instead, the products of their interaction with matter are observed. The way in which they interact depends on both the properties of the incident neutrino and the matter they interact with.

In the large-volume liquid-filled detectors used for neutrino detection, the interaction products will produce light which is detected by photosensors. The characteristics of the total light emission per interaction provide information on the particles directly detected and the incident neutrino.

2.1 Interactions with Matter

On the energy scale of reactor antineutrinos (up to $\sim$10 MeV), the dominant interaction mechanism in water and hydrocarbons is IBD with a cross section ranging from $\mathcal{O}(10^{-44})$ to $\mathcal{O}(10^{-41})\,\mathrm{cm}^2$ [177]. During IBD, an electron antineutrino interacts with a proton. An up quark becomes a down quark, forming a neutron, and a charged boson is exchanged to produce a positron. The equation for IBD is

$$\bar{\nu}_e + p \rightarrow e^+ + n,$$

with a Feynman diagram in Figure 2.1.

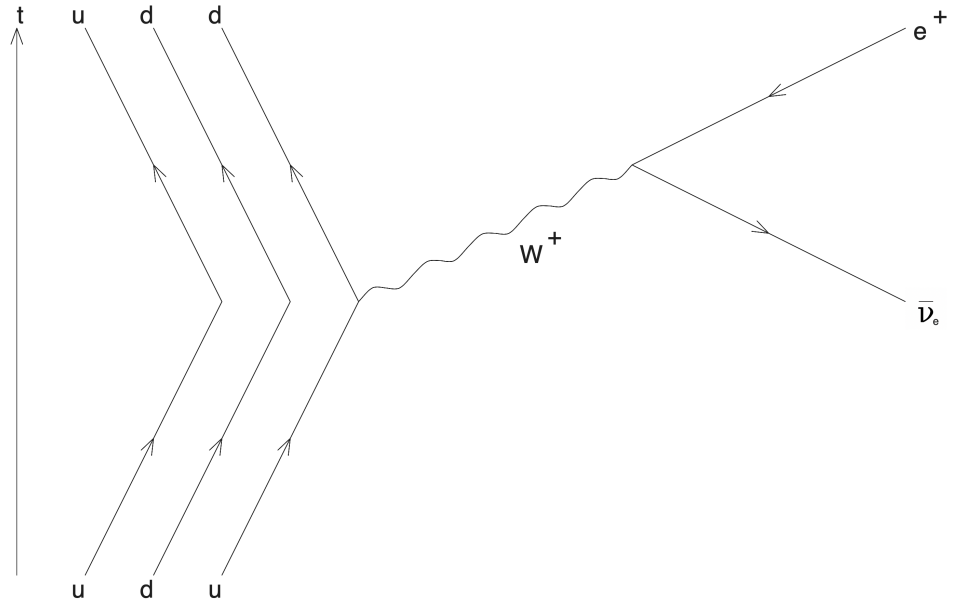

Figure 2.1: Feynman diagram of IBD.

The cross section of interaction for IBD in [178] is given by

$$\frac{d\sigma}{dt} = \frac{G_F^2 cos^2(\theta_c)}{2\pi(s-m_p^2)^2}|\mathcal{M}^2| \tag{2.1}$$

where G_F is the Fermi coupling constant, θ_C is the Cabibbo quark mixing angle, m_p is the proton mass, and $|\mathcal{M}^2|$ is the absolute of the matrix element squared and gives the probability of transition from the initial state to the final state. $|\mathcal{M}^2|$ is calculated in terms of the Mandelstam variables, as:

$$|\mathcal{M}^2| = A(t) - (s-u)B(t) + (s+u)C(t) \tag{2.2}$$

Here, $s = (p_{\bar{\nu}_e} + p_p)^2$, $t = (p_{\bar{\nu}_e} - p_e)^2$ and $u = (p_{\bar{\nu}_e} - p_n)^2$ are the Mandelstam variables with momenta $p_{\bar{\nu}_e}$, p_e, p_p and p_n for the antineutrino, positron, proton, and neutron respectively. $A(t)$, $B(t)$ and $C(t)$ are functions of the Mandelstam variable t.

By inserting

$$s - m_p^2 = 2m_p E_{\bar{\nu}_e}$$

$$s - u = 2m_p(E_{\bar{\nu}_e} + E_e) - m_e^2$$

$$t = m_n^2 - m_p^2 - 2m_p(E_{\bar{\nu}_e} - E_e)$$

where E_e and $E_{\bar{\nu}_e}$ are the positron and antineutrino energies respectively, and m_p is the proton mass, the cross section can be given as

$$\frac{d\sigma}{dE_e}(E_{\bar{\nu}_e}, E_e) = 2m_p \frac{d\sigma}{dt} \tag{2.3}$$

The cross section can be expressed as

$$\sigma_{\text{IBD}}(E_e) = 10.0 \times 10^{-44}\ p_e\ E_e\ E_{\bar{\nu}_e}^{\alpha}\ \text{cm}^2, \tag{2.4}$$

where

$$\alpha = -0.07056 + 0.02018 \ln E_{\bar{\nu}_e} \ln^3 E_{\bar{\nu}_e}.$$

This parameterised cross section is used to determine the detectable spectrum of a reactor at a site in [179].

Other calculations of the cross section have been performed, such as in [180]. A more recent calculation, in [177], reduced the uncertainties at higher energies but with no significant change in the absolute values. On the energy scale of reactor neutrinos, the difference between the cross sections in [177] and [178] is negligible. The overall uncertainty on the IBD cross section is under 1 %, with a full treatment including information on the neutron decay reducing the uncertainty to 0.52 %.

For IBD to occur, the antineutrino must have sufficient energy to overcome the threshold. This is determined by the mass of the particles involved, and can be expressed as

$$E_{\text{thr}} = \frac{(m_n + m_e)^2 - m_p^2}{2m_p} \tag{2.5}$$

in the laboratory frame. During IBD, the antineutrino energy is given entirely to the interaction products. The majority of the kinetic energy is taken by the positron, which is relativistic upon emission for detectable positrons from reactor antineutrinos. As such, the positron can provide information about the energy of the incident antineutrino through the approximation

$$E_{\bar{\nu}_e} = E_{e^+} + E_{\text{thr}} - m_e. \tag{2.6}$$

The positrons emitted during IBD have an almost isotropic distribution, with a slight bias in the backwards direction. The neutron, however, takes most of the antineutrino's momentum, causing the initial direction of emission to be mostly parallel to the antineutrino direction. This is due to the neutron dominating the total mass after the vertex of interaction. After emission, the neutron will random walk. It will

scatter successively in the detector medium, deviating from the original path as it does, until it thermalises. After thermalising, the neutron is captured on a nucleus in the detection medium e.g. hydrogen. This produces a signal from the de-excitation of the capture nucleus, which will occur within a small distance of and short time after the positron signal. This time and distance is determined by the detection medium, and creates a coincident pair of signals for an IBD interaction.

The other major mechanism for antineutrino interaction is the Elastic Scattering (ES) of antineutrinos on electrons, both neutral- and charged-current. The cross section of elastic scattering for reactor antineutrinos is $\mathcal{O}(10^{-45})$ to $\mathcal{O}(10^{-44})\,\mathrm{cm}^2$ [181], but there is no energy threshold for the interaction to occur and the number of target particles is significantly higher. Electrons are typically scattered in the same direction as the incoming antineutrino, but the antineutrino does not necessarily deposit all of its energy as it does in IBD. A comparison of the cross section of IBD and ES is seen in Figure 2.2.

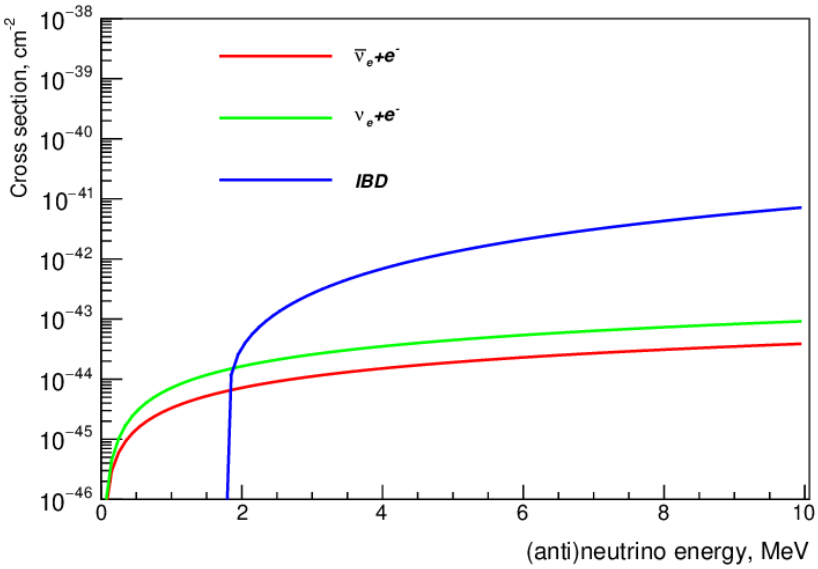

Figure 2.2: Cross section of IBD and elastic scattering for both electron neutrinos and antineutrinos. Reprinted from [181].

2.2 Light Production in Matter

For a particle to be observed in a detector, it must produce an observable signal. Neutrino detectors rely on light production by the products of a neutrino interaction. There are multiple mechanisms by which this can occur, depending on the detector design and interaction type.

2.2.1 Cherenkov Radiation

Water Cherenkov detectors are set up to look for Cherenkov radiation from an electron or positron that has been transferred kinetic energy from a neutrino. Cherenkov radiation is a phenomenon that occurs when a charged particle has a velocity v greater than the speed of light in a dielectric medium with refractive index n [182]:

$$v \geq \frac{c}{n}.$$

When the charged particle passes through the medium, polarisation followed by de-excitation of the molecules in the medium cause the emission of Electromagnetic (EM) radiation. When the particle travels faster than the speed of light in the medium, it disrupts the emitted EM radiation and creates constructive interference in the polarisation field. This creates a characteristic blue cone of Cherenkov radiation, the geometry of which is shown in Figure 2.3.

From this geometry, the particle's velocity can be determined. The opening angle of the cone is given by

$$\cos(\theta) = \frac{1}{n\beta},$$

where $\beta = v/c$. This yields the threshold for Cherenkov radiation of

$$\beta > \frac{1}{n},$$

and a maximum opening angle of

$$\theta_{\text{max}} = \cos^{-1}\left(\frac{1}{n}\right).$$

For a particle of mass m, the kinetic energy threshold to produce Cherenkov radiation is

$$E_{\text{thr}} = \frac{mc^2}{\sqrt{1 - \frac{1}{n^2}}}.$$

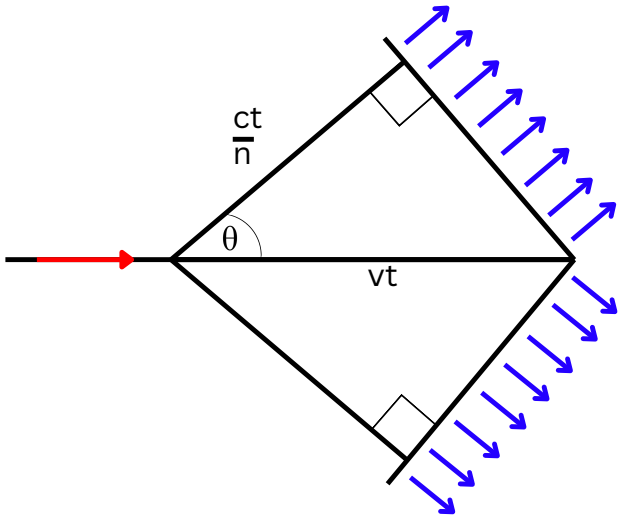

Figure 2.3: The geometry of a Cherenkov cone. The red arrow (left) shows the direction of travel of the particle, the blue arrows (right) show the propagation of Cherenkov radiation.

The frequency spectrum of Cherenkov radiation is given by the Frank-Tamm equation [183, 184]

$$\frac{\partial^2 E}{\partial x \partial \omega} = \frac{q^2}{4\pi}\mu(\omega)\omega\left(1 - \frac{c^2}{v^2 n^2(\omega)}\right) \text{ for } v > \frac{c}{n(\omega)}, \tag{2.7}$$

and yields the total energy radiated per unit length:

$$\frac{dE}{dx} = \frac{q^2}{4\pi}\int_{v>\frac{c}{n(\omega)}} \mu(\omega)\omega\left(1 - \frac{c^2}{v^2 n^2(\omega)}\right) d\omega, \tag{2.8}$$

where q is the electric charge of the particle and ω is the frequency, and μ is the permeability of the medium. This means the amount of light produced via Cherenkov radiation is related to the energy of the charged particle.

The cone of light reveals both the direction and energy of the charged particle, and will produce a ring pattern on a detector wall. This ring can be used to determine the interaction vertex. The light yield from Cherenkov radiation, particularly at the energy reactor antineutrinos are produced at, is low. This limits the resolution with which the energy and vertex location can be determined. The spectrum of Cherenkov radiation is continuous, with a peak at 420 nm and most light in the Ultra-Violet (UV) and blue regions. Photosensors for neutrino detectors are typically designed to have a peak sensitivity matching this region of peak emission.

2.2.2 Scintillation

The other major mechanism of light production in neutrino detectors is scintillation. Scintillators still rely on the products of neutrino interaction, but the light production differs.

Scintillators come in many forms, but the one typically used in neutrino detection is organic liquid scintillator [185]. In a scintillator, a charged particle will deposit energy and cause ionisation or excitation of the scintillator molecules. A subsequent de-excitation will radiate light.

In an organic scintillator, phenyl groups are the key source of radiative emission. Phenyl groups contain delocalised electrons in π-orbitals arising from hybridisation of s- and p-orbitals in carbon atoms in the groups [186]. The energy levels in these groups lead to the emission of blue to UV light [187], which is ideal for detection with common optical sensors.

Within a scintillator molecule, electronic energy states comprise several vibrational states with very small energy splitting. In most cases, the excitation of a π-electron will happen from the vibrational ground state of the electronic ground state to an excited vibrational state of an excited electronic state, which is known as the Franck-Condon principle [188, 189]. This occurs because the electronic transitions are nearly instant compared to the timescale of nuclear motion. Therefore, the excited state must be compatible with the previous state at the instant of transition for the transition to be able to occur.

The de-excitation of vibrational states is very quick (10^{-12} to 10^{-11} s) and non-radiative. The de-excitation of electronic states depends on the fine splitting. A singlet state will de-excite in $\mathcal{O}(10)$ ns, but a triplet will be milliseconds or longer as it requires two excited molecules due to forbidden transitions arising from angular momentum conservation between states. Forbidden transitions rely on a spin flip, which is forbidden by electric dipole transitions and requires the inclusion electric quadrupoles. As such, this process occurs at very low rates causing triplet state de-excitation to be very slow [186, 190]. The quick de-excitation of singlets states produces fluorescence, the slow de-excitation of triplet states produces phosphorescence; this gives rise to fast and slow scintillation components. Example energy levels for a fluorescent molecule are shown in Figure 2.4.

Scintillators containing a single solvent will suffer from self-absorption, where the emission and absorption spectra overlap and emitted light is re-absorbed. To overcome

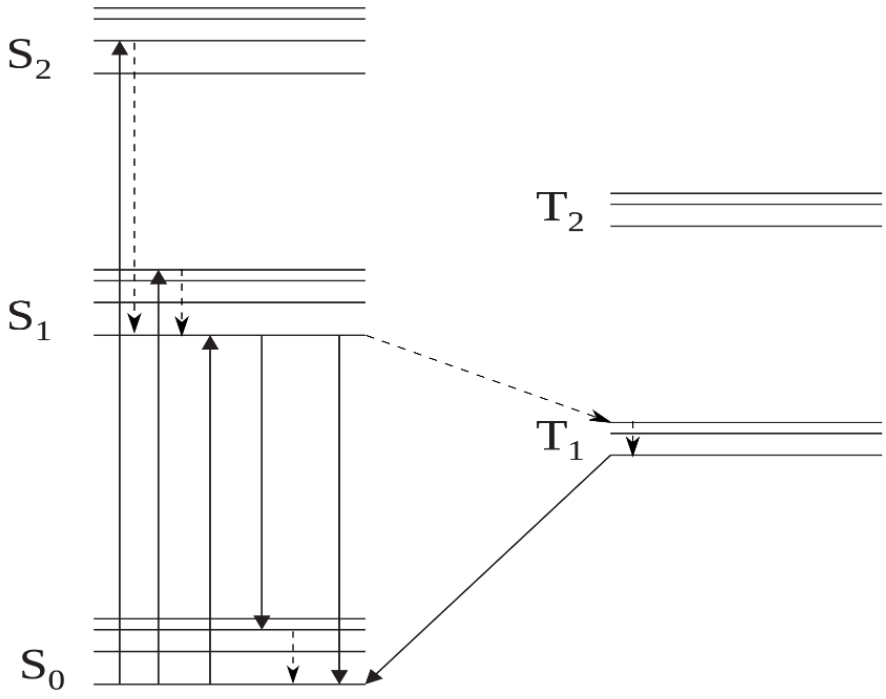

Figure 2.4: Energy levels of singlet (S) and triplet (T) states with corresponding vibrational levels shown for a fluorescent molecule. Radiative transitions (solid) and non-radiative transitions (dashed) are shown. Reprinted from [191].

this, one or more fluorescent molecules are used, with the effect of using two shown in Figure 2.5. Typically, a primary fluor is used to shift the radiated light to longer wavelengths (Stokes shift), through energy loss, where the scintillator is transparent. In some occasions, a secondary wavelength shifter is also used to shift the wavelength further. Energy transfer to the primary fluor is typically non-radiative, via Förster Resonant Energy Transfer (FRET) [192], but transfer after this is typically radiative.

A variety of solvents and fluors are used, with combinations picked to tune the performance of the detector medium. Linear Alkyl Benzene (LAB) is used in SNO+ [193], with it showing particularly good safety features, transparency, material compatibility and low cost [194–201]. Pseudocumene was used in Borexino for its high light yield [202], but is chemically aggressive [203–208]. Among the fluors, 2,5-diphenyloxazole (PPO) is a common choice [193, 195, 198–201, 204, 205, 209–211].

Where Cherenkov light is directional with a low light yield, scintillation light is isotropic but with a high light yield and very low threshold. Scintillators are generally

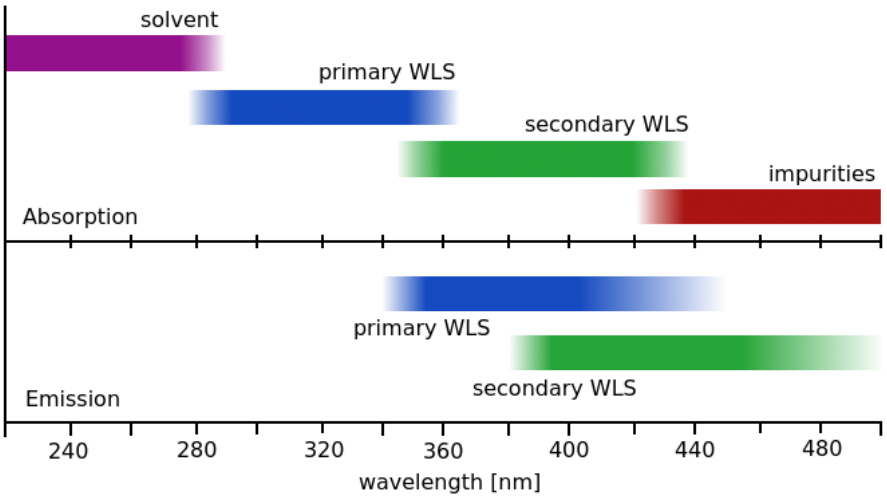

Figure 2.5: Typical arrangement of absorption and emission regions in a solvent with two wavelength shifters. Reprinted from [191].

used where a good energy resolution or low energy threshold is required.

2.2.3 Neutron Capture

The capture of thermal neutrons on nuclei can lead to the production of light. When a thermal neutron, one which has an average kinetic energy corresponding to particles in the ambient medium ($\sim$0.025 eV), captures on a nucleus, it leaves the nucleus in an excited state. The nucleus de-excites and emits one or more gamma rays with a discrete total energy characteristic to the nucleus' energy levels. These gamma rays can be used to tag the neutron capture. The total energy deposited due to the neutron capture is dependent on the Q value of the interaction, and determines the number of photons emitted by the neutron capture.

2.2.4 Light Loss Mechanisms

Whilst the detector medium, whether water or a hydrocarbon, will produce light, it will also attenuate light through numerous mechanisms.

Absorption occurs when the wavelength of light corresponds to energy levels in the medium in which it propagates. If the light matches the energy levels, it excites the

medium but is absorbed in the process. If light is re-emitted, it is isotropic and not directional. Pure water in a liquid phase absorbs mostly at longer wavelengths [212].

Scattering of light comes in three key forms. Rayleigh scattering is dominant in the liquid media used in neutrino detectors, and occurs when light scatters elastically off molecules much smaller than the wavelength of the light [213]. The light is polarised by the scattering and the wavelength remains the same as the incident light. The scattering is symmetric forwards and backwards with respect to the direction of the incident light. Mie scattering is also elastic, but occurs when the molecule scattered off is of a similar size to the wavelength of the light [214]. The scattered light is polarised as with Rayleigh scattering but is asymmetric, being scattered in the forward direction. The larger the molecule, the more the light is forward scattered. The third mechanism, Raman scattering, is subdominant. Raman scattering is inelastic, some energy is transferred between the molecule and the light (usually to the molecule) [215].

Quenching is the loss of deposited energy that results in a reduction in light yield in a scintillator. Ionisation quenching is the major form of quenching considered in organic liquid scintillators. When the energy loss (dE/dx) of the particle is small, the light yield of the scintillator is proportional to the energy of the particle. When dE/dx is large, the scintillator has a non-linear response. As the particle travels, it excites molecules along its path. When the particle is heavy or travelling slowly, the density of ionised and excited particles is high. The scintillator becomes saturated and interactions between excited molecules result in more non-radiative transitions, causing a reduction in emitted light. The scintillator is in effect at the maximum capacity for light production in the area the particle deposits energy in. A proton or an alpha particle will produce an order of magnitude less photons than an electron of the same energy [185] because of this effect.

Ionisation quenching is typically described by the empirical Birks' law [216]

$$\frac{dL}{dx} = S\frac{\frac{dE}{dx}}{1 + k_B\frac{dE}{dx}}, \tag{2.9}$$

where dL is the light produced along path dx, S is the light yield constant, k_B is Birks' quenching parameter and dE is the energy loss of the particle along path dx. This approach treats ionisation quenching as temporary molecular damage [217]. A more general version, Chou's equation [218], is often used too as it includes the effects of neighbouring molecules. Other forms of quenching, such as impurity and colour

quenching [219], can be mitigated by tuning the scintillator cocktail.

Pure water is typically measured to have a much longer attenuation length than scintillators. The attenuation length in SK with pure water was measured as ∼120 m at 400 nm [220], which is significantly longer than the 15.10 ± 0.35 m attenuation length in Daya Bay's Gd-doped LAB [221]. Attenuation in scintillator is dominated by absorption, with scattering lengths generally being less significant; SNO+ measured a scattering length of 71.90 ± 13.6 m [193]. The values quoted for Daya Bay and SNO+ here are fairly typical for scintillators [222].

2.3 Detector Fill Media

2.3.1 Gadolinium doping

As described in section 2.1, an electron antineutrino interacts via IBD to produce a characteristic positron-neutron coincident pair. The positron will produce a prompt signal via instantaneous Cherenkov radiation, the neutron will thermalise and then capture to produce a delayed signal. The delayed neutron capture can be used to tag the prompt positron, producing a distinctive coincident signal.

In both pure water and pure liquid scintillator, the neutron will capture on hydrogen [223]. Hydrogen has a neutron capture cross section of 0.3 b [224], leading to a capture time around 200 µs. The energy released is a single 2.2 MeV gamma. This leads to a weak signal that can be easily masked by backgrounds.

To boost the neutron capture signal, the detector medium can be doped with a neutron capture agent. Several options are present, including cadmium [225] and lithium [226]. Gadolinium is a common choice due to its high neutron capture cross section and non-toxic properties. Gadolinium has the highest neutron capture cross section of any stable element, 2.54×10^5 b for thermal neutrons on ^{157}Gd [227] and an average of approximately 4.9×10^4 b across all isotopes [228, 229]. Gadolinium will also emit an average 8 MeV gamma cascade upon neutron capture [230], significantly more than hydrogen, and capture a neutron within approximately 30 µs for a typical 0.1 % Gd loading in water. This creates a much clearer delayed signal, with a much tighter time and distance between the prompt and delayed IBD signals, when compared to hydrogen.

Gadolinium doping was first proposed in [231, 232], and tested in Evaluating Gadolin-

ium's Action on Detector Systems (EGADS) [233] in the form of a 0.2 % concentration of $Gd_2(SO_4)_3$ (0.1 % concentration of Gd). The optical properties of EGADS, in Figure 2.6, remained stable with good transparency and the neutron capture efficiency was calculated as 84.36 ± 1.79 % [234]. The neutron tagging efficiency on hydrogen in SK with pure water was determined as $(17.74 \pm 0.04_{stat} \pm 1.05_{sys})$ % [235]. As such, in 2020 SK started moving to a new phase with gadolinium included (SK-Gd) [236].

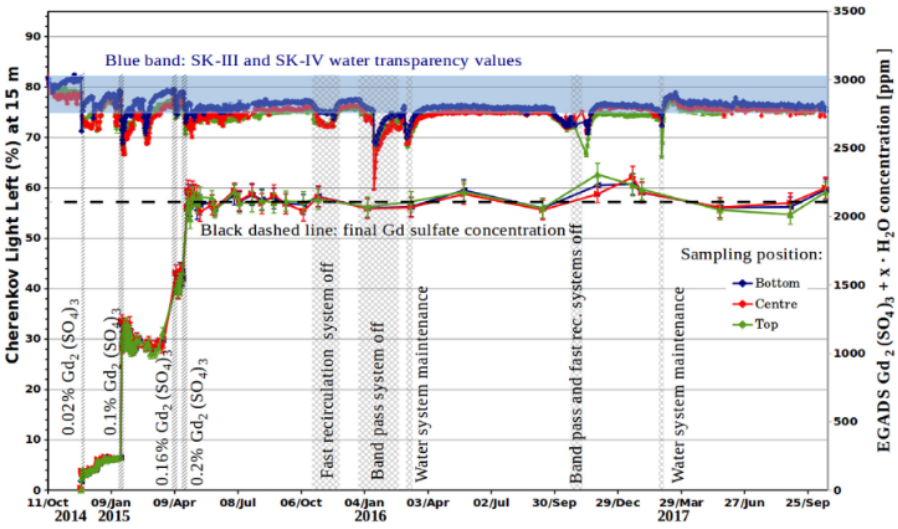

Figure 2.6: The water transparency in EGADS measured between October 2014 and September 2017. The blue band is where SK III and IV operated. Reprinted from [233].

2.3.2 Water-based Liquid Scintillator

As described in section 2.2, light can be produced via scintillation and Cherenkov radiation. Each of these mechanisms has benefits and drawbacks; Cherenkov radiation has a low light yield and high energy threshold to overcome, but is directional, whereas scintillation light has no threshold and a high light yield, but is isotropic. Liquid scintillator is also hard to scale to large detectors due to its absorption, cost, and availability, whereas water is much easier to scale to very large detectors.

A combination of water and liquid scintillator, in the form of Water-based Liquid Scintillator (WbLS), is a potential solution to get the benefits of both media. Current WbLS cocktails are based on LAB combined with water using a surfactant [237–240][1].

[1]New cocktails are based on di-isopropylnaphthalene (DIN) [241].

LAB is an oily, hydrophobic substance and so separates from water. The surfactant allows the formation of micelles, which have hydrophobic (non-polar) and hydrophilic (polar) surfaces [240]. This allows the LAB to combine with the water. The fluor used is PPO [242].

WbLS could lower the energy threshold of water-based neutrino detectors. Studies of WbLS-loaded detectors, such as THEIA [243], see an energy threshold of 0.6 MeV used in a detector with a 50 kT volume [244, 245]. This is significantly lower than SK, which is also 50 kT but has a threshold of 3 MeV [246] in its pure water fill. There would also be an expected boost in signal detection efficiency, accompanied by a boost in energy resolution due to the high scintillator light yield [247]. SK-III reached an energy resolution of 10 % at 30 MeV [100], but a WbLS cocktail with a 10 % scintillator concentration would be able to reach 12 % at 1 MeV [248]. This is due to an increased light yield compared to water, with a measurement of 127.9 ± 17.0 photons/MeV/(% concentration of scintillator) [247]. The relative light yield of WbLS is slightly lower than a pure LAB/PPO cocktail [249].

The directionality of Cherenkov radiation could be preserved if the scintillation and Cherenkov light could be separated. Scintillation light is emitted after a short delay, but Cherenkov radiation is immediate. A sufficiently fast photosensor, such as a Large Area Picosecond PhotoDetector™ (LAPPD™), could resolve the immediate Cherenkov and delayed scintillation components [250–253]. The Cherenkov/Scintillation Separation (CHESS) experiment aimed to demonstrate this concept [242, 254] and the time response of LAB/PPO combinations has been measured via X-ray excitation [239]. A simulation of WbLS can be seen in Figure 2.7, with the Cherenkov ring on the detector clearly visible.

As well as using fast photosensors, using slow fluors that use the triplet states to increase the time between the absorption and emission of the scintillation component can also allow the time separation of Cherenkov and scintillation light [256]. Alternatively, spectral separation is possible due to the long-wavelength photons being dominated by Cherenkov radiation and the short-wavelength photons being dominated by scintillation light [257, 258].

WbLS is expected to have good Particle Identification (PID) performance, with γ-neutron separation shown [259]. The Eos experiment is designed to investigate the PID performance further [260].

WbLS can be doped with a metal neutron capture agent, such as gadolinium, as

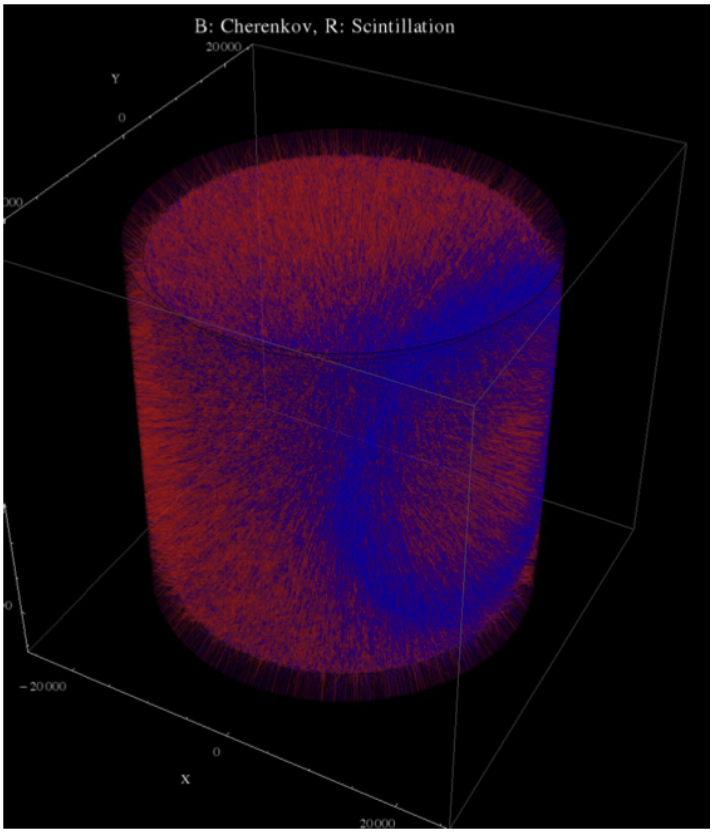

Figure 2.7: High-energy electrons in WbLS. The scintillation light (red) is isotropic whilst the Cherenkov radiation (blue) is directional and forms a cone of light. This is picked up by PMTs as it forms a ring of light on the wall. Reprinted from [255].

the metal can be loaded into the aqueous phase [261]. Previous studies have shown gadolinium-doped WbLS to be the only viable way of increasing low-energy neutrino detection for reactor neutrino monitoring with a water-based detector [262].

2.4 Summary

The choice of a detector's fill medium depends on the particle being observed. In the case of reactor antineutrinos, the dominant interaction mechanism is IBD, in which an electron antineutrino interacts with a proton to form a positron and neutron in a pair. The positron can be observed via Cherenkov radiation in water and scintillation light in a scintillator, and the neutron can be observed when it captures on a nucleus.

The efficacy can be boosted for both particles by tuning the detection medium. For

the positron, water will allow good directionality via Cherenkov radiation. However, in the case of reactor antineutrinos where the energy is low, the light yield from Cherenkov radiation is low. Scintillators offer a higher light yield and therefore make the positron easier to detect, but come with an increased cost, reduced scalability and no directionality. Combining the two, via WbLS, may give some benefits of each medium.

The neutron capture efficiency can be increased by using a neutron capture agent, such as gadolinium sulphate, with a high neutron capture cross section. This creates a distinct capture signal with the deposition of a large amount of energy via photon emission. By detecting the positron and neutron signals in coincidence with each other, IBD can be identified.

Chapter 3

PocketWATCH Water Cherenkov Detector Test Bed

New detectors require a significant amount of R&D to design and build, and equipment often requires characterisation before installation. To do this, smaller test bed facilities are often used to replicate the conditions found in a large detector. Before SK moved to gadolinium loading, EGADS was constructed and operated for a prolonged period to understand the effects of long-term gadolinium exposure [233].

The light injection system to be used for the dynamic calibration of HK's optical properties requires characterisation before it can be installed, as do PMTs before they can be effectively used. To carry out this work, the PocketWATCH test bed facility has been developed at the University of Sheffield to allow the development of optical light injectors, material compatibility testing with ultrapure and gadolinium-loaded water, and the operation of photosensors in single-photon mode. The system is normally operated with ultrapure, temperature-controlled water to match the expected conditions of HK, but can also be doped with $Gd_2(SO_4)_3{\cdot}8H_2O$ at 0.2 % to replicate gadolinium-doped detectors.

3.1 Facility Description

3.1.1 PocketWATCH Tank

PocketWATCH is a $2 \times 2 \times 1.25$ m tank (Figure 3.1) that contains 2000 L of water, allowing a 25 cm air gap directly above the water. The tank is constructed using 6 mm

thick SS316 plates and raised 20 cm off the floor on 6 legs, with a 3 mm thick SS316 lid on top. The air gap directly above the water allows for the installation of a gantry system and control electronics. A valve is located at the bottom of the tank to allow for draining of the system.

A gantry system can be installed at the water surface, allowing three-dimensional positioning of objects in the tank. Currently, a two-dimensional gantry is able to cover almost all of the water surface, with a platform that can be lowered to any height. This is to be used for automated positioning of the light injectors being characterised for HK, where a lowered platform will hold a mounting point that rotates in two angles.

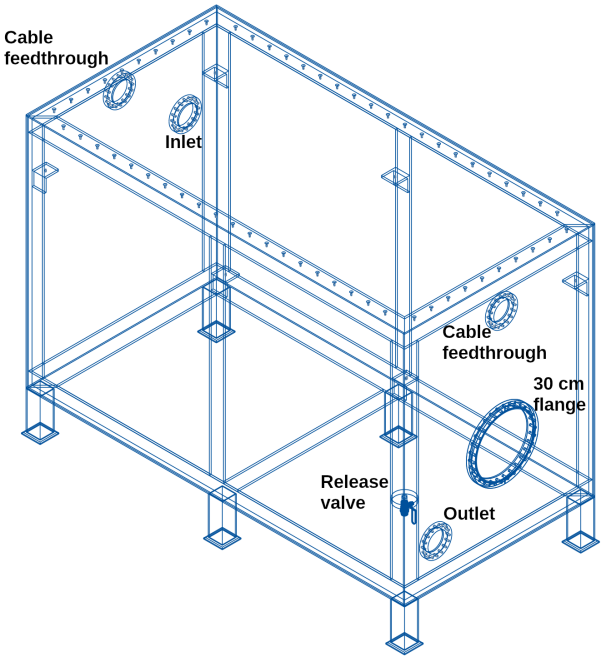

(a) Technical design drawing of PocketWATCH.

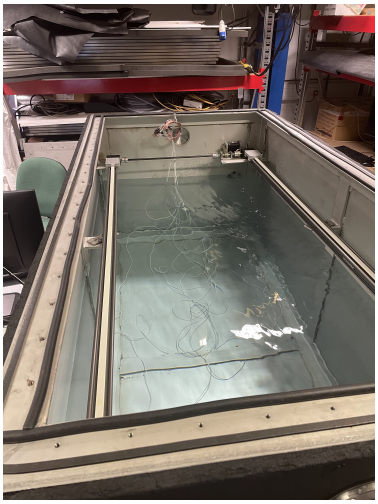

(b) PocketWATCH without lid and during filling with pure water. A two-dimensional gantry is installed at the water surface.

Figure 3.1: The PocketWATCH tank.

Water is circulated through inlet and outlet flanges at opposite diagonal corners below the water level. There are two outlet ports on the lower flange and three inlet ports on the upper flange. The two outlet ports each connect to an inlet port, one via a water purification system and one via a temperature-control system, forming two seperate loops. The third inlet is for filling the system. All five ports have a valve, allowing them to be sealed. A further 30 cm flange is positioned on one wall below the water surface to allow for future experimentation, and two smaller 10 cm flanges above

the water are used for feeding cables into the tank.

Access to the tank is provided by a two-tonne overhead crane and hand-pulled manual crane. This allows the lid to be safely removed and objects to be stably lowered into and raised out of the tank. The tank is capable of housing large objects and rigs, such as the one used for testing up to five 10" PMTs in section 4.6.

3.1.2 Water Filtration

The water is purified using a Veolia Water Technologies system which is able to provide 18.18 MΩ cm resistivity at 25 °C at a flow rate of 20 Litres Per Minute (lpm), giving an idealised turnover time of 1.7 hours. This system is in constant operation to allow continuous purification of the water, with a pump used to circulate the water.

The filtration system consists of several components, a schematic of which is seen in Figure 3.2. A deionisation (DI) cylinder is used to remove dissolved anions and cations in the water, such as Ca^{2+}, Cl^{-} and HCO_3^{-}. This uses a nuclear-grade mixed-bed virgin deionisation resin, with virgin resin used for its better performance when compared to recycled resins. Particulates are removed by a series of filters: 5 µm, 0.2 µm and 0.05 µm in size, and bacterial growth is suppressed using a 254 nm UV sterilisation lamp. The resistivity of the water, as well as its temperature, is monitored pre- and post-filtration. A second 5 µm filter is used in a separate loop during filling to remove large particulates in the main water supply before exposing the rest of the system to the impure water. Using a separate 5 µm filter extends the life of the one in the main filtration loop, which is in constant operation, by not exposing it to water with a high concentration of impurities.

The filtration system for PocketWATCH has four main modes of operation:

1. normal operation with ultrapure water,
2. normal operation with gadolinium-doped water,
    - the DI cylinder is bypassed in this mode
3. fill and recirculate,
4. sanitisation (see subsection 3.1.4).

During normal operation with ultrapure water, water is drawn from the tank using the pump and sent via the DI cylinder, particulate filters and UV lamp before returning

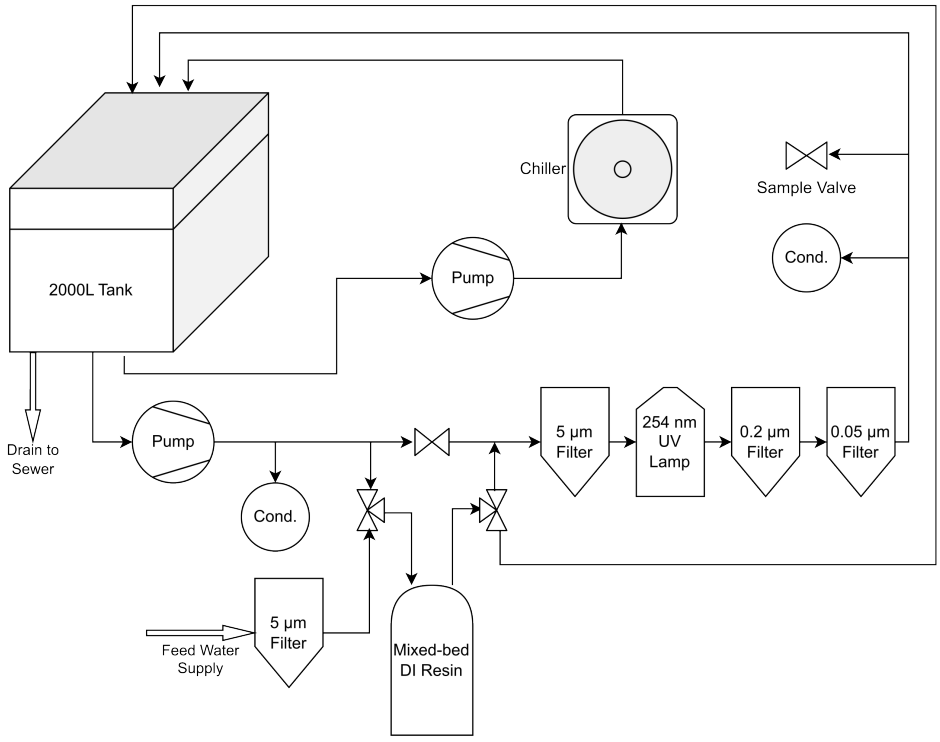

Figure 3.2: Schematic of the PocketWATCH filtration system. Figure by Matt Thiesse.

to the tank. The UV lamp is located between the 5 µm and 0.2 µm filters. For use with gadolinium-doped water, the DI cylinder is bypassed to avoid it removing the Gd^{3+} ions from the water. Options are available for Gd-compatible deionisation, which are discussed in more detail in subsection 3.2.3, but they are not currently deployed in PocketWATCH. During filling, water from the main water supply is fed through the separate 5 µm filter and the DI cylinder before entering the tank through the alternative filling port. Water is then drawn from the tank and circulates via the main filtration loop with the other three filters and the UV lamp, but not through the DI cylinder. Once filling is complete, the DI cylinder is returned to the main filtration loop and normal operation commences.

3.1.3 Water Temperature

The temperature of the water is controlled by an Applied Thermal Control Ltd. K4 4.5 kW chiller on a second loop. This unit can maintain the temperature of the water between 4 and 30 °C to within ± 0.1 °C at a flow rate of 17 lpm. An external pump with a higher water capacity than the K4's internal pump is used to circulate the water

through the loop. Alongside the standard vapour compression and expansion process used for cooling, the system also includes a hot gas valve to allow heating.

3.1.4 Maintenance

Once per year, the system is sanitised and undergoes necessary maintenance. All four particulate filters are removed alongside the UV lamp. The system is fully sanitised using a chemical sanitiser containing hydrogen peroxide, acetic acid and peracetic acid. The DI cylinder is bypassed to stop it removing the chemicals in the cleaning agent. The sanitiser is maintained at a concentration greater than 0.8 % w/w for at least one hour with all parts of the tank, chilling loop and filtration loop in contact. The system is then flushed, and new filters and a new UV lamp are installed. The DI cylinder is replaced less frequently and is done only when necessary.

3.2 Performance

3.2.1 Light Tightness

To operate photodetection experiments, particularly at the single-photon level, external sources of light must not interfere with the equipment. For PocketWATCH, this means any light entering the tank will limit the ability to operate equipment in single-photon mode or understand any light sources being used. Several measures are in place to restrict light from entering the tank and allow operation of equipment in single-photon mode. A 1 cm thick foam gasket between the lid and tank walls forms a hermetic seal when compressed by the lid. The flanges used for electronic feedthroughs and water inlet and outlet ports are all vacuum-compatible, and an extra cover is placed over the tank lid. All pipework is made using thick-walled ABS pipes, replacing the previous pipes which allowed blue and UV light to pass through. These measures exclude all external light from entering the tank, and were all in place during the PMT tests described in section 4.6.

Further measures were added in preparation for the characterisation of light injectors for HK. These included lining the internal walls and base with 3M 2080 Matt Deep Black vinyl to reduce reflections off the tank (Figure 3.3), and using black water-filled polypropylene balls on the water surface to suppress reflections from the boundary between the air and water. These balls provide a 91 % surface coverage through optimal

hexagonal circle packing.

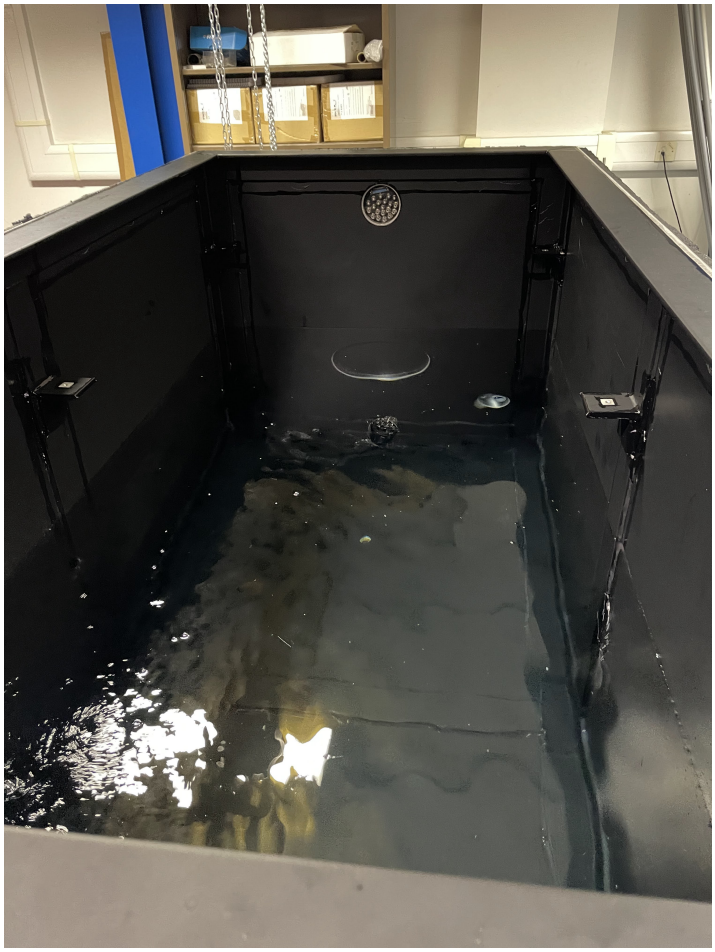

Figure 3.3: PocketWATCH lined with black vinyl.

3.2.2 Water Temperature

It is common for photosensors to be highly sensitive to ambient temperature. To characterise any equipment, the temperature must be maintained in a stable operating window to minimise any thermal effects. Alternatively, to determine the effects of temperature, the water temperature must be adjustable in a controlled and consistent way. The K4 chiller in the PocketWATCH circulation system is used for this purpose. The K4 chiller can maintain a water temperature to within $\pm$ 0.1 °C and adjust the temperature between 4 and 30 °C. However, there is a large surface area beyond the chiller from which heat can escape, reducing the efficiency and consistency. The pipes

between the chiller and the tank, and the tank walls and lid, provide a significant opportunity for heat loss.

Figure 3.4: PocketWATCH with insulation and an extra cover to prevent light entering the system. Cables can be seen entering the tank via a covered feedthrough at the top of the near side.

To maintain the bulk temperature, the outer walls of the tank are covered in 19 mm thick Armaflex Class O insulation with a thermal conductivity less than 0.033 W/(m·K) at 0 °C. All large sections of pipework between the chiller and the tank are also insulated with foam to maintain temperature, and the room itself is held at 20 °C by an air conditioning unit. Some of the measures to counter temperature loss, and to reject ambient light, are shown in Figure 3.4.

The bulk water and ambient temperatures are measured by a series of Pt100 RTD sensors in the bulk volume, filtration system and room. The bulk water temperature

is stable to within 0.012 °C, with a small offset between probes due to differences in the Analogue-to-Digital Conversion (ADC) calibration of the probes. The temperature stability is visible in Figure 3.5.

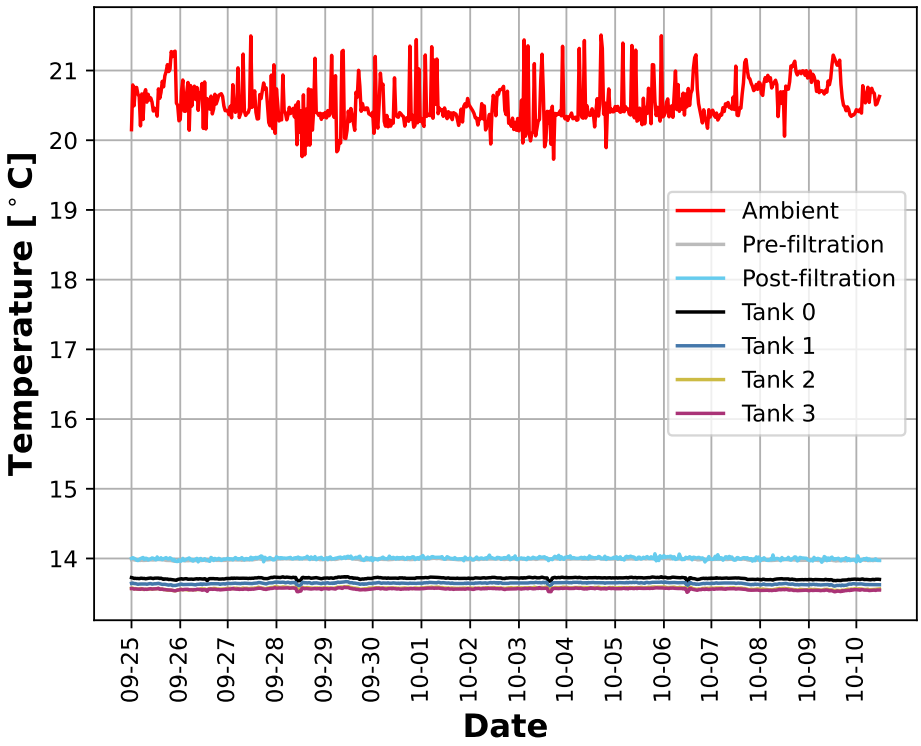

Figure 3.5: Measured PocketWATCH water and ambient temperatures. Small dips in the temperature measurements in the tank are due to electrical noise, and not actual temperature changes.

3.2.3 Water Quality

Liquid-filled particle detectors have great effort put into making their fill media as pure as possible. This is to reduce backgrounds from radioactivity and impurities, and maximise detector performance. Water-based detectors such as SK use ultrapure water which is continuously filtered and polished, and are able to achieve attenuation lengths reaching 100 m for light in the wavelengths of interest [263].

To replicate these conditions, PocketWATCH has a deionisation and filtration system in constant operation, and water conditions are closely monitored. The water quality is measured constantly via resistivity measurements pre- and post-filtration.

There is no *in situ* measurement of the bulk volume in the tank, so the post-filtration resistivity acts as the maximum resistivity of the water and the pre-filtration resistivity approximates the minimum resistivity assuming efficient mixing of impurities in the tank. The resistivity of the water leaving the tank is always lower than it is leaving the filtration system due to the dissolution of atmospheric gases and the leeching of chemicals from components in the system.

The resistivity running in pure-water mode is seen in Figure 3.6. The constant supply of ultrapure water is maintained, shown by the post-filtration measurement at over 18 MΩ cm, and has a small drop in resistivity as it enters the tank and passes through the system. The large drop in the pre-filtration measurement is caused by the tank being opened, allowing atmospheric gases to dissolve. Once the lid is replaced, the resistivity returns to its prior value.

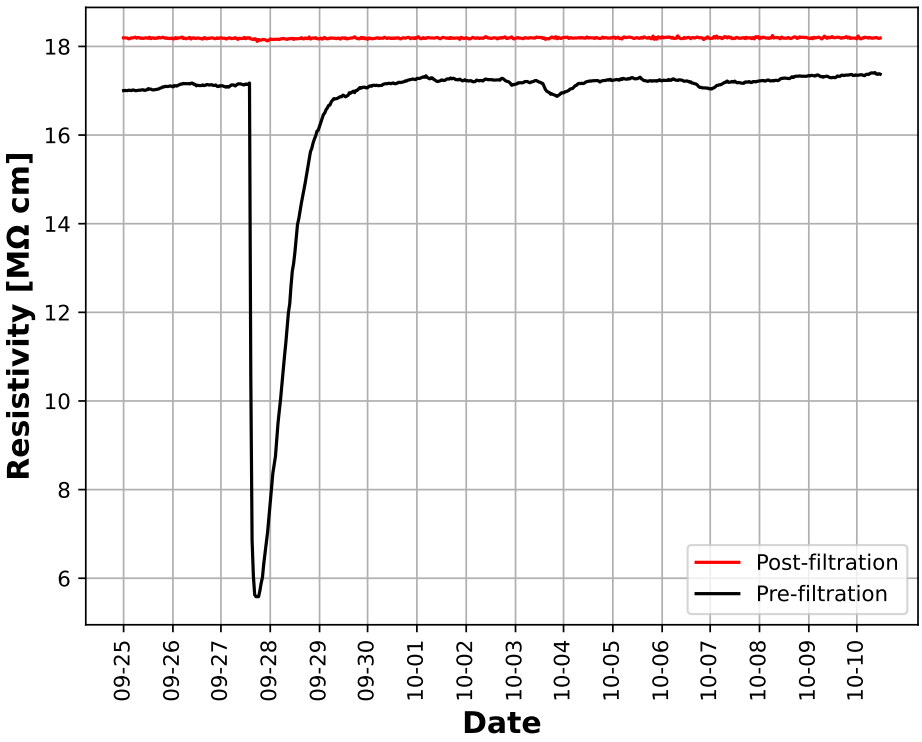

Figure 3.6: Resistivity of water in PocketWATCH before and after the filtration system. The large drop in the pre-filtration resistivity is caused by removing the tank lid, which allows atmospheric gases to dissolve into the water.

A more relevant metric for large Cherenkov detectors, which is not measured in PocketWATCH constantly due to the need for water extraction, is the ability to transmit

UV and visible light. Cherenkov light peaks in the blue and UV wavelength region, and photosensors are typically sensitive to these regions. For these measurements, a Shimadzu UV-2700i UV-Vis spectrophotometer, which uses a pair of lamps, double monochromator and adjustable slit to create a beam of a precisely known wavelength, is used with a 10 cm quartz test cell. Two measurement types are used: a 200 - 800 nm spectrum with a 5 nm slit width is measured for both ultrapure and gadolinium-loaded water, and a 250 - 300 nm spectrum with a 0.1 nm slidth width is measured for the gadolinium-loaded water only. The 200 - 800 nm spectrum is used to determine the transmission of light across the complete region of interest. The 5 nm slit width is chosen to increase the signal-to-noise ratio and give a better accuracy. The larger slit width has a lower resolution, and so cannot resolve sharp peaks as easily. However, for measurements of the full spectrum, these features are not the desired observation. The 250 - 300 nm measurement used for gadolinium-loaded water is a high resolution measurement of the gadolinium excitation peaks in this region (Figure 3.7) [264], and allows a determination of the relative concentration of gadolinium in the water over time from the maximum absorption for each peak. Here, the 0.1 nm slit width allows a good resolution when measuring narrow peaks.

Water is held in a 10 cm long quartz cuvette inside the spectrophotometer. A second 1 cm quartz cuvette filled with water from the same sample is used to measure the effect of the quartz and its boundary with both water and air. The transmission of the 1 cm cell is subtracted from the 10 cm cell, leaving the transmission of 9 cm of the sample water.

When the cuvettes are completely clean, they have an identical transmission. Subtracting the effects of one from the other when empty leaves a transmission of 100 % in an ideal situation. A cleaning procedure, in which the cuvettes are rinsed with acetone followed by deionised water after every use, and cleaned by soaking in nitric acid on a regular basis, is used to maintain the physical state of the cuvettes. However, it is not always possible to maintain perfect cleanliness during repeated testing. This results in the cuvettes showing slight differences in their transmission of light, and the subtraction of one from the other having a wavelength-dependent offset from 100 % transmission. To handle this, a correction is applied to remove this offet. The correction is determined by taking data with the cuvettes empty immediately before a measurement of a sample.

The metric for transmission used by SK is the "light left at X m", typically quoted as the "light left at 15 m" [233]. This is determined by creating a set of weights which are

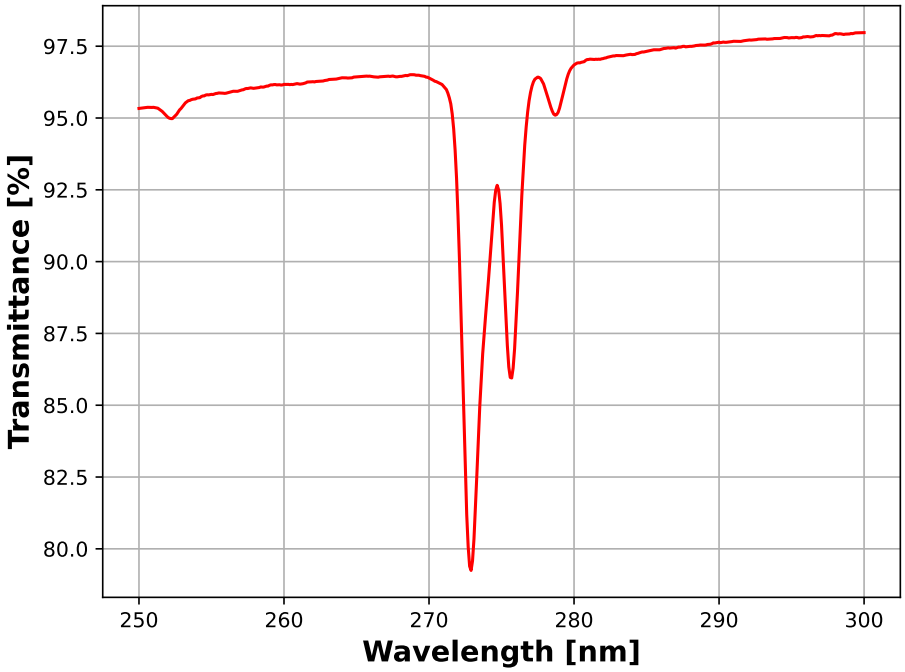

Figure 3.7: Spectrophotometer measurement of transmission between 250 and 300 nm of gadolinium-doped water. The troughs correspond to absorption due to the excitation of Gd^{3+} ions [264].

the normalised product of the SK PMT quantum efficiency and Cherenkov spectrum. These weights allow the wavelengths of interest in the SK detector to be prioritised. The weights are used to produce a weighted average of the percentage transmission for the path length of the measurement, with it being scaled to a chosen distance. The light left at X m is defined as

$$\%LL(X \text{ m}) = 100 \sum_{i}^{7} w_i \times e^{-X \cdot \alpha(\lambda_i)}, \tag{3.1}$$

where λ_i is the i^{th} wavelength, w_i is the weight and α is the attenuation length for the i^{th} wavelength. The attenuation length is calculated as

$$\alpha = \frac{pl}{\ln(P)}, \tag{3.2}$$

where pl is the path length used for measurements ($pl = 9$ cm for PocketWATCH measurements) and P is the probability of transmission of a given wavelength. The weights w_i are given in Table 3.1.

EGADS uses the Underground Device Evaluating Attenuation Length (UDEAL) system to measure water transparency, which is a system of seven lasers fired through a vertical water column of variable height up to a maximum of 8.2 m. The light intensity is measured by two integrating spheres, one before and one after the light is transmitted through the water, using photodiodes.

λ [nm]	337	375	405	445	473	532	595
w	0.252	0.253	0.206	0.141	0.106	0.039	0.003

Table 3.1: Wavelength of lasers used by UDEAL and their weights for the calculation of light left [233, 265, 266].

The $\%LL(15\,\text{m})$ in SK is typically greater than 80 %, and was in the 74 - 82 % range for SK-III and -IV [267]. EGADS observed values typically between 74 and 78 % with gadolinium-loading (Figure 2.6).

The $\%LL(X\,\text{m})$ metric and weights in Table 3.1 are used to determine the optical performance of the water in PocketWATCH, for both ultrapure water and $Gd_2(SO_4)_3$-loaded water.

3.2.3.1 Pure Water

The light left at 2 m, the length of the tank, in PocketWATCH is observed as 93 $\pm$ 2 % (Figure 3.9) with a transmittance of greater than 99 % across most of the relevant wavelength region (Figure 3.8). This allows Cherenkov radiation to be detected across the whole tank by a PMT similar to those in SK.

The light left at 15 m is $\sim$15 % lower than measured by SK and EGADS, however this may be in part due to methodology limitations. The measurements are significantly limited by the spectrophotometer setup, including the limited path length and cuvette cleanliness. The sensitivity of the spectrophotometer, which peaks in the 350 - 550 nm range, means very little UV light is absorbed over the measurement path length for the wavelengths of interest. Therefore, over the 9 cm test cell, very little detectable absorption occurs in this wavelength range. The UDEAL system used by EGADS has a length of 8.2 m [233], and SK is able to use the inner detector volume [220], giving a much larger path length for absorption to occur and be detected. However, extrapolating from a 9 cm path length to several metres is difficult and small effects can produce a large difference in the determined light left. The cleanliness of the

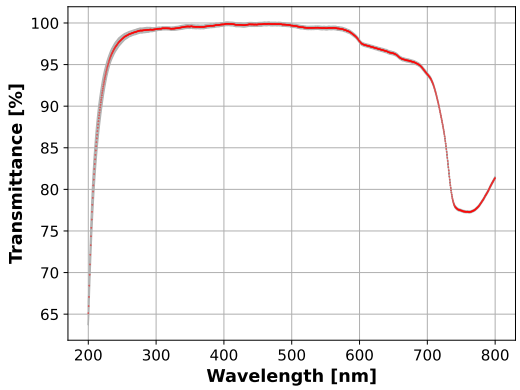

Figure 3.8: Percent transmittance of PocketWATCH water when running in pure water mode. Cumulative measurement errors from the UV-Vis spectrometer are also shown.

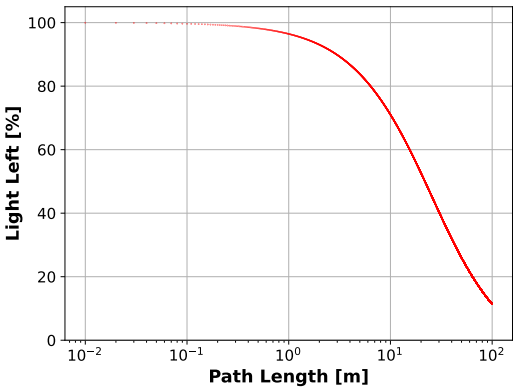

Figure 3.9: Percent light left shown as a function of distance in PocketWATCH pure water.

cuvettes can produce these effects, with difference between the sample and reference cells offsetting the measured transmission. Correcting for this effect by measuring the transmission of the empty cuvettes handles most of these issues, but any impurities introduced when filling the cuvettes, or any impurities that can be suspended in liquid, are harder to account for as they are only observable during sample measurements.

The uncertainty on the measured transmittance is determined from many repeat measurements over a large period of time, and accounts for the cuvette cleanliness, the handling of the sample between extraction from the tank and measurement of its spectrum, and the positioning of the cuvettes in the spectrophotometer.

3.2.3.2 Gadolinium Compatibility

PocketWATCH is designed to be fully compatible with gadolinium doping in the form $Gd_2(SO_4)_3{\cdot}8H_2O$ at a concentration of 0.2 %, which matches the gadolinium doping of EGADS. Using gadolinium sulphate in an octahydrate form allows easier dissolution into water than using pure gadolinium sulphate. Gadolinium compatibility allows testing for a wider range of experiments to take place, and materials were selected using the experience of EGADS. Most materials known to be compatible with ultrapure water are also compatible with Gd at the relevant concentration, except nylon and certain

PVC formulations.

The DI cylinder is not compatible with Gd however, as it would remove the ions from the water. Two proven methods exist to replace this, exchange resins with Gd counterions as used by SK and an EGADS-style bandpass filtration. The exchange resin works similarly to the standard DI cylinder used for PocketWATCH, but replaces removed ions with Gd ions. Therefore, if a Gd^{3+} ion is removed, it is replaced by another for no net loss in concentration. The band-pass system used by EGADS splits the water flow into a Gd-less water and concentrated Gd water flow using nanofilters after passing through a UV lamp and larger filters. The Gd-less water is then purified through deionisation before being recombined with the concentrated Gd water. For PocketWATCH, no Gd-compatible replacement for the DI cylinder is used. During the gadolinium-doped operational mode, only the particulate filters and UV lamp are used in the filtration system.

The water quality is measured in the same way as it is in pure-water mode, using resistivity and UV-visible light transmission, with emphasis on the optical transmission. To measure the stability and water quality over time, 4 kg of $Gd_2(SO_4)_3{\cdot}8H_2O$ was dissolved in the tank for a 0.2 % concentration, and regular optical transmission measurements were made over the course of a week. As the dissolving process on a large scale takes time, the lid of the tank was removed for a long enough period to allow a significant dissolution of atmospheric gases. A nitrogen buffer can be used above the water surface to prevent this. However, as this is unnecessary for the normal operation of the facility, the tank was not changed to incorporate this for the purpose of the Gd-compatibility test. To make a direct comparison to the water quality without Gd, transmission measurements of the pure water were made without the DI cylinder and with the lid off to replicate the conditions. If the DI cylinder was replaced with a Gd-compatible system, this would not be necessary as the dissolved atmospheric gases could be removed during deionisation without a reduction in the Gd concentration.

The measurements of Gd-loaded water and pure water, both with the DI cylinder bypassed, are comparable as shown by Table 3.2. The Gd-loaded water had an approximately 2 % reduction in light left after the 2 m length of PocketWATCH, and showed a similar transmittance, when compared to pure water with no DI. The transmittance and percent light left are shown for pure water with the DI bypassed in Figure 3.10 and Figure 3.11, with the equivalent for Gd water shown in Figure 3.12 and Figure 3.13. The small difference between the Gd-doped and pure water is not unexpected based on

Mode	$\%LL(2\,\mathrm{m})$	$\%LL(15\,\mathrm{m})$
Pure Water - DI	93 ± 2	62 ± 10
Pure Water - No DI	93 ± 2	64 ± 11
Gd Water - No DI	91 ± 2	53 ± 9

Table 3.2: Percent light left at 2 m and 15 m for PocketWATCH water.

the small difference seen by EGADS to SK-III and -IV.

The measurements of light left over time and with decreasing resistivity, both with and without Gd, with the DI cylinder bypassed are stable. The water resistivity and $\%LL(2\,\mathrm{m})$ for the pure water are shown in Figure 3.14 for measurements taken prior to the implementation of cuvette cleaning procedures and corrections. The absolute values of the $\%LL(2\,\mathrm{m})$ measurements are lower than those with the cleaning procedures used for the result in Table 3.2, but show the stability of UV transmission over time. The resistivity of the water drops off rapidly in the first day with the tank open and DI cylinder bypassed, before decreasing at a constant rate of approximately 9 % per day through the end of the test.

The water resistivity when Gd is loaded into the water falls to below $1.5\,\mathrm{k\Omega\,cm}$ before stabilising (Figure 3.15 (top)). The $\%LL(2\,\mathrm{m})$ remains stable throughout the test, and is comparable to the values obtained from pure water (Figure 3.15 (middle)). This stability implies no leeching of chemicals or material degradation due to reactions with the $Gd_2(SO_4)_3$. Analysis of the absorption peaks due to gadolinium showed no change over time once all $Gd_2(SO_4)_3$ had completely dissolved (Figure 3.15 (bottom)). This confirms that no gadolinium is being removed by the filtration system or is coming out of solution during circulation.

A combination of good optical properties when the water is gadolinium-loaded, no reduction in gadolinium concentration and no apparent material compatibility issues indicates that the system is compatible with gadolinium. This allows the replication of gadolinium-doped water Cherenkov detector conditions for equipment testing.

3.3 Summary

The PocketWATCH facility is a test bed designed for prototyping and characterising equipment for deployment in water Cherenkov detectors. It is able to replicate the water

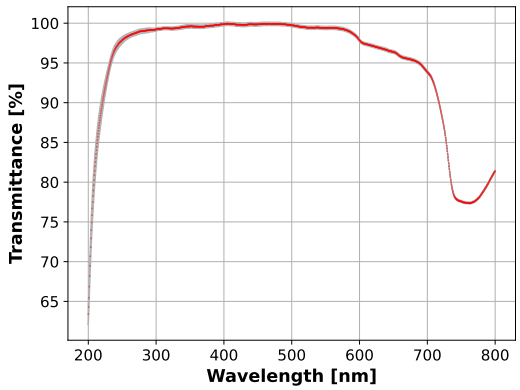

Figure 3.10: Percent transmittance of PocketWATCH water when running in pure water mode with the DI cylinder bypassed. Cumulative measurement errors from the UV-Vis spectrometer are also shown.

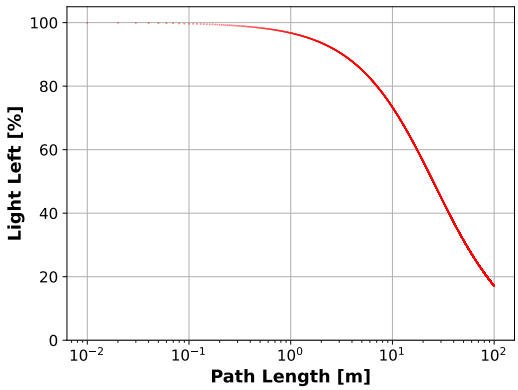

Figure 3.11: Percent light left shown as a function of distance in PocketWATCH pure water with DI cylinder bypassed.

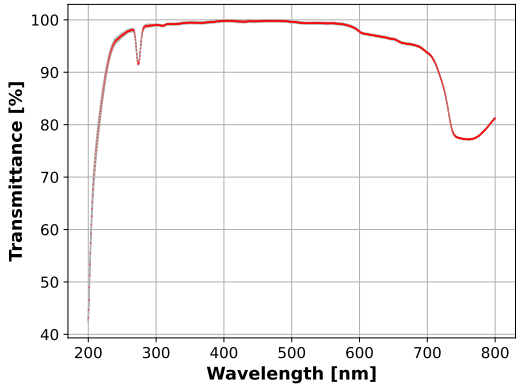

Figure 3.12: Percent transmittance of PocketWATCH water when running in Gd water mode with the DI cylinder bypassed. Cumulative measurement errors from the UV-Vis spectrometer are also shown.

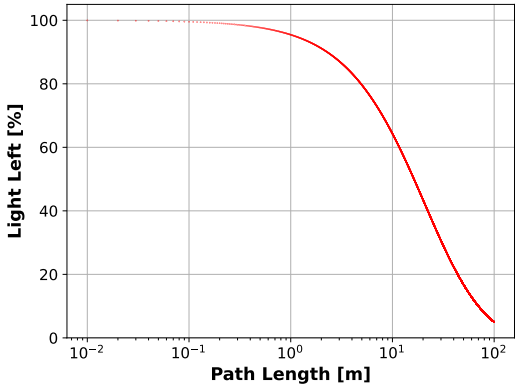

Figure 3.13: Percent light left shown as a function of distance in PocketWATCH Gd water with the DI cylinder bypassed.

and light conditions of large, ultrapure water detectors and those with gadolinium-loading.

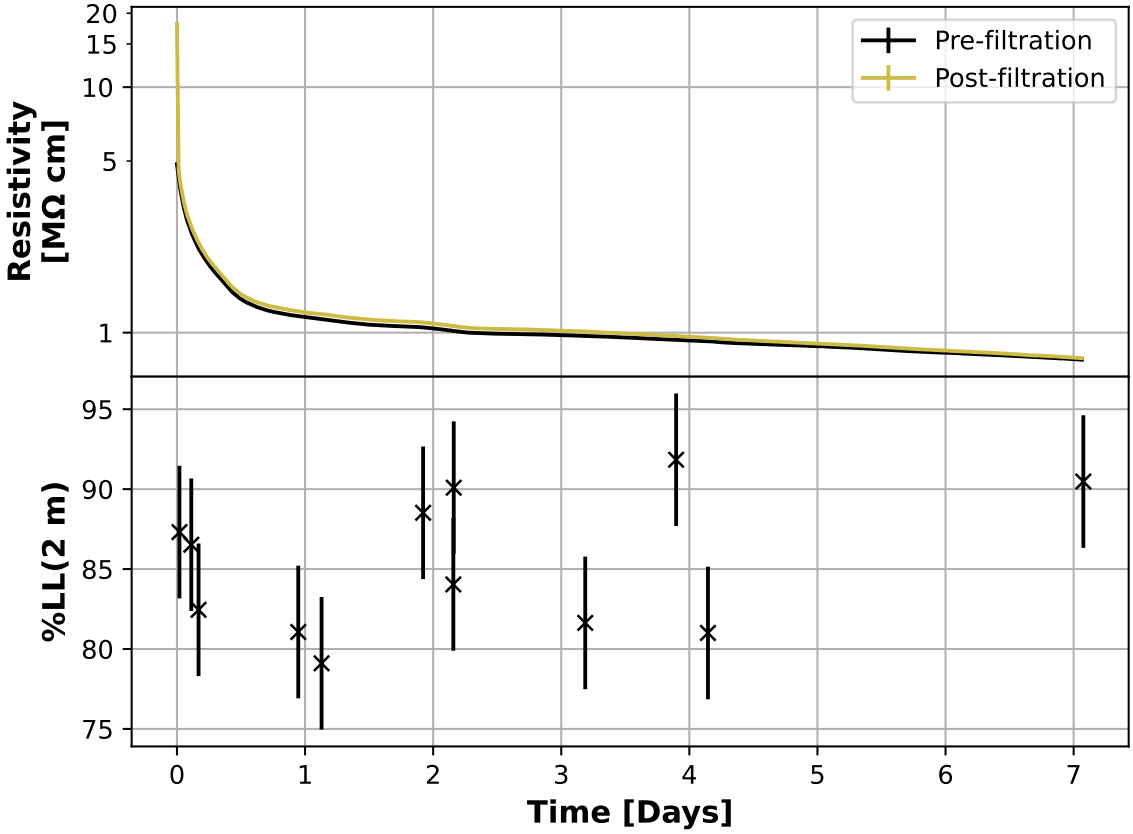

Figure 3.14: Pure water resistivity (top) and $\%LL(2\,\mathrm{m})$ results (bottom) over time since the DI bypass. The mean value was $\%LL(2\,\mathrm{m})$ here is $85 \pm 5\,\%$, but the standard cuvette cleanliness procedure was not followed. Instead, the stability of the $\%LL(2\,\mathrm{m})$ is of interest.

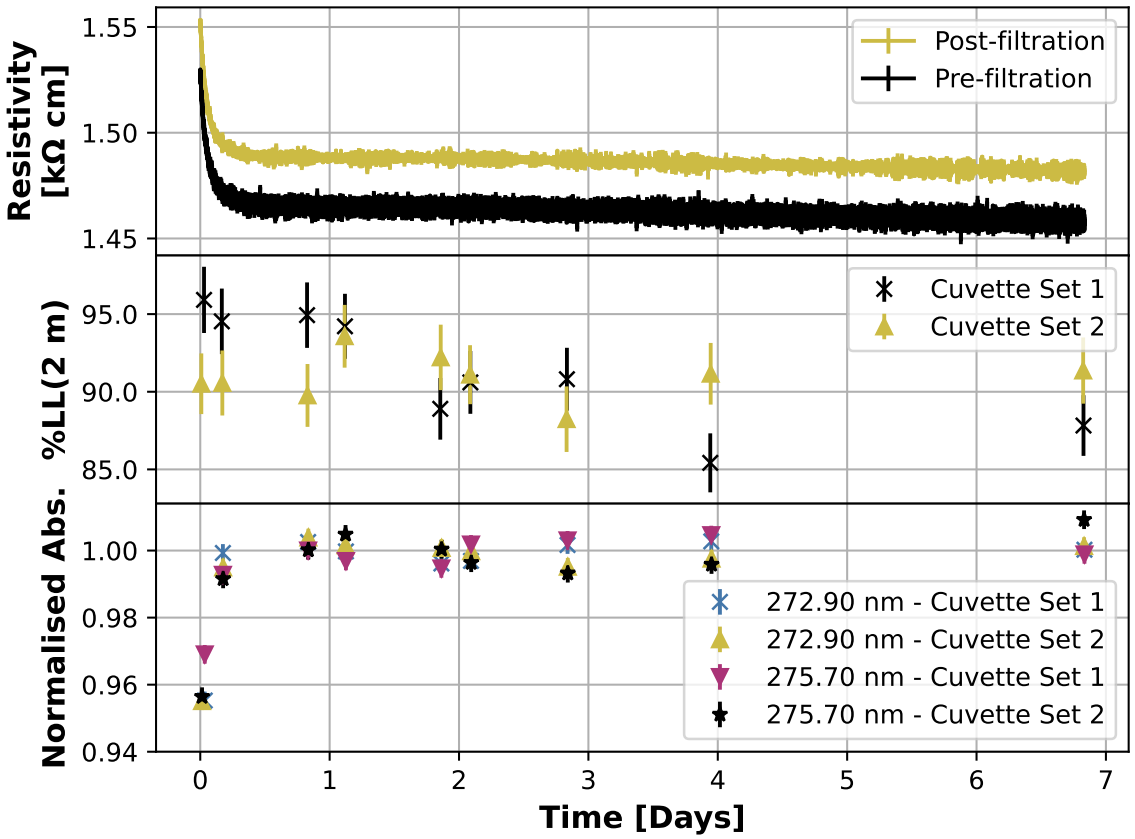

Figure 3.15: Gd water resistivity (top), $\%LL(2\,\mathrm{m})$ results (middle) and normalised peak absorbance for the largest two Gd absorption peaks (bottom). The approximately 1.5 % difference in resistivity readings from both sensors is consistent with the expected accuracy uncertainty of the cell constant, specified as $\pm$ 1 % for this range.

The water in the system is continuously filtered and polished to remove impurities, with resistivity measurements reaching those expected of ultrapure water. The optical properties of the water allow transmission in the wavelengths of interest for Cherenkov detectors, and are stable over long periods of time.

The system is completely gadolinium compatible, with no leeching of chemicals from materials in the system or degradation of the optical properties of the water. The filtration system does not remove the gadolinium ions, although an alternative deionisation system is required such as the resin used by SK.

The PocketWATCH tank is completely light tight and temperature-controlled, allowing a variety of testing regimes down to the single-photon level. The tank also has

the space and capacity for gantry systems to be installed at the surface of the water, or for large objects to be lowered in by an overhead crane.

These attributes produce a facility that can be used not only for equipment development, but also general experimentation. Cosmic ray muon detection in the water using a variety photosensors, with plastic scintillator placed on the tank lid for a coincidence trigger, can be performed. When loaded with gadolinium, neutron capture measurements originating from both cosmic ray muons and radioactive neutron sources can be made by measuring the nuclear de-excitation of the gadolinium. Detailed measurements of equipment, such as the testing of PMTs described in chapter 4, and experiments using larger photosensors are also possible using the facility. The combination of material compatibility, water purification, overhead access using a crane and light tightness allow a large range of particle detection experiments, creating a highly flexible and unique facility.

Chapter 4

Photomultiplier Tubes and their Characterisation

In a liquid-filled particle detector, the photons emitted due to particle interactions are used to observe and identify particles. In the case of neutrino detectors, these particles are the products of neutrino interactions. To detect the emitted photons, the detector is instrumented with photosensors. The common choice of photosensor is the Photo-Multiplier Tube (PMT). Photons, in particular when detected individually, produce small signals. PMTs are designed to amplify a photon signal, making them more easily observed.

The choice of photosensor is dictated by the requirements of the detector. Neutrino detectors require stability and longevity due to the long detector lifetimes, high photosensor coverage and therefore low cost per unit collection area, and sensitivity to the wavelengths produced by the detector medium. Large PMTs are the typical choice here. SK uses 11129 Hamamatsu 20" diameter PMTs in the inner detector and 1885 8" diameter PMTs in the outer detector [263, 268], the outer detector for LUX-ZEPLIN (LZ) uses 3" PMTs [269] and SNO+ uses 9362 8" PMTs previously used in SNO [85, 270]. Fast timing can be useful in some scenarios, such as Cherenkov/scintillation separation; fast detectors such as LAPPD™s are useful here [251, 253]. Some novel detectors require several channels in a single readout, in which case small multianode PMTs are beneficial [271, 272].

The PMTs used for performance studies of Neutrino Experiment One (NEO) from chapter 5 onward, and the ones that will be used in the Boulby Underground Test Tank for Observing Neutrinos (BUTTON) [3], are 10" Hamamatsu R7081-100s. This

PMT model and characterisation testing of these devices is described from section 4.3 onward.

4.1 Background on PMTs

PMTs are used to detect photons by converting them into a readable electrical signal. There are several key sections in a PMT, which are shown in Figure 4.1.

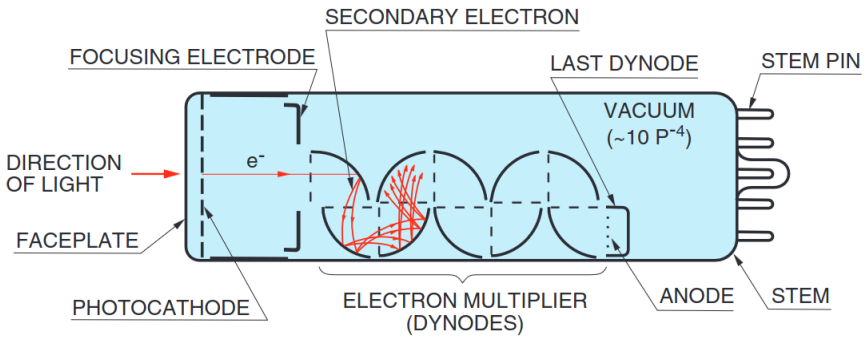

Figure 4.1: Structure of a PMT. Reprinted from [273].

There is an outer window layer at the front which has a low work function material deposited on the inside called the photocathode. On larger PMTs, the window is often a bulbous shape and the photocathode sits on the inside of the bulb. This is to increase the mechanical strength as inside the window is a vacuum region. A diagram of the Hamamatsu R7081, with its bulbous window, is shown in Figure 4.5. A photon in the energy range the photocathode is sensitive to has the potential to liberate an electron, called a photoelectron, via the photoelectric effect [274]. Liberated electrons are pulled by a potential across the vacuum region under the window towards a current amplification region. Current amplification is commonly done using dynode chains [274], but Micro-Channel Plates (MCPs) are also used as they are much thinner and so reduce the time for an electron to propagate through the system [275, 276]. Secondary electrons are emitted at each dynode, or MCP, to amplify the current. The amplified current is picked up by the anode, where the signal can be read out. PMTs with a gain, the ratio of the charge at the anode to the number originating photoelectrons for the pulse, of 10^6 or more allow single photoelectrons to be counted. The charge read out at the anode can allow multi-photon pulses to be analysed, as it is expected that

charge collected at the anode is linearly correlated with the number of photons hitting the photocathode.

PMTs have a typical response to a single photon liberating a Single Photo-Electron (SPE). This forms a characteristic pulse at the anode, the features of which are dictated by the PMT's design.

There are several ways in which PMTs can differ. Many features such as the timing characteristics, sensitive wavelengths, gain and dark rate are dictated by PMT design.

4.1.1 Window and Photocathode

The choice of photocathode material will impact the wavelengths that the PMT is sensitive to [273]. Bialkali photocathodes have a quantum efficiency, the probability of a photon incident on the photocathode being absorbed and liberating a photoelectron, that peaks for blue wavelengths [274]. An example of the wavelength-dependent quantum efficiency of a bialkali photocathode is shown in Figure 4.2. A quantum efficiency

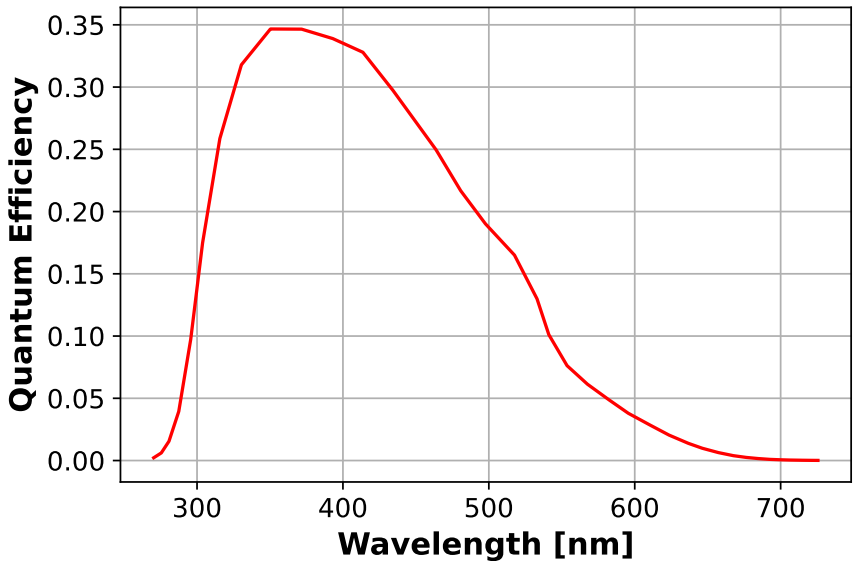

Figure 4.2: Quantum efficiency of the Hamamatsu R7081-100 with a high quantum efficiency bialkali photocathode as used in simulations for NEO [277].

of 35 % is considered to be high. Bialkali photocathodes, such as Sb-Rb-Cs and Sb-K-Cs, have a higher sensitivity and lower dark current (described in subsection 4.1.5) than an Sb-Cs photocathode. Low noise bialkali photocathodes e.g. Sb-Na-Cs are available.

They are able to withstand high operating temperatures, up to 175 °C compared to the standard 50 °C, and exhibit very low dark current.

The sensitivity is also determined by the window materials. The most common choice is borosilicate glass which is opaque at wavelengths shorter than 300 nm [273].

The PMT glass is a large source of background in detectors with many PMTs due to its inherent radioactivity. Low-radioactivity borosilicate glass can be used, where materials and processes that introduce less contamination are used. This can lower the rates of radioactive decays in the glass by an order of magnitude. There is a tradeoff between sensitivity, cost and radioactivity. Materials that offer both high sensitivity and low radioactivity tend to cost more to produce. This can be impractical for detectors with many photosensors.

4.1.2 Charge and Gain

The output charge distribution of a PMT is determined by several factors: the cathode, the amplification, and the charge collection [273]. The gain of a PMT is determined by the amplification mechanism. Dynode chains are split into several stages, typically between a few and around 20, and amplify the current by a factor between 10 and 10^9. More stages in the dynode chain will provide more amplification, with the total amplification being described by

$$\mu = \delta^n, \tag{4.1}$$

where μ is the gain, δ is the number of secondary electrons emitted per primary electron for the dynode material and n is the number of stages in the dynode chain. Materials used in the dynode are chosen for their secondary emission, with alkali antimonide (Sb), beryllium oxide (BeO) and magnesium oxide (MgO) being commonly used [273]. The material is coated onto a substrate electrode. The electrode is typically nickel, stainless steel or copper-beryllium alloy. The calculation of gain can be done from the charge distribution resulting from the integration of the waveforms output at the anode.

The total gain across the complete dynode chain (in the case of a roughly linear voltage divider) can be modelled as

$$\mathcal{A} = a^n \left(\frac{V}{n}\right)^{n\alpha}, \tag{4.2}$$

where V is the applied voltage, n is the number of dynodes, and a and α are constants specific to the PMT [274]. To reduce the need for very high gain PMTs, amplifiers are

often used to boost the output signal. The observed gain in this case is the gain of the whole system including additional amplification.

The linearity of the system, the degree of proportionality between the incident light and resulting electrical signal, will impact the charge output. The linearity in current through the cathode is typically limited to the µA level, above which the resistivity can impact the linearity of the PMT output. A high bias to the first dynode can help reduce this effect.

The uniformity of the electric field through the amplification structure will also impact the output. Edge effects and non-uniformity in the field between dynodes can cause charge to be lost as it propagates through the system.

The anode can also be a source of non-linearity in the system. For large pulses, the large amount of charge may impact the electric field as it passes through the anode which will impact the current at the anode. A higher potential means that a larger pulse is needed to disrupt the electric field, as the field will be larger relative to the pulse, and will improve linearity.

The charge distribution, such as the one shown in Figure 4.3, can be used to determine the resolution of the PMT i.e. how well photoelectrons can be resolved from each other; some PMTs are able to resolve single photoelectrons.

4.1.3 Timing

A PMT will produce an electrical pulse at the anode when charge is collected after a single electron is amplified through the system. The PMT will have a charge response and a time response to the single electron. The Single-Electron Time Response (SETR) is the distribution of arrival times in the electron cascade that constitutes the PMT output $i(t)$. It is assumed that the timing distribution for the amplification of a single electron starts as a δ-function at the first dynode, where secondary electrons are generated [274]. The secondary electrons are released without any time dispersion, but with different initial energies and directions. These electrons then arrive at the second dynode with an exponential time distribution. The timing distribution becomes an exponential folded with itself at each dynode. This creates an output function at the n^{th} dynode:

$$i_n(t) = t^n \exp(-\alpha t). \tag{4.3}$$

The impact on the timing characteristics of a pulse of this effect are seen in Figure 4.4, where the spread leads to a pulse with a width λ.

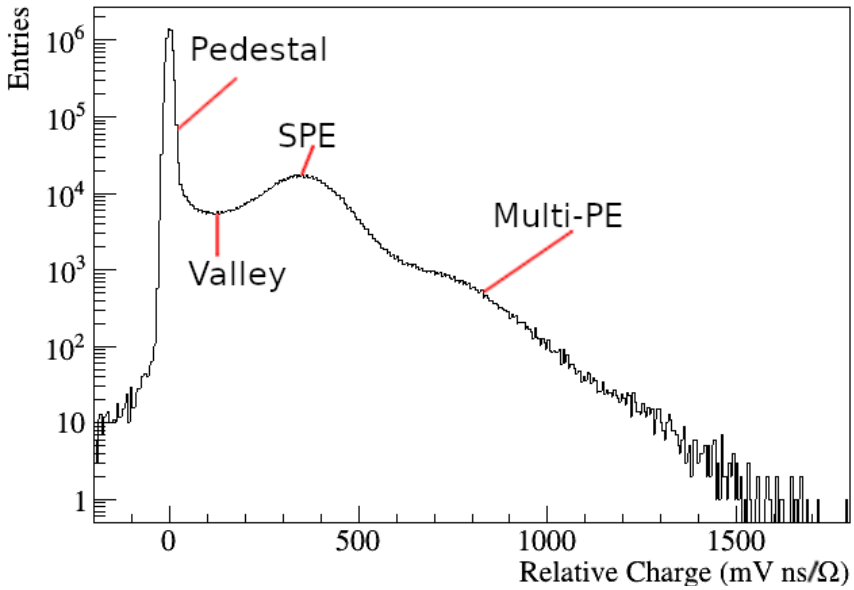

Figure 4.3: Typical relative charge spectrum of a Hamamatsu R7081 PMT with the key components labelled. The pedestal is due to waveforms with no pulses, the valley is caused by under-amplified signals, and the charge response contains an SPE peak with multi-PE peaks in the tail.

The transit time of a PMT is the time it takes from a photoelectron being liberated to the signal being produced at the anode. Transit time is statistical and so is quoted as an average. The distribution for transit time consists of several features; there is a prompt signal from a photoelectron which is Gaussian, a continuous random dark noise distribution and delayed pulsing peaks (see subsection 4.1.4). In multi-detector systems, such as neutrino detectors with a large number of PMTs, transit time is generally accounted for to synchronise the output. The transit time of a PMT is affected by λ, but in a complex and non-trivial manner.

Transit time has a dispersion from pulse to pulse for the prompt photoelectron signal. This dispersion is caused by several factors including the launch angle, emission energy and location of emission of the photoelectron from the photocathode, and the way is which the charge is collected by the anode. The standard deviation of the distribution of transit time is the Transit Time Spread (TTS). This spread will impact the ability to observe and reconstruct events.

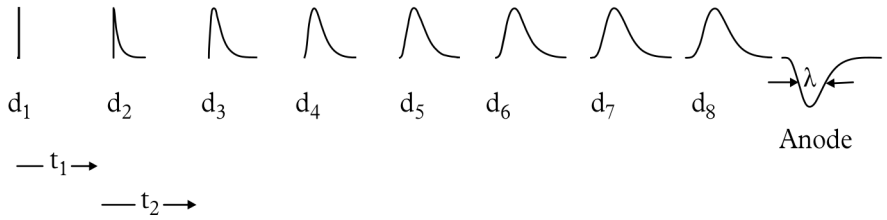

Figure 4.4: Pulse shape with the dynode steps. λ is the pulse width at the anode. Reprinted from [274].

4.1.4 Undesired Pulses

Most pulses will occur via the standard propagation route of a photoelectron passing from the photocathode through the dynode chain. However, a small number of pulses are affected by other mechanisms and can lead to early or late pulses [274]. There are several mechanisms for this and they all impact the observed pulse at the anode differently:

1. Backscatter of a photoelectron from the first dynode causes the photoelectron to travel toward the photocathode, decelerating in the electric field. The electron stops just short of the photocathode and then accelerates through the system as it would if liberated from the photocathode, creating a late pulse.

2. A photoelectron can be scattered inelastically from the first dynode, carrying away some energy. Fewer secondary electrons are emitted and two undersized pulses are produced, one of them being a late pulse.

3. A photon can be directly incident on the first dynode. An undersized pre-pulse is generated here.

4. Photons can be produced at the anode in high gain PMTs. If these photons reach the photocathode, a photoelectron can be emitted and a second pulse at twice the transit time is produced.

5. High-speed scattering of a photoelectron from the first to the second dynode can generate an undersized, slightly early pulse.

6. After-pulsing can occur due to ionisation of gases due to an imperfect vacuum in the PMT.

7. Induced charge passing through the anode mesh due to the electrons from the penultimate dynode can produce an early pulse. This pulse is normally very close in time to the main pulse and is often not resolved.

4.1.5 Dark Noise

PMTs used for single-photon detection have characteristic SPE pulses produced when a photon liberates an electron from the photocathode. However, photons are not the only mechanism by which electrons are liberated from the photocathode. Thermal energy, electric fields and particles can all liberate electrons if enough energy is transferred. From the waveform alone, it is impossible to distinguish the mechanism that produces an electron as the pulse is identical between mechanisms. A single electron will produce an SPE level pulse (a pulse with the same characteristics as a single-photon produced pulse).

Pulses produced in the absence of photons are referred to as "dark" pulses, PMTs each have a characteristic count rate of these, and are a dominant background to single-photon detection. Thermionic emission, where an electron is liberated from the photocathode by thermal energy, is one of the major mechanisms that produces dark counts and should be characterised in detail. There is also a dark current component due to leakage current. This is generally due to imperfect insulation in the system, and is more dominant at lower voltages. In neutrino detectors, dark noise can limit the ability to reconstruct events [278].

4.2 PMT Requirements for Reactor Antineutrino Detection

For instrumenting a reactor antineutrino detector with a kilotonne-scale volume, thousands of PMTs are needed. They need to be capable of detecting single photons to allow low energy interactions to be observed, and have the smallest background possible. If a PMT has a high intrinsic dark noise or radioactivity, when a large number are used the background can be overwhelming.

Before installation, the PMTs must also be well understood to optimise their performance. To ensure an even response from all PMTs in a detector after electronics are considered, the charge and timing characteristics must be well known. Not all PMTs

will produce the same gain for the same voltage due to internal differences, so their gain must be calibrated to ensure each one has the correct voltage. To correlate the pulses from all PMTs in the system, the time profiles and noise of the PMTs must be understood to allow the pulses to be digitised accurately. It is common for testing programmes to be carried out in advance of detector installation for these reasons. Some keys tests are given in Table 4.1.

Test Type	Description
Gain	Determine voltage for optimal gain
Peak-to-valley	Determine signal-to-noise
Dark Counts	Determine dark noise

Table 4.1: Key tests often performed on PMTs.

In the case of simulation studies of proposed detectors, such as those presented from chapter 5 onward, the timing and charge distributions need to be accounted for to simulate accurate data acquisition. The contribution to background, both due to radioactivity and dark noise, are also requirements for producing accurate results. Without this information, results from simulations will be optimistic and misleading.

The rest of this chapter details tests performed on PMTs for the BUTTON test experiment under construction at Boulby Underground Laboratory in the UK, and to be considered for a proposed reactor antineutrino detector.

4.3 Hamamatsu R7081-100 Photomultiplier Tube

The PMTs to be used in BUTTON are Hamamatsu R7081-100 10" tubes with a low radioactivity borosilicate glass window and a bialkali photocathode. An integrated base containing the dynode chain is supplied with the PMT, and is encapsulated to be waterproof and compatible for use in gadolinium-doped water. The base is shown in Figure 4.5 before encapsulation. An 80 m BELDEN YR53485 cable, connected by the vendor, is used to supply positive High Voltage (HV) and provide a return path for the signal as they are Alternating Current (AC) coupled. The electronics in the PMT base has an impedance of 50 Ω.

The R7081-100 has a 10 stage box and line dynode (Table 4.2), creating a 10^7 gain, and a 300 nm to 650 nm spectral response from the photocathode. The peak wavelength

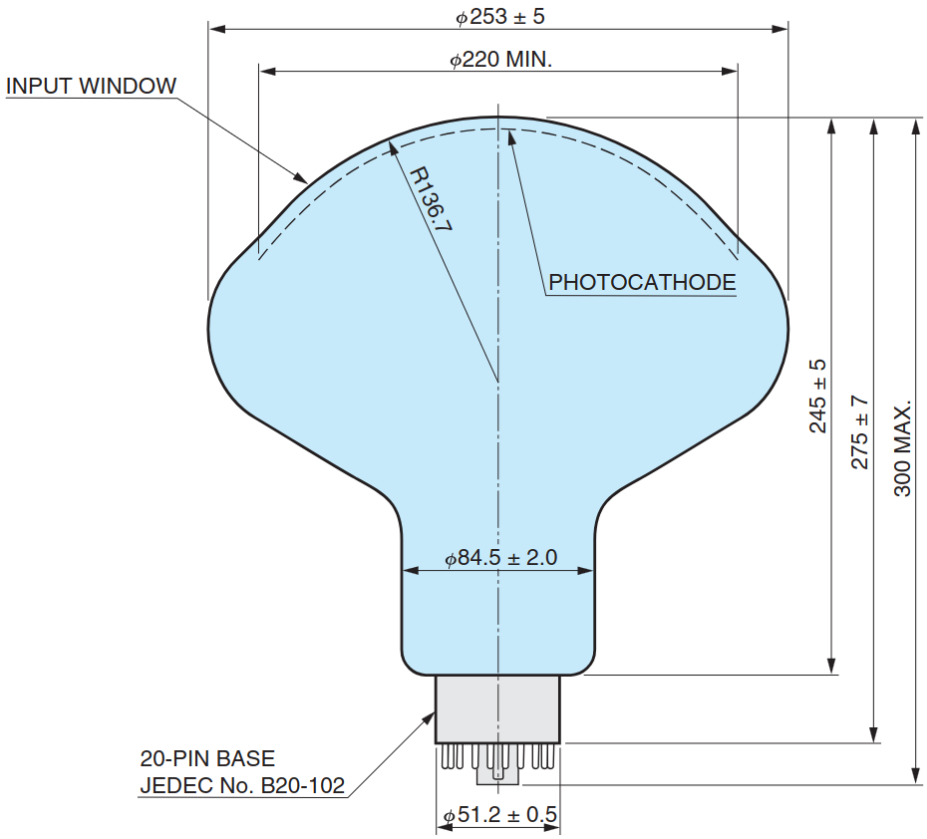

Figure 4.5: Diagram of the Hamamatsu R7081 10" PMT [277]. All measurements are in mm.

for sensitivity is 420 nm. The typical transit time is 62 ns, with a typical TTS of 3.4 ns and 3.8 ns pulse rise time. The dark count rate after 15 hours in darkness is designed to be typically 8 kHz, with a maximum count rate of 16 kHz [277]. The minimum effective photocathode diameter is 220 mm.

Electrodes	K	D1	F2	F1	F3	D2	D3	D4	D5	D6	D7	D8	D9	D10	P
Ratio	-	16.8	0	0.6	0	3.4	5	3.33	1.67	1	1.2	1.5	2.2	3	2.4

Table 4.2: Ratios for the voltage divider chain used for biasing the R7081 PMT [279]. K = Cathode, D = Dynode, P = Anode, F = Focus

4.4 Electronics Used for Testing of Hamamatsu R7081 PMTs

The PMTs are powered via a CAEN V6534P positive polarity HV board. As the PMTs are AC coupled, the AC signal and Direct Current (DC) HV need to be separated. A custom "splitter" board (Figure 4.6), using a capacitor in a resistor-capacitor circuit as a high-pass filter, is used to block the DC components and eliminate the DC offset from the AC signals. The splitter is designed to have the same impedance, 50 Ω, as the electronics in the PMT base to reduce signal reflections caused by impedance mismatches; 50 Ω cables and connectors were also used.

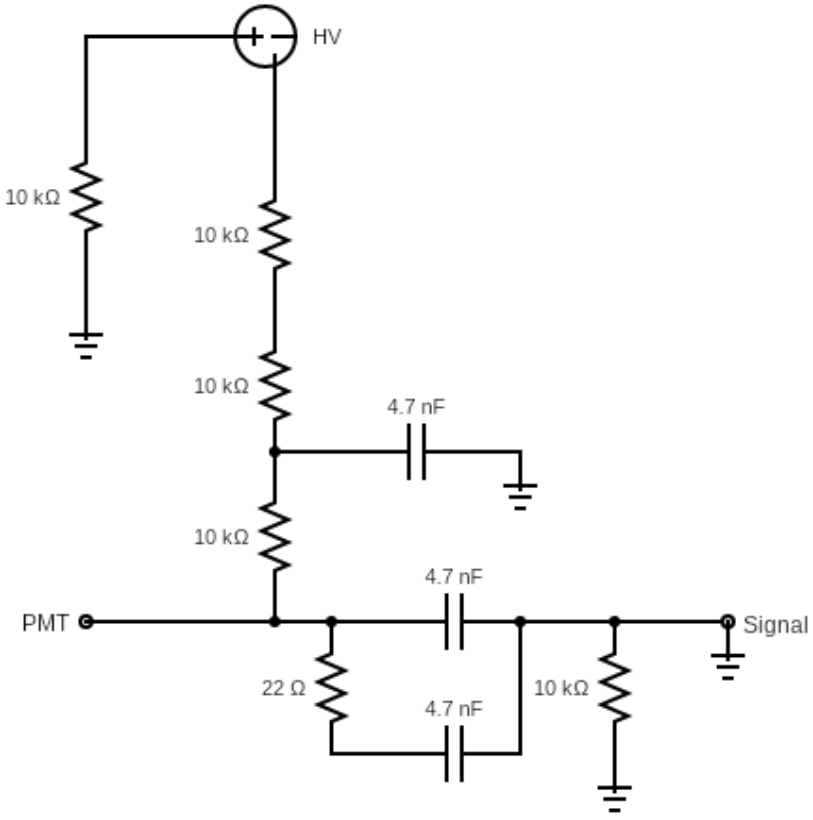

Figure 4.6: Splitter board channel design to separate the signal output from the PMT and the HV supply to the PMT.

As the SPE signal from these PMTs has a mean amplitude of approximately 4 mV, the signal is amplified by a CAEN N979 10× fast amplifier. It is then digitised by a

CAEN V1730B 500 MS/s digitizer where a 10 kHz external trigger is used to open a 220 ns acquisition window. The digitiser is read out via an optical link to a CAEN A2818 PCI CONET controller. For testing involving a light source, the trigger to the digitiser is a delayed copy of the LED trigger from a gate generator. The delay accounts for the time the signal due to the LED takes to propagate through the system. A flow diagram of the electronics used is presented in Figure 4.7.

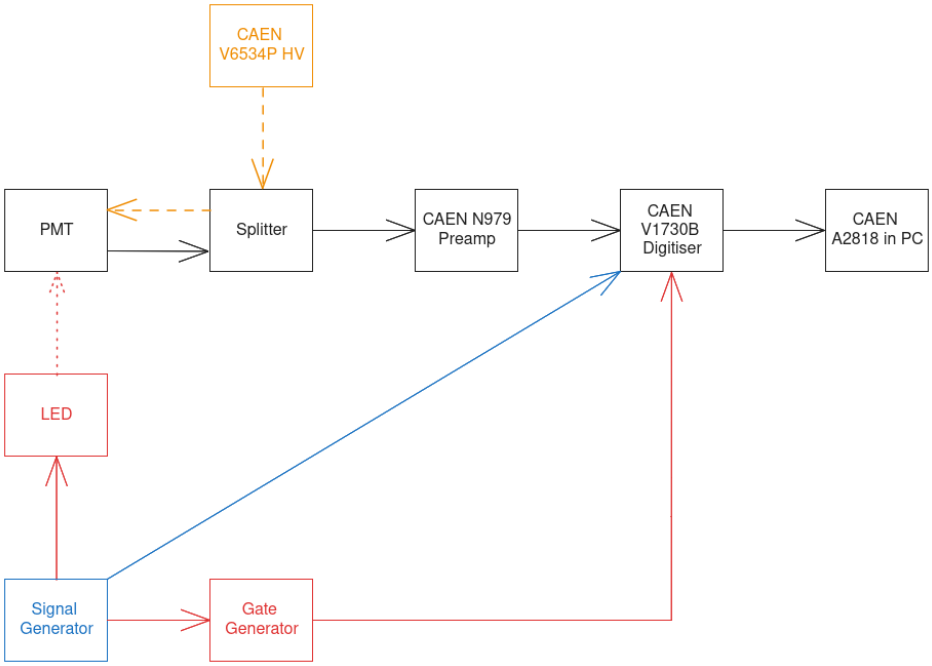

Figure 4.7: Flow diagram of electronics used for testing PMTs. When an LED is used, the digitiser is triggered by a delayed copy of the LED trigger from the gate generator (red). For dark rate tests, the digitiser is triggered directly by the signal generator (blue).

4.5 Quality Assurance and Acceptance Testing

Before acceptance of a PMT for a detector, Quality Assurance (QA) tests are usually performed. These are designed to check the manufacturer specifications are met by the tubes before installation. Electrical tests of 87 Hamamatsu R7081-100 PMTs were performed.

4.5.1 Setup

The electronics used are as described in section 4.4. Testing was carried out inside an aluminised Mylar tent that acted as both a dark box and a Faraday cage, a fitted cloth cover was placed over the tent to further restrict stray light from the surroundings entering the tent. A custom-built rig was used to hold PMTs during testing.

For tests requiring a light source, a 470 nm LED was connected to a driver with a 10 kHz trigger designed to generate pulses of a few ns in length. The light intensity was set by the driver voltage and chosen so that the PMT output was dominated by SPE pulses. A PMMA diffuser was used to create a uniform distribution of light on the PMT surface. The PMTs were left in the dark under a bias voltage for 18 hours to allow the dark rate to stabilise. The tests were conducted at ambient room temperature, which was determined as 21 - 23 °C. The setup is shown in Figure 4.8.

4.5.2 Data Taking, Processing and Quality

Four key tests were performed to confirm that PMTs met the manufacturer specifications and the requirements of a neutrino detector. The tests, as listed in Table 4.3, were of the nominal HV as provided by Hamamatsu for a gain of 10^7, the gain versus voltage, the peak-to-valley ratio and the dark count rate.

	Test Type	Trigger pulses (10^6)	Duration (mins)	Gate (ns)	Description
1	Nominal HV	3.0	5.0	220	SPE at nominal HV
2	Gain	3.0	5.0	220	SPE for 5 HV steps
3	Peak-to-valley	3.0	5.0	220	SPE at 10^7 gain
4	Dark Counts	9.0	15.0	220	No LED

Table 4.3: Summary of tests performed for quality assurance of Hamamatsu R7081-100 PMTs. SPE data is taken with an LED set to yield an SPE output from the PMT.

The charge output at the anode was determined by integrating a 50 ns window around the SPE peak, with histograms of this used in the gain and peak-to-valley tests. An example, with key components labelled, is shown in Figure 4.3. The integration window was chosen to start 15 ns before the mean arrival time of the peak to ensure the entire SPE peak was within the window when trigger jitter was accounted for. The

Figure 4.8: Four PMTs mounted in the rig in the Mylar tent at the University of Edinburgh. The diffuser is fixed at the top of the tent directly above the rig, with optical fibres guiding in light from the LED outside of the tent.

width of the deviation in the arrival time of the peak was ∼8 ns, which is consistent with the PMT TTS, LED timing characteristics and trigger jitter.

Several sources of noise were present in the system after grounding and isolating the system. Fourier transform analysis of waveforms showed frequencies consistent with

USB protocol transport and a local radio transmitter. A Radio-Frequency (RF) noise filter was applied to reject noisy waveforms. The filter rejected any waveforms where the maximum and minimum amplitudes were within a factor of 2. This accounted for a maximum of 1 - 2 % of the total waveforms when the LED was used.

4.5.3 Gain

To determine the gain, it was modelled and fit to the output charge distribution. The relative charge output for an SPE, Q_{SPE}, requires characterisation of the charge response and inherent charge backgrounds. The gain is calculated from Q_{SPE} via

$$\mathcal{A} = \frac{2\ Q_{\mathrm{SPE}} \times 10^{-12}}{e\ f_{\mathrm{amp}}\ Z}, \tag{4.4}$$

where $f_{\mathrm{amp}} = 10$ is the amplifier gain, $Z = 50\,\Omega$ is the impedance, e is the charge of an electron and the factor of two comes from the $50\,\Omega$ termination in both the PMT and the CAEN N979 preamplifier which halves the charge.

There are three key regions in the charge spectrum (see Figure 4.3): the charge response due to electrons liberated from the photocathode, the valley due to under-amplified events and thermionic emission from the dynodes, and the pedestal where there is no pulse. The charge response region consists of an SPE peak and a tail which contains multiple-photoelectron peaks.

There are two contributions to the charge response: the photoelectric effect at the photocathode, and the amplification at each dynode. The photoelectric conversion at the cathode is the convolution of the number of photons hitting the cathode and the conversion of these to photoelectrons. These are a Poisson process and binary process respectively, and give a distribution of

$$P(n, \mu) = \frac{\mu^n e^{-\mu}}{n!}, \tag{4.5}$$

where $P(n, \mu)$ is the probability that n photoelectrons will be observed when the mean number of photoelectrons collected at the first dynode is μ.

The amplification can be modelled using Gaussian functions. For larger amplifications, ≥ 4 and preferably > 10, the photoelectron peaks can be approximated with

$$G(x) = \sum_{n=0}^{\infty} \frac{1}{\sigma_{\mathrm{SPE}}\sqrt{2\pi n}} \exp\left(-\frac{(x - nQ_{\mathrm{SPE}})^2}{2n\sigma_{\mathrm{SPE}}^2}\right), \tag{4.6}$$

where σ_{SPE} is the width of the SPE distribution, x is the charge variable and Q_{SPE} is the SPE charge output. For lower amplifications, the photoelectron peaks are replaced with the sum of Gaussians

$$G_n(x) = \sum_{m=0}^{\infty} \frac{(n\frac{Q_{\mathrm{SPE}}}{Q_{\mathrm{SPE},2}})^m e^{-n\frac{Q_{\mathrm{SPE}}}{Q_{\mathrm{SPE},2}}}}{m!} \cdot \frac{1}{\sigma_{\mathrm{SPE},2}\sqrt{2\pi n}} \exp\left(-\frac{(x - mQ_{\mathrm{SPE},2})^2}{2m\sigma^2_{\mathrm{SPE},2}}\right), \tag{4.7}$$

where m is the number of electrons produced at the first dynode, $Q_{\mathrm{SPE},2}$ is the charge output by a single electron emitted from the first dynode, and $\sigma_{\mathrm{SPE},2}$ is the width of the distribution in the Gaussian approximation.

The ideal PMT charge response is a convolution of the amplification and photoelectric conversion processes, and is modelled as

$$S_{\mathrm{ideal}}(x) = \sum_n P(n,\mu)G(x). \tag{4.8}$$

The background regions consists of the pedestal and valley distributions. The pedestal is approximated as a Gaussian distribution, and the valley is an exponential. The sum of these processes gives the total background distribution:

$$B(x) = P(0,\mu)\frac{1}{\sigma_0\sqrt{2\pi}} \exp\left(-\frac{x^2}{2\sigma_0^2}\right) + P_{\mathrm{exp}}\theta(x)\alpha\exp(-\alpha x), \tag{4.9}$$

where $P(0,\mu)$ is the Poisson probability that zero photoelectrons are produced, σ_0 is the width of the pedestal, P_{exp} is the probability that valley-producing background is present and α is the coefficient of the exponential decrease of the valley. The condition $\theta = \begin{cases} 0 & x \leq 0 \\ 1 & x > 0 \end{cases}$ ensures there is only an exponential component for $x > 0$.

The total charge distribution is the sum of the charge response and background distributions:

$$Q(x) = S_{\mathrm{ideal}}(x) + B(x). \tag{4.10}$$

This modelling regime is adapted from [280]. An example of the fit is shown in Figure 4.9.

The PMTs were tested at five voltage steps, chosen to be approximately flat in gain, and the gain versus voltage fit using

$$\mathcal{A} = \left(\frac{V}{V_{\mathrm{opt}}}\right)^{\beta}, \tag{4.11}$$

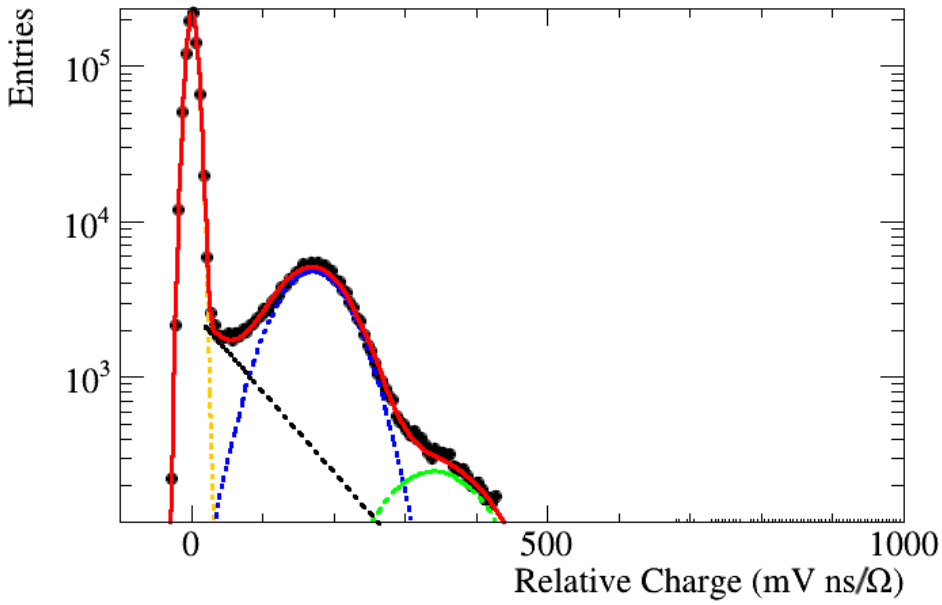

Figure 4.9: Fit of models for gain to output charge distribution. A double-Gaussian fit to the pedestal (yellow), Gaussian fit to the SPE (blue) and double-photoelectron peaks (green), and exponential fit to the valley (black) combine to give a total fit (red). Errors (not visible) on the relative charge are between 0.1 and 2.0 mV ns/Ω.

where V_{opt} is the operating voltage that gives 10^7 gain and both V_{opt} and β are free parameters [281]. The fit is shown for one PMT in Figure 4.10. A comparison between the obtained voltage for 10^7 gain was made to Hamamatsu's nominal voltage for the same gain.

At higher voltages, pulses lasted longer above threshold (i.e. were wider) and arrived sooner relative to the trigger, with the timing variation being consistent with the transit time decreasing by ∼12 ns from 1300 V to 2000 V as suggested in the data sheet [282]. The integration window (subsection 4.5.2) was chosen to account for this effect.

The mean value determined from Equation 4.2 of $\alpha = 6.9$ agrees with the expected value of 7.0 for a 10^7 gain across the 10 dynodes. Comparison to the Hamamatsu values (Figure 4.11) show a factor 1.02 offset, which is ∼20 V. Hamamatsu perform tests before the 80 m cable is applied, which may account for the difference. A single PMT was found to not meet the 10^7 gain requirement within Hamamatsu's recommended upper limit of 2000 V, requiring 2003 V. Due to this being very close to the acceptance limit, this PMT will still be deemed acceptable for use.

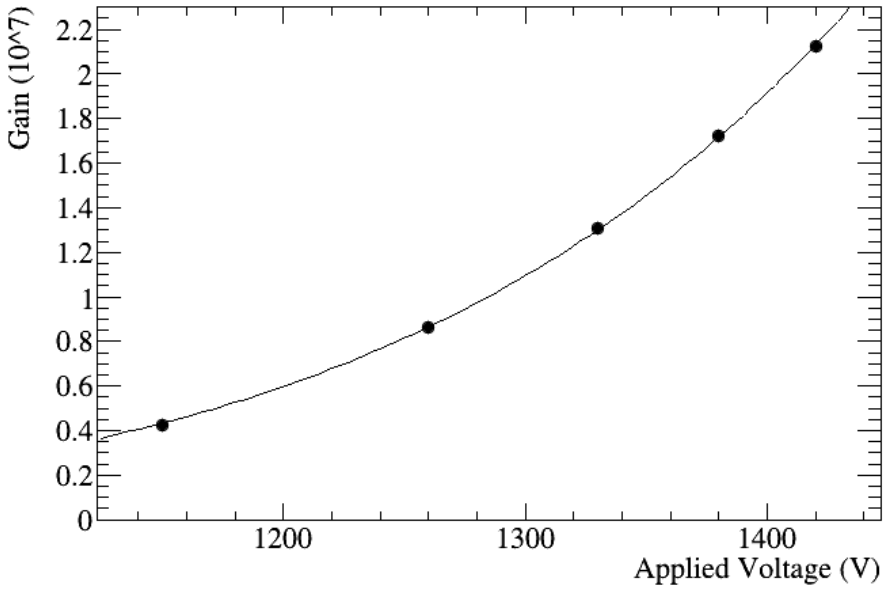

Figure 4.10: Fit of gain curve using Equation 4.11 for five HV steps. Errors (not visible) are 0.0001 V.

4.5.4 Peak to Valley

The peak-to-valley ratio, the ratio of the mean charge of the SPE peak to the charge at the minimum point between the pedestal and the SPE peak in the charge distribution (Figure 4.3), is a good measure of the signal-to-noise of the PMT. It is determined by fitting to the charge data taken at the operating voltage determined as giving a 10^7 gain in subsection 4.5.3. A Gaussian is fit to the signal region of the charge distribution, and parabola to the valley between the pedestal and SPE peak. The ratio of the maximum of the Gaussian and minimum of the parabola are then taken to give the peak-to-valley ratio. The uncertainties come from the fitting parameters and are in the region 0.01 - 0.02 (absolute); the peak-to-valley ratios are $\sim$2 - 3.

Results are shown in Figure 4.12. There is some correlation between provided Hamamatsu data and these measurements, but the measurements consistently fall below the Hamamatsu data. A rejection criterion of a peak-to-valley ratio of 2 was not met by some PMTs. However, moving the PMTs within the holder showed that the measured magnetic field in the laboratory could impact the peak-to-valley ratio by up to $\sim$0.5. Neutrino detectors use magnetic shielding and compensation coils to correct for this, with these PMTs passing the threshold for acceptance when shielded. This highlights

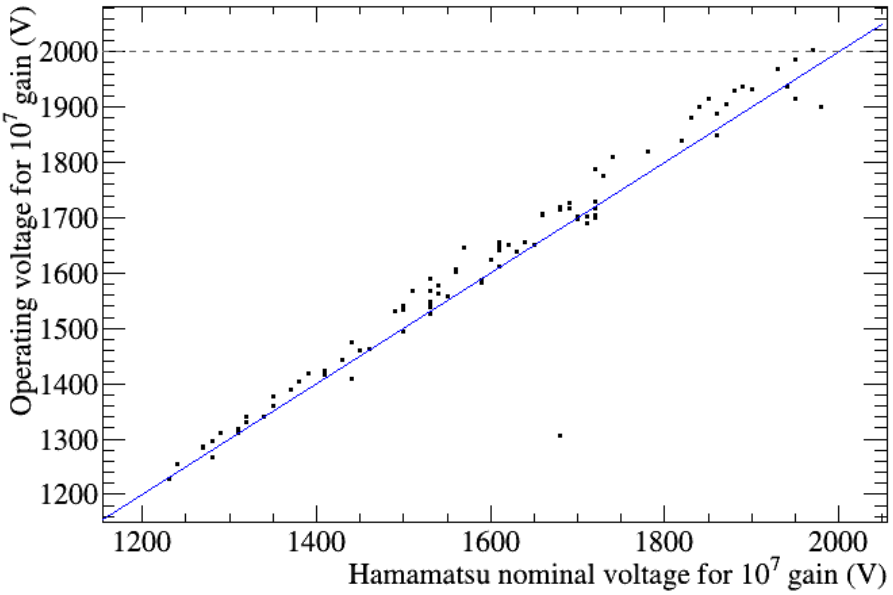

Figure 4.11: The determined operating voltages for a 10^7 gain compared to Hamamatsu's nominal voltages. The grey dashed line represents the maximum operating voltage of 2000 V. The outlier is potentially due to an error in the Hamamatsu data from pre-shipping tests.

the impact of the electric field that transports the photoelectron from the cathode to the dynode chain. PMT illumination also impacts the peak-to-valley ratio, specifically the spacial light distribution over the photocathode. The diffuser used in these tests gave a flat illumination at the 10 % level.

4.5.5 Dark Counts

The acceptance requirement set for these PMTs for the dark counts was a maximum rate of 10 kHz, with the typical dark rate after 24 hours storage in darkness quoted as 8 kHz on the data sheet [282]. This value is with a lower-level discriminator set at one quarter of the mean SPE signal amplitude.

Before data taking, the PMTs were held at their determined operating voltage for at least 18 hours to allow the dark rate to stabilise. No light source was used in this data acquisition process. The threshold was set at 10 mV, equivalent to ∼0.25 of the mean SPE signal amplitude as determined from the peak-to-valley tests, with a dark pulse being deemed to have occured if this threshold is exceeded. A maximum of one

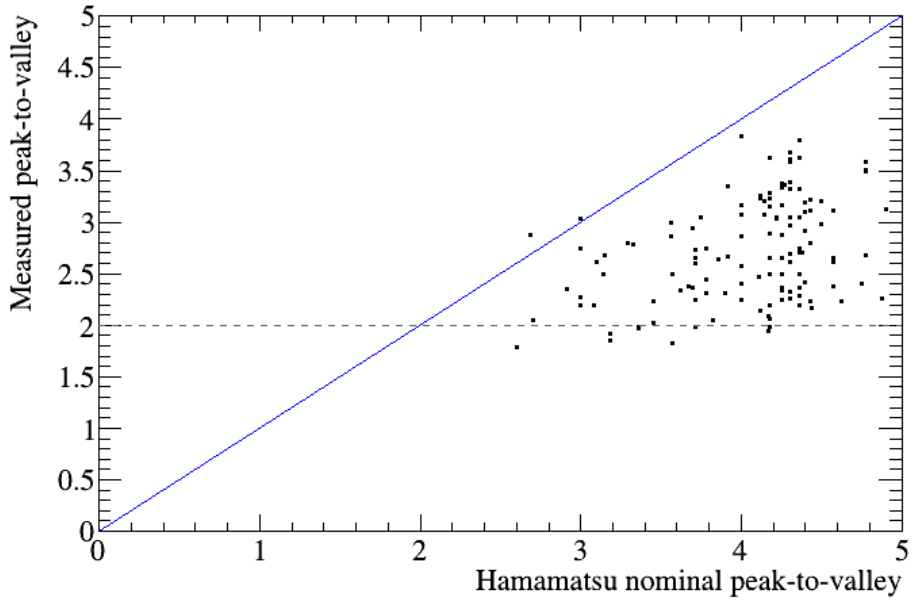

Figure 4.12: Measured peak-to-valley ratios versus the Hamamatsu data sheet values. The grey dashed line shows a potential requirement of a peak-to-valley ratio of 2. Errors on the values (not visible) are between 0.01-0.02 (absolute uncertainty).

dark pulse per 220 ns waveform was counted, with the probability of multiple true dark counts in a single waveform being deemed negligible; multiple pulses were treated as multiple-pulsing phenomena.

Values in the data sheet are quoted at 25 °C, so a correction was applied to the dark rate obtained to allow a direct comparison. More detail about temperature-dependent dark rate is in section 4.6.

All PMTs passed the acceptance test, with a mean dark rate of 1.8 kHz, and there was a good correlation to the Hamamatsu data but with outliers in both directions. The obtained dark count rates and comparison to Hamamatsu data are summarised in Figure 4.13.

4.5.5.1 Temperature-dependent Measurements as Part of QA Testing

A climate chamber was used to allow the dark rate to be measured against temperature. Several PMTs were tested, with the measurements for one shown in Figure 4.14. The results are consistent with those reported by Double Chooz [281].

The Richardson law of thermionic emission was fit to the data, with it being deemed

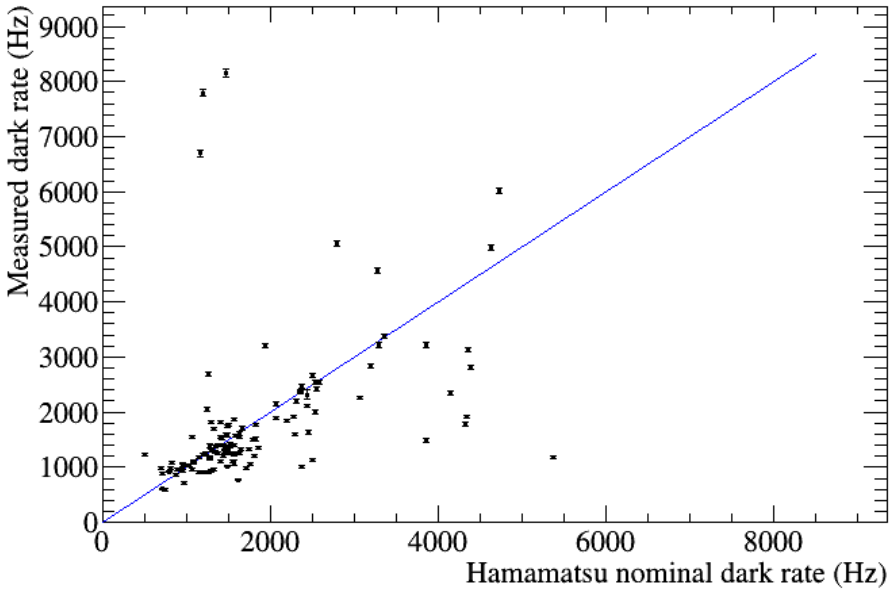

Figure 4.13: Comparison of the measured dark count rates and the Hamamatsu nominal rates.

a good description of the data, and the work function of the photocathode being determined to be in the range 1.2 - 1.5 eV.

A more detailed study of the temperature-dependent dark rate was performed, and is described in section 4.6.

4.6 Temperature-dependent Measurements in Water

In many detectors, particularly neutrino and dark matter detectors, the PMTs are submerged in a liquid medium such as pure water or liquid scintillator. However, they are typically characterised in air, normally at a single ambient temperature, before installation into a detector [281, 283–288].

It has been seen in detectors that the rate of pulses changes depending on the medium the PMTs are installed in and its conditions, e.g. in the LUX-ZEPLIN dark matter detector [289]. As such, it is important to characterise PMTs in a realistic dielectric and magnetic environment, and with varying temperature to understand the performance and thermionic dark noise contribution that can be expected in a detector.

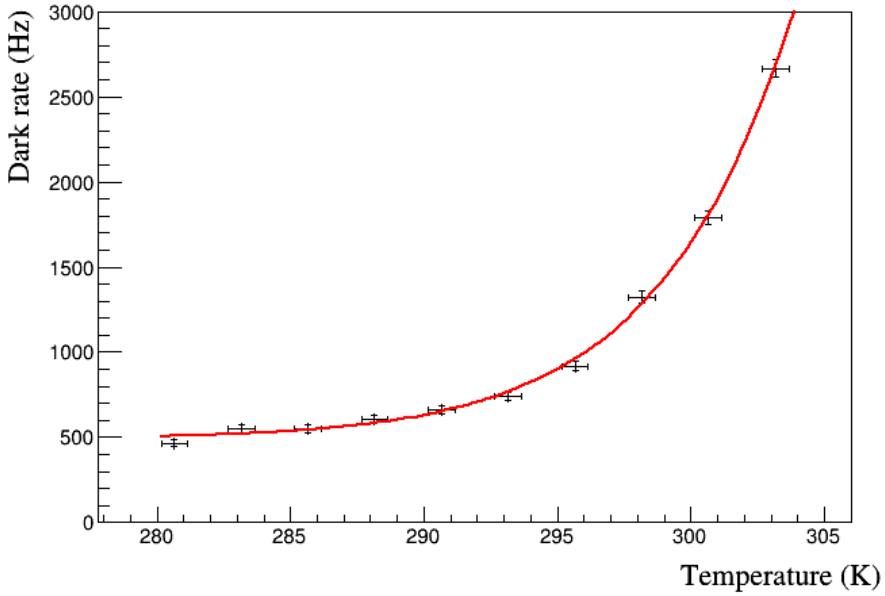

Figure 4.14: Dark rate versus temperature for an R7081 tube. A fit to the Richardson form is superimposed (see subsection 4.6.2).

The temperature-dependent dark rate of the Hamamatsu R7081-100 PMT has been characterised using a subset of PMTs used in the QA tests in section 4.5.

4.6.1 Measurement Procedure

To take measurements, a set of up to five PMTs were placed in a holder and lowered into the tank described in chapter 3 as shown in Figure 4.15. A lid was placed on the tank and the cables connected to the splitter board after passing through a Safe High Voltage (SHV) to SHV feedthrough. The electronics used are those described in section 4.4.

To measure the rate of dark pulses, 15 minute runs with the 10 kHz external trigger were used. Each run equates to 1.98 s of live time, or approximately 9×10^6 waveforms each 220 ns in length. Four runs were taken across a two hour period at each temperature to ensure consistency between runs. The water temperature was adjusted between 7 °C and 25 °C in 2.5 °C steps, except for between 12 °C and 15 °C where 0.5 °C steps were used. This region was chosen to surround the operating temperature of Super-Kamiokande [220].

As measurements of the dark rate were desired, the inside of the tank needed to

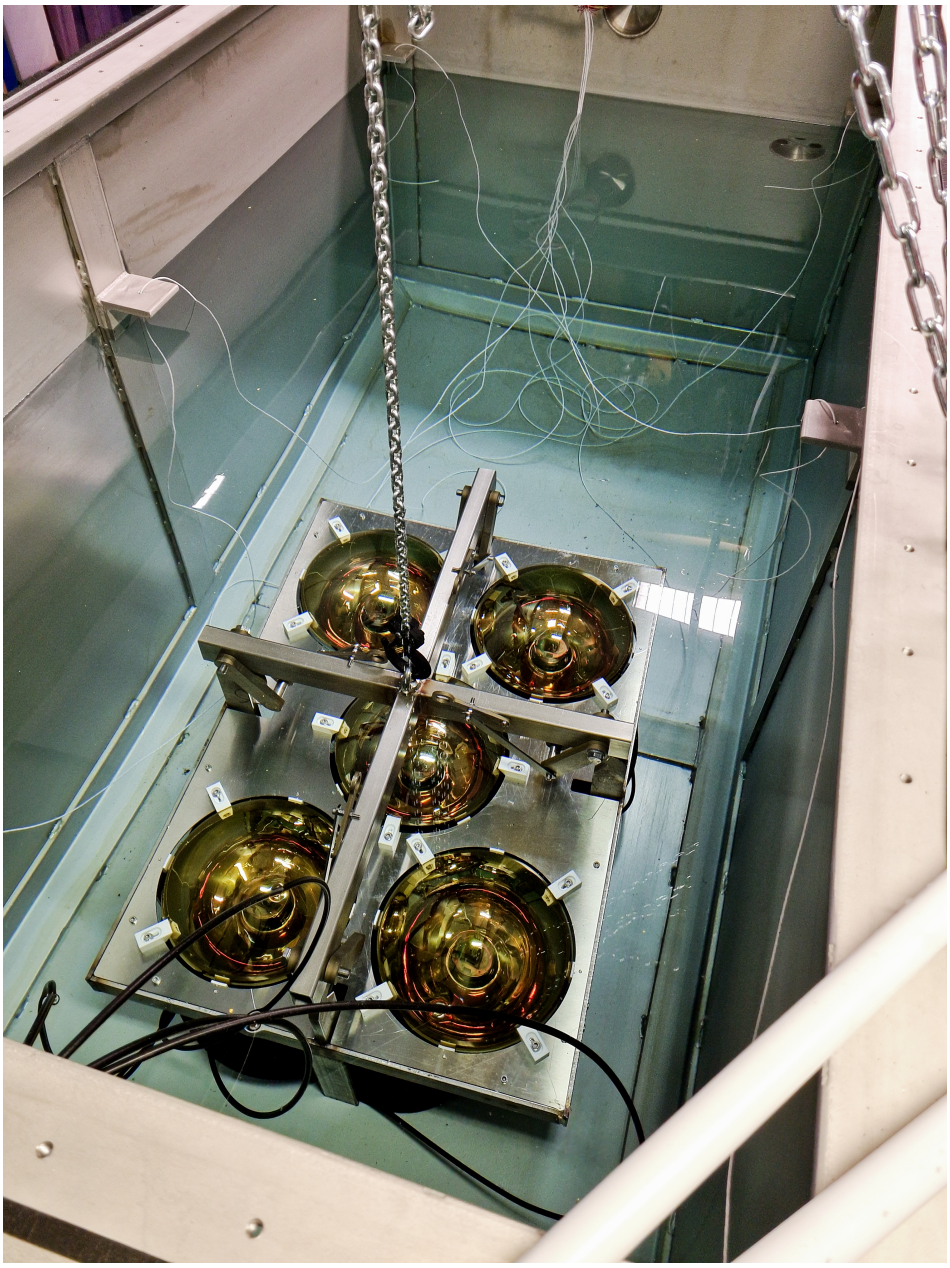

Figure 4.15: A batch of five PMTs inside the tank. Covers can be added to each PMT individually for further optical isolation.

be kept optically isolated from the tank's surroundings. To confirm no external light was entering the tank, runs were taken with the room lights on and off for each PMT deployment with no difference being observed. The final data was taken with the room lights off.

When PMTs are exposed to significant levels of light, they have an increased dark

rate for several hours to days after the exposure. This "cooldown" period was measured by exposing the PMTs to large levels of light and then recording the dark rate every hour for five days at a fixed temperature. The outcome, in Figure 4.16, shows that after approximately two and a half days the dark rate is at its pre-exposure level. Therefore, the PMTs were left in total darkness for at least two and a half days, 60 hours, before attempting to take measurements.

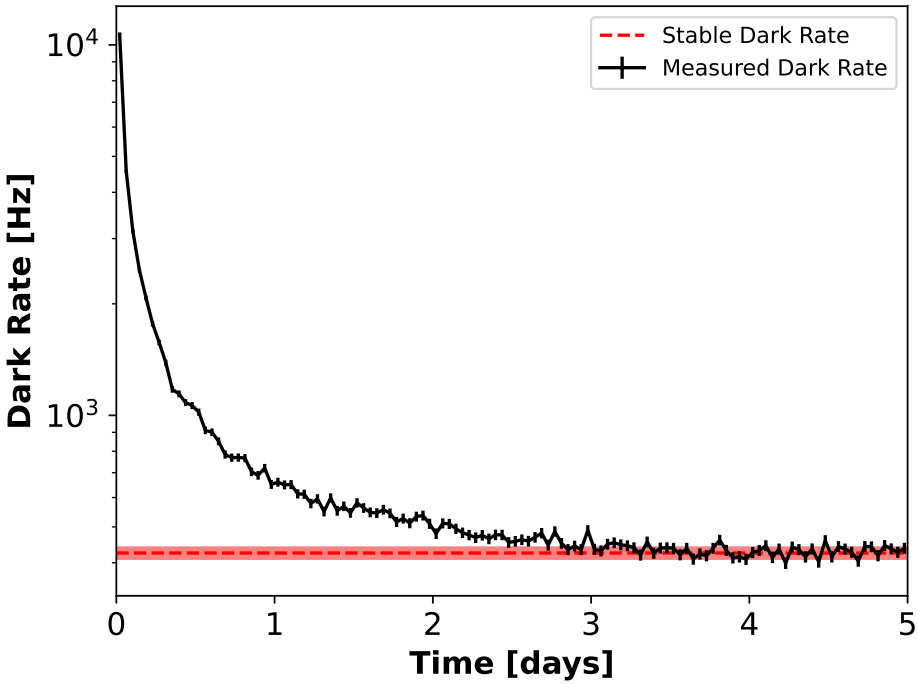

Figure 4.16: The dark rate with time in complete darkness after large light exposure for PMT0103 (black). The rate takes around two and a half days to settle at the pre-exposure level of 425 Hz (red, dashed) within error.

Despite light from outside the tank being blocked from entering the system, light could still be produced inside the tank. Cosmic ray muons will produce Cherenkov radiation as they pass through the water. As the tank is on the Earth's surface and near sea level, the rate was approximately $1\,\mathrm{cm}^{-2}\,\mathrm{min}^{-1}$ [290]. This, alongside the large amount of light produced per muon and the amount the light reflects in the steel tank, produced a significant increase in SPE level pulses observed by the PMTs. Alongside muons, radioactive backgrounds, in particular from the PMT glass, can produce Cherenkov and gamma radiation. It is also possible for light to be produced by the final dynodes in the PMT itself [291]. Most single-photon detecting PMTs have countermeasures [274],

but it is possible for photons to escape and trigger that or neighbouring PMTs.

To combat the light produced inside the system and isolate the thermionic emission and intrinsic dark rate, each PMT was individually covered in a black plastic sheet. This allowed them to be optically isolated from each other and any light produced in the water.

4.6.2 Analysis

4.6.2.1 Pulse Analysis

An SPE pulse was characterised as having a mean amplitude of 40 mV after amplification, and a width above threshold of around 20 ns where the rise is very sharp (few ns) and the fall is exponential. An example is shown in Figure 4.17. A threshold of 25 % of the mean SPE amplitude, 10 mV in this case, was used in line with Hamamatsu [282], and a rise time cut of $< 20\,\%$ was applied. An upper amplitude limit of 80 mV was applied to remove multiple-photon backgrounds e.g. from cosmic ray muons. The probability of multiple true dark pulses in a single acquisition window was assumed to be negligible.

Despite attempting to match the impedance between the PMT electronics and the splitter board, there was still a mismatch due to the circuit board used in the splitter board. This mismatch caused reflections of large pulses in the cables, which caused a large baseline shift within the data acquisition window when these pulses occured just before the external trigger. The system as a whole also contributed to these shifts. The water circulation systems contain several pumps and motors, and the water tank is difficult to shield. As such, the system is susceptible to noise which causes further shifts in the baseline. SPE level pulses can be impacted by these baseline shifts, as shown in Figure 4.18.

To compensate for this, a baseline correction similar to the Linear Common Mode Suppression algorithm described in [292] was applied. This correction has several steps:

1. The mean of the waveform is subtracted.

2. Any linear slope in the data is corrected for.

3. Data points more than one standard deviation from the mean are removed.

4. The mean of the new waveform is subtracted.

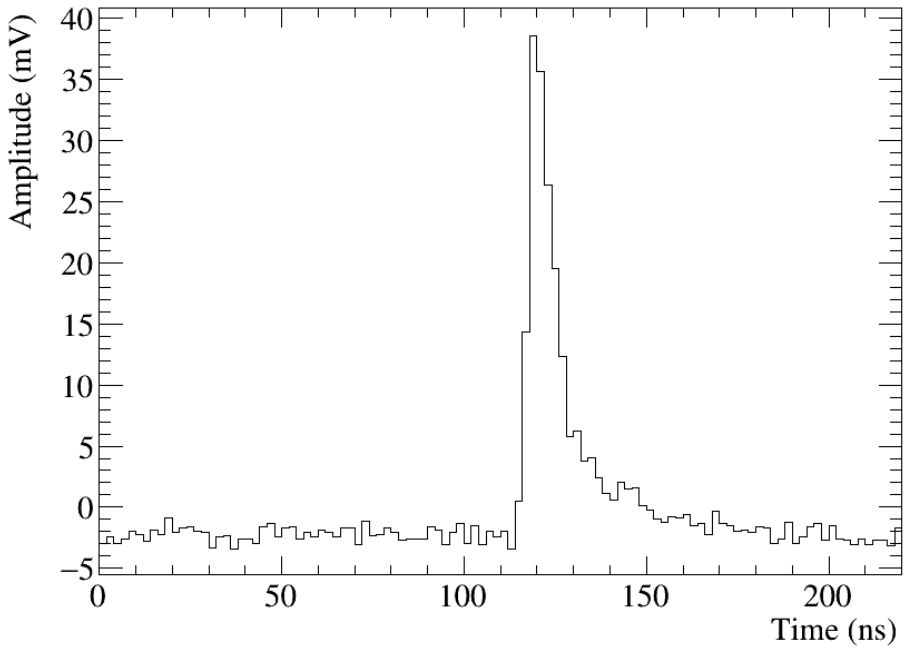

Figure 4.17: Typical SPE level pulse after 10x amplification. These make up approximately 90 % of the pulses above threshold.

5. Any linear slope in the new waveform is corrected for.

6. Outlying data points with corrections applied (changes determined in steps 4 and 5) are re-added to the waveform.

This acts to counter the reflections and leave a pulse with a flat baseline centred on 0 mV such as the one in Figure 4.18, making the analysis of SPE level pulses more robust.

4.6.2.2 Thermionic Emission

Thermionic emission can be modelled using Richardson's law [293] in Equation 4.12,

$$N = AT^2 \exp\left(\frac{-e\phi}{k_B T}\right). \tag{4.12}$$

Here, N is the rate of electrons emitted from the photocathode by thermionic emission, A is a scaling factor containing a material-specific correction factor, T is the absolute

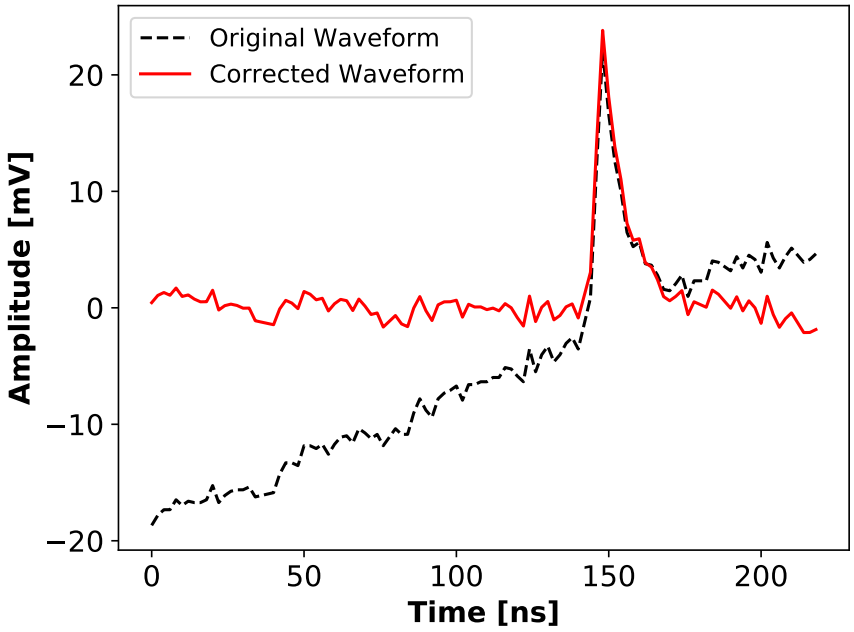

Figure 4.18: Corrections applied to a waveform with a shifted baseline (red, solid), with the original waveform (black, dashed) shown for reference.

temperature, ϕ is the work function, e is the electron charge and k_B is the Boltzmann constant. A constant offset was also applied as a free parameter.

The electrons emitted will produce SPE level pulses, at the rate N. By measuring the dependence of N on T, the work function ϕ can be obtained for the photocathode and any divergence between the data and Richardson's law for thermionic emission can be observed.

4.6.3 Results

The results show that Richardson's law fits the data well, with results for one batch of three covered PMTs shown in Figure 4.19. The data occasionally has a small plateau-effect below 15 °C as the thermionic emission component of dark rate reduces. A comparison between the SPE level pulse rates when covered and uncovered for these PMTs is shown in Figure 4.20, suggesting that when the PMTs are uncovered, more than half of the counts come from sources other than dark pulses.

The work functions for the PMTs, obtained by fitting Richardson's law to the data,

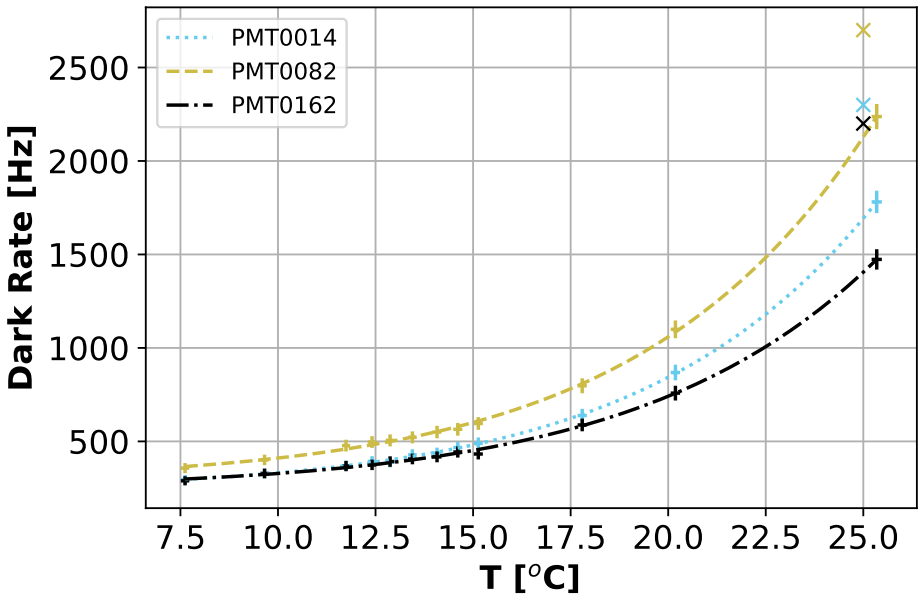

Figure 4.19: Dark rate versus temperature for covered PMTs. The fit to Richardson's law is superimposed to the data, and the "x" at 25 °C is the Hamamatsu data sheet value [282].

match the range measured in air with values between 1.2 and 1.5 eV.

Runs with the room lights on and off are consistent with each other, confirming no stray light entered the system.

To confirm the results, a series of tests were conducted on PMT0103 in isolation. To do this, PMT0103 was deployed in the tank on its own. Temperature-dependent measurements of dark rate were taken and compared to the measurements taken from PMT0103 when deployed with other PMTs. The results, in Figure 4.21, show very little difference between the two runs. The PMT was also exposed to light before measuring the dark rate every hour for five days which confirms the optical cooldown period of 60 hours is sufficient, with results in Figure 4.16.

The impact of water resistivity was tested by bypassing the deionising cylinder and allowing the water resistivity to drop gradually, and taking data every hour during this. The water resistivity and dark rate results, in Figure 4.22, confirm the resistivity has no clear impact on the intrinsic PMT dark rate.

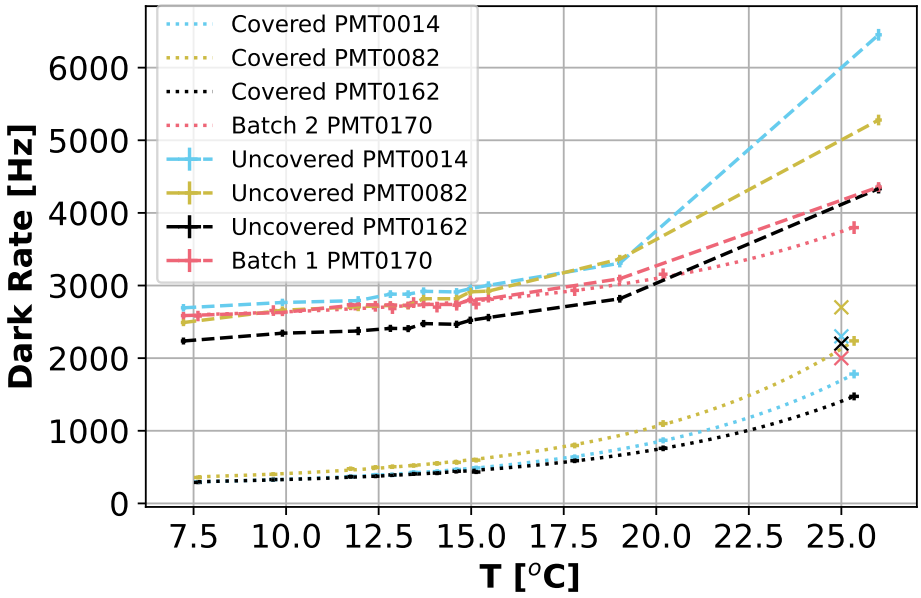

Figure 4.20: Covered versus uncovered PMTs. PMT0170 was kept uncovered to act as a control. Covering the PMTs lowers the SPE level count rate significantly, and brings them closer to the measurements made by the vendor [282] ("x" at 25 °C). The measurements for the covered PMTs have the fit to Richardson's law superimposed.

4.6.4 Discussion

The results of the measurements of temperature-dependent dark rate across thirteen PMTs are in good agreement with thermionic emission as modelled using Richardson's law in Equation 4.12 in the 15 °C to 25 °C temperature range. However, below 15 °C there are occasionally small deviations above the expected rate as thermionic emission rates reduce. This suggests that there are non-thermionic emission contributions to the dark rate that become more dominant at lower temperatures. It is seen in [274, 294] that the temperature-dependent dark rate does not always follow Richardson's law of thermionic emission.

An assay of the PMT glass, performed at the Boulby UnderGround Screening (BUGS) facility and shown in Table 4.4, suggests that the PMT glass has a low contribution to the background at approximately $3.4\,\mathrm{Bq\,kg^{-1}}$. The mass of these PMTs is 1.4 kg, yielding < 5 Bq per PMT assuming the glass is the majority of the PMT mass. Not all of these events will cause light emission, further lowering the potential contribution to the overall count rate.

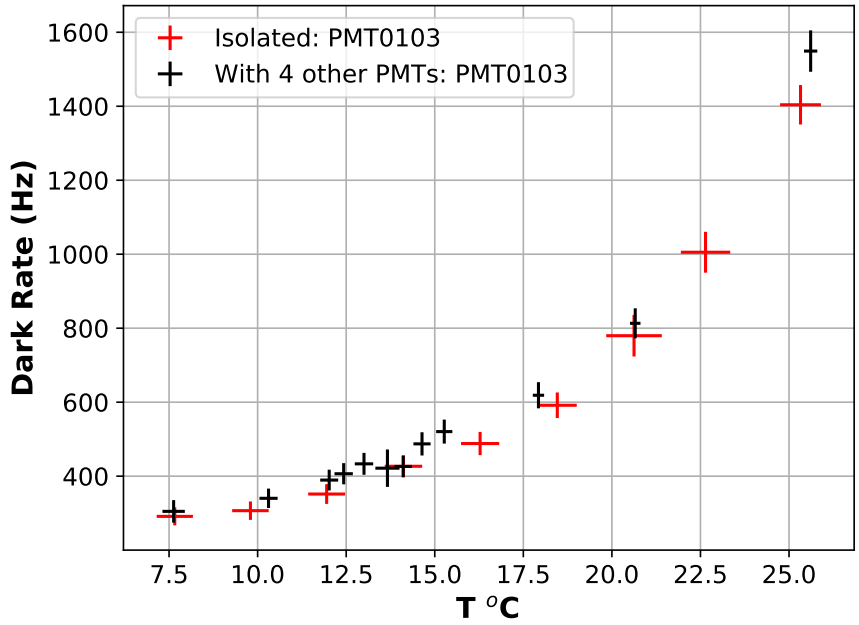

Figure 4.21: The dark rate with temperature for PMT0103 measured when the PMT is part of a batch of PMTs (black) compared to in isolation (red).

Measurements of the SPE level pulse rate with changing water resistivity confirm that the water resistivity has negligible impact on the intrinsic SPE level pulse rate.

The largest non-thermal contribution to SPE level counts in a liquid medium is light. Despite the system being optically isolated from its environment, the liquid fill allows light production via interactions from cosmic ray muons and radioactive decays. Cosmic ray muons are incident on the tank at an expected rate of the order several hundred Hz as the tank has a $2\,\mathrm{m}^2$ top surface area, and a further $6\,\mathrm{m}^2$ on the sides. This light is also likely to be reflected, which will further increase the number of photons hitting PMTs, due to the steel tank. Without simulations, it is hard to quantify the expected number of hits from muon-produced photons, but it expected to be a significant contributor to the total number of counts observed by the PMTs. Along with the direct detection of photons, the consistent light exposure leads to a prolonged increase in PMT activity leading to a further increase in the SPE level pulse rate. As such, simply vetoing cosmic ray muons and accounting for radioactive backgrounds might not allow all contributions to the SPE pulses due to light to be removed. Beyond light production in the tank, high gain PMTs are known to produce light in the final dynodes around the anode

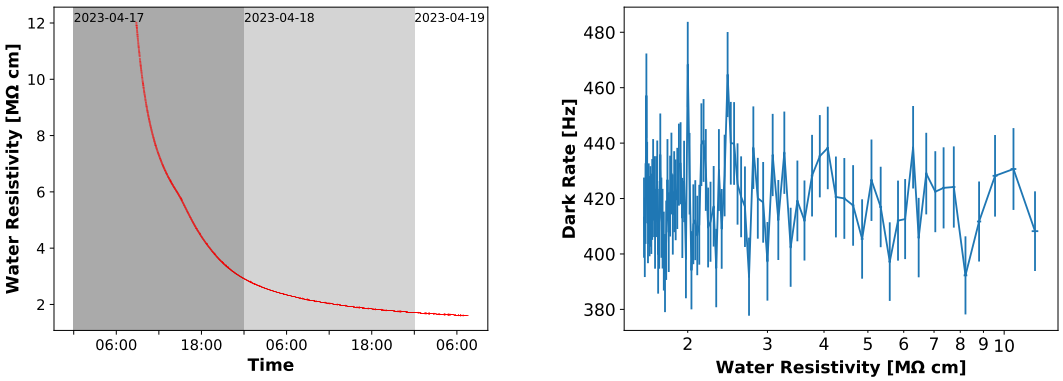

(a) Evolution of water resistivity with time.

(b) Dark rate with water resistivity.

Figure 4.22: (a) The water resistivity with time after the deionising cylinder is bypassed. The resistivity drops when the deionising cylinder in the filtration system is bypassed. (b) The dark rate of a covered PMT with resistivity. There is no clear connection between intrinsic PMT dark rate and water resistivity.

[291]. This light can trigger both the PMT emitting the light and its neighbours. By optically isolating PMTs from the system and their neighbours, the SPE level pulse rate drops by a factor of ∼2.5 as shown in Figure 4.20.

A comparison between dark rate measurements made in water and air (both as part of the QA tests and by the vendor [282]) at 25 °C is presented in Table 4.5. The measurements in air show good agreement. The water measurements agree with expectation when the time in darkness before data taking is accounted for. The measurements made in air are after approximately 18 hours in complete darkness, whereas those in water are after at least 60 hours. The dark rate reduces significantly over this time. For PMT0103, the dark rate after 18 hours is 1.8 times the rate after 60 hours, as shown in Figure 4.16.

This is significant for detector application, as it suggests that there is no intrinsic difference in PMT dark rate when the medium of deployment changes. Therefore, any differences seen in PMT rates when in a liquid are likely to be due to external contributions such as light production in the system. In the case of LUX-ZEPLIN [289], the raised pulse rates that occur after the tank is opened and the water resistivity drops is likely related to contaminants in the water or optical cooldown after light exposure, and not an intrinsic effect of water resistivity on the PMTs.

Isotope	mBq/kg	ppx	
^{238}U	660(40)	54(3)	ppb ^{238}U
^{226}Ra	430(20)	35(1)	
^{210}Pb	610(50)	50(4)	
^{235}U	30(5)	50(7)	
^{228}Ra	440(20)	108(5)	ppb ^{232}Th
^{224}Ra	370(10)	89(2)	
^{40}K	830(50)	27(2)	ppm ^{40}K

Table 4.4: PMT glass assay results from data taken at the BUGS facility using a Mirion (Canberra) BE6530 BEGe-type HPGe detector. Uncertainties in mBq/kg are 1 σ statistical errors only. True coincident summing effects are not accounted for, and introduce an additional error of up to $\mathcal{O}(10\,\%)$. For comparison only, the ^{235}U value is given as a ^{238}U ppb equivalent where conversion is performed using the standard ^{nat}U activity ratio for ^{238}U: ^{235}U of 21.6 [295]. Results courtesy of Paul Scovell, Boulby Underground Laboratory.

4.6.5 Conclusion of Temperature-dependent Dark Rate Characterisation

The temperature-dependent dark rate of Hamamatsu R7081-100 10" PMTs has been characterised when submerged in water, and shows a good match to the measurements taken in air and by the vendor [282]. Richardson's law of thermionic emission fits the data well, especially in the 15 °C to 25 °C range, with other contributions becoming more noticeable at lower temperatures.

The impact of light on the SPE level pulse rate is significant, and simply using a light tight water tank is not sufficient to remove all light. This is due to light production in water from cosmic ray muons, radioactive backgrounds and possibly the PMTs themselves. The impact of radioactivity from individual PMTs and water resistivity are shown to have a negligible effect on the intrinsic dark rate, but exposure to light has a lasting impact. The source of raised SPE level pulse rates in liquid detectors is likely to be external to the PMTs.

It can be concluded that intrinsic PMT dark rate is consistent across different media, and that characterising a PMT in air is sufficient, based on the comparison of temperature-dependent dark rates measured in air and water when all light is removed.

PMT	**Dark Rate at 25 °C [Hz] (after time in dark)**		
ID	**Water (60 hours)**	**Air (18 hours)**	**Vendor**
14	1,708	2,409	2,300
82	2,149	2,793	2,700
162	1,396	2,141	2,200
3	1,804	4,401	3,600
112	1,730	1,855	1,500
159	1,235	2,489	2,000
26	1,329	3,702	3,600
104	3,276	1,667	1,500
143	865	1,439	1,400
155	3,535	4,193	5,000
15	1,397	2,259	2,200
29	1,487	1,729	1,900
103	1,428	1,759	1,600
148	954	1,892	2,100

Table 4.5: The dark rate measured at 25 °C in water, air and by the vendor (air) [282]. The tests in water were conducted after at least 60 hours in complete darkness, the other tests after approximately 18 hours. Uncertainties are 1 - 4 % for the water and air measurements.

4.7 Pressure Testing

In large, liquid-filled detectors, the pressure at the bottom can be very high. The pressure increases by 1 atm for every 10 m of depth in water, so the pressure at the bottom of SK is ∼4 atm. In 2001, when SK was half full, a PMT imploded and set off a chain reaction of imploding PMTs [296, 297], destroying 6665 out of the 11146 installed at the time. The Hamamatsu R7081 PMTs to be used in BUTTON have a low-radioactivity borosilicate glass window. The mechanical strength of this, particularly after prolonged exposure to gadolinium, has not been directly tested.

A pressure vessel[1], rated to 10 atm of overpressure, was constructed for testing the ability of PMTs and their housings to withstand the pressure they would experience at the bottom of a large, water-filled detector. The vessel is able to hold a 10" PMT and is filled mostly with water. Nitrogen gas is pumped in to increase the pressure. Design drawings of the vessel are shown in Figure 4.23.

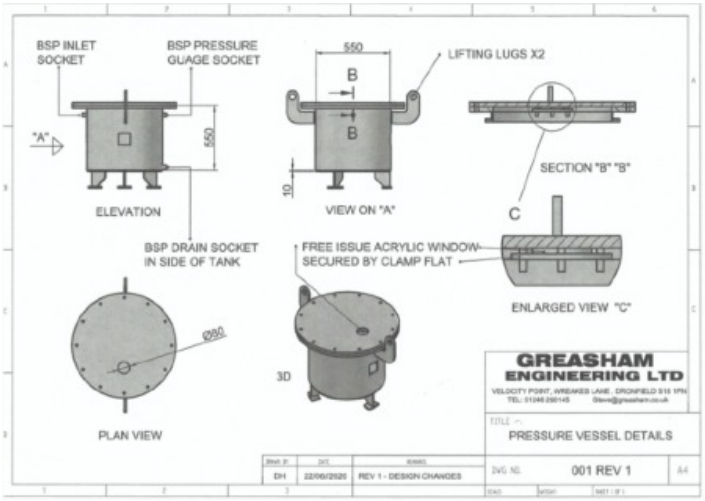

Figure 4.23: Design of the pressure vessel used for pressure testing.

4.7.1 PMT Soak Testing in Gadolinium-doped Water

To test the effect of gadolinium exposure on the mechanical strength of PMT glass, 12 PMTs were soaked in gadolinium-doped water for a prolonged period before being pressure tested.

[1]The vessel was christened "Freddie" by Sam Fargher and Chris Toth after Freddie Mercury

4.7.1.1 Selection

Of the batch of 96 PMTs available, only 12 could be soak tested due to space constraints. As the glass bulbs are hand blown, there is variation in the glass both within individual PMTs and across batches. To get a wide range of glass properties, a selection process based on the thickness of the glass across the window was developed.

Measurements of the thickness of glass were made at 25 points on the window of 45 PMTs using a handheld ultrasound probe. Measurements were taken at three different circumferences (C1, C2 and C3) and at 45° intervals around the glass window, with a measurement at the central top point of the window also taken. The breakdown of the measurement locations is shown in Figure 4.24. Several PMTs were retested multiple times by two people to confirm the precision of the measuring process.

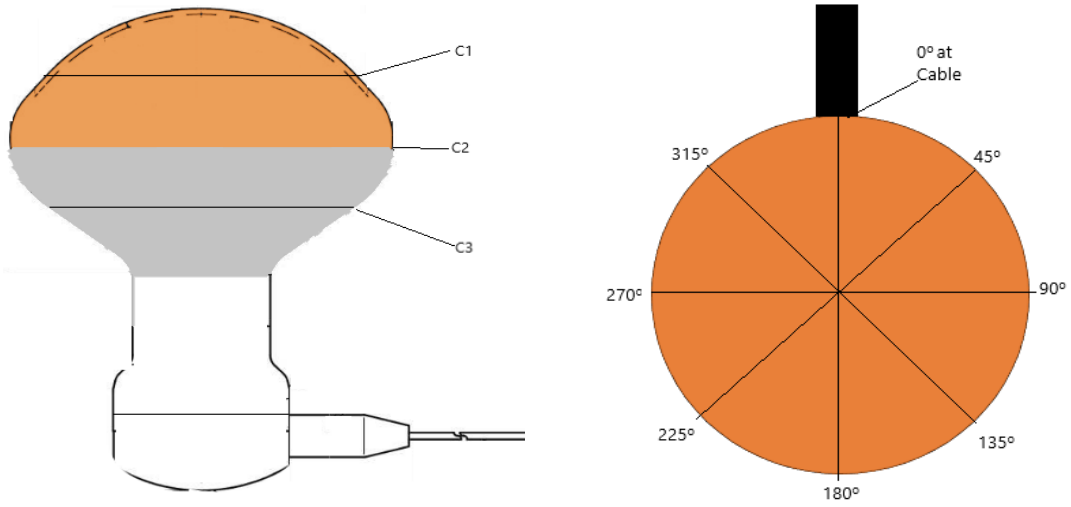

(a) Side view with three circumferences measurements are made at.

(b) Top view with the angular positions measurements are made at.

Figure 4.24: Diagram of the Hamamatsu R7081, with the photocathode region in orange and the lower reflective surface in grey.

Selections were made based on the average glass thickness, the variation in the thickness and the thickness of the measurements of the C3 circumference. The reason for the emphasis on C3 is due to the shape of the glass and the proximity to the region where the glass and base connect. This is expected to be a weak region under high pressure.

The measurements of the glass thickness are shown in Figure 4.25, Figure 4.26 and

Figure 4.27. The PMTs considered for soaking had varying glass thickness properties to allow an understanding of the impact of each property, and whether particular focus on certain glass properties is needed as part of QA testing.

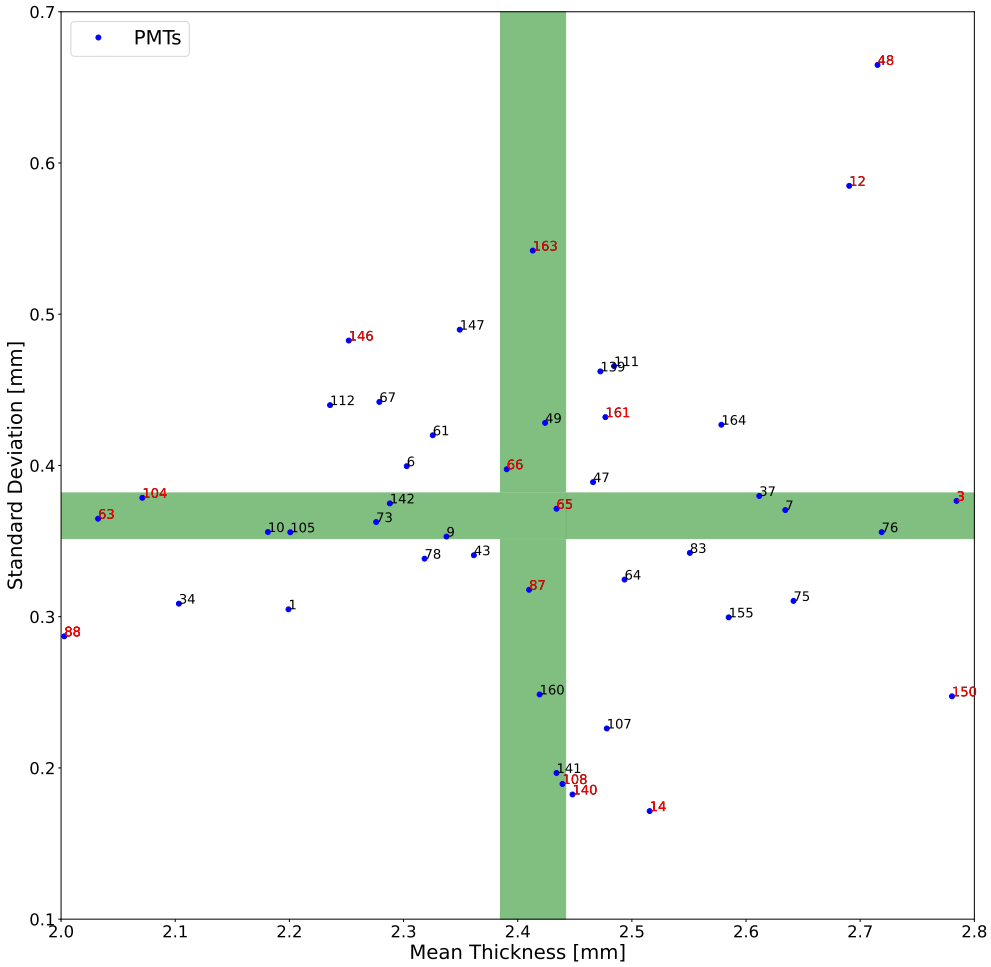

Figure 4.25: The mean glass thickness of measured PMTs. Those with red numbers were considered for the soak testing. The green bars represent the average mean thickness and standard deviation with uncertainties.

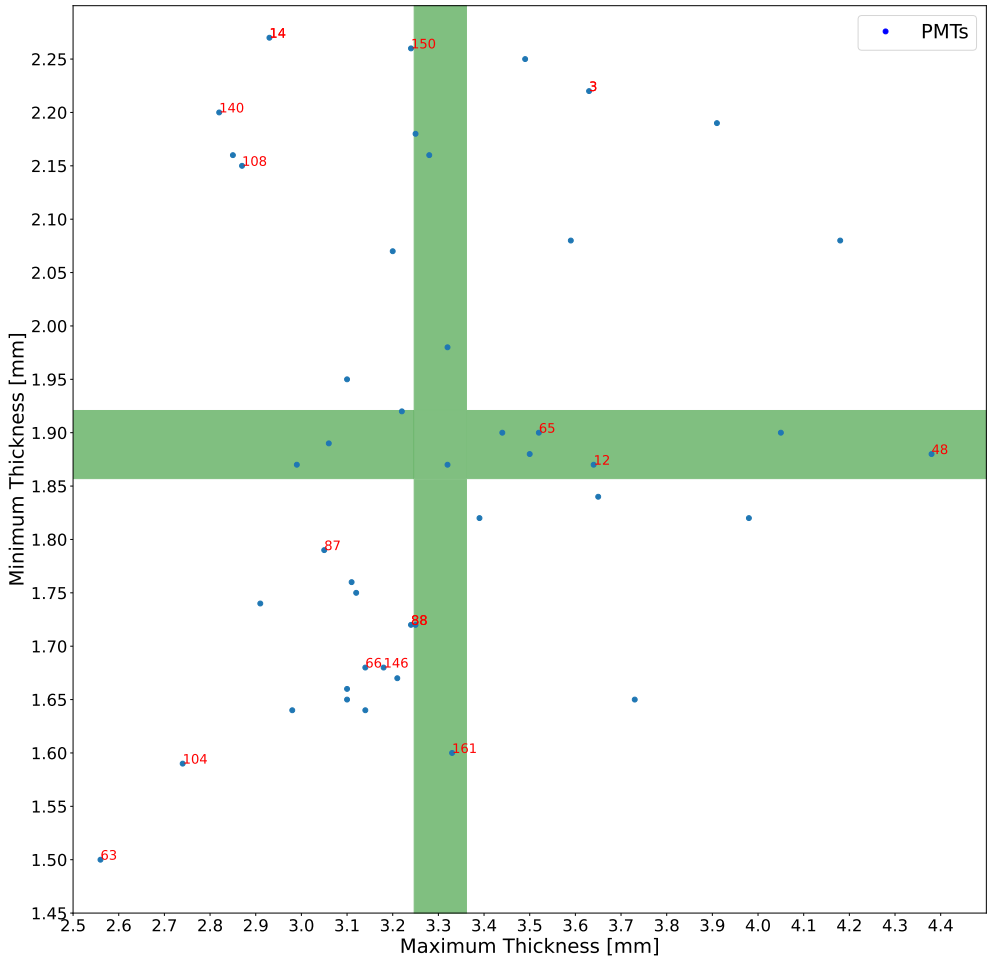

Figure 4.26: The minimum and maximum glass thickness of measured PMTs. Those with red numbers were considered for the soak testing. The green bars represent the average minimum and maximum thickness with uncertainties.

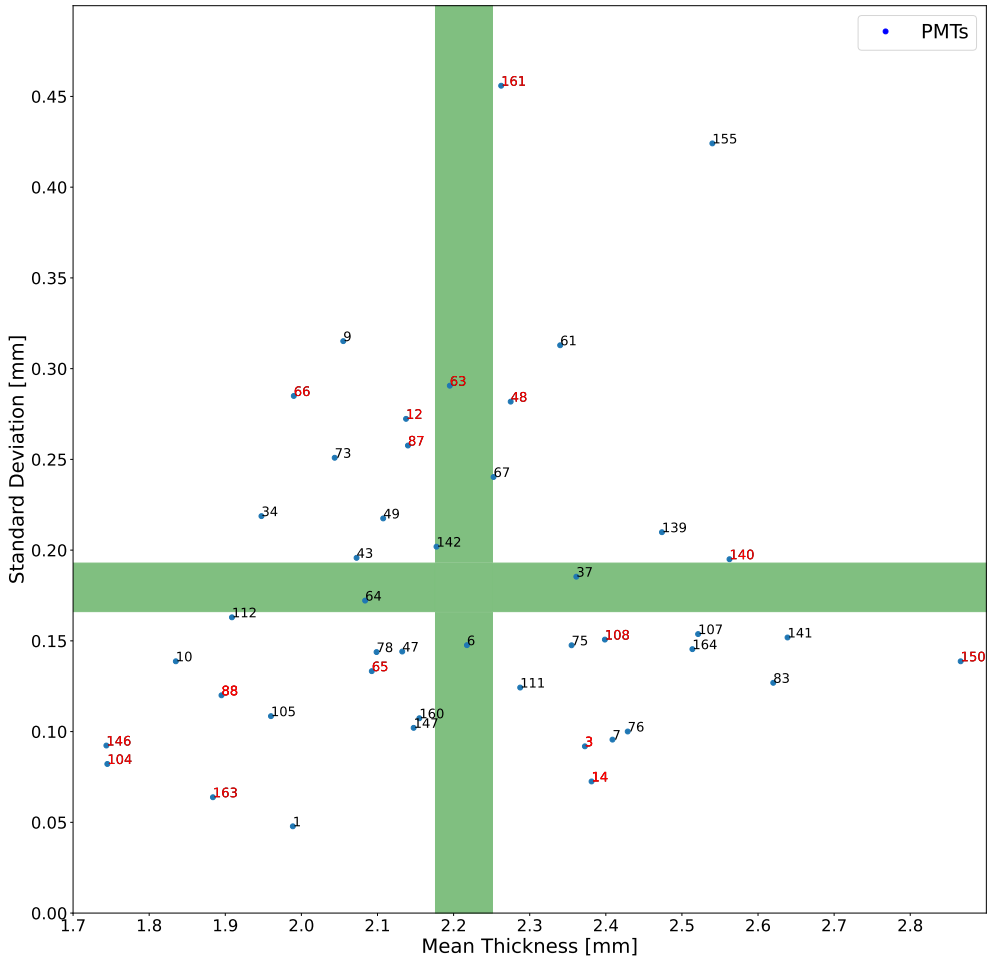

Figure 4.27: The mean glass thickness of C3 for measured PMTs. Those with red numbers were considered for the soak testing. The green bars represent the average C3 mean thickness and standard deviation with uncertainties.

4.7.1.2 Detailed Glass Thickness Testing

The thickness of the glass window of a single PMT was tested in detail by the Non-Destructive Testing (NDT) team at the Atomic Weapons Establishment (AWE). These tests also used ultrasound scans, but made 208 measurements compared to the 25 hand-made measurements of the other PMTs, and produced a three-dimensional map of the glass (Figure 4.28).

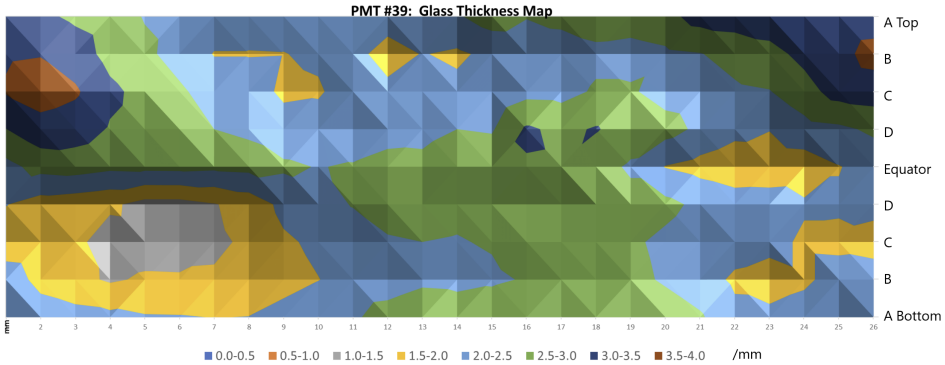

Figure 4.28: Glass thickness map measured using ultrasound scans by the NDT team at AWE. Figure courtesy of Steve Quillin, AWE.

A Computerised Tomography (CT) scan was also performed, allowing the internal structure of the PMT and its electronics to be seen (Figure 4.29).

The ultrasound and CT scans yielded consistent results, and the observations were comparable to those made of the other PMTs using the handheld ultrasound probe.

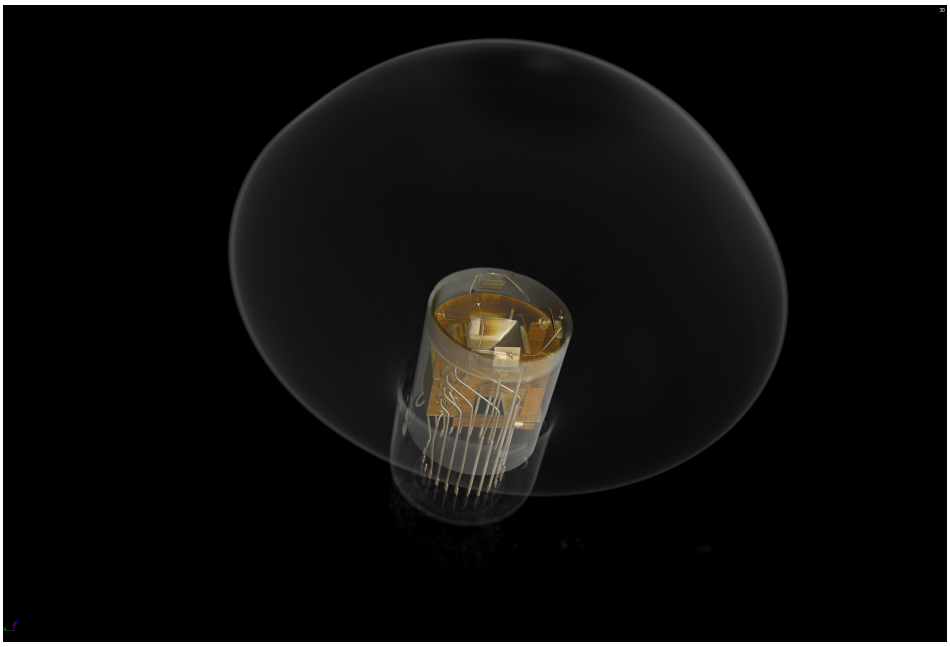

Figure 4.29: CT scan of a PMT performed by the NDT team at AWE. Figure courtesy of Steve Quillin, AWE.

4.7.1.3 Gadolinium Soaking

A total of twelve PMTs were soaked, with ten in a 1 % gadolinium concentration to replicate prolonged use in a Gd-doped environment, and one each in 0.1 % gadolinium concentration and pure water to act as controls. The initial soak period was planned as ∼1 - 3 months, but the soaking lasted over a year due to COVID restrictions.

The control PMTs, in no or low Gd concentration, showed no observable change after a year of soaking. The PMTs in the 1 % Gd all had a cloudy effect on the surface (Figure 4.30). The glass was cleaned using various methods, including deionised water

Figure 4.30: PMT with cloudiness after a year of soaking in a 1 % gadolinium concentration.

rinses, isopropyl alcohol, glass cleaner, acetic acid and physical cleaning with both clean and alcohol-soaked wipes. No change was observed after cleaning. Two of these PMTs were tested for gadolinium crystal deposits using X-ray fluorescence, with all results being negative. Repeats of the glass thickness testing were inconclusive, giving no clear indication that the cloudiness is due to etching.

The most likely cause of this effect is a small etching of the glass due to the acidic nature of gadolinium sulphate when dissolved in water. The etching is enough to change the optical properties of the glass surface, but is within the resolution of the ultrasound probe.

4.7.1.4 Pressure Testing

The PMTs were then pressure tested up to 6 atm of overpressure in the pressure vessel. This was done by increasing the pressure in increments of 2 atm and holding it for 15 minutes. All PMTs passed the testing, with no sign of mechanical damage. This would suggest that the gadolinium does not impact the integrity of these PMTs, although the cloudiness should be understood. However, as this effect is not seen in EGADS, and does not occur at the 0.1 % Gd concentration that is used in doped detectors, this is unlikely to be a major concern in the use of these PMTs in a detector.

The gadolinium soak tests were deemed inconclusive. The increased gadolinium concentration does not replicate the conditions of a 0.1 % doped detector, and the cloudy effect is only seen at the higher concentrations. The prolonged period of the soaking, with no access possible, due to COVID means the cloudiness could not be monitored over time or understood at an earlier stage.

4.7.2 Acrylic Vessels

Acrylic vessels, such as the one in Figure 4.31, are planned for use in BUTTON to allow compatibility with many fill materials without the need for extended prior testing. These vessels will house one Hamamatsu R7081 PMT each, and are rated to withstand 3 atm of pressure.

To confirm the rating, they were tested in the pressure vessel. Two designs were tested, with the only difference being the curvature of the acrylic near the bolts that hold the two hemispheres together. One vessel was tested to destruction, with the other two being tested to 2 atm.

During the tests, the housings were loaded one at a time into the pressure vessel (Figure 4.32) and sealed in. The pressure was increased in 0.5 atm steps, with the housing being removed and checked for water ingress at each step. Of the two tested to 2 atm, one was held at 2 atm overpressure overnight. Both of these housings passed the pressure tests.

The third housing, tested to destruction, was taken to the rated 3 atm of overpressure and held there. After no sign of issues, the pressure was slowly increased until the vessel imploded at 3.17 atm. As the housing fragmented, it was not clear where the weaker spots were. However, the section around the cable feedthrough came away cleanly in one piece and there was significant damage to the plastic around the flange that

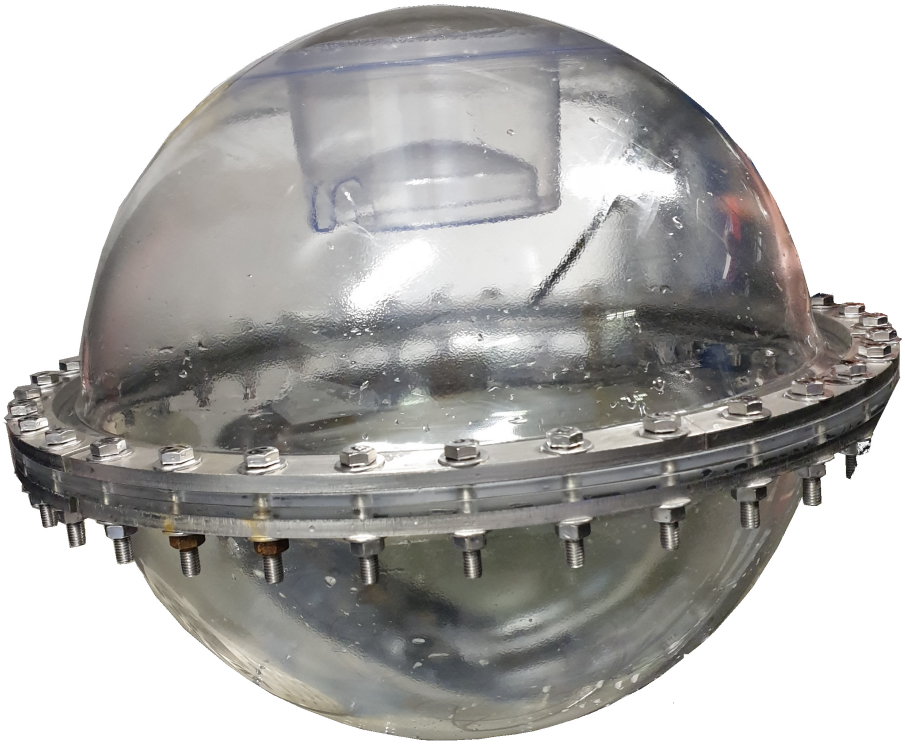

Figure 4.31: Acrylic housing for Hamamatsu R7081 PMT to allow material compatibility with different fill media.

connects the two hemispheres of the housing (Figure 4.33).

Based on the results, with no water ingress at over 2 atm of overpressure and the implosion occurring at over 3 atm, the housings are deemed to be suitable for use in a small detector such as BUTTON. For larger detectors, in excess of 30 m, these housings would not be suitable. In the case of large detectors, the materials and PMTs are specified to have compatibility with the liquid fill as these detectors very rarely change the fill medium over the course of the detector lifetime. However, for a test bed like BUTTON, changes in fill material are expected and flexibility is required. Using housings such as these can provide that flexibility as the PMTs can be kept constant across different fills.

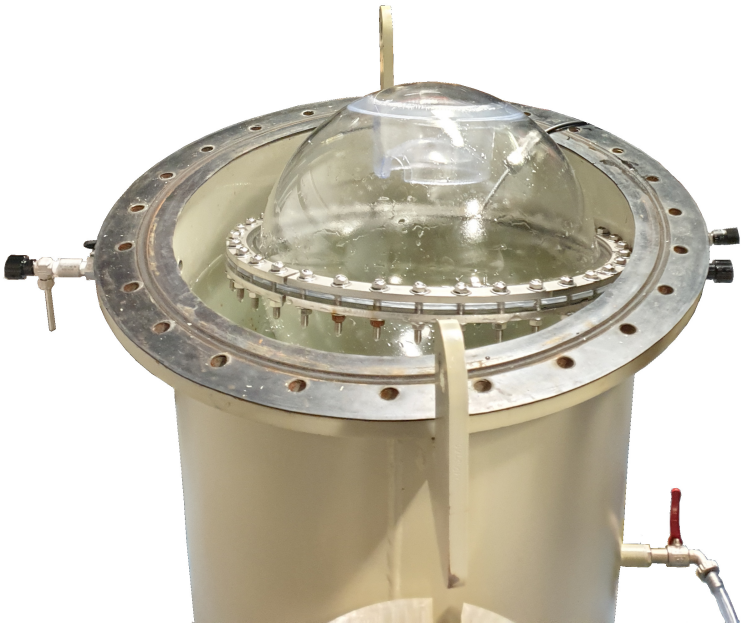

Figure 4.32: An acrylic housing being lowered into the pressure vessel. A lid is bolted on top with a cable feedthrough to seal the housing in.

Figure 4.33: An acrylic housing that imploded at 3.17 atm of overpressure.

4.8 Summary

PMTs are commonly used in liquid-filled neutrino detectors to observe light emitted by particle interactions. In large detectors, several thousand are used, with their output

combined to allow a detailed reconstruction of observed events. To allow the optimal usage of PMTs, they are characterised in detail before installation into a detector.

Several characterisation regimes have been developed, both in air and water, and applied to the Hamamatsu R7081-100 PMTs to be installed in BUTTON and used in simulations of NEO. The testing in air confirms the tubes are up to manufacturer specifications, with a generally good relationship between Hamamatsu's in-house testing and the data obtained. To confirm the properties of the PMTs remain consistent when submerged in water, as they would be in a water-based neutrino detector, a subset of PMTs were tested in detail in the PocketWATCH facility described in chapter 3. In particular, their dark rate was confirmed to be dominated by thermionic emission and independent of the fill media.

Their compatibility with gadolinium was tested by prolonged soaks in 0.1 % and 1 % concentrations of gadolinium-doped water, with the 0.1 % concentration showing no changes. The 1 %-soaked PMTs showed a cloudiness on the glass, but this concentration is not representative of a doped detector and provided no meaningful conclusions. This type of effect has not been observed in EGADS, and therefore is not a cause for concern.

The mechanical strength of both the Hamamatsu R7081 PMTs and acrylic housings for material compatibility have been tested in a pressure vessel, with all equipment tested being deemed suitable for their planned use in BUTTON.

Chapter 5

Neutrino Experiment One: A Remote Reactor Antineutrino Monitor

Nuclear reactors raise concerns over the proliferation of nuclear weapons, as discussed in detail in section 1.3. Safeguarding currently exists and is performed by the IAEA, and is generally sufficient for the current generation of power reactors. However, there are potential gaps in the current methods used for safeguarding. Documented cases of research reactor misuse and the development of advanced reactors types in the future may necessitate new methods [145].

One such method is to use the antineutrino emission from the fission processes in a reactor core. Antineutrinos are unshieldable, and their flux is directly determined by the core composition and power output. Observation of reactor antineutrinos can provide information on the operation of a core. Antineutrino observation can also be performed remotely, offering a less intrusive method than traditional safeguarding techniques.

5.1 Requirements for Reactor Antineutrino Monitor

To observe reactor neutrinos, an antineutrino detector is required. Antineutrinos from reactors have been observed previously at short standoffs from reactor cores and as amalgamated signals at larger distances. KamLAND has previously made observations

of antineutrinos from distant reactors and has used them to make oscillation measurements [298], whilst Daya Bay successfully measured reactor spectra and was able to unfold a spectrum for each fissioning isotope [299]. However, mid- to far-field monitoring of reactor operations and core evolution for the purpose of non-proliferation has not yet been performed. Before using this technology in the field, it must be demonstrated by a prototype to both prove utilty and optimise the design.

To construct a detector of sufficient sensitivity to yield the required information, several requirements must be met. Neutrinos are a very weakly interacting particle, producing very low interaction rates in a detector in comparison to their flux. As such, backgrounds can dominate over the observed antineutrino rates. Suppression of these backgrounds is vital to ensure the antineutrino signal can be measured. This can be achieved through both detector location and design.

The design of the detector must be such that the antineutrino signal can be easily observed. Choosing the detector size, type and fill medium will all impact the efficiency of detection, as well as the ability to distinguish the signal from the backgrounds that cannot be suppressed.

Finally, for a prototype to be useful, it must be situated in a reactor landscape that replicates a realistic situation. A signal is needed from a target reactor, with backgrounds provided by other reactors, so that the ability to observe a potentially "unknown" reactor against "known" reactors can be understood. Ideally, a landscape that provides several reactors that can act as an observation target would be used for any prototype.

The rest of this chapter details the design, location and simulations of the the Advanced Instrumentation Testbed (AIT)-Neutrino Experiment One (NEO) facility-detector prototype proposal for reactor antineutrino monitoring.

5.2 Location and Facility

5.2.1 Underground Facility

As rarely interacting particles, the neutrino signal can be easily masked by backgrounds. In the case of reactor neutrinos, the largest non-radiological background comes from cosmic ray muons, due to the spallation products they produce and their high rate in comparison to neutrino interaction rates. These products can be produced outside

a detector and propagate inside, such as energetic neutrons produced in rock, or be produced inside the detector itself, such as radionuclides from the spallation of oxygen.

Cosmic rays are energetic particles from astrophysical events, and are composed mostly of protons (∼90 %) and helium nuclei (∼9 %) [300]. When they reach Earth, they interact with atoms in the atmosphere at an altitude of approximately 15 km and produce showers of secondary particles. These secondary showers typically consist of protons, neutrons, charged pions and charged kaons. The charged pions and kaons are unstable and will decay, generally producing muons (99.99 % branching ratio for pions, 63.50 % branching ratio for kaons). These muons can reach the Earth's surface and even penetrate deep into rock due to their behaviour as minimum ionising particles, caused by their unusually long mean lifetime (2.2 µs [40]) and high mass (105.66 MeV [40]). At sea level, the expected rate of cosmic ray muons is $\sim 1\,\mathrm{cm}^{-2}\,\mathrm{min}^{-1}$ [290] at an average energy of ∼4 GeV [301].

As cosmic rays come from above, a solution to their dominant rate is to go underground. Large neutrino detectors, such as SK and SNO, are constructed in underground laboratories [85, 302]. This allows the muon flux to be attenuated as muons will interact and deposit their energy in the rock. A potential choice of location for AIT-NEO is the Science & Technology Facilities Council (STFC)'s Boulby Underground Laboratory, situated in Israel Chemicals Ltd (ICL) Boulby Mine near Whitby, North Yorkshire, UK. The laboratory is situated 1100 m underground, with a flat overburden. This depth in rock salt corresponds to 2800 m.w.e, and produces an $\mathcal{O}(10^6)$ reduction in cosmogenic muons compared to the surface [303]. Figure 5.1 shows how the muon flux at Boulby compares to other underground laboratories. The muon flux at SK has an $\mathcal{O}(10^5)$ muon reduction and SNOLAB sees a 5×10^7 muon reduction compared to sea level [304].

Boulby has been home to several deep underground physics experiments since the 1990s including the ZEPLIN dark matter detector and part of the CYGNUS (formerly DRIFT) directional dark matter detection programme, as well as the BUGS world-class material assay facility, giving it a proven track record of supporting rare-event and low-background science. A schematic of the lab is shown in Figure 5.2.

Beyond its significant muon attenuation, Boulby is renowned for its low radon levels. The radon concentration in the air at Boulby averages $< 3\,\mathrm{Bq\,m}^{-3}$ [313]. This is orders of magnitude lower than equivalent laboratories with SNOLAB, the host laboratory for SNO and SNO+, seeing $129.5 \pm 5.9\,\mathrm{Bq\,m}^{-3}$ [314], and Kamioka having seasonal variations between $> 1000\,\mathrm{Bq\,m}^{-3}$ April to November and $< 500\,\mathrm{Bq\,m}^{-3}$ November to

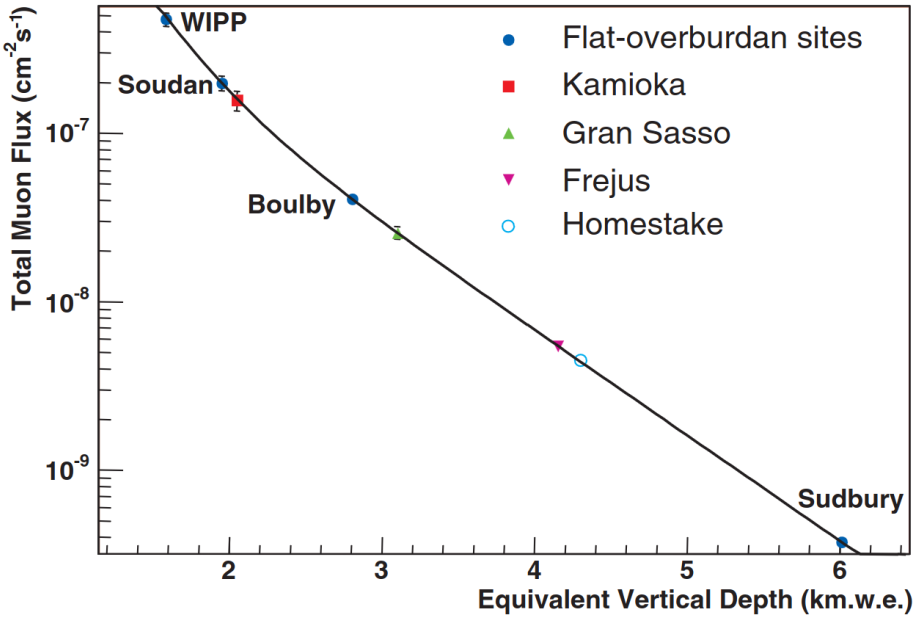

Figure 5.1: Total muon flux for various underground laboratories. The smooth curve is a global fit to data taken at sites with a flat overburden [305]. Kamioka has a mountainous overburden and a depth of 2700 m.w.e at the location of SK [302]. Data from [298, 305–311]. Reprinted from [305].

April [315]. The dome above the SK detector has a radon air concentration of 40 - 100 Bq m^{-3} [316].

The ultra-low backgrounds in the lab are not the only reason Boulby is a suitable choice of location for a reactor antineutrino monitoring prototype; Boulby is located near the United Kingdom's AGR fleet, giving a variety of monitoring scenarios to consider.

5.2.2 Reactor Landscape at Boulby

The reactor landscape at Boulby is ideally suited for a prototype mid- to far-field reactor antineutrino detector for non-proliferation purposes. The proximity to the UK's and northern France's reactor fleet allows for reactors at standoff distances between 26 km and ∼440 km to be considered as targets for observation. The map in Figure 5.3 shows the distribution of reactors around Boulby.

There are two reactor types within this distance. The reactors in northern England

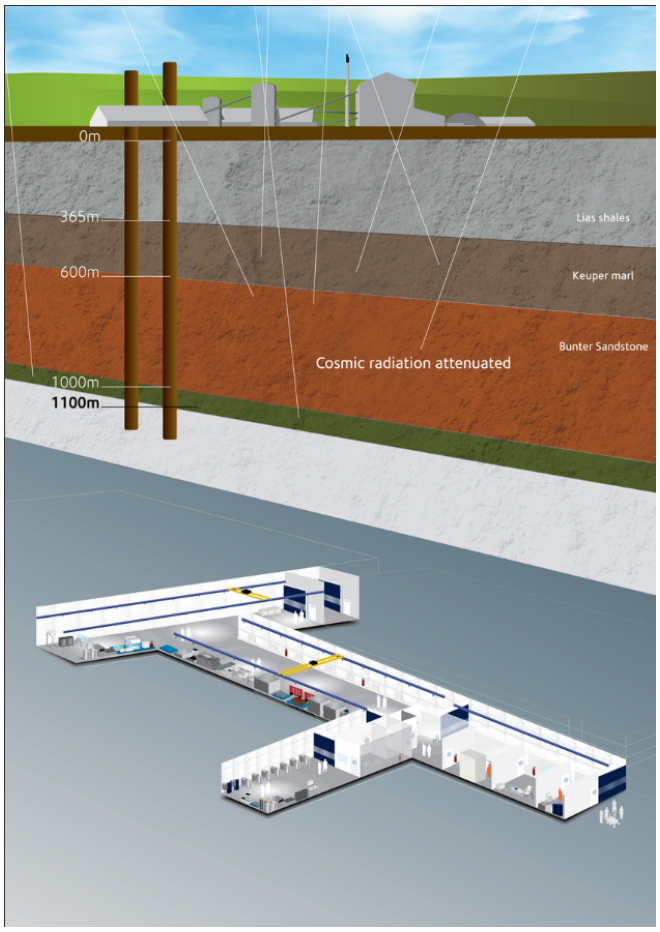

Figure 5.2: Schematic of the laboratory at Boulby within the layers of rock in the mine [312].

and Scotland are AGRs; the reactors in southern England[1] and northern France are PWRs. The reactors, their types and their distance to Boulby are summarised in Table 5.1.

The two AGR types are similar designs, with the second generation AGR-2 cores being constructed slightly later using updated and modified designs from the first generation AGR-1 cores.

The nearest reactor, Hartlepool, is a first generation dual-core AGR with a thermal power output of ∼1500 MW per core [318]. As the nearest reactor to the proposed AIT-NEO site at Boulby, the WATCHMAN collaboration who proposed the project formed a strong relationship with EDF, who operate the UK's reactor fleet. EDF were able to

[1]Including the currently under construction Hinkley Point C.

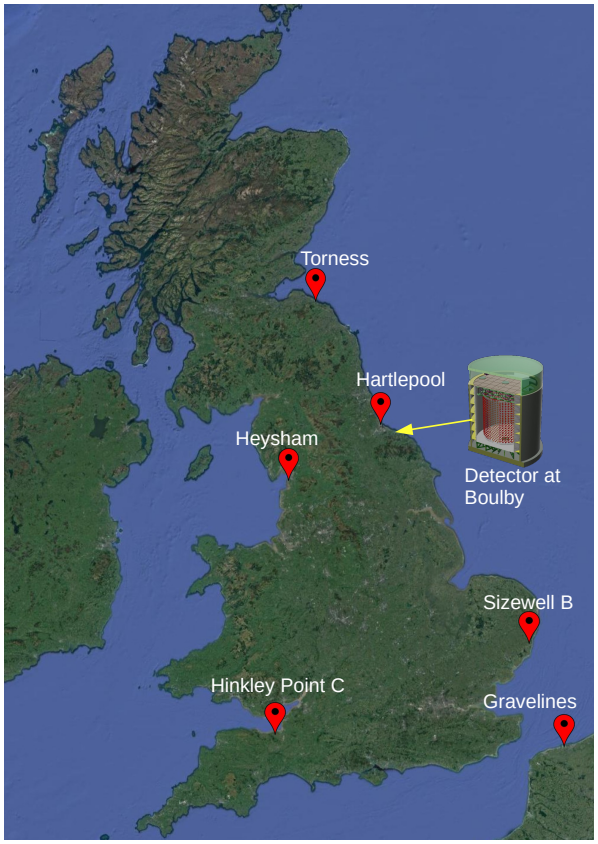

Figure 5.3: Map showing the location of the detector at Boulby and the nearest operating reactor sites [317].

provide significant information on a confidential basis surrounding the operation of the Hartlepool cores. This included information about the assembly types, hourly reactor power variations, daily mean channel power and daily channel irradiation. This allowed detailed modelling of the antineutrino flux, and allowed more accurate simulations. Work on modelling the Hartlepool antineutrino flux is available in [131].

Hartlepool uses 110 tonnes of $\sim$3 %-enriched UO_2 pellets in each core. There are 332 graphite channels that enclose eight fuels elements of 1 m in length per channel, forming the reactor core. Figure 5.4 is a schematic of an AGR fuel element. Each element contains 36 stainless steel pins which contain the fuel pellets [131]. The CO_2 coolant is able to flow through the graphite channels, which are shown partially complete in Figure 5.5.

The AGR dual-core power stations are usually continuously run by maintaining the

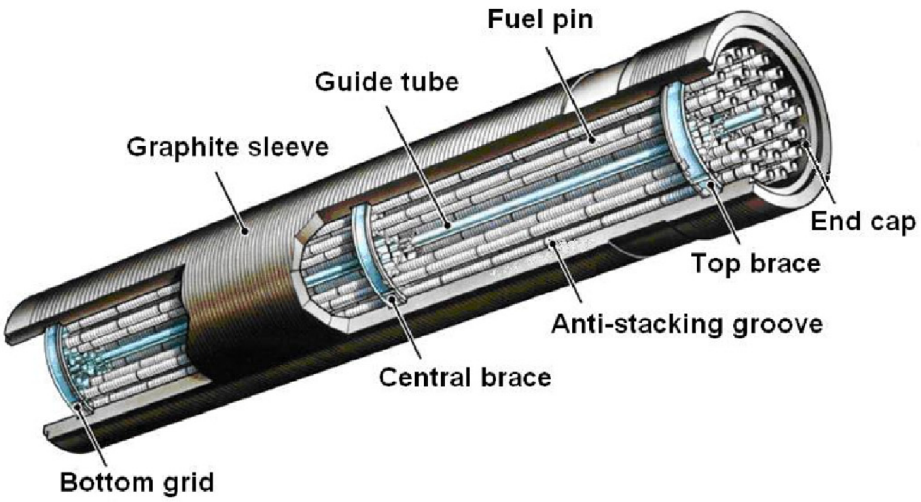

Figure 5.4: Fuel element for an AGR core, with 36 fuel pins enclosed in graphite. The fuel pins are 1 m long and contain UO_2 pellets. Reprinted from [319].

operation of one core as the other is refuelled. The refuelling is regular, twice per year, and takes approximately two weeks per core.

The EDF Hartlepool power station is due for decommissioning[2] in 2026 [320], so any detection would be required before then. However, due to the proximity of other reactors to Boulby, Hartlepool is not the only option for reactor detection. The Heysham complexes at 149 km are two dual-core AGR sites. Heysham 1 is an AGR-1 with a decommissioning date in 2026 like Hartlepool [320], Heysham 2 is an AGR-2 with a decommissioning date in 2028 [320]. The capacity for power output and operation of Heysham 1 is nearly the same as Hartlepool as it is the same basic design [318]. Heysham 2 has a slightly higher capacity of $\sim$1550 MW_{th} per core [318]. Torness, at 187 km, is an AGR-2 dual-core station with a 1623 MW_{th} power capacity per core [318].

Beyond the AGR stations, there are also PWR stations at greater distances. Sizewell B, with a 3425 MW_{th} power capacity, is a currently-operating single core site. The current decommissioning date is 2035 [320], but a review of a long term extension is ongoing [321]. Gravelines, in northern France, consists of six PWR cores each of 2785 MW_{th}. These are due to be decommissioned in 2031 [322]. Hinkley Point C is currently under construction, and is expected to be producing power around 2030 [323] and have an initial 60 year lifetime. The station is expected to produce 3.260 GW_e,

[2]All decommissioning dates were accurate at the time of writing, but are subject to change.

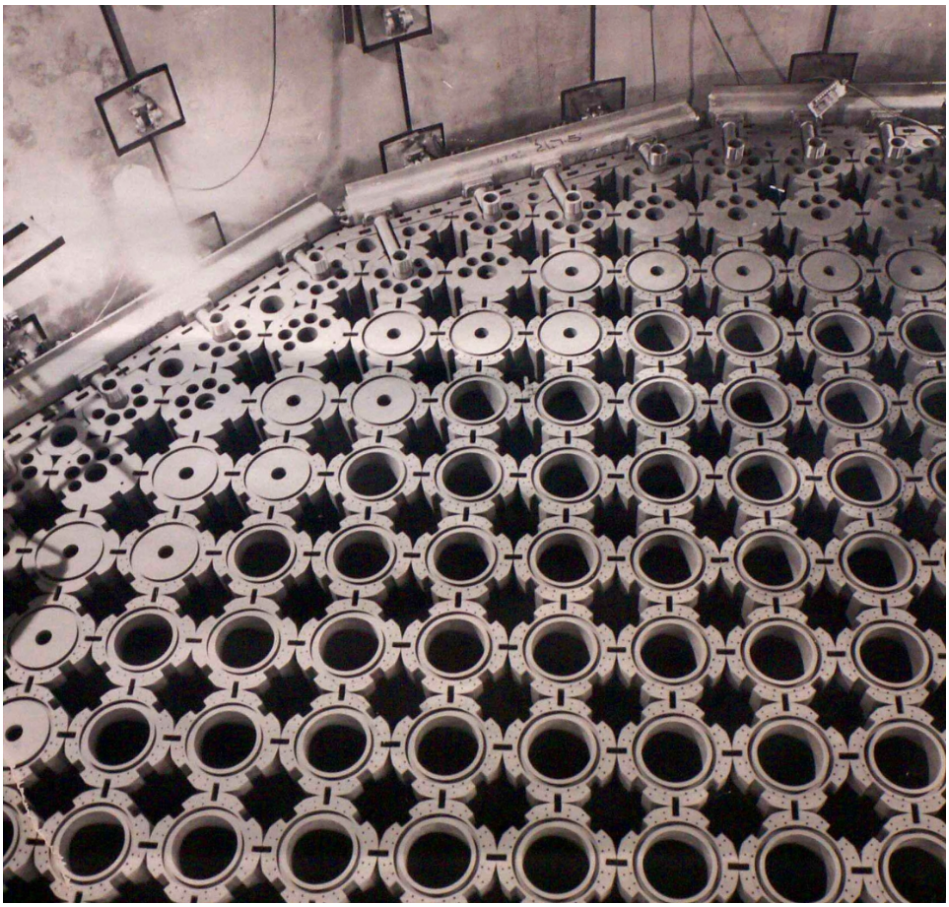

Figure 5.5: An incomplete AGR core composing of graphite blocks that house the fuel elements. Image courtesy of EDF Energy.

which can be empirically related to thermal energy via [324]

$$3.260\,\mathrm{GW_e}\left(\frac{4.3\,\mathrm{GW_{th}}}{1.6\,\mathrm{GW_e}}\right) = 8.76\,\mathrm{GW_{th}}.$$

The energy not converted to electrical energy is lost as thermal energy to the cooling water system, and later the surrounding environment. A summary of the decommissioning dates of the reactors nearest to Boulby is in Table 5.1.

Reactor	Number of cores	Type	Standoff distance [km]	Power [MW_{th}]	Decommissioning date
Hartlepool	2	AGR-1	26	3000	2026
Heysham 1	2	AGR-1	149	3000	2026
Heysham 2	2	AGR-2	149	3100	2028
Torness	2	AGR-2	187	3246	2028
Sizewell-B	1	PWR	306	3425	2035
Hinkley Point C	2	PWR	404	8760	2086
Gravelines (France)	6	PWR	441	16710	2031

Table 5.1: Summary of reactors closest to Boulby. Decommissioning dates are from [320, 322, 323]. Sizewell B was under review for a long term extension beyond 2035 at the time of writing [321]. Power data is from [318].

Due to shutdowns for refuelling and maintenance among other things, the average thermal power reactors are operated at is lower than their thermal power capacity.

5.3 Detector

5.3.1 Cavern

The overall design of the detector prototype is determined by a combination of the signal, background, and facility. For the AIT facility, the largest cavern to house an underground detector is a 25 m height and diameter upright cylinder [262]. This is based on a combination of engineering requirements and cost; a larger cavern would require a different way of supporting the cavern roof. This restricts the largest detector to be a 22 m height and diameter upright cylinder. The geology for a smaller cavern option at Boulby is shown in Figure 5.6.

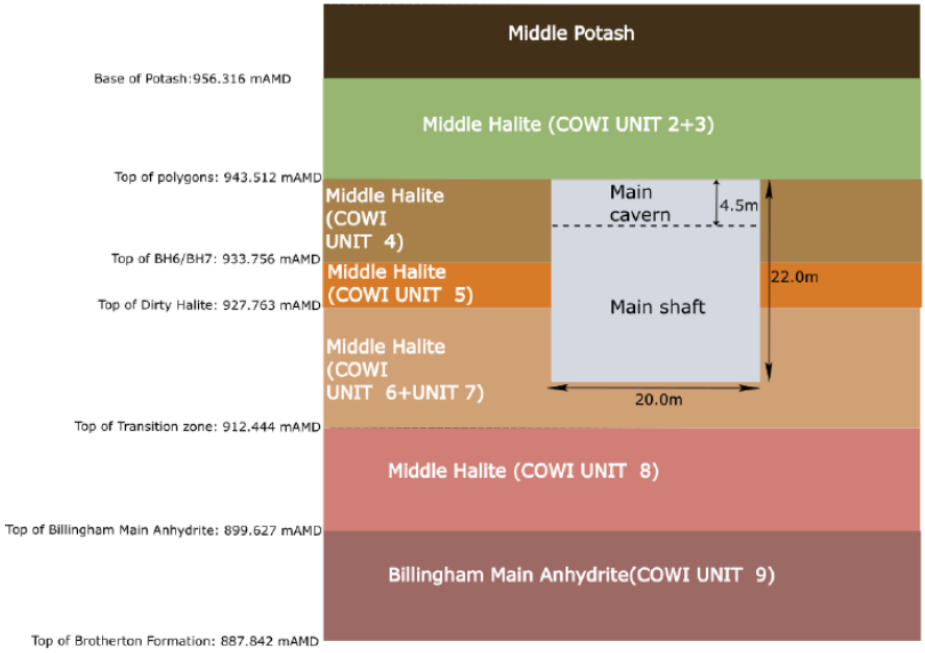

Figure 5.6: The geology of a potential cavern to house AIT at Boulby. Figure by COWI UK Ltd.

5.3.2 Rejected Designs

Several designs for a reactor monitoring prototype have been considered [262, 325], such as a rectangular prism of height and width 8 m and length of either 50 m or 80 m, and a small upright cylinder of 12 m or less in height and diameter. Both of these general designs would significantly reduce the engineering costs and requirements of supporting a large cavern underground. However, studies of these detector designs show neither would be suitable for observing the nearest reactor cores at Hartlepool 26 km away [325]. These designs are limited by backgrounds, as neither could accommodate an outer detector region to shield against external backgrounds such as cosmic ray muons. The rectangular prism would experience a large amount of background for its internal volume, as backgrounds scale with detector surface area and a rectangular prism has a high surface area to volume proportion. The signal in the smaller cylinders would be too small to be able to observe a significant signal above backgrounds.

5.3.3 Neutrino Experiment One

The final general design of the detector is an upright cylinder in the larger cavern size (25 m) [262, 326]. It is instrumented with Hamamatsu R7081 10" PMTs, which are described in detail in chapter 4, to a coverage of at least 15 %. The choice of 15 % PMT coverage comes from previous simulations, which found that the sensitivity of a detector to a reactor drops off sharply below this coverage [262].

The detector is split into two key regions by the PMT Support Structure (PSUP), a large Inner Detector (ID) region which is used to detect the signal and a smaller Outer Detector (OD) region to shield against backgrounds. The OD is uninstrumented i.e. no PMTs face this region. This is different to many detector designs, such as SK [246], which have instrumented active veto regions. In a detector with an active veto, any particles observed in the OD will be vetoed from the data. This allows backgrounds that enter the tank from the outside, such as muons, to be efficiently removed from the data. However, this adds significant cost to the detector design. In an effort to reduce costs, the design for NEO initially has a passive outer buffer. If the detector is sufficiently sensitive without the requirement for outwards facing PMTs, they can be omitted. The inner and outer detectors are optically divided by opaque black sheeting to stop light from interactions in the OD reaching and triggering the ID. The detector also has a 1.5 m air gap to the cavern wall. Whilst this is due to access requirements, the air gap acts to further suppress backgrounds produced outside of the detector. A schematic of the design is shown in Figure 5.7.

Within the general detector design, several variations are considered. Two detector sizes are considered, a 22 m height and diameter detector that is the largest possible detector with the cavern design, and a 16 m height and diameter detector which should be the minimum viable size to observe the reactor signals. The key specifications are detailed in Table 5.2.

Tank diameter and height [m]	PSUP radius [m]	OD buffer width [m]	Inner PMT coverage [%]	Number of PMTs
16	5.7	2.3	15	1824
22	9.0	2.0	15	4600

Table 5.2: Summary of detector geometries used in this study. The PSUP radius determines the size of the ID.

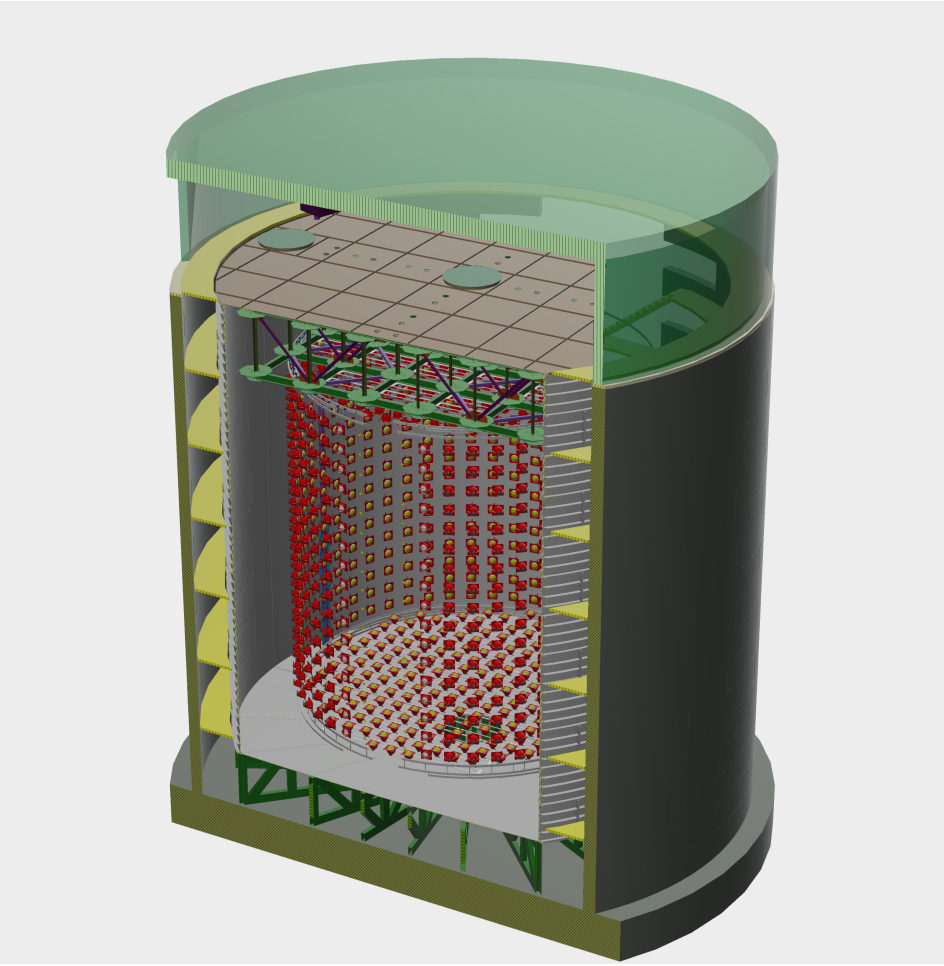

Figure 5.7: Schematic of the detector design by Jan Boissevain (University of Pennsylvania), showing the tank supported on a steel truss structure and the PSUP inside.

On top of the two basic detector designs, two fill media are considered. They are:

- Gd-H_2O with 0.2 % $Gd_2(SO_4)_3$ doping (for 0.1 % Gd concentration),
- Gd-WbLS with 0.2 % $Gd_2(SO_4)_3$ doping and ∼100 photons per MeV WbLS. The WbLS corresponds to a ∼1 % scintillator concentration.

Having four possible detector configurations gives the effect of upper and lower limits for the sensitivity of NEO based at the AIT site at Boulby to the UK's nuclear reactor fleet. The largest tank with the Gd-WbLS fill should be the most sensitive detector. It has the largest target volume, the highest light yield and the lowest energy threshold. The 16 m detector with a Gd-H_2O fill should be the least sensitive detector. If

the performance of the most and least sensitive detectors are understood, the optimal balance of cost and performance can be extracted. If the most sensitive detector is unable to achieve a reasonable level of sensitivity, it would suggest the concept is difficult to achieve with current technology.

5.4 Simulations

As NEO is a proposed and not a currently operating experiment, no data exists. To understand the detector's performance in terms of its ability to observe and measure distant reactor antineutrino signals in a realistic environment, it has been simulated in detail.

Full Monte Carlo (MC) simulations of the detector and particles were carried out with the Reactor Analysis Tool - Plus Additional Codes (RAT-PAC) simulation package [327], which has been adapted for AIT-NEO. RAT-PAC makes use of the Class Library for High Energy Physics (CLHEP) libraries [328], and uses GEometry ANd Tracking 4 (Geant4) [329, 330] as a command interpreter for macro execution. RAT-PAC also uses Geant4 for compilation. Much of the RAT-PAC structure is designed to interface with the Generic Liquid-scintillator Anti-Neutrino Detector or *GenericLAND* (GLG4sim) package [331]. GLG4sim is a self-contained application in which a set of tools, libraries and classes for generic Geant4 liquid scintillator detectors are defined. It was originally adapted from KamLAND's MC package, but for use with generic detectors. It is also set up to allow it to act as a library or starting point for specific detector simulations. GLG4sim's features include support for input and output operations, handling of databases, optical models for both materials and PMTs alongside PMT hit collection, and classes for particle generator implementation. RAT-PAC uses the classes defined within GLG4sim to create an MC particle and detector response simulation. The data analysis framework ROOT [332] is used to handle data input and output, and file structure.

The optical models for materials are custom definitions using libraries and classes from GLG4sim. The optical properties of each material are defined based on measurements or manufacturer specifications, and used to form the optical response. The WbLS models of emission profile and material composition are from [244], and are based on time profile measurements [239, 247] and Gd-WbLS light yield and scattering measurements [333]. The PMT simulation is extracted from GLG4sim, with the

properties tuned to those for the Hamamatsu R7081. The PMT response for charge and time are stored as Probability Density Functions (PDFs) which are sampled when a photon is absorbed by the photocathode, for which the probability of absorption is dictated by the quantum efficiency distribution of the photocathode. To reduce the simulation time, the PMTs are simulated in a small envelope. Whether a photon hits a PMT is only checked if the photon is within this envelope to reduce the usage of the PMT optical models. The triggering and Data Acquisition (DAQ) are handled directly in RAT-PAC.

Particle generators are also custom models implemented with GLG4sim libraries. The IBD generator uses the cross section model in [178] to define the direction and energy of the outgoing particles, which define how these particles are generated. Radioactive decays use custom definitions of decay chains, branching ratios and decay modes to define the particular particle to be simulated, and fast neutrons use the model in [305]. The light emission from neutron capture on gadolinium is handled by DICEBOX [334], which simulates the γ decay of excited nuclei.

RAT-PAC acts as an event-loop, handling single particle instances at a time to produce an interaction-by-interaction detector response model. Detector geometry and composition can be defined as a fixed design, or use a detector factory based on requested properties such as photocoverage, size and fill. The two implemented NEO detector designs use fixed geometries as inputs.

5.4.1 Detector

The detector simulations are a simplified version of the detailed design concept proposed for NEO [262, 325, 326, 335], and detailed in subsection 5.3.3. The complex structures, such as the I-beams, trusses and PSUP are simplified to their approximate position and volume. This allows their contribution to the background to be considered without extending the CPU time required. A cutaway of the detector model implemented into RAT-PAC is shown in Figure 5.8.

The detector is surrounded by 2 m of rock in simulations. This distance is deemed sufficient as combined with the minimum 2 m OD buffer and 1.5 m air gap, the backgrounds due to radioactivity from the rock are not expected to penetrate the fiducial volume of the detector. This distance is also deemed sufficient for fast neutrons as the total neutron flux attenuation is 2+ orders of magnitude in 3.5 m of rock or water [305]. The minimum air gap between the cavern wall and the detector, the smallest OD and

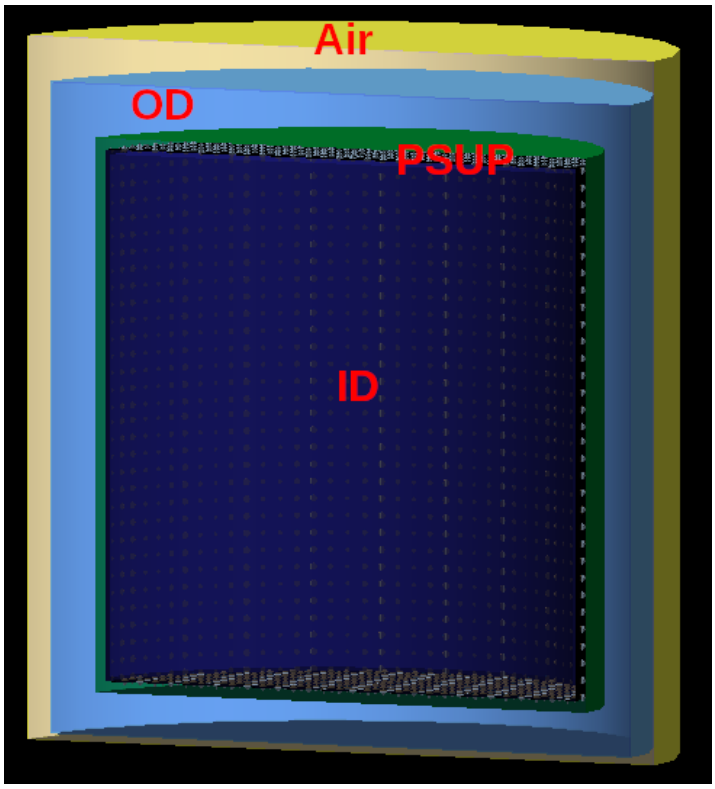

Figure 5.8: Cutaway view of the 22 m detector implemented into RAT-PAC. The layers from inside to outside are: the ID, the PMTs and support structure, the plastic sheeting between the ID and OD, the OD and the air gap to the cavern wall. The outer surface of the OD is the tank wall, and the surface outside of the air gap is the cavern wall.

the dead space due to the PSUP combined are in excess of 3.5 m. Fewer than 0.5 % of the cosmogenic neutrons generated in the outer 1.9 m of rock trigger a detector response, with approximately 2 % in the inner 10 cm. This is before vertex reconstruction and analysis cuts are applied, which further reduce the observed rate. The triggering of the radioactive-decay produced particles from this layer is negligible, and the fast neutron trigger rate drops off rapidly beyond this distance. Consistent with previous studies of NEO and its predecessor reactor prototype designs, radioactive decay backgrounds were generated in the inner 10 cm of the rock layer to reduce simulation time.

5.4.2 Reactor Modelling and Signals

5.4.2.1 Input Spectra

To simulate the reactors in subsection 5.2.2, their detectable antineutrino flux is modelled. The detectable antineutrino emission consists of three components, the emission flux (subsection 1.3.4), the interaction cross section (section 2.1) and the survival probability of electron antineutrinos (subsection 1.2.3). These three components are convolved to produce a spectrum of antineutrinos that could be detected for each reactor in NEO. Matter oscillations are neglected as they have very little effect at the energy of reactor antineutrinos.

To calculate the reactor antineutrino emission flux, the Huber-Mueller model in Equation 1.17 is used [151, 152] alongside the average thermal output for 2020 based on IAEA load factors. The mid-cycle fission fractions are assumed, which for AGRs is appropriate due to their short refuelling cycle and expected $\mathcal{O}(1\,\%)$ antineutrino flux variation during the cycle. The most up to date β spectra and antineutrino flux predictions that resolve the reactor antineutrino anomaly have not been used as the work was started before accepted solutions to the anomaly were available. Instead, the anomaly is incorporated into the systematic uncertainty.

Spectra for each of the reactors are generated from geoneutrinos.org [179], a web tool that takes detector locations and IBD emission from various sources, and produces observable spectra and rates for that location. The integrated rate of interaction is calculated from the antineutrino spectra [179] in Neutrino Interaction Units (NIU), which is the interactions per 10^{32} target particles per year. This unit is used by geoneutrino.org and normalises the spectra to allow easier comparison across sources and detectors. This is converted to an IBD rate using

$$R_{\mathrm{IBD}} = R_{\mathrm{NIU}} \times \frac{N_{\mathrm{kT}} \times N_{\mathrm{p}}}{10^{32}}, \tag{5.1}$$

where N_{kT} = mass of water in the detector in kilotonnes and $N_{\mathrm{p}} = 6.686 \times 10^{31}$ is the number of free protons per kilotonne of water. The IBD generator then draws antineutrinos from the relevant spectrum. The generator allows the simulation of the time and position distribution of IBD based on reactor antineutrino spectra, and weights the angle between the positron and antineutrino by the $\cos^2(\theta)$-dependent cross section. Positron and neutron energies and momenta forming an IBD pair are calculated to the first order correction for finite nucleon mass [180]. The time and distance between interactions for simulated IBD pairs is in Figure 5.9. The mean time between IBD

pairs is ∼28 µs and the mean distance is ∼6 cm. The true antineutrino energy spectra for Hartlepool, Heysham 2 and Torness at Boulby are shown in Figure 5.10, with the normalised spectra in Figure 5.11 to show the effect of neutrino oscillations.

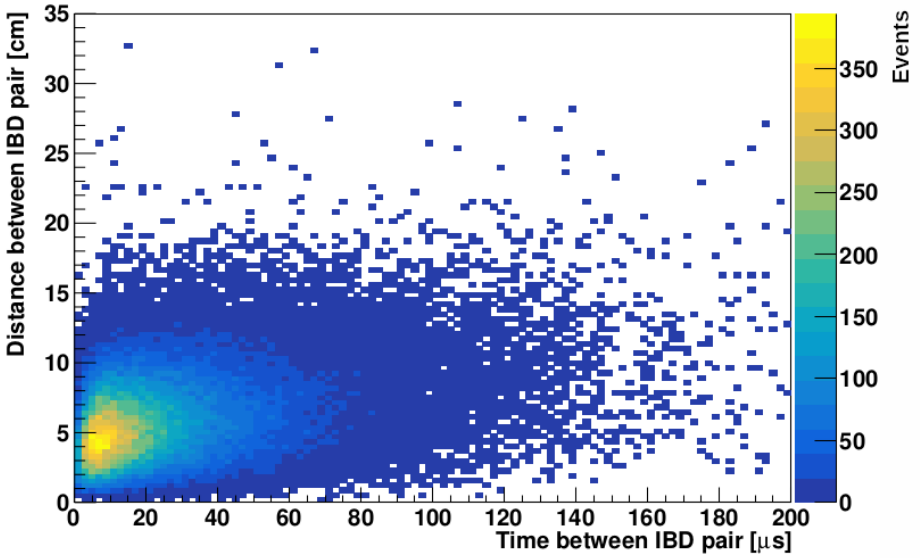

Figure 5.9: The time and position distribution of simulated IBD pairs.

5.4.2.2 Spectral Shape Comparison

For the spectral analyses in section 7.2, the spectral shape of a reactor if it was at a given distance needs to be modelled. To do this, a simplified version of the model used to generate the spectra of known reactors is used.

The antineutrino emission is simplified to

$$\phi(E_{\bar{\nu}}) = \sum_i f_i \lambda_i(E_{\bar{\nu}}), \tag{5.2}$$

where f_i is the fission fraction for the i-th isotope and $\lambda_i(E_{\bar{\nu}})$ is given by Equation 1.18. The cross section is taken as

$$\sigma(E_e) = p_e E_e, \tag{5.3}$$

where E_e and $p_e = \sqrt{E_e^2 - m_e^2}$ are the positron energy and momentum respectively, and m_e is the positron mass. The total detectable spectrum is then given by

$$f(E_{\bar{\nu}}|L) = \phi(E_{\bar{\nu}})\sigma(E_{\bar{\nu}})P(L, E_{\bar{\nu}}), \tag{5.4}$$

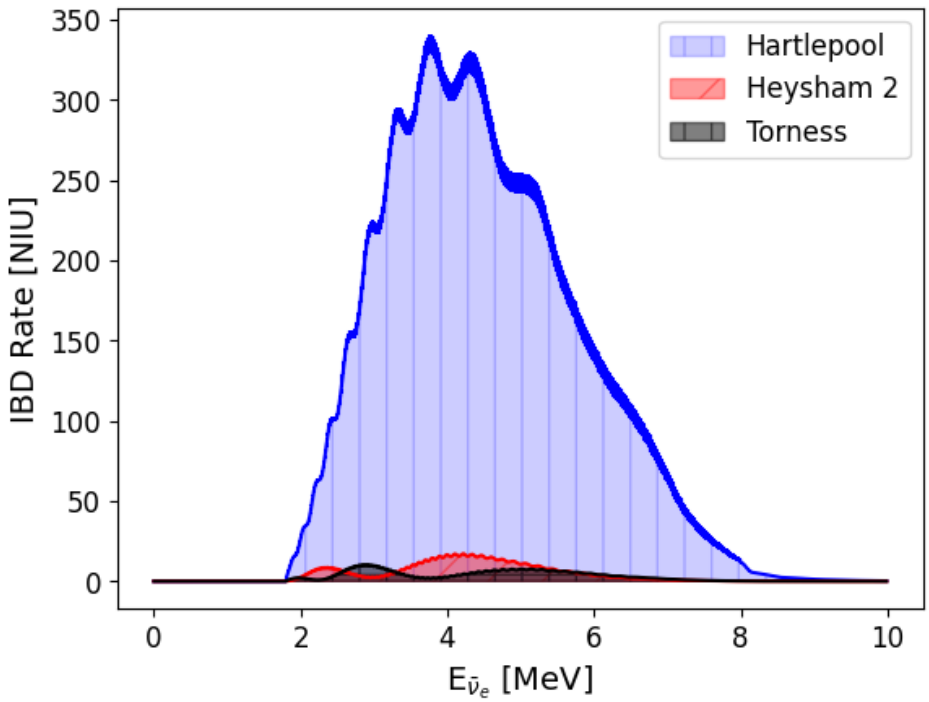

Figure 5.10: The antineutrino spectra at Boulby for Hartlepool (26 km), Heysham 2 (149 km) and Torness (187 km). Data from [179].

where $P(L, E_{\bar{\nu}})$ is the survival probability of electron antineutrinos of energy E travelling distance L (Equation 1.12), and the other terms are as defined in Equation 5.2 and Equation 5.3. This spectrum is then normalised to yield the spectral shape for a reactor at distance L.

5.4.3 Backgrounds

There are several background sources for reactor neutrino detection. Due to the coincident pair nature of IBD, the backgrounds of most concern are the ones that are also coincident pairs. However, uncorrelated single particle interactions can also cause accidental coincidences which mimic the pair signal. Some backgrounds are also omitted due to having negligible rates in the detector once reconstruction and analysis cuts are applied. One such case is spontaneous fission of ^{238}U and ^{232}Th in the detector. When the rejection of instances of more than two interactions is performed, the rate of accepted triggers drops to $\mathcal{O}(2)$ per year [336]. Raw rates for the key background components are in Table 5.3.

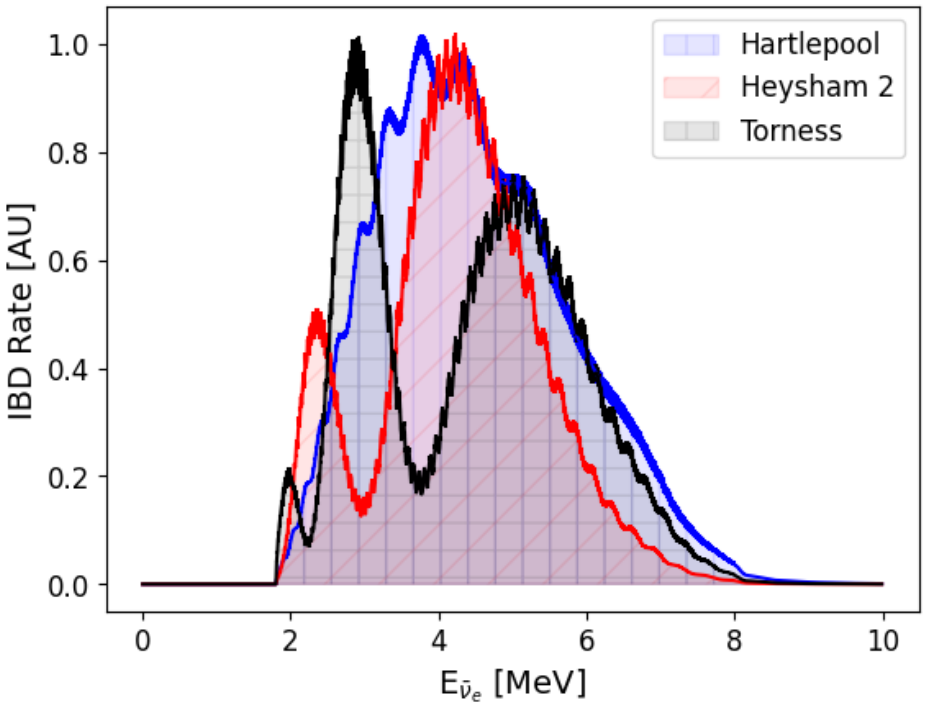

Figure 5.11: The antineutrino spectra at Boulby for Hartlepool (26 km), Heysham 2 (149 km) and Torness (187 km) normalised to show the effect of neutrino oscillations. Data from [179].

5.4.3.1 Uncorrelated Single Particles

By far the most numerous interaction type in the detector is single particle interactions from natural radioactivity in the materials in the detector and its environment. These interactions are physically independent of each other, but if they occur in proximity to each other, they can mimic a correlated event pair.

As these particles are produced by natural radioactivity, their rate depends on the composition and cleanliness of the detector, support structures and cavern. Whether these particles trigger the detector and are reconstructed depends on the detector's energy threshold, vertex position and resolution, and the distance of the fiducial volume to the detector walls and cavern. Due to this, not all particle sources are simulated. Only those that have sufficient energy and half-life, and therefore can physically trigger the detector, are simulated. The background rates due to radioactivity are determined by a combination of data and manufacturer specifications [233, 303, 305, 337–348]. Previous experiments, such as ZEPLIN and DRIFT, have been used to determine rates

Component	Pair Rate [Hz]
^{17}N β-n	1.99×10^{-5}
^{9}Li β-n	3.25×10^{-5}
Reactor IBD	1.47×10^{-5}
Geoneutrino IBD	2.60×10^{-6}
	Single Rate [Hz]
Fast neutrons	3.22×10^{-2}
Uncorrelated single β	3.57×10^{7}

Table 5.3: The raw background rates in the 22 m NEO design. The reactor IBD is for all reactors further away than Gravelines.

at Boulby alongside material assays performed at Boulby [341, 349].

The largest contribution to the uncorrelated background is the PMT glass, with the ^{238}U and ^{232}Th decay chains being the main source of activity. This contribution can be mitigated by using low-radioactivity glass, such as on the Hamamatsu R7081-100 PMTs described in section 4.3 to be used in NEO. The rates in Table 5.3 assume low-radioactivity glass is used. The contribution to the background from the PMT glass would increase from $\sim 10^4$ to $\sim 10^5$ Bq if standard borosilicate glass was used. Fiducial cuts can also significantly reduce the rate of triggers coming from PMT glass, as they tend to trigger in the volume nearest the PSUP. Steel in the tank and PSUP contains ^{60}Co and ^{137}Cs, both of which will β decay and produce γ radiation. This can also be suppressed by fiducial volume cuts, the effect of which are seen in Figure 5.12.

Not all uncorrelated backgrounds occur near the edge of the detector or the PSUP. Radon, part of the ^{238}U decay chain, is a gas and can be supported in the water. This causes it to circulate and reach throughout the detector. Despite the ultra-low radon levels of 3 Bq m^{-3} in Boulby Mine, radon can still be produced in the ^{238}U decay chain in the PMT glass. The rate of radon diffusion from PMT glass to water is not well known. This makes the radon background complex to understand and handle. There is also a natural ^{40}K component found in water which is hard to remove, even through purification.

Although there is a large number of uncorrelated backgrounds from a variety of sources, not all need to be considered in detail. Many backgrounds do not trigger a detector response, and many do not have a large enough rate to be observable in NEO.

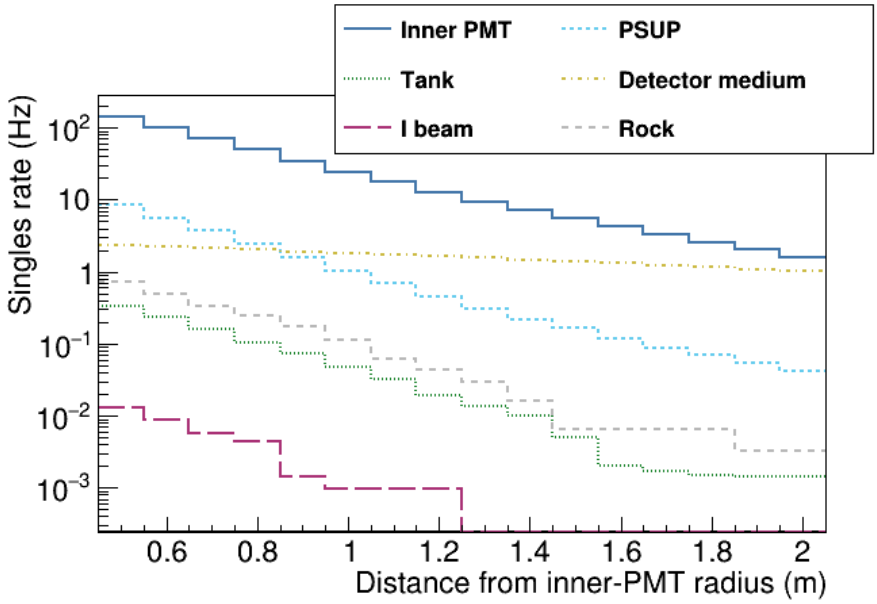

Figure 5.12: Rate of triggers due to uncorrelated single interactions from radioactivity against the distance from the PSUP in the ID after vertex reconstruction and a 10 PMT hit threshold. Moving away from the edge of the detector causes the background rates to drop off significantly except for those in the fill medium such as radon. Reprinted from [350].

Isotopes where the beta decay endpoint is $< 0.5\,\text{MeV}$ are neglected from simulations as they will not produce a signal. Decays where the branching ratio is $< 0.1\,\%$ are also neglected. The DAQ trigger will naturally suppress many interaction types. The DAQ requires 6 PMT hits within 200 ns, so many low energy particles or interactions near the edge of the ID will not trigger the detector.

Alpha decays can also be neglected. In water, α particles will not produce Cherenkov radiation as they are not relativistic. In scintillator, the effect of ionisation quenching means that very little light is produced as a result of the α particle. These particles are unable to propagate very far, so will only trigger near the location they are produced. This means they interact near the PSUP or detector walls, and would either fail to produce enough PMT hits to trigger the DAQ or be easily removed by fiducialisation.

To simulate the large number of uncorrelated components, they are combined into a single simulation with their respective rates interleaved. The total rate from each contributor to the single interaction background in the 22 m design is given in Table 5.4;

Component/ Decay chain	Rate [Bq]	Source
^{40}K	1.37×10^5	Liquid, PMT, PSUP, Tank, I-beam, Rock
^{238}U	3.16×10^7	Liquid, PMT, PSUP, Tank, I-beam, Rock
^{232}Th	3.67×10^6	Liquid, PMT, PSUP, Tank, I-beam, Rock
^{235}U	3.15×10^4	Liquid, PSUP, Tank, I-beam
^{60}Co	1.17×10^5	PSUP, Tank, I-beam
^{137}Cs	1.23×10^5	PSUP, Tank, I-beam

Table 5.4: Contributions to the uncorrelated single β rate in the 22 m NEO design.

each component can originate from multiple locations within the detector and its environment. The liquid is the smallest contributor to the rate of radioactivity, with $\mathcal{O}(10)$ Bq per decay chain. The PSUP contributes $\mathcal{O}(10^3)$ Bq per decay chain, with the tank and I-beams producing $\mathcal{O}(10^4)$ Bq per decay chain. The rock dominates the total rate, at $\mathcal{O}(10^6)$ Bq, but these particles very rarely reach and trigger the detector. Interleaving the different contributions allows a single output with uncorrelated particles having a realistic time and position distribution.

5.4.3.2 Cosmogenic Muons

As stated in section 5.2, muons are a significant source of background and the reason that the AIT facility and NEO detector would be located underground in Boulby Mine. The muons themselves are easily rejected owing to the fact they are through-going and leave a clear track inside the detector.

However, muons produce backgrounds that are significantly harder to reject. Muons can interact with the rock surrounding the detector and the detector materials, producing secondary products through spallation. These secondary particles can be produced in multiplicity, forming coincident event pairs, or decay via β-neutron emission. These backgrounds can also propagate or be long-lived, so a time veto after a muon track is not always sufficient. An outer detector, whether passive as with NEO or active like SK, can mitigate and reject some of these backgrounds.

The average muon energy in Boulby Mine is 264 GeV [305]. Lower energy muons will not reach as deep into the rock, leaving a high energy muon flux. SK, at Kamioka with its lower m.w.e depth, has an average energy of 259 GeV [351]. The total muon

flux in Boulby Mine is [303]

$$\Phi_\mu = (4.09 \pm 0.15) \times 10^{-8}\,\mathrm{cm}^{-2}\,\mathrm{s}^{-1}.$$

5.4.3.3 Fast Neutrons

Fast neutrons are energetic neutrons produced when muons interact in the rock in the cavern wall. They are able to propagate into the detector and through successive spallation and neutron evaporation interactions, in which a nucleus de-excites and emits a neutron, produce further neutrons. Neutrons from the rock with energy less than 10 MeV are not penetrating enough to cross the air gap between the detector wall and rock and cross the OD to trigger in the ID; these lower energy neutrons are neglected as a result.

The spectral flux of neutrons is defined as [346]

$$\frac{dN}{dE_n} = A\left(\frac{e^{-7E_n}}{E_n} + B(E_\mu)e^{-2E_n}\right), \tag{5.5}$$

where A is a normalisation constant, E_n is the neutron energy, E_μ is the muon energy and $B(E_\mu) = 0.52 - 0.58e^{-0.0099E_\mu}$ as determined from FLUKA simulations. The muogenic neutron spectrum is also defined in [305]. The spectral flux for neutrons produced by 264 GeV muons at Boulby is shown in Figure 5.13 with the average energy of these neutrons being 88 GeV. The flux at the cavern wall above 10 MeV is calculated through a combination of experimental data and simulation as [305]

$$\Phi_n(> 10\text{ MeV}) = 1.11\ \times\ 10^{-9}\,\mathrm{cm}^{-2}\,\mathrm{s}^{-1}\ \times\ \text{cavern surface area}.$$

There is a 27 % uncertainty on this flux due to the uncertainty on the muon flux and neutron production rates. Neutron backgrounds from the rock at Boulby have been measured previously, such as in [352] where a rate of $(1.72 \pm 0.61(\mathrm{stat.}) \pm 0.38(\mathrm{sys.})) \times 10^{-6}\,\mathrm{cm}^{-2}\,\mathrm{s}^{-1}$ above 0.5 MeV was determined. This study included radioactive decays in the rock. The muogenic-only neutron flux in [305] agrees with the one in [353].

The direction of the primary neutrons, direct from the muon interaction, is dictated by the muon direction. Muons originating from cosmic rays are strongly biased in the downward direction at the high energies required to penetrate down to the AIT cavern location. The muon angular distribution at Earth's surface is described in [347], and the attenuation of muons as they propagate through the Earth is dependent on the

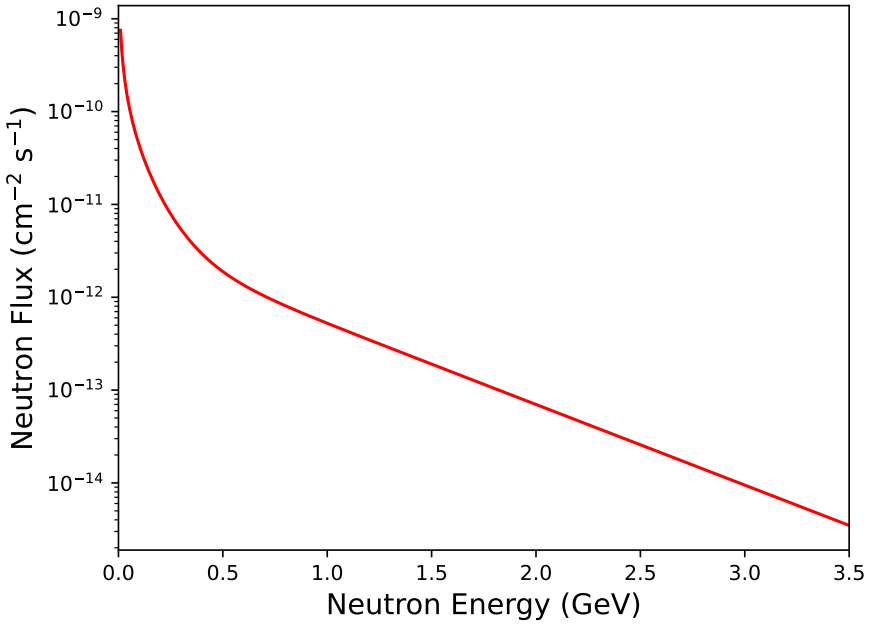

Figure 5.13: Neutron spectral flux for 264 GeV muons at Boulby using Equation 5.5.

angle. The neutron angular distribution is described as [305]

$$\frac{dN}{d\cos(\theta)} = \frac{A_\theta}{(1-\cos(\theta))^{B_\theta(E_\mu)} + C_\theta(E_\mu)}. \tag{5.6}$$

Here, A_θ is a constant, $B_\theta(E_\mu) = 0.482E_\mu^{0.045}$ and $C_\theta(E_\mu) = 0.832E_\mu^{-0.0152}$ as determined from FLUKA simulations. The primary neutron distribution is peaked parallel to the muon direction. The secondary neutrons from evaporation are emitted isotropically, which creates a flattening effect in the neutron angular distribution. This can be seen in Figure 5.14 for neutrons from 264 GeV muons. The primary neutrons tend to be easily rejected due to the high energy and direction, but secondary neutrons are more difficult.

The number of neutrons produced by a muon depends on the muon energy when it interacts and the material it interacts in. This also depends on the depth of the cavern as more energetic muons will reach deeper underground. The multiplicity in the rock at Boulby can reach as high as 100 neutrons, but is generally much lower with an average of 6.03 per muon in an assumed rock density of 2.7 g cm^{-3} [305]. The multiplicity is [346]

$$\frac{dN}{dM} = A_M(e^{-B_M(E_\mu)M} + C_M(E_\mu)e^{-D_M(E_\mu)M}), \tag{5.7}$$

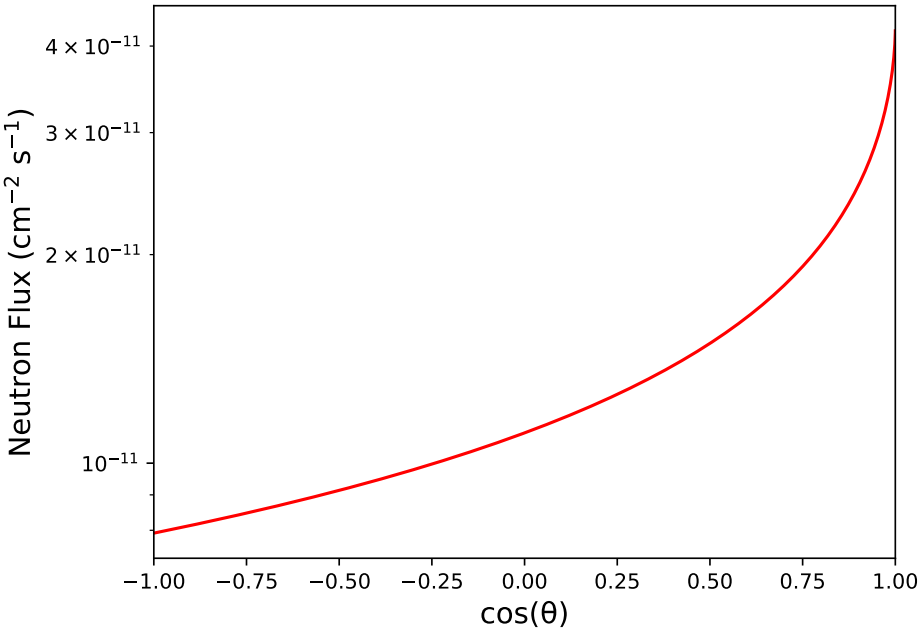

Figure 5.14: Neutron angular distribution for 264 GeV muons at Boulby using Equation 5.6.

where A_M is a normalisation constant, $B_M(E_\mu) = 0.321E_\mu^{-0.247}$, $C_M(E_\mu) = 318.1e^{-0.01421E_\mu}$ and $D_M(E_\mu) = 2.02e^{-0.006959E_\mu}$ as determined from FLUKA simulations [305]. As these neutrons are produced in multiplicity, they can create event pairs. The flux versus multiplicity for 264 GeV muons is shown in Figure 5.15. The mean time between these neutron interactions is 20 µs and the mean distance is ∼80 cm, which is similar to IBD. This can be seen in Figure 5.16.

There are several methods to suppress the fast neutron flux. A buffer region to attenuate neutrons in the OD, potentially combined with an active veto, can reduce the flux of neutrons that trigger the ID. This is by either stopping them reaching the ID or by vetoing them if they trigger an active OD. The design of NEO described in subsection 5.3.3 relies on a passive OD to attenuate backgrounds. Rejecting neutrons in high multiplicity groups can also suppress the fast neutron background, allowing only triggers with a multiplicity of two or less to be counted. Applying a time veto after high-energy triggers will reduce the number of products of these interactions that trigger the detector. The light profile of neutrons in water differs from that of positrons. The isotropic nature of neutron capture light can potentially be distinguished from directional Cherenkov radiation produced by positrons.

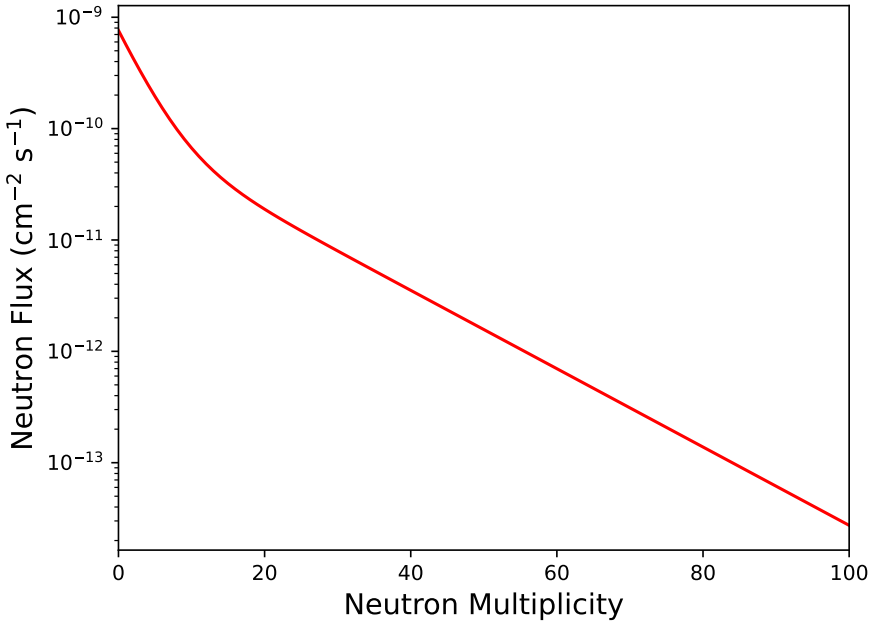

Figure 5.15: Neutron multiplicity for 264 GeV muons at Boulby using Equation 5.7.

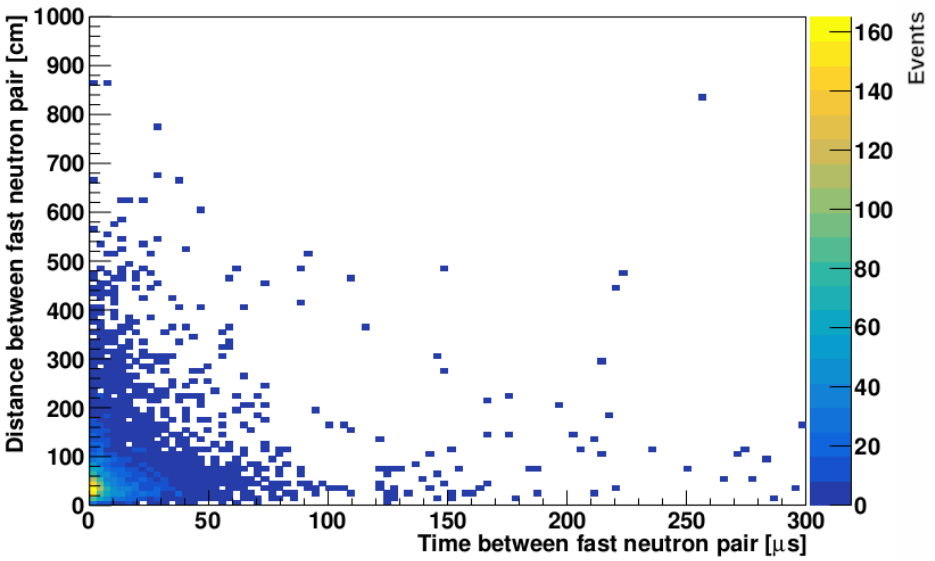

Figure 5.16: The time and position distribution of simulated fast neutrons.

5.4.3.4 β-Neutron Emitting Radionuclides

Alongside fast neutrons, cosmic ray muons can also produce radionuclides through successive spallations. These spallations generate hadronic and EM showers, with the hadronic showers being the principle production mechanism for long-lived radioisotopes. Only 11 % of these radioisotopes were found to be produced directly by muon spallation, and 4 % by throughgoing muons, in SK [342]. These isotopes are unstable and decay, producing the radionuclide background. The isotopes of most concern for NEO are the β-neutron emitters, which produce a near identical signal to the positron-neutron emission from IBD. The β particle will produce prompt Cherenkov radiation or scintillation, and the neutron will capture to produce the delayed capture signal.

In water, the spallation occurs predominantly on oxygen regardless of the inclusion of gadolinium or in the form of WbLS. The radionuclides of concern produced by this are ^{17}N and ^{9}Li, as they both have high yields and β-n branching ratios. The spallation products from oxygen are shown in Table 5.5. In simulations, ^{16}C and ^{11}Li are neglected due to their low yields. Measurements of the ^{8}He β-n yield in SK were consistent with zero, and a 90 % upper confidence limit of $0.9 \times 10^{-7}\,\mu^{-1}\,\mathrm{g}^{-1}\,\mathrm{cm}^2$ was adopted [340]. Therefore, ^{8}He is also neglected.

The β-n decay rates are calculated using

$$R_{\mathrm{iso}}(\mathrm{s}^{-1}) = R_{\mu}(\mathrm{s}^{-1}) \times L_{\mu}(\mathrm{cm}) \times Y_{\mathrm{iso}}(\mu^{-1}\,\mathrm{g}^{-1}\,\mathrm{cm}^2) \times br \times \rho(\mathrm{g\,cm}^{-3}) \times \left(\frac{E_{\mu,\mathrm{Boulby}}}{E_{\mu,\mathrm{Super-Kamiokande}}}\right)^{\alpha}, \quad (5.8)$$

where $R_{\mu} = \Phi_{\mu}\times$ tank surface area, L_{μ} is the muon path length, Y_{iso} is the isotope yield, br is the branching ratio for the β-n decay, $\rho = 1\,\mathrm{g\,cm}^{-3}$ for water and E_{μ} is the average muon energy at the given location. The path length in [342] is taken as vertical height of the SK detector, making the assumption all muons are downward going, which sets a conservative upper limit. The same assumption is made for NEO, and rates are calculated for the full detector volume. A depth-related correction to the average muon energy E_{μ}^{α} is applied, where $\alpha = 0.73 \pm 0.10$ [305], as higher-energy muons will survive to greater depths on average.

There are two options for the isotope yield for ^{9}Li, theoretical and experimental values. The measured yield in SK was found to be $0.50 \times 10^{-7}\,\mu^{-1}\,\mathrm{g}^{-1}\,\mathrm{cm}^2$ with neutron tagging and $0.51 \times 10^{-7}\,\mu^{-1}\,\mathrm{g}^{-1}\,\mathrm{cm}^2$ without [340], with an 18.1 % systematic uncertainty. This is approximately a factor of four lower than the theoretical value in Ta-

Isotope (β-n br)	Half life (s)	Total yield ($10^{-7}\,\mu^{-1}\,\mathrm{g}^{-1}\,\mathrm{cm}^2$)	Production process	β endpoints (MeV)
^{17}N	4.173	0.59	^{18}O(n,n+p)	3.3 (50%), 4.1 (38%)
^{16}C	0.747	0.02	^{18}O(π^-,n+p)	4.7 (84%), 3.7 (16%)
^{11}Li (85%)	0.0085	0.01	^{16}O(π^+,5p+π^++π^0)	16.6 (22%), 12.5 (16%)
^{9}Li (50.8%)	0.178	1.9	^{16}O(π^-,α+2p+n)	11.2 (29%), 10.8 (12%)
^{8}He (16%)	0.119	0.23	^{16}O(π^-,3H+4p+n)	5.3 (8%), 7.5 (8%)

Table 5.5: β-neutron backgrounds. Isotope yields in water calculated with FLUKA [342] for SK. Principal β endpoint energies with approximate branching ratios taken from [343–345].

ble 5.5. The cause of this was proposed as the spallation of ^{16}O ejecting many nucleons. This is supported by the large disparity also being visible in the ^{8}Li/^{8}B yields. All other values are within 2σ of the theoretical values. To use the experimental yield in NEO, the difference in the average muon energy between Kamioka and Boulby would need to be corrected for. The difference between the experimental and theoretical yields would also need to be incorporated into the systematic uncertainties, creating an uncertainty on the ^{9}Li rate given by

$$\frac{\sigma_{R_{\mathrm{iso}}}}{R_{\mathrm{iso}}} = \sqrt{\frac{\sigma^2_{Y_{\mathrm{iso}}}}{Y_{\mathrm{iso}}} + \frac{\sigma^2_{E^{\alpha}_{\mu}}}{E^{\alpha}_{\mu}}}. \tag{5.9}$$

The uncertainty on the yield is

$$\sigma_{Y_{\mathrm{iso}}} = \frac{|Y_{\mathrm{theor}} - Y_{\mathrm{exp}}|}{Y_{\mathrm{theor}}}. \tag{5.10}$$

The uncertainty on the muon flux is not required as no assumption on the muon flux is made in the experimental measurements. The 18.1 % systematic uncertainty on the SK measurement would become a minimum uncertainty in NEO.

The theoretical yield can be used as a more conservative approach due to the higher yields. The uncertainty on the theoretical yield is given by

$$\frac{\sigma_{R_{\mathrm{iso}}}}{R_{\mathrm{iso}}} = \sqrt{\frac{\sigma^2_{\Phi_{\mu}}}{\Phi_{\mu}} + \frac{\sigma^2_{E^{\alpha}_{\mu}}}{E^{\alpha}_{\mu}}}, \tag{5.11}$$

where $\sigma_{\Phi_{\mu}} = 0.15 \times 10^{-8}\,\mathrm{cm}^{-2}\,\mathrm{s}^{-1}$ is the uncertainty on the muon flux. The uncertainty on the energy dependence is

$$\sigma_{E^{\alpha}_{\mu}} = \sqrt{(E^{\alpha}_{\mu}\ln(E_{\mu})\sigma_{\alpha})^2 + (\alpha E_{\mu}\sigma_{E_{\mu}})^2}. \tag{5.12}$$

The average muon energy uncertainty σ_{E_μ} is due to uncertainties on the atmospheric muon energy spectrum and the muon energy loss in the rock, which is not highly correlated with rock composition and precise depth [303]. It is assumed to be negligible in simulations for NEO. The systematic uncertainty on the theoretical yield of ^{9}Li is very low, $< 1\,\%$.

The theoretical radionuclide yields with low uncertainties represent a more cautious approach than using the experimental values, which are a factor of four lower, with higher uncertainties. This cautious theoretical approach has been adopted in NEO.

The rates in NEO do not account for the difference in muon energy loss in the detector between SK and NEO. This is assumed to be negligible due to the energy loss being small compared to the muon energy, so the interaction cross sections do not change by a significant amount in the detector.

The spectra of the key β-n emitters in NEO, ^{9}Li and ^{17}N, simulated in a 22 m detector according their theoretical rates are shown in Figure 5.17.

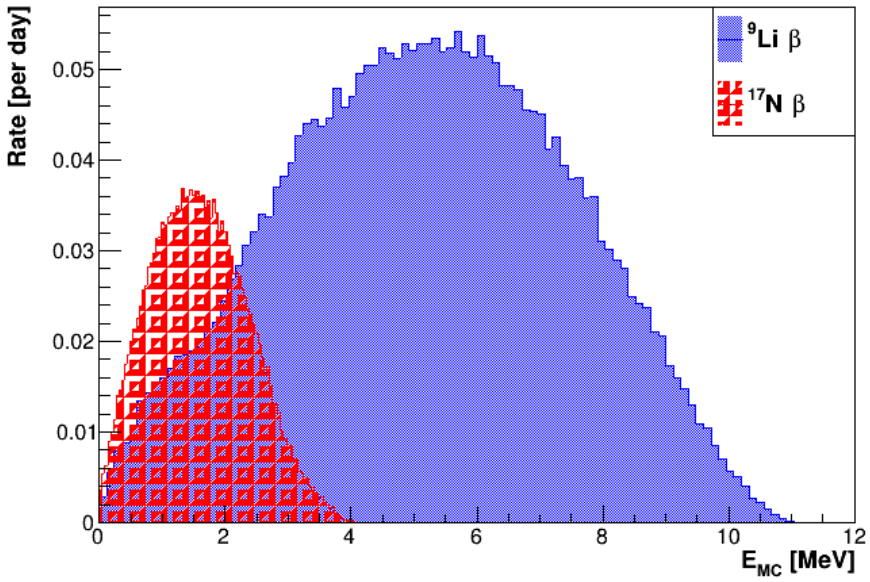

Figure 5.17: Simulated spectra of ^{17}N and ^{9}Li β particles in NEO.

To suppress radionuclides, correlating the interactions to a muon track can allow the rejection of some by applying a time veto. Long-lived isotopes may survive a time veto, but effective tracking allows a transverse distance cut to the muon track without extending the detector dead time. Locating the hadronic showers that produce the

radionuclides can also allow radionuclide interactions to be identified and rejected.

5.4.3.5 IBD Backgrounds

Some background sources produce IBD, which makes them nearly indistinguishable from reactor antineutrinos. One source is geological electron antineutrinos, or geoneutrinos, which come from the beta decays in the ^{238}U and ^{232}Th chains and of ^{40}K in the Earth's crust and mantle.

The spectra of the geoneutrino components used in NEO are from [179], and are determined by summing the contribution of each decay in the chains weighted by their branching ratios. The expected IBD rate due to geoneutrinos in NEO comes from integrating the product of the differential geoneutrino flux, IBD cross section, geoneutrino energy spectrum and electron antineutrino survival probability. The geoneutrino flux at the surface is pre-calculated and adjusted for variations in the density of the mantle and isotope abundance.

Geoneutrinos are generally very low energy, and as such many will not meet the IBD threshold. For a 0.6 MeV positron energy threshold, 76 % of the total geoneutrino flux can contribute; for a 1 MeV positron energy threshold, 43 % of the total geoneutrino flux can contribute. In both cases, the contribution to the geoneutrino flux above threshold is entirely from the ^{238}U decay chain. The rate is also low, with a total rate approximately an order of magnitude lower than Heysham 2, and so they are a subdominant background. Although it is possible for potassium to capture an electron and form argon, which emits mono-energetic geoneutrinos, these are neglected for NEO due to the low β endpoint energy of 1.5 MeV and branching ratio of 11 %.

Reactors that are not the target of observation provide a significant background, especially when the target reactor is a weaker signal. The signals from different reactors are nearly indistinguishable, with only changes to the antineutrino spectra due to oscillations causing any differences. The major way to handle this background is by having knowledge of the expected IBD rate and looking for an excess due to the target reactor.

The background due to reactors is split into individual components for the nearest reactors to Boulby, detailed in Table 5.1, and an amalgamated world reactor background for all others. The reactor and geoneutrino backgrounds at Boulby with the Heysham 2 cores as the target of observation are shown in Figure 5.18.

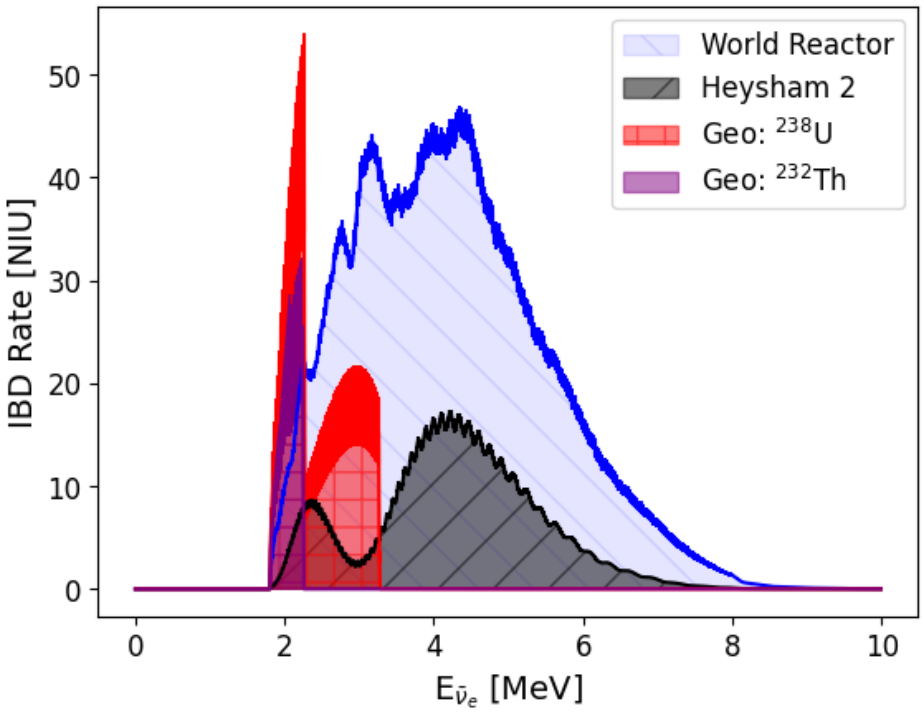

Figure 5.18: The antineutrino spectra for the Heysham 2 cores and IBD backgrounds. Data from [179].

5.4.4 Systematic Uncertainties on Signal and Background

The uncertainties on signal and background components used for simulation studies are displayed in Table 5.6. The uncertainty on uncorrelated backgrounds due to radioactivity is assumed to be negligible.

5.5 Summary

A prototype detector, Neutrino Experiment One (NEO), has been designed to monitor reactor antineutrinos for non-proliferation purposes. The design options include a 16 m height and diameter upright cylinder and a 22 m height and diameter upright cylinder, with a gadolonium-doped water-based fill medium and 15 % PMT coverage. Two fill media are considered, alongside the gadolinium doping: pure water and WbLS.

To suppress backgrounds, the detector will be located underground in Boulby Mine. This gives a very low radon rate of $< 3\,\mathrm{Bq\,m^{-3}}$ and cosmic ray muon attenuation of $\mathcal{O}(10^6)$. The location is also in proximity to the UK's reactor fleet, allowing various

Component	Uncertainty
Hartlepool	2.5 %
Heysham	2.0 %
Torness	2.6 %
Sizewell B	2.75 %
Hinkley Point C	3.0 %
Gravelines	3.4 %
World Reactor	6.0 %
Geoneutrinos	25 %
^{9}Li	0.2 %
^{17}N	0.2 %
Fast Neutrons	27 %

Table 5.6: Uncertainties on signals and backgrounds. Data taken from [5, 179, 305].

combinations of signal and background tests to be performed.

The detector has been simulated, along with its signal and background components, in detail via MC simulations in RAT-PAC. RAT-PAC uses classes and libraries from the GLG4sim package, as well as libraries and tools from CLHEP and Geant4, to produce an interaction-by-interaction detector response simulation. The signal and background components have been modelled using combinations of experimental data and theory, with conservative options chosen where possible and time-saving assumptions where appropriate. These simulations can be used to determine the performance of the detector designs with respect to the observation of the various reactors.

Chapter 6

Event Reconstruction and Data Reduction

The signal in a neutrino detector is in the form of PMT electrical output upon the detection of photons. In a real detector, with thousands of PMTs, there is a large amount of electrical noise and number of background particle interactions mixed in with the signal. This gives a lot of PMT hits that need to be handled and backgrounds that need to be rejected, and poses a significant challenge to the observation of a particular signal.

To overcome this challenge, the positions of the interaction vertices in a detector are reconstructed based on the PMT hit patterns and timing, producing information on the origin of each hit. This allows noise to be removed, as it is likely to only produce single PMT pulses with no interaction vertex that can be reconstructed. The PMT hits can also be used to reconstruct the energy of a detected particle based on the amount of light collected. This can be done via the number of PMTs hit for a given reconstructed interaction or the amount of charge collected by the PMTs.

Once triggers in the detector are reconstructed to locate the interaction vertices, data reduction is applied to reject backgrounds and extract potential signal events. This allows particle interactions that are not of interest to be separated from those that are. This, in combination with vertex and energy reconstruction, is designed to efficiently select out signal events.

In the case of NEO, the signal event is a positron and neutron pair from IBD. The majority of particle interactions in a neutrino detector are not reactor neutrinos, or neutrinos at all. They come from a combination of sources, of which the key ones

are described in subsection 5.4.3, and comprise many particle interaction types. To observe reactor antineutrinos, the background must be suppressed sufficiently through data reduction.

This chapter first reviews traditional vertex fitting, energy reconstruction and triggering algorithms, before exploring a new data reduction method using a combination of likelihoods and machine learning. The algorithms reviewed are in the context of simulations of NEO described in section 5.4, and use real time triggering based on estimating the data rates produced in the NEO detector.

6.1 Event Reconstruction

Detector data, in the form of signals from the PMTs, needs to be processed and reconstructed to allow useful information to be extracted. Reconstruction makes use of the timing distribution of the detected light and the pattern it makes across the PMTs on the detector wall. For NEO, the response is simulated so that the MC output replicates the expected response of a real NEO detector, including all known detector effects such as PMT charge and timing response, dark noise and radioactive backgrounds. The reconstruction can then be applied to the simulated data in the same way it can to observed data.

6.1.1 Vertex Reconstruction

The vertex reconstruction applied to the simulated data is an adapted version of the Branch Optimization Navigating Successive Annealing Iterations (BONSAI) algorithm, the low-energy (up to ∼100 MeV) vertex reconstruction algorithm currently deployed by SK [354].

BONSAI is a time-based fitting algorithm that maximises a likelihood for PMT hit times. The likelihood is based on the hit time residuals of the signal and dark noise, and is given by

$$\ln \mathcal{L}(\mathbf{x}, t_0) = \ln(\prod_{i=1}^{N} P(\Delta t_i(\mathbf{x}))), \tag{6.1}$$

where $P(\Delta t_i(\mathbf{x}))$ is the PDF of time residuals from true vertices, $\mathbf{x}$ is the vertex position, t_0 is the emission time and $\Delta t_i(\mathbf{x})$ is the time residual for the hit at the i^{th} PMT such that

$$\Delta t_i(\mathbf{x}) = t_i - t_{\mathrm{tof},i} - t_0. \tag{6.2}$$

Here, t_i is the hit time at the i^{th} PMT and $t_{\text{tof},i} = |\mathbf{x}_i - \mathbf{x}|/c_{\text{water}}$ is the time of flight from the vertex to the i^{th} PMT.

Observed data has an inherent PMT dark noise contribution. As the simulated data does not, the dark noise is added in during reconstruction at a rate of 3 kHz. This is deemed to be a conservative value based on measurements of the Hamamatsu R7081 PMT's dark rate, such as those in chapter 4. Dark noise is added into the reconstruction by taking the window $t_i - t_{\text{tof},i}$ and scaling the rate of hits outside this window to its size.

The timing residual (Figure 6.1) contains effects from the detector, such as the PMT timing characteristics, the photocoverage, and the total scattering which depends on the detector medium and size. PMT timing characteristics dominate the shape of the distribution for hit-time residuals. The prompt signal peak is at 0 ns, with a double-pulsing peak at ∼50 ns and an after-pulsing peak at ∼70 ns. The key parameter affecting the reconstruction is the TTS of the PMT, which results in the width of the prompt peak.

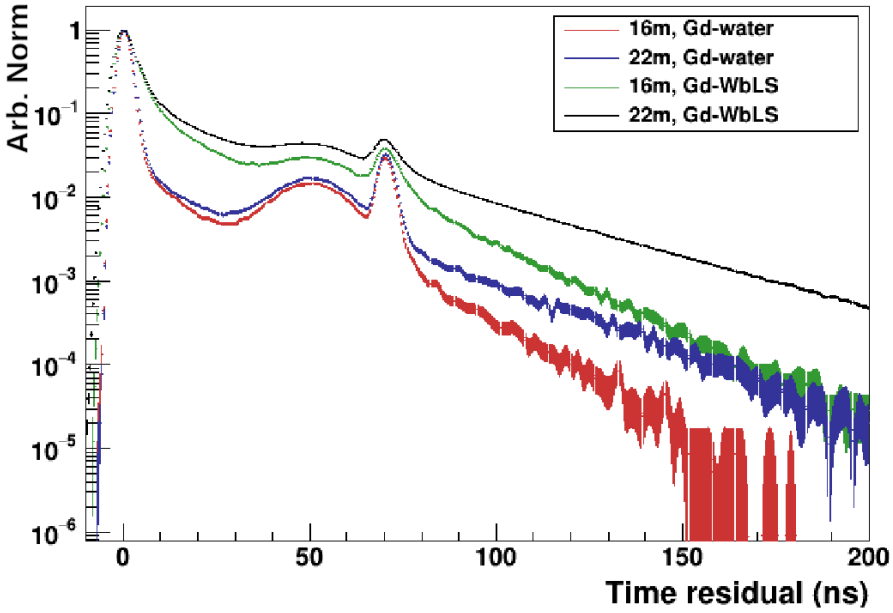

Figure 6.1: PDFs of the true hit-time residuals for the combinations of detector and media considered in subsection 5.3.3, normalised to a maximum of 1. Reprinted from [355].

Scattering of light has a large impact on the distribution. The tail is pushed out to

longer times, and the addition of scintillator causes the prompt peak to widen which means the double-pulsing and prompt peaks are less well-defined. This is due to the absorption and re-emission in the scintillator. This is specific to the cocktail used, as the decay constant of different scintillator cocktails can differ by $\sim$5 ns, which is comparable to the photopeak width. BONSAI was developed for use in pure water for the SK detector, but is also capable of effectively reconstructing interaction vertices in liquid scintillator. The time profile differs due to the scintillation decay constant, seen in Figure 6.1, but the increase in light yield offsets the changes in the time profile.

There are several steps the reconstruction algorithm goes through to determine the vertex of an interaction, which are summarised as:

1. **List of PMT hits created** - This allows vertices that form the starting point of the likelihood maximisation to be created. A pair of PMT hits separated by time Δt must be sufficiently far apart that light could not travel directly between them in the same Δt to ensure that primarily unscattered light is used. This is so that the light used to generate the vertices could come from the same interaction.

2. **Hits grouped into fours** - At least four hits are required for reconstruction in three dimensions. These hits are required to have a hit-time residual of zero. Each group of four defines a point in the detector and allows a list of initial test vertices to be created. If only one starting point is used for the likelihood maximisation, the probability of local maxima affecting the result is increased.

3. **Number of hits reduced using variable time window** - This increases the speed of reconstruction as the number of quadruples of hits is proportional to the total number of hits to the fourth power (N^4). Groups with a small spread in time are given preference. The window is selected to contain a predetermined number of combinations, with all combinations in the window being maximised over. The three hits that immediately follow each hit in the window are taken to form more groups of four.

4. **Test vertices for all combinations averaged over nearby points** - The test vertices are evaluated and averaged over nearby points in 60 cm and 150 cm steps to reduce the number of starting points for the likelihood maximisation.

5. **The likelihood is maximised** - The determined starting vertices are used, and emission time and dark noise are free parameters.

6. **The vertices with the best log likelihoods in a range are taken to the next iteration** - This is done after each step in the likelihood maximisation, and the range is a fraction of the total range for all test vertices and is reduced each step. This reduces the chance of local maxima degrading the result, with the algorithm converging at the best vertex with each iteration.

7. **The vertex is the centre of a dodecahedron** - This occurs for each iteration, and allows the new test vertices for the next iteration to be defined as the vertices of this dodecahedron. The radius of the dodecahedron reduces with each step.

8. **The final vertex is selected** - The vertex with the maximum log likelihood is selected as the reconstructed vertex.

Although four hits are required to reconstruct position in three dimensions, in practice more are needed to allow the algorithm to converge on a single vertex. To ensure the algorithm is able to consistently and efficiently converge on a vertex, a minimum of nine digitised hits are required per trigger for reconstruction to be attempted. This improves the speed of reconstruction as triggers with few hits take longer to reconstruct, and will often result in either a poorly reconstructed vertex or a failure to reconstruct a vertex.

Reconstructing the interaction vertex is necessary for background discrimination. If several hits are observed as coming from a single point in the detector, it is far less likely to be a random dark noise coincidence than if individual PMT hits are observed. This also allows position constraints to be applied to observed interactions such that particles can be rejected based on their interaction point.

An adapted version of BONSAI to harness the neutron capture light when reconstructing IBD has been developed in [355]. This makes use of positron Cherenkov radiation and neutron capture emission as a pair to provide a stronger constraint on the interaction vertex of IBD. By using the large amount of light from the neutron capture to tag the positron during reconstruction, the efficiency and resolution of reconstruction can be improved, and the energy threshold lowered.

The first six Legendre polynomials, in terms of $\cos(\theta)$ where θ is the angle of the incident photon on the PMT, are used as an estimate of the isotropy of light in the Gd-H_2O fill. Cherenkov light is anisotropic, forming a cone, but neutron capture light is isotropic. The difference in the first Legendre polynomial for positrons from IBD and fast neutrons is shown in Figure 6.2.

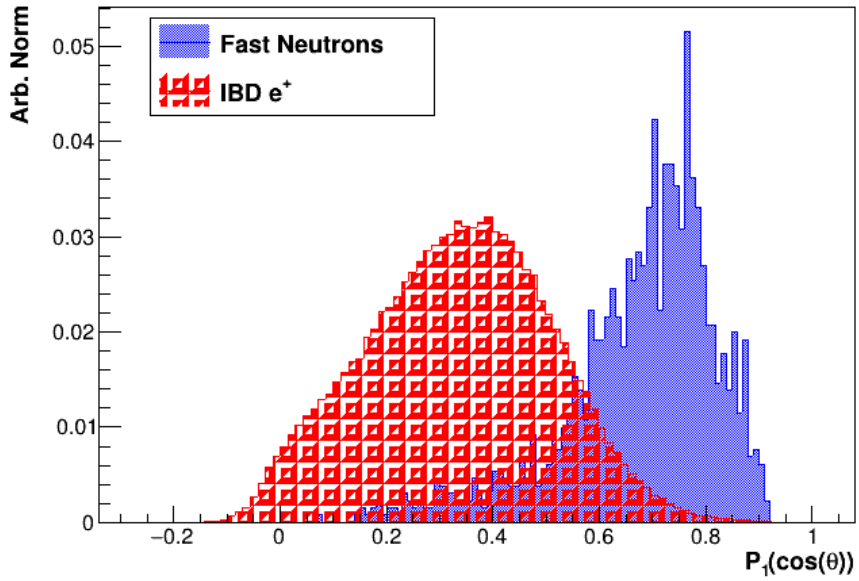

Figure 6.2: The first Legendre polynomial for IBD positrons and fast neutrons in the 22 m Gd-H_2O detector.

6.1.2 Energy Reconstruction

As stated in section 2.2, the amount of light produced by a charged particle in a medium relates to the energy of the particle. As such, the amount of light produced can be used to determine the energy of the particle.

There are multiple ways in which the energy can be determined based on the observed light. The number of PMT hits within a time window can be used, as can the collected charge from the observed particle. These are often used in tandem with calibration data, in which radioactive sources with known energies or an electron Linear Accelerator (LINAC) with a tuned energy output are used to compare particles of known energy with their light yield, and corrections for detector effects.

6.1.2.1 Energy Reconstruction in Super-Kamiokande

In SK, the energy response of the detector is calibrated using a LINAC to produce low energy electrons ($\sim$ 5 - 16 MeV) [356] and ^{16}N to produce 4.3 MeV electrons [263]. The energy of observed particles is reconstructed by taking the effective number of PMT hits in a 50 ns window from the interaction [100]. The effective number of hits, N_{eff}, is determined from the number of hits in a 50 ns window, N_{50}, with corrections applied

to account for various effects. The effective number of hits is defined as:

$$N_{\text{eff}} = \sum_{i}^{N_{50}} \{(X_i + \epsilon_{\text{tail}} - \epsilon_{\text{dark}}) \times \frac{N_{\text{all}}}{N_{\text{alive}}} \frac{1}{S(\theta_i, \phi_i)} \times \exp\left(\frac{r_i}{\lambda(t)}\right) \times G_i(t)\}. \tag{6.3}$$

The explanation for each component that determines N_{eff} is:

X_i: This provides an estimate of the effect of multiple photoelectrons for the i^{th} PMT hit. Interactions occuring close to the PMTs will have a Cherenkov cone that does not have sufficient space to expand, giving a small number of observed hits for the same overall light yield. X_i is defined as

$$X_i = \begin{cases} \frac{\log(\frac{1}{1-x_i})}{x_i}, & x_i < 1 \\ 3.0, & x_i = 1 \end{cases} \tag{6.4}$$

where x_i is the ratio of hit PMTs in a 3×3 PMT grid surrounding the i^{th} PMT to the total number of live PMTs in the grid. The log term is derived from Poisson statistics and is the estimated number of photons per PMT in the grid, and is based on the number of triggered PMTs in the grid. If every PMT in the grid is hit, it is assumed that the number of photons incident on the i^{th} PMT is 3.

ϵ_{tail}: Not all photons travel directly to a PMT; some are scattered and will therefore arrive later. This creates PMT hits outside of the 50 ns window. To account for this effect, ϵ_{tail} is applied.

$$\epsilon_{\text{tail}} = \frac{N_{100} - N_{50} - N_{\text{alive}} \times R_{\text{dark}} \times 50 \text{ ns}}{N_{50}} \tag{6.5}$$

uses the number of alive PMTs in the ID, N_{alive}, the number of PMT hits in a 100 ns window, N_{100}, and the measured dark rate for the data-taking period, R_{dark}, to define a correction for late-arriving photons.

ϵ_{dark}: The dark noise in the PMTs can have a large impact on the data, and is corrected using

$$\epsilon_{\text{dark}} = \frac{50 \text{ ns} \times N_{\text{alive}} \times R_{\text{dark}}}{N_{50}}. \tag{6.6}$$

$\frac{N_{\text{all}}}{N_{\text{alive}}}$: This accounts for the number of live PMTs in the data-taking run. The number of live PMTs is not constant across the detector lifetime due to factors such as electronics failures.

$\frac{1}{S(\theta_i,\phi_i)}$: This is a geometric factor determined by MC simulation, and checked with LINAC and Deuterium-Tritium (DT) neutron generator data. $S(\theta_i, \phi_i)$ is the effective

photocathode area of the i^{th} hit PMT as viewed from the angles (θ_i, ϕ_i). This accounts for shadowing of the PMT and glancing angles.

$\exp(\frac{r_i}{\lambda(t)})$: The water transparency will affect the way in which produced light is observed. This factor, in which r_i is the distance between the i^{th} PMT and the reconstructed vertex and $\lambda(t)$ is the measured water transparency for the data-taking period, accounts for the transparency.

$G_i(t)$: The relative quantum efficiency of the PMTs is adjusted as not all PMTs have an identical response.

A fit between true energy and N_{eff} obtained from MC simulation is used to reconstruct the particle energy. This method yields an energy resolution described by

$$\sigma(E) = -0.0839 + 0.349\sqrt{E} + 0.0397E$$

in SK-IV [357].

6.1.2.2 Energy Resolution of NEO

The energy resolution of NEO is determined entirely through simulation. As the NEO designs have different properties to the SK detector, a different energy reconstruction technique is applied. The Hamamatsu R7081-100 PMTs considered for NEO, described in chapter 4, are newer and have a better charge resolution than the 20" PMTs used in SK. To make the most of this, the energy reconstruction applied for NEO uses collected charge in place of the number of effective PMT hits method used in SK. The energy resolution is then compared to SK for a water fill as a performance benchmark.

To reconstruct the energy of an observed particle, a linear fit between the number of observed photoelectrons and true particle kinetic energy is used to convert between charge and energy. For a given distance between the reconstructed vertex and the PSUP, the relationship exhibits a strong linearity when only well constructed particles with a good residual are used. This is shown by Figure 6.3 for electrons at the centre of the tank.

The position of an interaction will impact the number of observed photoelectrons for a given energy. Particles far from the PSUP will generally appear in the same way, but as the interaction vertex approaches the PSUP, the probability of multiple photons hitting the same PMT increases. SK apply a correction based on the number of neighbouring PMTs that are hit. For the method used in NEO simulations, adjusting the fit to account for reconstructed vertex position allows this effect to be accounted

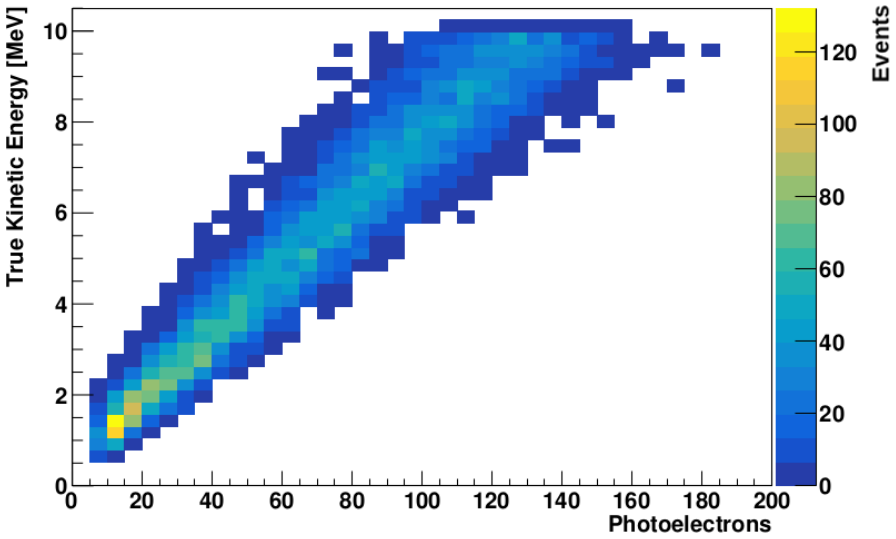

Figure 6.3: Detected photoelectrons versus true electron kinetic energy in the 22 m NEO tank with 15 % photocoverage and filled with Gd-WbLS.

for. This is useful when the fiducial volume of the detector is maximised and pushed close to the PSUP, but not required if the fiducial volume is constrained away from the edge of the ID.

To determine the resolution in a given energy range, a Gaussian fit is applied to the difference between the true and reconstructed energy. The standard deviation of the Gaussian fit ($\sigma(E)$) is the energy resolution. For easy comparison across energy scales, this is often quoted as a fractional resolution ($\sigma(E)/E$). This fit can be seen for electrons with kinetic energies between 4.9 and 5.1 MeV in the NEO 22 m design with 15 % photocoverage and a Gd-WbLS fill in Figure 6.4.

The energy resolution with varying energy is described by

$$\frac{\sigma(E)}{E} = \frac{a}{\sqrt{E}} + b + \frac{c}{E}, \tag{6.7}$$

where a, b and c are optimised constants. These constants are generally associated with different effects that move the energy resolution away from the ideal situation of $\sigma(E) \propto \sqrt{E}$. These include:

- a: stochastic fluctuations.
- b: detector imperfections, inhomogeneities in equipment and calibration, non-linearity of readout electronics.

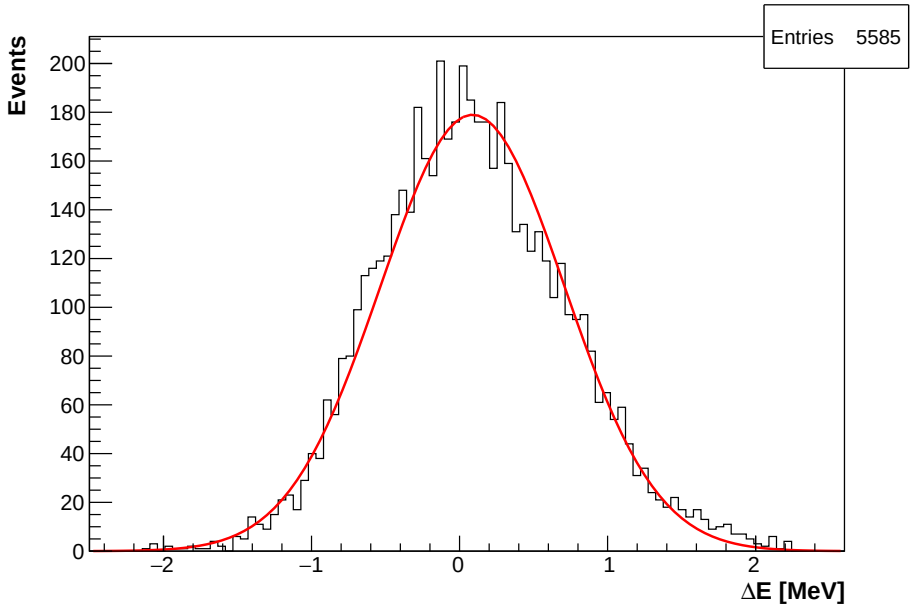

Figure 6.4: Reconstructed kinetic energy - true kinetic energy for ∼5 MeV electrons in the 22 m NEO tank with 15 % photocoverage and filled with Gd-WbLS. The Gaussian fit is used to determine the resolution, with a width of 0.62 MeV giving a resolution of 12.4 %.

- c: noise in detector and readout electronics.

The energy resolution of reconstructed electrons in the NEO 22 m design is compared to SK in Figure 6.5. The addition of increasing concentrations of scintillator offers an improvement in energy resolution due to the higher light yield. The charge-based method of energy reconstruction in NEO offers a better energy resolution here than SK above the 3 MeV threshold SK employs. The sharp reduction in energy resolution below 3 MeV for Gd-water in NEO is not an improvement, but an artefact of the lower energy particles being harder to reconstruct. A lower energy particle will produce less light and therefore less PMT hits. Only particles with a sufficient signal to reconstruct the vertex will be successfully reconstructed, other particles will not produce enough light or a usable PMT hit pattern. As such, only the well reconstructed vertices with a good resolution are kept. This means that whilst the energy resolution appears to be very good, the efficiency is very low and no useful signal can be extracted in this region to discriminate from backgrounds. SK is able to make use of calibration and validation against real detector data to produce a validated model across the entire

energy range. The scintillator's lower energy threshold and higher light yield makes vertex reconstruction more robust down to sub-MeV energies.

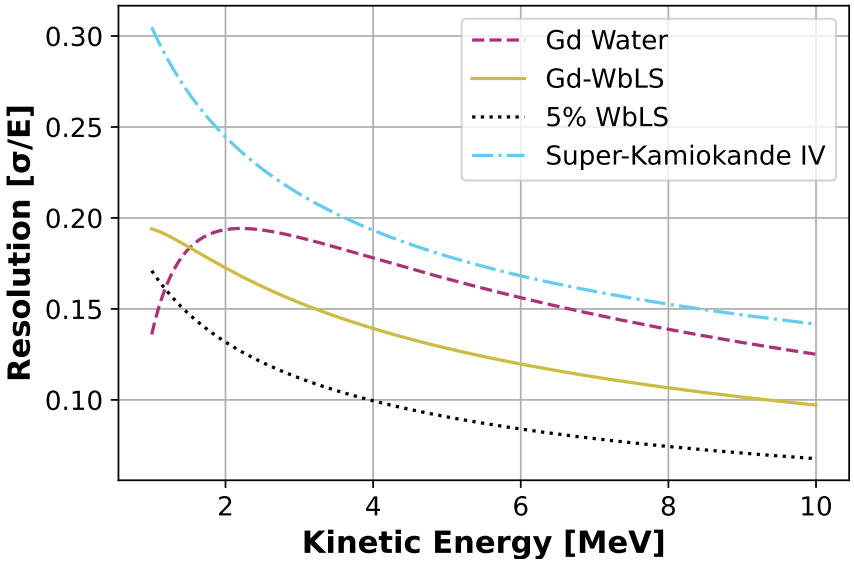

Figure 6.5: Energy resolution for electrons in the 22 m NEO tank design with 15 % photocoverage. The Gd-WbLS cocktail used is approximately equivalent to a 1 % scintillator concentration with a 100 photons/MeV light yield. The SK-IV resolution is from [357].

The key factor dictating the energy resolution of a detector is the light collected per MeV. A higher light yield, such as a scintillator, will produce more light that can be collected, and a higher PMT coverage will allow more light to be collected. A 20 % PMT coverage offers an approximately 2 % improvement in $\sigma(E)/E$ for the same fill media compared to the 15 % PMT coverage used for NEO. Moving from the ∼100 photons/MeV Gd-WbLS to the ∼500 photons/MeV 5 % WbLS also offers an approximately 2 % improvement in $\sigma(E)/E$ for the same detector. However, the energy resolution of WbLS is still significantly worse than pure scintillator. Borexino, which used a pseudocumene fill, achieved an energy resolution of $\frac{5\,\%}{\sqrt{\mathrm{MeV}}}$ down to 200 keV [358].

The potential improvement versus SK is due to the improved charge resolution of the PMTs. However, direct comparison beyond the order of magnitude being in agreement is difficult to make as real world detector effects, such as dead PMTs and bad electronics readout channels, are not accounted for in NEO simulations. The Gd-water is also not a like-for-like medium comparison, although the energy resolution of pure water and

pure water doped with gadolinium is expected to be similar due to their similar light yields.

6.1.3 Energy Analogues in NEO

Analogues for deposited energy can be used as an estimate of particle energy in place of full energy reconstruction. This is useful when relative energy is required, which is the case in certain data reduction methods, and can be quicker and less intensive than determining the absolute energy. This is because the output of the already applied vertex reconstruction can be used, and no new fits are applied.

The number of PMT hits in a time window around the peak light intensity is used in NEO, with the choice of time window varying depending on the detector size and fill medium. The number of hits is termed N_X, where X is the length of the window in nanoseconds e.g. N_{100} is the number of hits in a 100 ns window. The time window is intended to ensure only light directly from the desired particle interaction is used to estimate the particle's energy, and reduces the effect of scattering. The length of the window is related to the time taken for the light to reach the PMTs from the particle interaction, with this being dependent on the detector size and light production mechanism.

In water, smaller time windows are used as the Cherenkov radiation produced is instantaneous. When scintillator is added, longer windows are used to allow the slower scintillation mechanisms to occur. As detectors get larger, the amount of time light takes to cross the detector and reach the PMTs increases. The time window used therefore increases. The time window starts a few ns, up to 10 ns, before the peak in Cherenkov light intensity to allow all direct light to be used.

In the 22 m NEO design, N_{100} is used. This window runs from 10 ns before the peak Cherenkov light intensity to 90 ns after. This window gives a maximum energy resolution in the WbLS cocktails; longer windows allow too much scattered light and shorter ones decrease the amount of light being used. This window is used for the water fill in this detector, but is not optimised.

The 16 m NEO design uses a 9 ns window, 3 ns before the Chernekov peak to 6 ns after, for the water fill to give N_9 PMT hits in the window. However, the N_{100} analogue is used when WbLS is utilised.

The amount of light left in the detector drops sharply after the PMT after-pulsing peak at ∼70 ns, shown by the time residuals in Figure 6.1. Full optimisation, including

electronics and physical calibration, of the longer time windows could reduce these significantly. The amount of light left 90 ns after the peak light intensity drops by almost two orders of magnitude for the 22 m detector with the Gd-WbLS fill, and more for the other configurations. Optimising and shortening the time windows may reduce the electronic and computational requirements by using less data without significantly reducing detector performance.

6.2 Data Reduction using LEARN

To suppress backgrounds and extract IBD events, the Likelihood Event Analysis of Reactor Neutrinos (LEARN) chain has been developed. LEARN utilises a likelihood ratio test, supervised machine learning using AdaBoost [359], and energy analogue cuts to reduce backgrounds whilst maintaining signal rates.

During the data reduction and analysis, a "trigger" is a single particle interaction which triggers the detector and successfully undergoes vertex reconstruction, an "event" is two triggers deemed to be in a coincident-pair such as IBD. The signal for the LEARN pathway is a positron followed by a neutron capture produced during IBD of a reactor antineutrino.

There are several steps in the LEARN pathway. MC simulations are produced as described in chapter 5 and vertex reconstruction is performed as described in section 6.1. A multiplicity cut of two is applied to reject chains of neutrons, before a likelihood test is carried out to remove uncorrelated single particle triggers that produce accidental coincidences. Triggers deemed to be in a pair from these steps are passed into a machine learning algorithm designed to identify and remove fast neutrons. Once fast neutrons are suppressed, energy cuts are optimised to reject radionuclides and low-energy backgrounds, before an analytical post-muon veto is used to reject muon spallation products.

6.2.1 Neutron Multiplicity

As stated in subsubsection 5.4.3.3, fast neutrons are able to produce further neutrons in the detector through neutron evaporation and spallation. This can result in chains of several neutrons in the detector which, when triggering in pairs close together in time and space, can mimic the IBD signal. After vertex reconstruction, the mean number

of neutrons in a chain is just over 2 (Figure 6.6), with a maximum of 21 in the NEO simulations. This creates a large probability of pairs being detected as IBD.

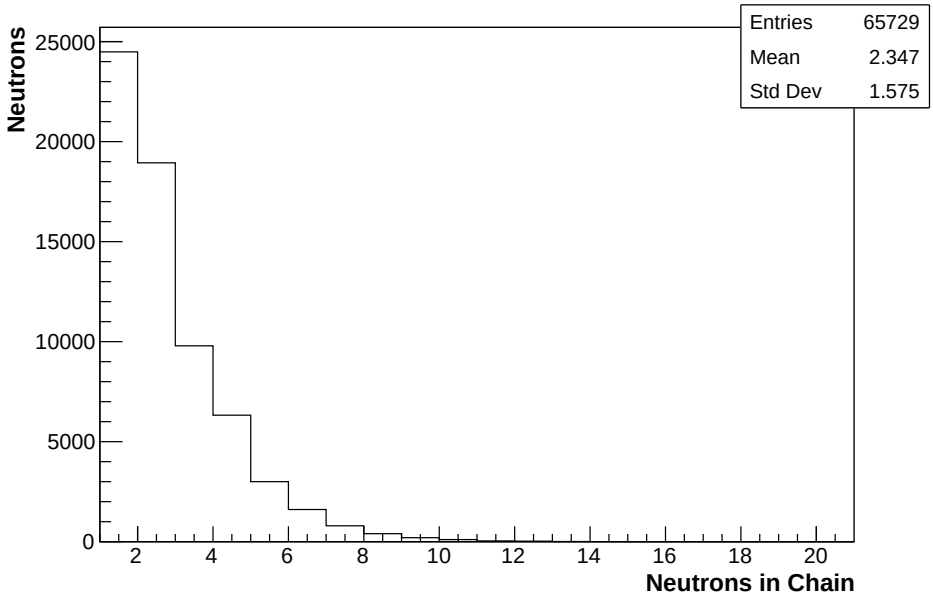

Figure 6.6: The number of fast neutrons in a chain after vertex reconstruction. The maximum number in a chain here is 21.

To reduce the likelihood of fast neutrons being detected in pairs, and therefore the total flux contribution to the background, a multiplicity cut is applied. When several neutrons are reconstructed in proximity, they can be grouped together. If more than two neutrons are grouped, the cluster is removed. In the 22 m tank with Gd-WbLS, this corresponds to a reduction of $\sim$84 % in the total fast neutron rate.

6.2.2 Rejection of Radioactive Singles

Two versions of the likelihood technique to reject radioactive singles have been developed. The first version was used in work published in [5], and has been cross-checked against an independent analysis on the same MC simulations, whilst the second version represents an improvement in the method.

6.2.2.1 Version 1: Likelihood Ratio Test

The likelihood component of the analysis chain is used to handle accidental coincidences from radioactive backgrounds occurring naturally in the detector and surrounding environment. The majority of these particles originate from the PMTs and so occur close to the edge of the ID volume. As these particles are uncorrelated to any other interactions, have very low energies and occur near the edge of the inner volume, they can be distinguished from correlated events.

The MC is split into two parts, a training data set and an evaluation data set. PDFs are created using the training MC for each signal and background source for each parameter, before being used to create signal and background likelihoods. LEARN uses a likelihood ratio test based on five parameters to separate out uncorrelated interactions. The parameters are:

1. number of PMTs hit in a 100 ns window (9 ns for 16 m Gd-H_2O) around the peak of light intensity from a trigger (N_{100} (N_9)),
2. number of PMTs hit in a 100 ns (9 ns for 16 m Gd-H_2O) window around the peak of light intensity from a trigger for the previous trigger,
3. time between two consecutive triggers,
4. distance between two consecutive triggers,
5. distance from PSUP.

The signal and background likelihood values of a trigger are determined, and a test statistic is defined as

$$\Lambda(x) = -2\ln\left(\frac{L(x|\theta_b)}{L(x|\theta_s)}\right) \tag{6.8}$$

where θ_s and θ_b are the probability distributions of the parameters for the correlated and uncorrelated components respectively, and L is the likelihood. The statistic is used to discriminate between the correlated and uncorrelated components by tuning a cut to match the bounds of the distribution produced by uncorrelated triggers. This is to allow the removal of all uncorrelated triggers whilst keeping the maximum number of signal events possible. Evaluation data are then passed through the PDFs to determine their test statistic, and events are kept for further analysis if they pass the previously optimised cut. Some triggers may be determined to have a non-zero probability of being

signal and a zero probability of being background from the PDFs, but be rejected by the optimised cut. In this situation, the events are kept. When a trigger passes the cut and a second trigger close in time and distance is found to make a pair based on the characteristics of neutron capture in a 0.1 % Gd-doped fill, both are kept as an event. An example of the distribution of the test statistic for IBD events from Heysham 2 and uncorrelated triggers, with the cut made to remove uncorrelated triggers, is displayed in Figure 6.7.

A summary of the trigger acceptance by the likelihood ratio test is:

- Prompt trigger passes cut
  - Keep prompt trigger and search for delayed trigger that can be deemed part of the same pair, keeping this trigger if found.
- Delayed trigger passes cut
  - Keep delayed trigger and search for prompt trigger that can be deemed part of the same pair, keeping this trigger if found.
- Prompt trigger does not pass cut and no delayed trigger found
  - Reject trigger as a single uncorrelated trigger.

The nature of Figure 6.7, with its multiple peaks, is due to the trigger types being compared. Correlated and uncorrelated triggers are passed through both their own PDFs and the other trigger type's PDFs. The uncorrelated interactions are single triggers and create smooth distributions, whereas the correlated events have two triggers (the positron and neutron for IBD) within their distributions. This results in peaks caused by the differing trigger types within the correlated event likelihood distributions. When the likelihoods are divided, these peaks propagate through and give the distributions shown in Figure 6.7.

Since the null hypothesis (uncorrelated background) is one, continuous component, whereas the alternative hypothesis (coincident signal pair) is made up of two distinct components, there are times when one or other of the components are not defined for the background, leading to the two distinct peaks in the test statistic for the uncorrelated backgrounds.

The three peaks in the Heysham 2 distribution correspond to triggers with different properties. The first peak, with a value of $\Lambda(x) < 50$, is mostly neutrons in IBD pairs.

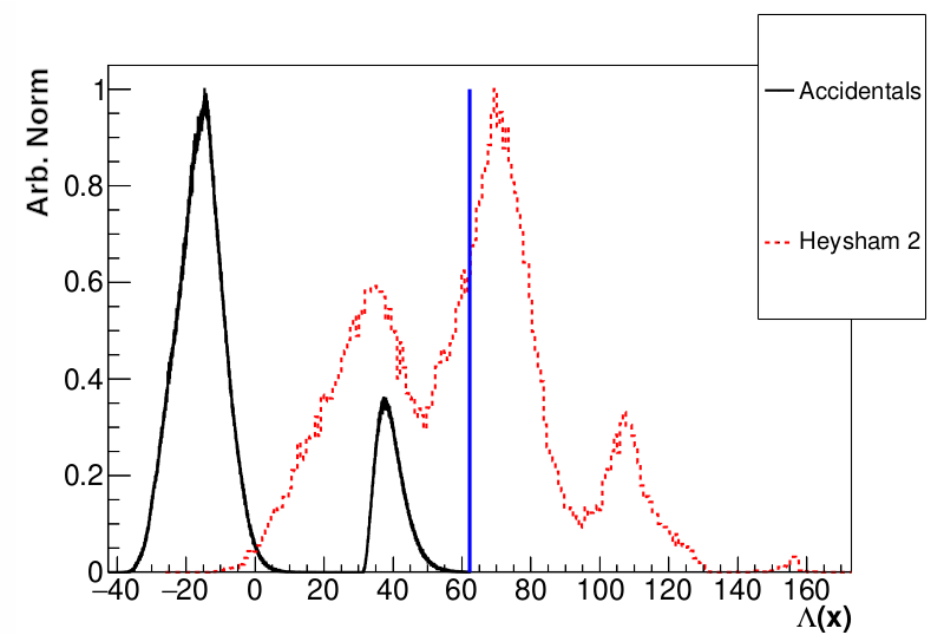

Figure 6.7: The test statistic defined in Equation 6.8 for the uncorrelated triggers (solid black) and IBD from Heysham 2 (dashed red) in the 22 m Gd-WbLS configuration, both normalised to a maximum of 1. The blue vertical line is the upper boundary of the distribution for the uncorrelated triggers.

There is a tail that extends across the majority of the positive $\Lambda(x)$ distribution. The second peak, with $50 < \Lambda(x) < 90$, consists mostly of positrons in an IBD pair where both particles trigger. As such, the first two peaks are closely linked. The third peak is generally positrons with a much higher number of PMT hits within the time window. This is because they deposit a higher amount of energy and so produce more light. The N_{100} distributions of the second and third peak are shown in Figure 6.8. These positrons are also less likely to be followed by a neutron that triggers the detector. They pass the optimised cut as they have a much higher energy than single radioactive particle interactions and occur much nearer the centre of the detector, therefore they do not need the correlated trigger to be discriminated from radioactive backgrounds.

6.2.2.2 Version 2: Improvement to the Rejection of Radioactive Singles

The likelihood ratio test described in subsubsection 6.2.2.1 was the first version developed and used as a part of a study into the feasibility of the detectors described in subsection 5.3.3. This method was designed for use with the Gd-WbLS fill. The data re-

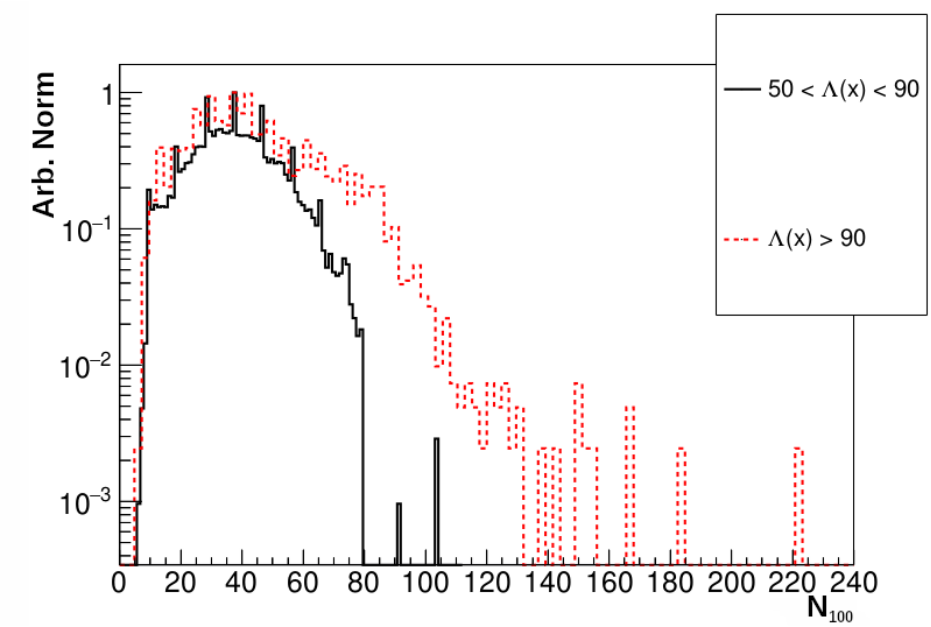

Figure 6.8: The number of PMT hits within a 100 ns window around the trigger (N_{100}) for the positrons in the likelihood ratio peaks in Figure 6.7 corresponding to $50 < \Lambda(x) < 90$ (solid black) and $\Lambda(x) > 90$ (dashed red), both normalised to a maximum of 1.

duction including this method for single radioactive trigger rejection was cross-checked with an independent analysis during this feasibility study.

Following this study, the single trigger rejection step was improved to handle the lower reactor IBD event rates in Gd-H_2O. The first version passed triggers into PDFs for both the signal and background, before taking the ratio of the likelihoods formed from these PDFs. However, it was observed that passing triggers only into the background PDFs allowed the second trigger in the pair to be used more effectively. The difference in the likelihood produced using single trigger PDFs between the neutrons in IBD and radioactive single triggers is shown in Figure 6.9.

The IBD neutron has a significantly different distribution to the singles background due to its proximity to the IBD positron. As with the likelihood ratio method, the bounds of the radioactive singles distribution are used to define whether triggers are accepted or rejected. The first trigger in a pair will generally be rejected by this method as it highlights the difference between a trigger that closely follows another trigger and triggers that do not follow another. This in effect places emphasis on the second trigger in a correlated pair to determine whether to accept an event. The timing of the first event in a pair will look more like a single trigger in this case.

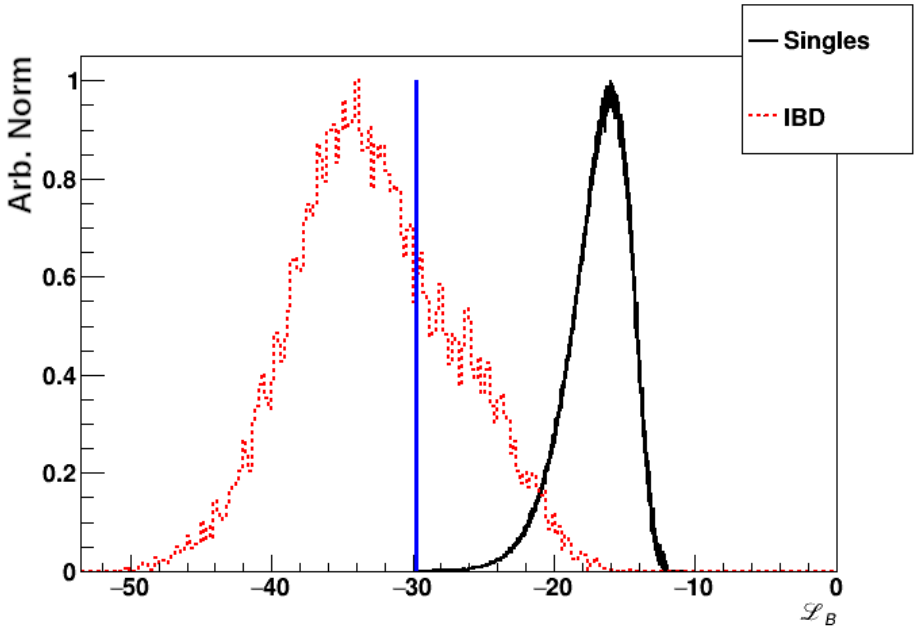

Figure 6.9: Log likelihood produced using single trigger PDFs for the IBD neutron from Heysham 2 (dashed red) and radioactive single triggers (solid black) in the 22 m Gd-WbLS detector, both normalised to a maximum of 1. The vertical blue line corresponds to the minimum log likelihood for the radioactive singles.

A summary of the trigger acceptance is:

- Delayed trigger passes cut
  - Keep delayed event and search for prompt trigger that can be deemed part of the same pair, keeping this trigger if found.

By applying a likelihood-based rejection in this way, a factor three increase in the number of accepted IBD events is seen. All other steps in the data reduction remain unchanged from those used alongside the method in subsubsection 6.2.2.1, although a more aggressive optimisation can be applied due to the increased signal rates at each stage.

6.2.3 Fast Neutron Rejection

Once coincidences are evaluated and uncorrelated backgrounds removed, the data are passed into a machine learning model to remove fast neutrons. The model used is a

boosted decision tree called AdaBoost [359], in which data are passed through a "forest" of short decision trees and events are classified by their features. Misclassified data are given an increased weighting on each iteration (boosted), allowing harder-to-classify events to be prioritized. A decision score can also be given and is based on how many times an event is classified as signal or background as it passes through the forest.

The model is trained on the training MC data set used in the likelihood analysis step, with the final classification made on the pairs of events in the evaluation data kept by the likelihood ratio test. The model trains on several parameters, most of which are the same as used in the likelihood ratio test, with additional parameters taking into account vertex reconstruction quality and more detail on the position of the interaction. The difference in the distribution of interaction positions is shown in Figure 6.10 and shows good discrimination between fast neutrons and IBD events, since IBD events happen throughout the detector whereas fast neutrons are concentrated near the edge. As such, additional position information allows a better classification of events.

The model is applied to look for a specific background source, fast neutrons, and not a signal source as is often the case. This is done to harness the differences in properties between the fast neutrons that reach the ID volume and other correlated sources. Event pairs tagged as fast neutrons are removed from the data. This is done with $> 94\,\%$ efficiency and keeps $\sim$99 % of reactor IBD, which is shown by the confusion matrix for Heysham 2 in the 22 m Gd-WbLS configuration in Figure 6.11a, with the decision score associated with this classification shown in Figure 6.11b. The majority of the falsely rejected events are ^{9}Li, which further reduces background. This is likely due to the higher energy of the prompt ^{9}Li electron, which produces light more comparable to a fast neutron than an IBD positron. A comparison between the kinetic energy of the prompt particles from ^{9}Li and Heysham 2 IBD is presented in Figure 6.12.

6.2.4 Energy Cuts

Following the removal of uncorrelated single triggers and the suppression of fast neutrons, there are still several types of correlated events. These originate from reactor antineutrinos, muon-induced radionuclides, geoneutrinos and the remaining fast neutrons. At this stage, the fast neutron rate has been suppressed from $> 30\,\%$ of the event pairs to being $< 1\,\%$, although the high uncertainty means they are not neglected. The radionuclides make up 50 - 60 % of the event pairs and the geoneutrinos are $\sim$5 %. Although different reactors cannot be distinguished in these detector configurations,

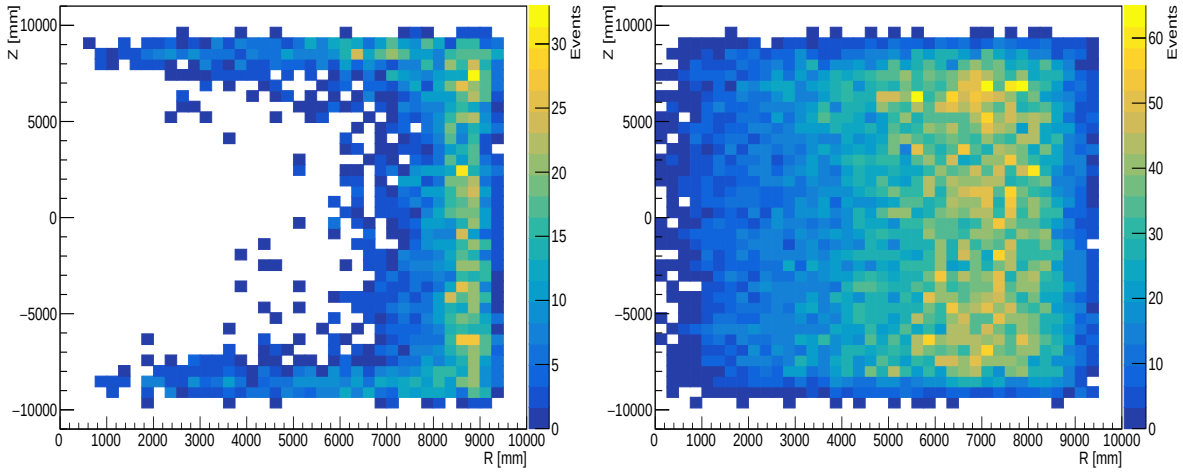

(a) Fast neutrons.

(b) IBD.

Figure 6.10: Reconstructed position in 22 m tank filled with Gd-WbLS for (a) fast neutrons and (b) IBD events. This is used in the machine learning model to help discriminate between the signal and fast neutron background.

except where oscillations cause the signal and reactor IBD background spectra to diverge significantly, the other background types can be further reduced due to their difference in energy to reactor IBD.

Geoneutrinos tend to have a lower energy than reactor antineutrinos (Figure 5.18), whilst fast neutrons and ^{9}Li can have a higher prompt energy than the positron produced via IBD from reactor antineutrinos. Energy cuts in terms of an energy analogue (subsection 6.1.3) can be optimised to harness these differences. The energy analogue chosen here is N_{100} for Gd-WbLS to make the most of the slower scintillation light by allowing 100 ns of light from an event to be used. The same time window is also used for the 22 m Gd-H_2O detector, but N_9 is used for the 16 m Gd-H_2O design as a longer window would cause scattered light to be observed. Threshold and maximum values for N_9 or N_{100} are optimised during analysis for the prompt signal in a pair, and the pair is kept if the prompt trigger passes both cuts. Minimum and maximum N_9 or N_{100} values for the delayed signal are also optimised, with the pair being removed if the delayed particle energy is not within these two values. For some configurations, cuts on the delayed signal energy were not required. In the case of Hartlepool, where the reactor signal forms ∼80 % of the IBD signal, adding further thresholds reduces

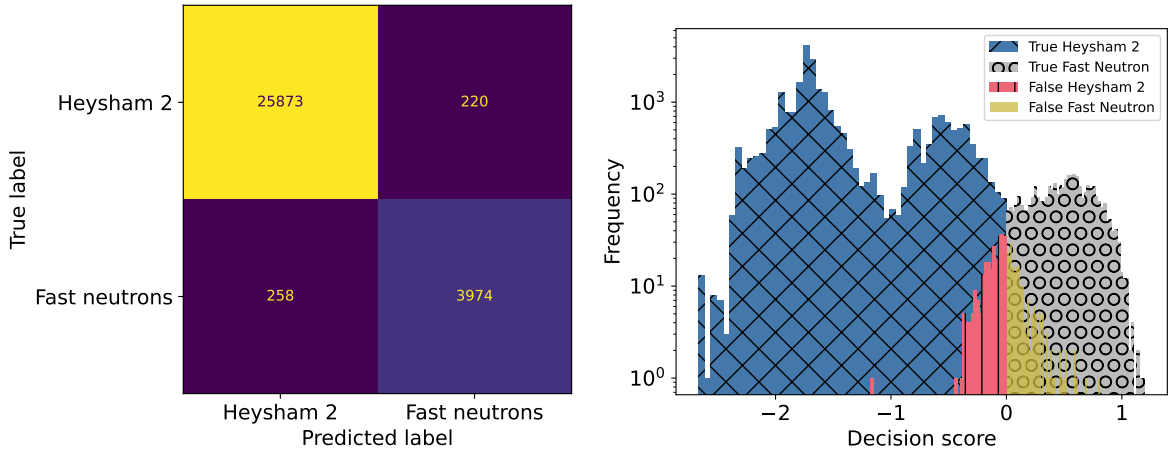

(a) Confusion matrix.

(b) Decision score.

Figure 6.11: The classification of fast neutrons in the 22 m tank filled with Gd-WbLS with Heysham 2 as the target reactor for the evaluation data set. Only 220 out of 26093 Heysham 2 events are rejected by the classifier, with 258 out of 4268 fast neutrons passing the classifier.

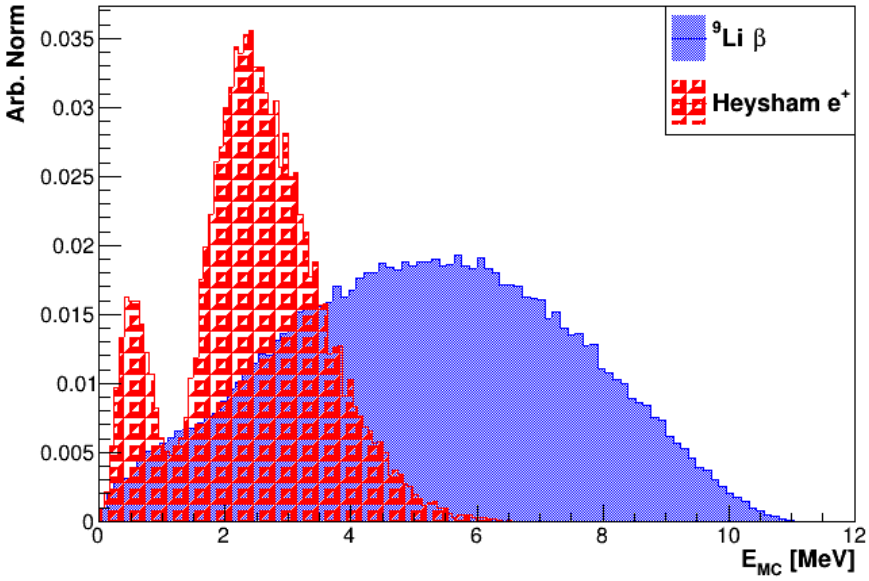

Figure 6.12: Heysham positron versus ^{9}Li β particle kinetic energy spectra. The areas have been normalised to allow a comparison of the spectral shapes.

the observed signal rate but has no positive effect on the signal-to-background. Table 6.1 shows the optimised cuts for the Gd-WbLS configurations. These cuts reduce the radionuclides down to ∼25 % of the total rate, and keeps the geoneutrino and fast neutron components suppressed.

Signal	Prompt threshold [hits]	Prompt upper limit [hits]	Delayed threshold [hits]	Delayed upper limit [hits]
Hartlepool 1 & 2	10 (0)	90 (102)	N/A (N/A)	N/A (N/A)
Hartlepool 1	0 (0)	110 (104)	N/A (N/A)	N/A (N/A)
Heysham	20 (22)	70 (70)	80 (N/A)	190 (N/A)
Heysham 2 & Torness	20 (24)	80 (85)	80 (N/A)	250 (N/A)
Heysham 2	20 (24)	80 (64)	80 (N/A)	250 (N/A)

Table 6.1: Optimised energy cuts in the 16 m (22 m) Gd-WbLS detector for anomaly detection of all signal combinations using LEARN (section 7.1). Cuts on the delayed signal energy are not required in all cases.

Following the energy cuts, an analytical post-muon veto is applied as detailed in subsection 6.2.5 to further reduce trigger rates from muon-induced backgrounds.

6.2.5 Analytical Post-Muon Veto

When high-energy cosmic ray muons pass through a large detector, they generally produce a track which is simple to identify. As such, the muon itself is not a key background to IBD. Muons can, however, induce other processes that are a significant background. Two of the key backgrounds to IBD, the radionuclides ^{17}N and ^{9}Li, are produced through muon-induced spallation on oxygen. An analytical post-muon veto, which uses the correlation between the radionuclide events and the muon track, has been developed to handle these events and reduce their influence.

The half lives of the key radionuclides are $\mathcal{O}$(s) and so they survive short time vetoes based on the muon entry and exit times. By tracking the muon through the detector, longer time vetoes can be applied over a limited transverse distance from the muon track. This allows the radionuclides to be suppressed without creating a large dead time in the detector. The remaining rate of a radionuclide's activity is based on theoretical calculations combining the muon detection efficiency and radionuclide half

life [360], and is given by

$$R_{\mathrm{iso},(t_{\mathrm{veto}})} = \left(1 - \epsilon + \epsilon \frac{\int_{t_{\mathrm{veto}}}^{\infty} e^{-\ln(2)t/t_{1/2}}\mathrm{dt}}{\int_{0}^{\infty} e^{-\ln(2)t/t_{1/2}}\mathrm{dt}}\right) R_{\mathrm{iso,tot}}, \tag{6.9}$$

where t_{veto} is the veto time, ϵ is the muon detection efficiency and $t_{1/2}$ is the half life of the radionuclide.

For a detector with an active outer detector veto region, such as SK, the muon detection efficiency can reasonably be expected to reach 99.9 % when electronics issues are accounted for. Using a passive buffer, the efficiency in the fiducial volume can be assumed to be the same. However, a passive buffer leaves the situation where a muon passes through the OD undetected but induces spallation events that reach the ID as a possibility. This account for this, a conservative 95 % muon-detection efficiency is used. Applying a 1 s veto with a 95 % muon-detection efficiency yields radionuclide rates of

$$R_{^{9}\mathrm{Li(1\ s)}} = 0.069\ R_{^{9}\mathrm{Li,tot}},$$
$$R_{^{17}\mathrm{N(1\ s)}} = 0.85\ R_{^{17}\mathrm{N,tot}}.$$

A 1 s time veto is assumed to give a negligible detector dead time if it is applied over a limited transverse distance to the muon track in the fiducial volume, using the reasonable assumption that the muon can be tracked in the ID.

6.3 Summary

Algorithms to reconstruct the vertex position and energy of interactions in the detector have been adapted and developed to allow the extraction of desired interactions from the data. Vertex reconstruction is performed using an adapted version of SK's BONSAI, with custom energy reconstruction developed for NEO.

The Likelihood Event Analysis of Reactor Neutrinos (LEARN) data reduction chain has been developed to extract pairs of triggers which are reactor IBD candidates from the single-trigger background caused mostly by radioactive decays. LEARN uses a combination of likelihoods, machine learning and energy cuts to first remove the single triggers, and then suppress muongenic products such as fast neutrons and radionuclides.

Two versions of LEARN exist, which differ only in their application of the likelihood test. The second version offers a significant improvement over the first version, with the

first being validated against an alternative data reduction. A summary of the number of events at each stage of the data reduction with Heysham 2 as the target of observation in the 22 m Gd-WbLS detector is shown in Table 6.2 (LEARN version 1) and Table 6.3 (LEARN version 2).

LEARN acts to suppress backgrounds, extracting the maximal amount of signal possible, with both the likelihood and machine learning being optimised to suppress a particular background as much as possible. This yields a dataset that can be analysed to search for a desired signal. The energy cuts are optimised during this analysis, which is described in section 7.1.

Signal	Events Remaining After Step [%]			
	MC	Likelihood	Machine Learning	Energy Cuts & Muon Veto
Heysham 2	100	26.1	25.8	21.2
Torness	100	26.0	25.6	18.0
Sizewell B	100	24.8	24.5	18.2
Hinkley Point C	100	25.4	25.2	18.0
Gravelines	100	25.5	25.2	17.2
World Reactor	100	25.2	24.5	17.5
Geoneutrinos	100	21.2	20.9	10.4
^{9}Li	100	37.6	25.8	0.74
^{17}N	100	22.2	21.5	11.1
Fast Neutrons	100	0.055	0.0024	0.0017

Table 6.2: The percentage of events remaining after each step in the first version of the data reduction in the 22 m Gd-WbLS detector with Heysham 2 as the signal.

Signal	Events Remaining After Step [%]			
	MC	Likelihood	Machine Learning	Energy Cuts & Muon Veto
Heysham 2	100	89.2	52.2	38.3
Torness	100	89.6	52.5	32.0
Sizewell B	100	87.4	52.0	33.7
Hinkley Point C	100	88.5	52.2	32.2
Gravelines	100	88.3	52.2	31.0
World Reactor	100	88.3	52.2	32.2
Geoneutrinos	100	47.4	36.6	12.9
^{9}Li	100	99.4	53.8	1.43
^{17}N	100	72.3	46.7	18.6
Fast Neutrons	100	0.12	2.1×10^{-4}	2.1×10^{-4}

Table 6.3: The percentage of events remaining after each step in the second version of the data reduction in the 22 m Gd-WbLS detector with Heysham 2 as the signal. The fast neutron rates are consistent with 0 after the machine learning step, so the 95 % Poisson upper confidence limit is used.

Chapter 7

Sensitivity of Neutrino Experiment One

Two types of analysis of the NEO detector simulations in chapter 5 have been developed to work with the reconstruction and data reduction algorithms in chapter 6 to assess detector performance.

The first analysis type is a rate-only analysis to determine the sensitivity of a detector to the antineutrino signals from reactors in the UK and northern France. This uses sensitivity metrics for an anomaly observation above the expected background and a measurement of an observed signal consistent with a signal-plus-background scenario. The performance is measured in terms of the number of days of observation, at the average reactor power exhibited in 2020, to make an anomaly detection or signal measurement at 3σ significance for a given reactor. This allows two use cases for reactor monitoring to be tested: detection of an unknown reactor operation and measurement of a known reactor signal. Both versions of the data reduction, with the differing likelihood implementation, are applied with the first version being cross-checked against an independent analysis chain.

The second type is spectral analysis, applied directly to the signal and background spectra obtained from the rate-only analysis, to determine the distance to an observed reactor based on neutrino oscillations.

The simulations do not have detector systematic uncertainties included, only systematic uncertainties on the expected incident rate for each interaction component (subsection 5.4.4). These uncertainties are included as part of the expected rates after analysis, but do not include any energy-dependence that may be exhibited by detector

systematics.

7.1 Required Observation Time

The main goal for the AIT-NEO facility and experiment is to determine the sensitivity of a remote reactor monitoring prototype to real reactors in a realistic environment. The performance of the detector designs is determined using the *dwell time*, the amount of time it takes to make an observation to a predetermined level of a reactor signal against known backgrounds. The data reduction, described in chapter 6, is optimised to suppress backgrounds and extract an IBD signal, with the energy cuts in subsection 6.2.4 being optimised to maximise a sensitivity metric.

There are two key scenarios that the sensitivity has been determined for, the observation of an anomaly signal and the measurement of the signal. Each scenario has its own metric, which are described below. More detail on the derivation of the metrics is available in [361].

All measurements assume that the reactors have the same average power output as quoted by the IAEA for 2020, with no abnormal shutdowns. Regular maintenance and refuelling are accounted for in the IAEA load factors.

7.1.1 Anomaly Detection Metric

An anomaly detection of an unknown reactor is defined as the rejection of the null hypothesis that the rates are consistent with the expected background rates. A significance of 3σ (or equivalent) is considered a sufficient level to reject the null hypothesis to for non-proliferation scenarios of this type.

For anomaly detection, two metrics are available depending on the signal strength relative to the background. Both are derived from the p-value of the background-only hypothesis and a test statistic based on the profile likelihood ratio of the chosen distribution (Gaussian or Poisson). In the situation where the signal rate is much less than the background rate and the total number of signal counts is greater than ∼20 - 30, the metric is derived from the Gaussian significance [361];

$$N_\sigma = \frac{st}{\sqrt{\sum_{i=0}^{n} b_i t + \sum_{i=0}^{n} (\sigma_{b_i} t)^2}}, \tag{7.1}$$

where N_σ is the number of Gaussian standard deviations from the expected background counts, s is the signal rate, b_i is the rate of the i^{th} background, σ_{b_i} is the systematic uncertainty on the i^{th} background rate and t is the length of time of observation. The dwell time is then given by

$$t_{\text{dwell}} = \frac{N_\sigma^2 \sum_{i=0}^{n} b_i}{s^2 - N_\sigma^2 \sum_{i=0}^{n} \sigma_{b_i}^2}, \tag{7.2}$$

and is calculated for $N_\sigma = 3$.

When the background rate is not much larger than the signal rate, or only a few signal counts are observed in time t, the Gaussian approximation is replaced by a Poisson distribution. The Poisson significance is given by [361]

$$Z = \left[2\left((st + \sum_{i=0}^{n} b_i t)\ln\left[\frac{(st + \sum_{i=0}^{n} b_i t)(\sum_{i=0}^{n} b_i t + (\sum_{i=0}^{n} \sigma_{b_i} t)^2)}{(\sum_{i=0}^{n} b_i t)^2 + (st + \sum_{i=0}^{n} b_i t)(\sum_{i=0}^{n} \sigma_{b_i} t)^2}\right] - \frac{(\sum_{i=0}^{n} b_i t)^2}{(\sum_{i=0}^{n} \sigma_{b_i} t)^2}\ln\left[1 + \frac{(\sum_{i=0}^{n} \sigma_{b_i} t)^2 st}{\sum_{i=0}^{n} b_i t(\sum_{i=0}^{n} b_i t + (\sum_{i=0}^{n} \sigma_{b_i} t)^2)}\right]\right)\right]^{\frac{1}{2}}. \tag{7.3}$$

This can be expressed as a function with time t as a free parameter, and a value of t_{dwell} determined at a significance of $Z = 3$.

The chosen metric for NEO is the Gaussian dwell time. This is an experimental convention from the WATCHMAN collaboration based on previous studies. For situations where the signal rate is much less than the background rate, and where the observation time is long enough that the number of observed counts is large, the Gaussian significance approximates the Poisson significance. In previous studies, this approximation was valid, and therefore the Gaussian metric was used. To maintain consistency with previous studies and allow a direct comparison of results, the same Gaussian metric has been used where valid. This is the case for all reactors more distant to Boulby than Hartlepool.

However, with improvements to data reduction techniques and detector design, the Gaussian significance is not valid for the observation of the Hartlepool cores. This is due to the low observation times leading to low total signal counts, and the high signal-to-background ratio. In the case of the anomaly observation of the Hartlepool cores, the Poisson distribution metric is used as this is always valid in a counting experiment.

7.1.2 Reactor Measurement Metric

The measurement of rates consistent with the expected signal-plus-background rates is a more complex scenario for the detection of an unknown reactor, and a 3σ significance is considered sufficient as with anomaly detection.

The derivation is very similar that of Equation 7.2, starting with a Gaussian significance. However, the additional inclusion of signal uncertainties gives a significance defined as

$$N_\sigma = \frac{st}{\sqrt{st + (\sigma_s t)^2 + \Sigma b_i t + \Sigma(\sigma_{b_i} t)^2}}, \tag{7.4}$$

σ_s is the systematic uncertainty on the signal rate. The dwell time is then given by

$$t_{\text{dwell}} = \frac{N_\sigma^2(s + \Sigma b_i)}{s^2 - N_\sigma^2(\sigma_s^2 + \Sigma\sigma_{b_i}^2)} \tag{7.5}$$

and is evaluated for $N_\sigma = 3$.

7.1.3 Sensitivity Results

The time required to observe a reactor, either as an anomaly or a measurement, to 3σ significance is the metric used to assess the sensitivity of a detector to that reactor. The reactors used to determine the detector performance are split into two types, detailled in subsection 5.2.2 and Table 5.1, with the AGRs being located nearer to the AIT facility at Boulby. The breakdown of signal and background contributions of the AGR fleet is in Table 7.1, with the equivalent for the PWRs in Table 7.2. In the case of the AGR cores, all PWRs are assumed to contribute to the background; for the PWRs, the AGRs are assumed to be decommissioned.

The results presented here are from the rate-only analysis of the reactor signals and backgrounds coming from the application of the data reduction in chapter 6, with energy cuts optimised to minimise the dwell time. In the case of the Hartlepool cores where the signal is large, Equation 7.3 is used to determine the significance. In all other cases, the dwell times are calculated using Equation 7.2 and Equation 7.5 for anomaly detection and reactor measurement respectively.

7.1.3.1 Data Reduction Version 1

The dwell time results in both the anomaly detection and reactor measurement scenarios are given for the AGRs in Table 7.3 and for the PWRs in Table 7.4 when the likelihood

Signal combination	Hartlepool 1	Hartlepool 2	Heysham 1	Heyhsam 2	Torness	World
Hartlepool 1 & 2		**1041**				**207**
Hartlepool 1	**595**					**693**
Heysham 1 & 2				**70**		**147**
Heysham 2 & Torness					**65**	**122**
Heysham 2				**40**		**147**
Torness					**25**	**162**

"World" = Total world reactor background

Table 7.1: Combinations of reactor signals and backgrounds evaluated for AGR cores. Reactors marked black contribute to the signal, reactors marked grey contribute to the background. Those with a slash are assumed to be decommissioned in the given scenario. Rates are given in NIU.

Signal combination	Sizewell B	Hinkley Point C	Gravelines	World
Sizewell-Hinkley-Gravelines			**37**	**84**
Sizewell-Hinkley		**22**		**99**
Hinkley-Gravelines			**29**	**92**

"World" = Total world reactor background

Table 7.2: Combinations of reactor signals and backgrounds evaluated for PWR cores. Reactors marked black contribute to the signal, reactors marked grey contribute to the background. Rates are given in NIU.

ratio test in subsubsection 6.2.2.1 is incorporated into the data reduction. This data reduction method was designed to be used primarily in Gd-WbLS and was not optimised for Gd-H_2O. As such, the results for Gd-H_2O are not presented.

From the results, it can be immediately seen that even for the smallest detector, the observation of Hartlepool poses little difficultly. However, moving to more distant reactors and hence significantly smaller signals, the sensitivity rapidly reduces. The 16 m detector would require approaching three years of observation at the operating power the reactors averaged in 2020 to make a 3σ anomaly observation of the total Heysham complex or a combination of the AGR-2 cores at Heysham 2 and Torness. The 22 m detector is much more sensitive due to the much larger volume allowing more antineutrino interactions. The smallest observable signal in the AGR fleet as seen at Boulby, Heysham 2, can be measured in under two years. This, alongside other

Detector	Scenario	Hartlepool 1 & 2	Hartlepool 1	Heysham 1 & 2	Heysham 2 & Torness	Heysham 2
16 m Gd-WbLS	Anomaly	5	24	1017	963	2968
16 m Gd-WbLS	Measurement	11	34	1301	1227	3510
22 m Gd-WbLS	Anomaly	2	9	196	164	577
22 m Gd-WbLS	Measurement	5	12	263	221	715

Table 7.3: Results summary for AGR signals using the LEARN data reduction with the likelihood method described in subsubsection 6.2.2.1. The dwell time is given in days and is the observation time for a 3σ significance detection.

Detector	Scenario	Size-Hink-Grav	Hink-Grav	Size-Hink
22 m Gd-WbLS	Anomaly	744	1638	5980
22 m Gd-WbLS	Measurement	896	1905	6786

"Size" = Sizewell B, "Hink" = Hinkley Point C, "Grav" = Gravelines

Table 7.4: Results summary for PWR signals using the LEARN data reduction with the likelihood method described in subsubsection 6.2.2.1. The dwell time is given in days and is the observation time for a 3σ significance detection.

safeguarding methods, shows potential for non-proliferation applications.

The results for PWR cores are only given for the larger detector. Dwell times for the 16 m detector did not converge due to the detector having no sensitivity to these distant cores. The 22 m detector could make an anomaly detection of the combination of Sizewell B, Gravelines and Hinkley Point C, assuming the nearer AGRs have been decommissioned, in just under two years. These distant cores, up to 440 km, allow the limit of sensitivity of the biggest NEO detector in the AIT facility to be identified.

This version of the LEARN data reduction chain was developed to test the feasibility of the detector and facility designs in chapter 5. As no data was available, it was developed in parallel to another independent reconstruction-analysis pathway Coincident-Background Reactor Antineutrino Analysis (Cobraa) by Liz Kneale [5, 350]. Both chains used identical MC simulations, but differed in all other aspects with the exception of the analytic muon veto. Cobraa is a different approach entirely, optimising a series of cuts on measured parameters and using an IBD pair reconstruction called Combined Reconstruction (CoRe) [355]. The comparison between two analysis chains using different concepts allows a cross-check of results and can be used to build trust. A

comparison between the results in the Gd-WbLS detectors for both AGRs and PWRs is given in Table 7.5 and Table 7.6.

Analysis	Detector	Scenario	Hartlepool 1 & 2	Hartlepool 1	Heysham 1 & 2	Heysham 2 & Torness	Heysham 2
Cobraa	16 m Gd-WbLS	Anomaly	7	35	738	1022	3008
LEARN	16 m Gd-WbLS	Anomaly	5	24	1017	963	2968
			(29 %, 2)	(31 %, 9)	(27 %, 279)	(6 %, 59)	(1 %, 40)
Cobraa	22 m Gd-WbLS	Anomaly	2	8	152	192	647
LEARN	22 m Gd-WbLS	Anomaly	2	9	196	164	577
			(0)	(11 %, 1)	(22 %, 44)	(15 %, 28)	(11 %, 70)
Cobraa	22 m Gd-WbLS	Measurement			176	206	808
LEARN	22 m Gd-WbLS	Measurement	5	12	263	221	715
					(33 %, 87)	(7 %, 15)	(12 %, 93)

Table 7.5: Comparison between the dwell time results to 3σ for the AGRs for the LEARN (using subsubsection 6.2.2.1) and Cobraa [350] data reduction methods in the Gd-WbLS detectors. The percentage and dwell time differences between the two are shown in brackets.

Analysis	Size-Hink-Grav	Hink-Grav	Size-Hink
Cobraa	785	1641	7077
LEARN	744	1638	5980
	(5 %, 41)	(0.2 %, 3)	(16 %, 1097)

"Size" = Sizewell B, "Hink" = Hinkley Point C, "Grav" = Gravelines

Table 7.6: Comparison between the dwell time results to 3σ results for the PWRs for LEARN (using subsubsection 6.2.2.1) and Cobraa [350] data reduction methods in the 22 m Gd-WbLS detector. The percentage and dwell time differences between the two are shown in brackets.

The two analysis paths agree well for many signal-detector configurations, and within 31 % for all for anomaly detection scenarios. The small dwell times and rounding dwell times to the nearest day can lead to a larger percentage difference for Hartlepool signals, but the dwell times still agree within a few days.

The differences in results between the two analyses comes from the fundamental differences between them. As a cuts-based analysis, Cobraa maps out all parameter cuts and their impact on the rates of every interaction component in the detector. The

parameters include cuts on the same energy analogues LEARN uses (subsection 6.2.4), as well as cuts on the size of the detector's fiducial volume, the time between events and the quality of the pair reconstruction by CoRe. The optimal cuts are then chosen to minimise the dwell time using a particular metric. Cobraa was developed for use in Gd-H_2O detector fills, and favours total background suppression during its optimisation.

As a result of the different methodologies, different trends can be seen in the results and observed rates. The rates per day of signal and backgrounds are shown for the various AGR signals in Table 7.7 in the 22 m Gd-WbLS detector. The signal and background rates for Heysham 2 in both detectors are shown in Table 7.8. These rates show a general trend of LEARN observing a higher signal and background, with Cobraa observing a lower signal and background. The exception is the Hartlepool 1 case, which is the only case presented that is not background dominated. These differing trends present themselves in the dwell time results, in particular the Heysham 1 & 2 and Heysham 2 & Torness results where the opposite trends are seen. This is also where the largest discrepancies in dwell time are generally seen. The Heysham 2 & Torness scenario yields a lower signal than the Heysham 1 & 2 scenario, but also has less background to contend with. LEARN, which favours maintaining a higher signal, is able to make an observation in a shorter dwell time for the Heysham 2 & Torness case due to this. Cobraa, which favours suppressing the background and signal to lower levels during optimisation, performs better on Heysham 1 & 2 with its higher signal and higher background. The spectrum for Heysham also peaks at higher energy than Torness due to neutrino oscillation, allowing Cobraa to make more aggressive energy cuts during optimisation than LEARN. For the Heysham 2 & Torness scenario, Cobraa has minimum and maximum N_{100} cuts on the prompt trigger in a pair of 27 and 55, compared to 20 and 80 for LEARN. This allows Cobraa to restrict both low energy backgrounds such as geoneutrinos and high energy backgrounds such ^{9}Li more than LEARN. Due to this, Cobraa is able to perform better in scenarios where higher suppression of backgrounds is required.

Unlike Cobraa, LEARN only optimises energy cuts using the chosen metric. The rest of the data reduction places focus on a particular background type at each step, acting to suppress it. The likelihood step replaces some of the role of CoRe, extracting the triggers not expected to be caused by uncorrelated radioactive decays and leaving event pairs. However, the machine learning step deviates entirely from the Cobraa chain to suppress fast neutrons. By using more complex methods to focus on individual

Signal combination	Analysis	s	Σb_i	^{9}Li & ^{17}N	Fast n	$IBD_{reactor}$	geo	$\sigma(\Sigma b_i)$
Hartlepool 1	Cobraa	2.2	3.2	0.27	0.54	2.4		0.20
	LEARN	1.9	2.7	0.29	0.27	2.0	0.093	0.079
Heysham 1 & 2	Cobraa	0.18	0.48	0.13	0.044	0.30		0.021
	LEARN	0.19	0.65	0.19	0.059	0.35	0.058	0.025
Heysham & Torness	Cobraa	0.13	0.33	0.085	0.038	0.21		0.016
	LEARN	0.22	0.75	0.25	0.058	0.37	0.075	0.029
Heysham 2	Cobraa	0.091	0.39	0.097	0.034	0.26		0.018
	LEARN	0.13	0.71	0.21	0.047	0.39	0.057	0.024

Table 7.7: Representative rates per day from optimisation in the 22 m detector with Gd-WbLS fill. Accidental coincidences, and geoneutrino IBDs for Cobraa, are omitted as they are sub-dominant backgrounds consistent with zero.

Detector	Analysis	s	Σb_i	^{9}Li & ^{17}N	Fast n	$IBD_{reactor}$	geo	$\sigma(\Sigma b_i)$
16 m Gd-WbLS	Cobraa	0.017	0.068	0.020	0.0035	0.044		0.0028
	LEARN	0.024	0.14	0.044	0.010	0.079	0.0072	0.0043
22 m Gd-WbLS	Cobraa	0.091	0.39	0.097	0.034	0.26		0.018
	LEARN	0.13	0.71	0.21	0.047	0.39	0.057	0.024

Table 7.8: Representative rates per day from optimisation in both Gd-WbLS detector configurations for the Heysham 2 signal. Accidental coincidences, and geoneutrino IBDs for Cobraa, are omitted as they are sub-dominant backgrounds consistent with zero.

background types which present specific challenges, LEARN is able to maintain large numbers of signal events prior to the optimisation of energy cuts. This results in it favouring a higher signal rate over suppression of all backgrounds as it places emphasis on the backgrounds of most concern during data reduction; this method does mean that backgrounds with a pair-event signal in the detector can be harder to remove.

Despite the general agreement in the analyses, the larger discrepancies such as the 279 days for Heysham 1 & 2 in the 16 m Gd-WbLS detector cannot be ignored. The ability to explain the differences between the results does breed confidence, however, and produces a good understanding of what could be expected from the detector designs.

Overall, a combination of general agreement and a good understanding of the differences gives the conclusion that analyses provide a good cross-check and validate the methods applied. Without data, it is not possible to draw a definitive conclusion on the validity of the analyses, but the results are close enough to reasonably assume that they are valid.

7.1.3.2 Data Reduction Version 2

Under the assumption that the results quoted above are validated by their consistency with an independent analysis, the change to the data reduction made by adjusting the single event rejection as explained in subsubsection 6.2.2.2 can be deemed reasonable as the method change is only minor. The results for this data reduction are detailed in Table 7.9 and Table 7.10. The results are consistently a factor of more than two better than those under the previous data reduction, and sensitivity in the Gd-H_2O detector is seen. This occurs due to the improvement in single trigger rejection, which is able to accept approximately three times the number of pair events. This allows much higher signal rates to be observed for the same reactor core once all other data reduction steps are applied. Due to this, much smaller signals can be observed, such as more distant reactors or by using less sensitive detectors. An example of this is the 16 m Gd-WbLS detector is able to see the PWR cores, and the 22 m Gd-WbLS detector is able to obtain dwell times of under a year for both detection scenarios for the PWRs.

Detector	Scenario	Hartlepool 1 & 2	Hartlepool 1	Heysham 1 & 2	Heysham 2 & Torness	Heysham 2
16 m Gd-H_2O	Anomaly	7	37	863	688	3114
16 m Gd-H_2O	Measurement	17	53	1112	920	3651
16 m Gd-WbLS	Anomaly	3	14	275	320	983
16 m Gd-WbLS	Measurement	6	17	370	429	1184
22 m Gd-H_2O	Anomaly	1	7	170	202	1195
22 m Gd-H_2O	Measurement	3	9	218	256	1403
22 m Gd-WbLS	Anomaly	1	3	67	78	237
22 m Gd-WbLS	Measurement	2	5	90	105	287

Table 7.9: Results summary for AGR signals using the LEARN data reduction with the likelihood method described in subsubsection 6.2.2.2. The dwell time is given in days and is the observation time for a 3σ significance detection.

Detector	Scenario	Size-Hink-Grav	Hink-Grav	Size-Hink
16 m Gd-WbLS	Anomaly	1186	2541	10732
16 m Gd-WbLS	Measurement	1433	2968	12238
22 m Gd-WbLS	Anomaly	287	615	2357
22 m Gd-WbLS	Measurement	347	720	2694

"Size" = Sizewell B, "Hink" = Hinkley Point C, "Grav" = Gravelines

Table 7.10: Results summary for PWR signals using the LEARN data reduction with the likelihood method described in subsubsection 6.2.2.2. The dwell time is given in days and is the observation time for a 3σ significance detection.

The number of events remaining after each step of the data reduction for Heysham 2 in the 22 m Gd-WbLS detector is shown for version 1 of the data reduction in Table 6.2 and for version 2 in Table 6.3. The updated radioactive singles rejection allows almost three times the number of pair events to pass through. This allows a more aggressive reduction in coincidence backgrounds such as IBD from other sources and fast neutrons, by optimising the energy cuts and training the machine learning to reject all fast neutrons. This can be seen by the significant increase in the number of events removed by the machine learning and energy cut steps.

The rates for Heysham 2 in the Gd-WbLS detectors for version 1 and 2 of the LEARN data reduction are compared in Table 7.11, and the anomaly sensitivity metrics with observation time are shown in Figure 7.1. The signal and backgrounds are approximately doubled by the new reduction. This allows a more aggressive treatment of fast neutrons, removing them almost completely. As fast neutrons carry a 27 % systematic uncertainty, removing them yields a large improvement in detector sensitivity. The overall background uncertainty increases much less than the signal rate due to the removal of fast neutrons and the new optimisation.

The rates for Heysham 2 for all detector designs using LEARN version 2 are presented in Table 7.12, with the anomaly significance shown in Figure 7.2. The larger detector with Gd-H_2O is able to obtain higher signal and background rates than the smaller detector with Gd-WbLS, and the newer data reduction obtains similar rates for the 22 m Gd-H_2O detector as the first version did for the 22 m Gd-WbLS detector (Table 7.11). However, the machine learning has not been as successful at suppressing fast neutrons for the 22 m Gd-H_2O detector, resulting in a higher background uncertainty

Detector	Version	s	Σb_i	^{9}Li & ^{17}N	Fast n	$\text{IBD}_{\text{reactor}}$	geo	$\sigma(\Sigma b_i)$
16 m Gd-WbLS	1	0.024	0.14	0.044	0.010	0.079	0.0072	0.0043
	2	0.056	0.29	0.090	0.0023	0.18	0.018	0.0078
22 m Gd-WbLS	1	0.13	0.71	0.21	0.047	0.39	0.057	0.024
	2	0.23	1.15	0.36	0.0058	0.71	0.071	0.031

Table 7.11: Representative rates per day for both LEARN versions from optimisation in both Gd-WbLS detector configurations for the Heysham 2 signal. Accidental coincidences are omitted as they are sub-dominant backgrounds, with a rate consistent with 0.

relative to the total background rate. This causes the sensitivity to approach its limit more quickly for this detector, and is the reason that the significance increases slower at larger times in Figure 7.2 than for the 16 m Gd-WbLS detector.

Detector	s	Σb_i	^{9}Li & ^{17}N	Fast n	$\text{IBD}_{\text{reactor}}$	geo	$\sigma(\Sigma b_i)$
16 m Gd-H_2O	0.021	0.13	0.036	0.0020	0.0086	0.0053	0.0030
16 m Gd-WbLS	0.056	0.29	0.090	0.0023	0.18	0.018	0.0078
22 m Gd-H_2O	0.12	0.75	0.22	0.095	0.39	0.035	0.030
22 m Gd-WbLS	0.23	1.15	0.36	0.0058	0.71	0.071	0.031

Table 7.12: Representative rates per day for both fill media for the Heysham 2 signal using LEARN version 2 as the data reduction. Accidental coincidences are omitted as they are sub-dominant backgrounds, with a rate consistent with 0.

The improvement to the data reduction fundamentally changes the utility of the detector. Where it would previously take approaching two years to observe a reactor complex at ∼150 km in the most sensitive detector, it could now take as little as two months. The measurement of the reactor signal at ∼150 km in the signal-plus-background scenario would take only three months. Even without WbLS, a 22 m detector could still make the same measurements in six to nine months using technology already deployed in EGADS and SK. This makes the use of neutrino detectors a very real prospect for reactor monitoring, and it could be paired with other safeguards for non-proliferation purposes in a co-operative monitoring environment.

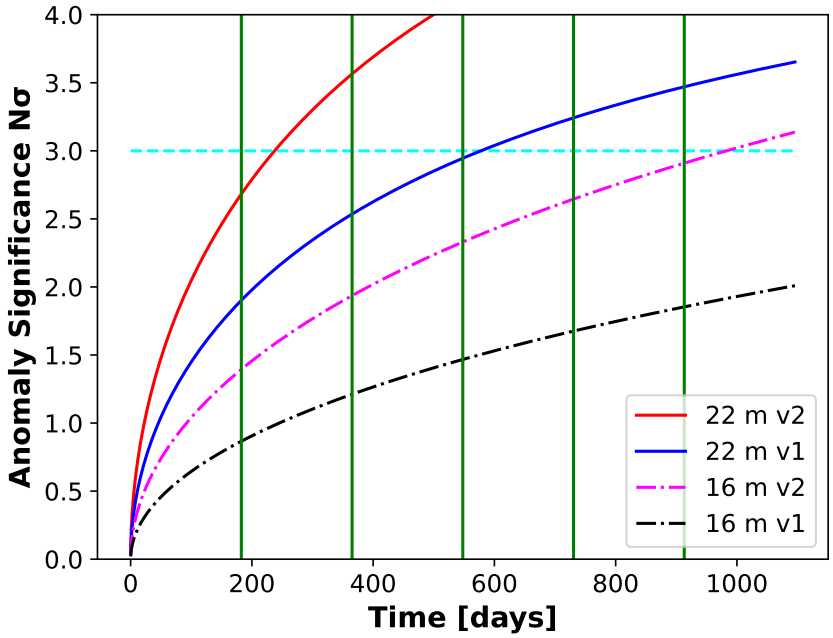

Figure 7.1: The significance for anomaly detection of Heysham 2 over three years of observation for the Gd-WbLS detector fill using both versions of LEARN. The vertical solid green lines represent six-month intervals, the horizontal dashed cyan line is the 3σ significance threshold for observation.

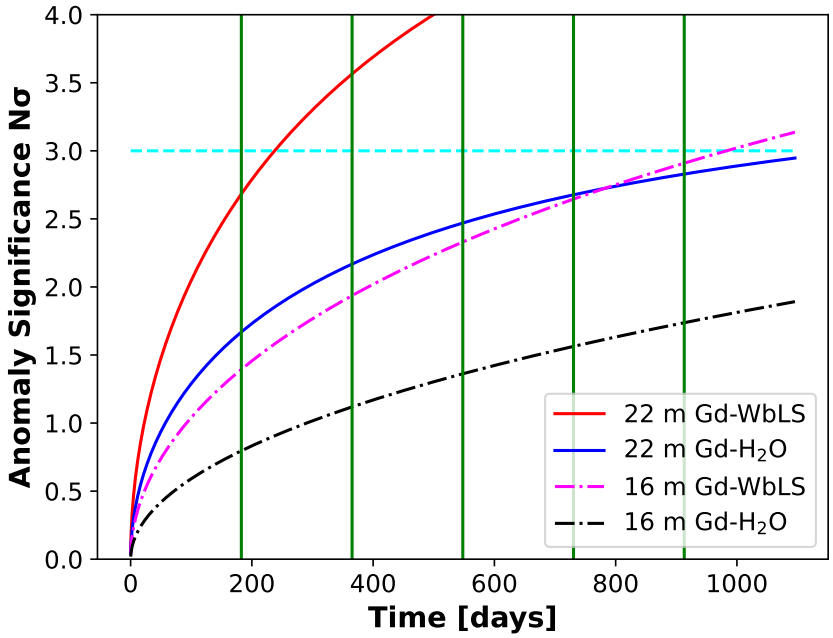

Figure 7.2: The significance for anomaly detection of Heysham 2 over three years of observation for all detector designs using LEARN version 2. The vertical solid green lines represent six-month intervals, the horizontal dashed cyan line is the 3σ significance threshold for observation.

7.2 Remote Reactor Ranging

The data reduction in chapter 6 and optimisation in section 7.1 form a rate-only analysis. As such, this analysis does not reveal information beyond the operation of a core. The observed spectrum can be used to extend this analysis.

Due to neutrino flavour oscillation, the distance to a neutrino source can be determined from the detected spectrum (subsection 1.2.3). As reactor antineutrinos are both emitted and detected as electron flavour, the survival probability of electron flavour antineutrinos is of importance (Figure 7.3).

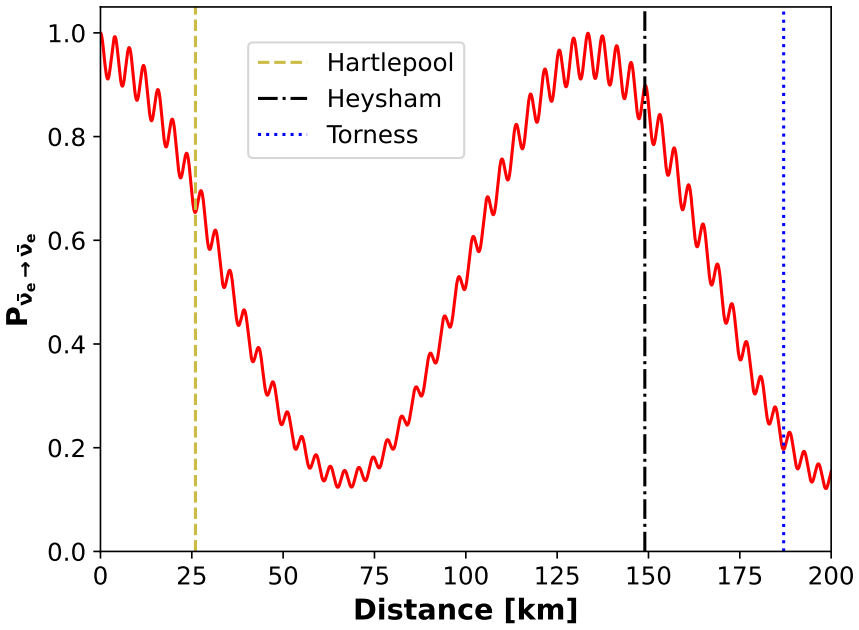

Figure 7.3: The survival probability of 4 MeV electron antineutrinos as a function of distance they travel.

By applying spectral analysis to the reduced data, the distance to a reactor can be determined. This could be a useful tool in the reactor monitoring arsenal as it could provide supporting evidence for whether a reactor is responsible for the observed signal e.g., by determining the distance to the reactor or showing that the spectrum is not consistent with expectation for known operations. Figure 7.4 shows how the reactors in the UK fleet can be resolved if their distance can be determined.

Spectra and rates are taken directly from the LEARN data reduction output, and

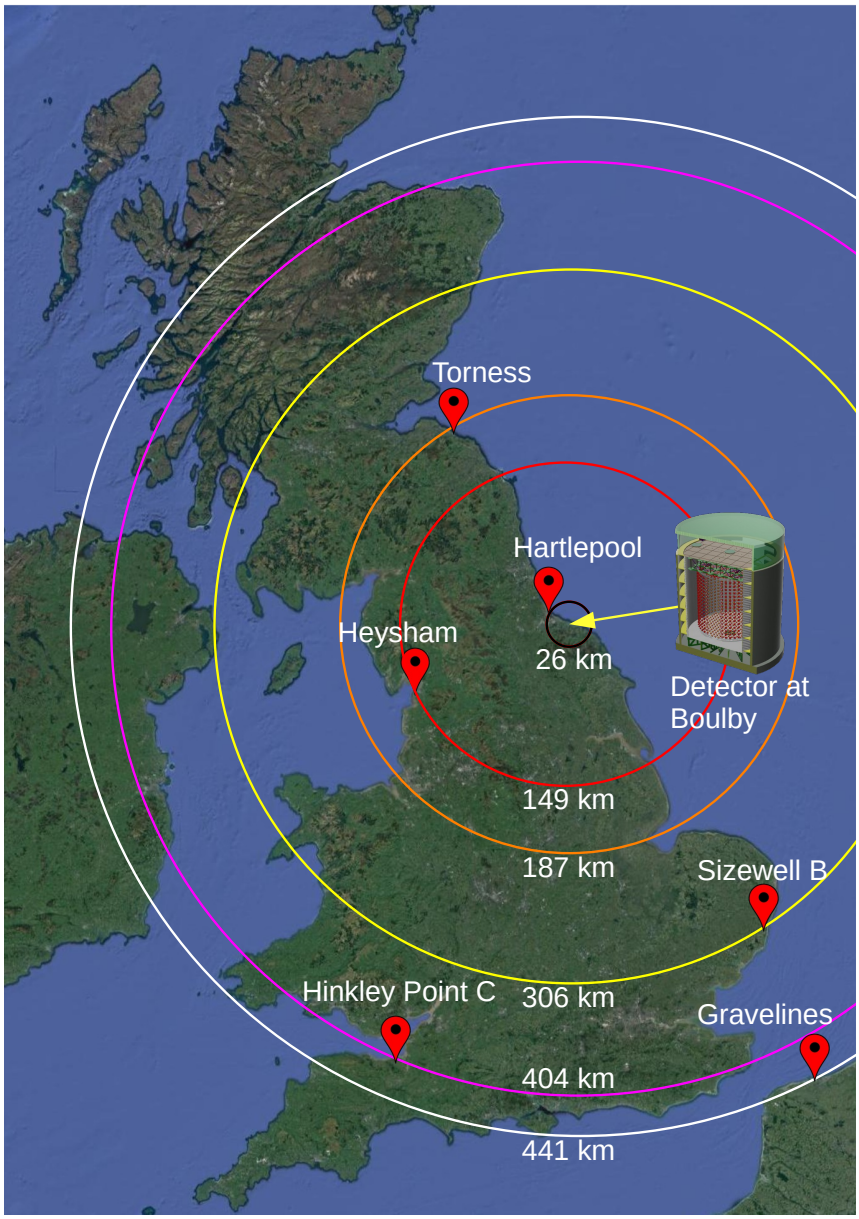

Figure 7.4: Map of the reactors analysed, with their distance to the NEO detector at Boulby shown as a circle on the map.

two spectral analyses have been developed and applied to the 22 m Gd-WbLS detector configuration. The choice of using the first or second version of the LEARN data reduction has a minimal impact on the observed spectra, affecting mostly the detected

rate. As such, all spectral analysis initially performed on the output of the first version of LEARN has been retained.

7.2.1 Background Inclusion

The impact of both backgrounds and energy resolution are tested by applying energy reconstruction and/or background uncertainties. This is done to test the limitations of both the detector and the analyses by determining what effects can be handled. The energy reconstruction is applied as in subsection 6.1.3, where a fit between simulated particle energy and PMT hits is applied. To remove energy resolution effects, the simulated MC particle energy is used.

To apply background uncertainties, it is assumed the background rates are known at the rates observed in subsection 7.1.3 with some Gaussian uncertainty, and can be suppressed so only fluctations due to their uncertainties will impact the observed spectrum. For each bin in the observed spectrum for the target reactor, a rate is drawn from the uncertainty distributions and combined with the reactor rate for that bin. As the background rates can fluctuate up or down due to their uncertainties, when combined with the signal, it can cause the observed signal rates to fluctuate. The uncertainties are those in Table 5.6, and are from uncertainties in the modelling of incident rates for each background component. However, energy-dependent detector systematic uncertainties are not included.

To determine the uncertainty on the range caused by background uncertainties and statistical fluctuations, each "observation" is repeated one hundred times. An observation is defined as the determination of the range for a particular reactor after drawing from the background distributions once, with the number of events drawn corresponding to the length of observation. By repeating this, the effect of statistical fluctuations due to background systematic uncertainties on the determined range are accounted for.

The impact of both energy resolution and background uncertainties are assessed on the nearer AGRs, but only the energy resolution is included for the more distant PWRs due to the small signal which is obscured by background uncertainties, as seen in Figure 7.5. In the case of the Hartlepool cores, the assumption that backgrounds are suppressed is not used. Instead, all backgrounds remaining after data reduction including their uncertainties are applied, and full energy reconstruction is used.

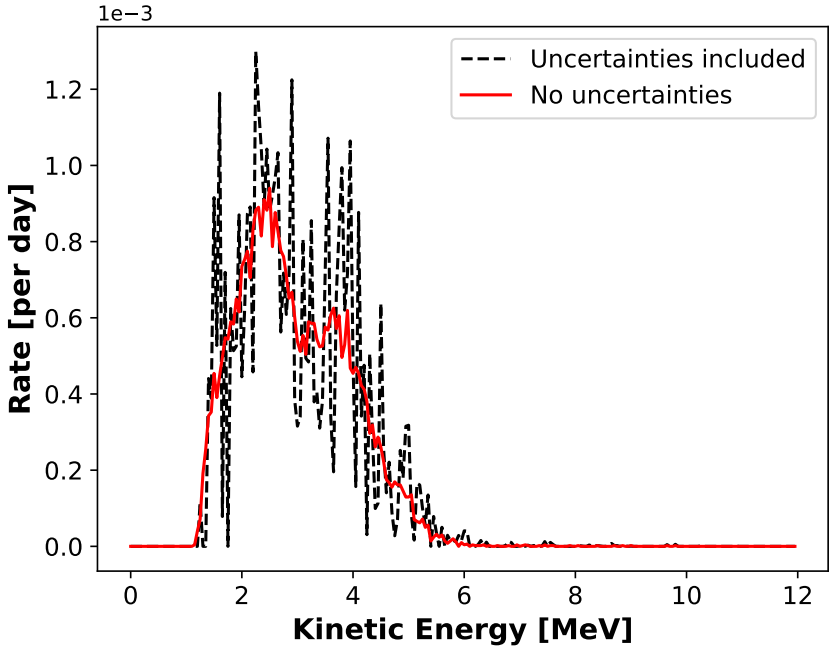

Figure 7.5: The reconstructed energy spectrum for a single observation of Hinkley Point C with (dashed black) and without (solid red) background uncertainties included after data reduction using version 1 of LEARN. A description of the application of background uncertainties is given in the text.

7.2.2 Minimum Chi-Squared Analysis

The first spectral analysis uses a minimum chi-squared method. This method minimises the difference between the positron spectrum from analysis from LEARN and models produced using Equation 5.4 with the antineutrino energy converted to detected positron kinetic energy. The chi-squared is given by

$$\chi^2 = \sum_i \frac{(\Phi_i - f_i)^2}{f_i}, \tag{7.6}$$

where f_i is the value of Equation 5.4 for a given distance and the energy corresponding to the i_{th} bin, and Φ_i is the data content in the i_{th} energy bin. This method aims to match the pattern of the observed spectrum to a model, with the best match corresponding to the minimum chi-squared. Both the spectra after data reduction and Equation 5.4 are normalized to a maximum of 1 to mitigate the effects of reactor power. The distance for the model reactor is incremented between 0 and 500 km at 0.1 km intervals and the

value of Equation 7.6 indicating the difference between the data reduction output and the model is minimised to yield an "observed" range for a reactor.

7.2.3 Fourier Transform Analysis

The second spectral analysis is a Fourier Transform (FT) analysis. As shown in Equation 7.8, the oscillation probability of one neutrino flavour state to another is proportional to $\sin^2(\frac{1.27\Delta m^2_{ij}L}{E_{\bar{\nu}}})$, where Δm^2_{ij} is the square of the mass difference between flavours i and j, L is the distance the antineutrino travels and $E_{\bar{\nu}}$ is the energy of the antineutrino. As such, the oscillation of neutrino flavour is sinusoidally dependent on the distance of travel and energy of the neutrino. The kinetic energy of the positrons from IBD can be measured and the antineutrino energy determined from this, meaning a FT can be used to switch from antineutrino energy to the distance of travel.

The survival probability of an electron flavour antineutrino is given as

$$P(L, E_{\bar{\nu}}) = 1 - P_{ex}, \tag{7.7}$$

where

$$\begin{aligned} P_{ex} = \cos^4(\theta_{13})\sin^2(2\theta_{12})\sin^2\left(\frac{1.27\Delta m^2_{21}L}{E_{\bar{\nu}}}\right) + \\ \cos^2(\theta_{12})\sin^2(2\theta_{13})\sin^2\left(\frac{1.27\Delta m^2_{31}L}{E_{\bar{\nu}}}\right) + \\ \sin^2(\theta_{12})\sin^2(2\theta_{13})\sin^2\left(\frac{1.27\Delta m^2_{32}L}{E_{\bar{\nu}}}\right), \end{aligned} \tag{7.8}$$

assuming charge-parity-time invariance [179]. Here, θ_{ij} is the mixing angle between flavours i and j.

As the oscillation probability depends on $\sin^2(\frac{1.27\Delta m^2_{ij}L}{E_{\bar{\nu}}})$, the identity $\sin^2(\theta) = \frac{1-\cos(2\theta)}{2}$ can be used to express the FT as

$$\mathrm{FCT}(L) \propto \int_{\frac{1}{E_{max}}}^{\frac{1}{E_{min}}} f(L, E_{\bar{\nu}}) \cos\left(2 \times \frac{1.27\Delta m^2_{ij}L}{E_{\bar{\nu}}}\right) d\frac{1}{E_{\bar{\nu}}}. \tag{7.9}$$

Here, Equation 7.9 is defined as a Fourier Cosine Transform (FCT). A $\frac{\pi}{2}$ phase shift can be applied for a Fourier Sine Transform (FST).

$$\mathrm{FST}(L) \propto \int_{\frac{1}{E_{max}}}^{\frac{1}{E_{min}}} f(L, E_{\bar{\nu}}) \sin\left(2 \times \frac{1.27\Delta m^2_{ij}L}{E_{\bar{\nu}}}\right) d\frac{1}{E_{\bar{\nu}}}. \tag{7.10}$$

The difference between the FCT and FST due to the phase shift can be used to improve the precision of the analysis by combining the two. As the distance is varied, the peak amplitude of the FCT and the zero amplitude values of the FST are the points of interest that correspond to the "observed" range. The FCT can be used to determine the range due to the peak, and the steep gradient around the value of zero for the FST can be used to reduce the uncertainty. Figure 7.6 shows how the FCT and FST can be used in combination to reduce the possible ranges responsible for the detected spectrum by only considering the regions in which they match. This can halve the uncertainty on the observed range.

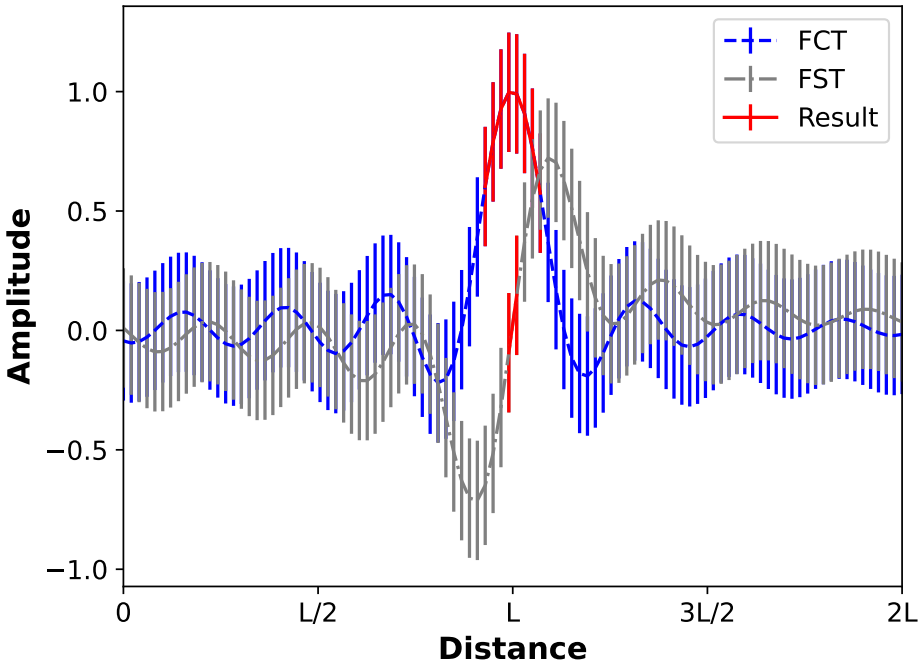

Figure 7.6: The combination of an FCT (blue dashed) and FST (grey solid) allows the area of interest (red solid) to be narrowed down to reduce uncertainties by comparing where the maxima of the FCT and zeroes of the FST occur at matching distances.

Both Equation 7.9 and Equation 7.10 include terms not associated with neutrino oscillations within the term $f(L, E_{\bar{\nu}})$. To isolate the oscillation terms, a spectrum where no oscillations are assumed is simulated i.e., the model in Equation 5.4 but only including the terms from Equation 5.2 and Equation 5.3 (i.e. the survival probability $P(L, E_{\bar{\nu}}) = 1$). A FT is performed on this spectrum, and it is then subtracted from the one performed on the original spectrum. The effect of this can be seen clearly in

Figure 7.7, where the peak associated with factors not related to neutrino oscillations is removed.

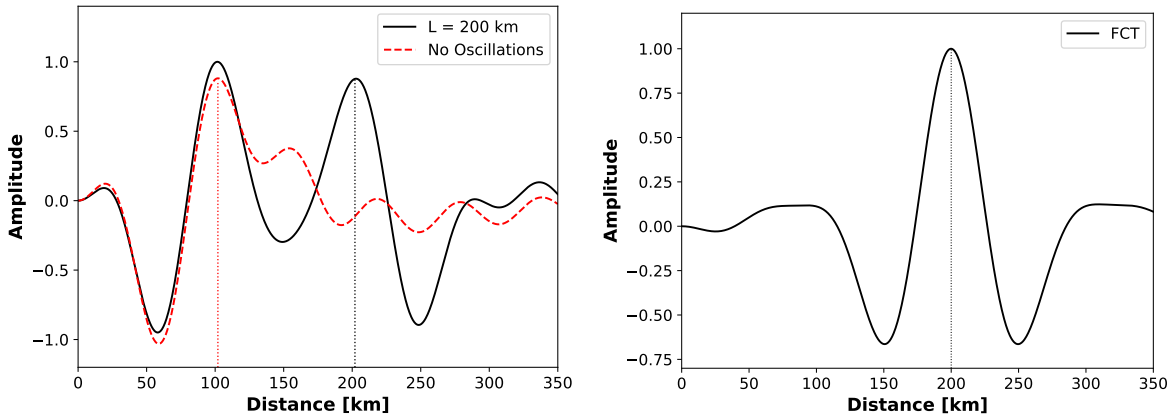

(a) (b)

Figure 7.7: (a) Comparison of the FCT for oscillations (black solid) and no oscillations (red dashed) in the reactor spectrum modelling for a 200 km standoff distance, and (b) the subtraction of the no oscillation situation from the original reactor model for the same reactor standoff. The reactor model has peaks for 100 km and 200 km before the subtraction, and only the expected peak at 200 km after subtraction.

Due to the detector resolution, only the θ_{12} oscillation pattern can be resolved. As such, the FTs are normalized to the θ_{12} term, and θ_{13} and θ_{23} are neglected. This creates a lower limit to the range that can be observed with this method, as at least one full wavelength of the oscillation pattern must be visible in the spectrum for a FT to work. Figure 7.3 shows how the larger changes in electron antineutrino survival probability due to θ_{12} do complete a cycle until over 100 km distance of travel. The oscillations due to θ_{13}, that occur at short distances, produce much smaller changes in the survival probability. A lower limit of approximately 80 km, due to the requirement of a full wavelength of the oscillation pattern, can be seen in Figure 7.8.

7.2.4 Ranging Results

7.2.4.1 Minimum Chi-Squared

For the minimum chi-squared method, a single analysis was performed. This was the ranging of the EDF Hartlepool reactor with all limitations, such as complete backgrounds including uncertainties and detector effects, considered as part of the dwell

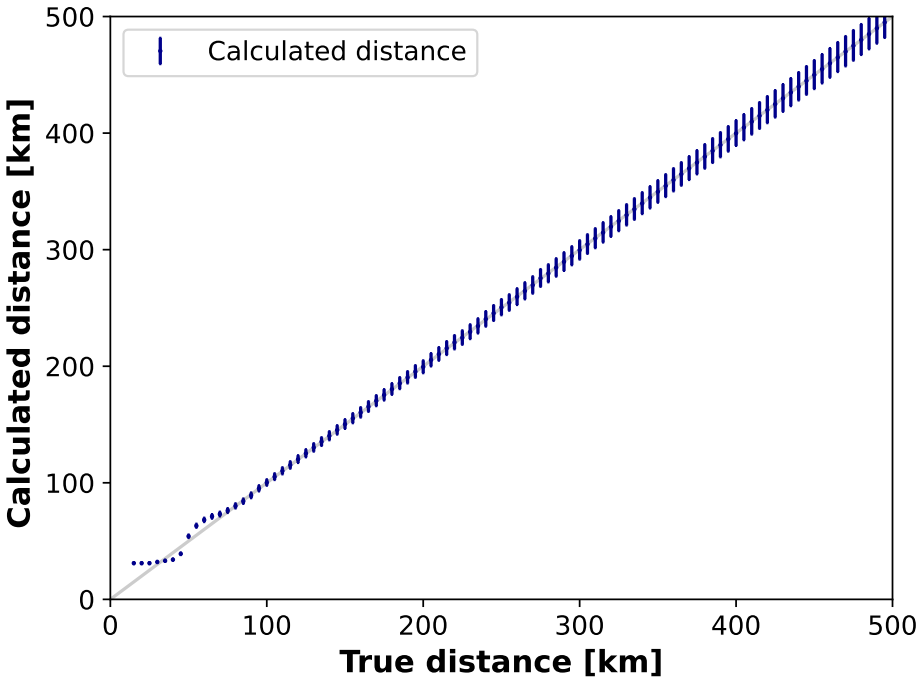

Figure 7.8: The calculated range of reactor signals with true distance using the Fourier transform analysis applied to Equation 5.4. The FT relies on resolving the θ_{12} oscillations, which are not obviously present at ranges below 100 km, as the θ_{13} oscillations are smaller than the detector's energy resolution.

time analysis with the LEARN analysis chain. The obtained range, shown in comparison to the true range in Table 7.13, is 50 % from the expected value. The uncertainty on the result is determined by repeating the analysis one hundred times to allow the effect of fluctuations in the detected spectrum, due to background and statistical uncertainties, and to be observed.

	True	Chi-squared
Distance (km)	26	39 ± 1

Table 7.13: Observed distance in km for the chi-squared method for Hartlepool.

Hartlepool is the dominant signal after data reduction, so assuming all backgrounds are known only improves the observed range slightly to ∼35 km. The biggest cause of the discrepancy between the observed and true range is the depletion of the low energy events caused by the data reduction. To remove the numerous radioactive background

triggers, low energy cuts are applied. This reduces the low-energy event rate more than the higher energy events, biasing the spectrum to higher energy. The detector also has an increasing efficiency with increasing energy as the light yield increases. This further biases the spectrum toward higher energy events, causing the spectrum to appear to shift to higher energy after data reduction, impacting the observed range. The impact on the observed spectrum in comparison to the models for the true range at 26 km and observed range at 39 km can be seen in Figure 7.9a and Figure 7.9b respectively.

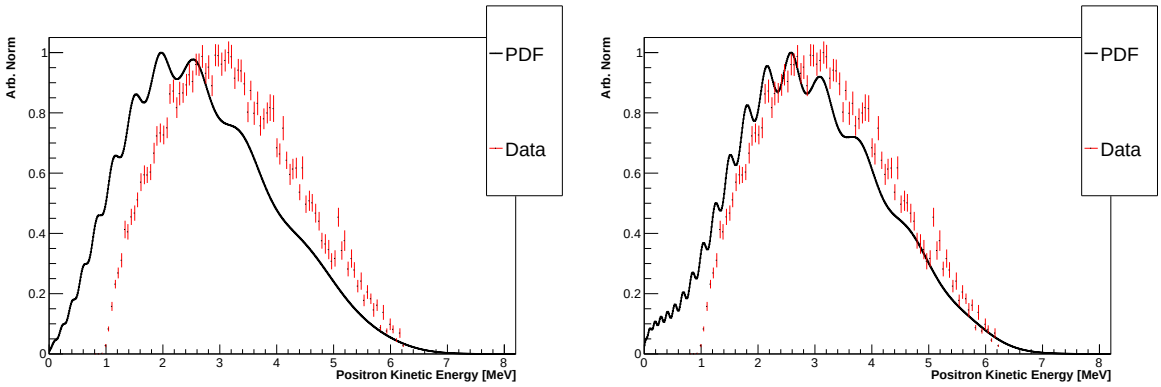

(a) (b)

Figure 7.9: Comparison of the analysed Hartlepool reactor complex spectrum (red points) and models (black solid line) for the (a) true range of 26 km and (b) observed range of 39 km. The shift to higher energy after data reduction can be seen. This shift limits the ability to range the reactor as the shape of the spectrum is used to determine the range. All spectra are normalised to a maximum of 1.

The observation time needed to range Hartlepool to this accuracy is 12 (40) months for the second (first) version of the data reduction, with the uncertainty dropping to a consistent level in Table 7.13 by around 18 (50) months, as demonstrated by Figure 7.10.

Due to the simplicity of the method, and the need for a signal-dominated spectrum, this analysis is not appropriate for higher-background situations such as more distant reactors. This analysis matches the shape of a spectrum to a model, which requires the detected spectrum to have the shape of the expected reactor spectrum to be effective. Due to the matching of a shape to a model, overlapping spectra causes further issues. If the observed spectrum does not well-represent the reactor being observed, this analysis will not be able to determine an accurate range. Further analysis would be required to isolate a complete reactor spectrum for this method to be effective at larger distances.

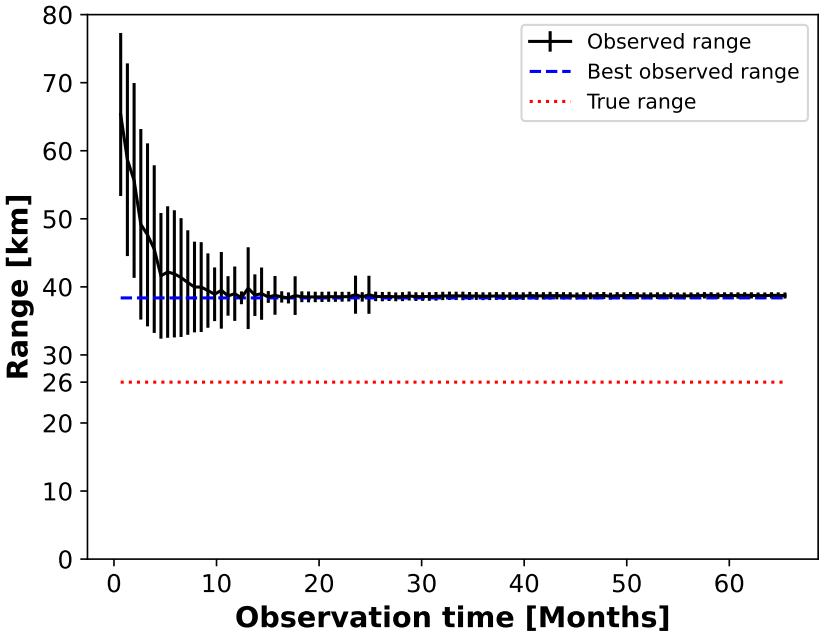

Figure 7.10: The observed range of the Hartlepool reactor complex with observation time using the second version of LEARN.

7.2.4.2 Fourier Transform

The Fourier Transform (FT) method is applied in four possible scenarios on five reactor complexes. The scenarios are combinations of including background uncertainties and detector energy resolution.

The results of the FT method shown in Table 7.14 show that for reactors at large distances, the range can be determined when the detector's energy resolution is accounted for. However, reactors beyond 300 km do not have a large enough signal to be ranged effectively when background uncertainties are included. The two nearer reactors, AGRs at Heysham and Torness, can be ranged close to the true value when background uncertainties are included.

As shown in Figure 7.8, reactors within approximately 80 km of the detector cannot be accurately ranged by the FT method. As such, the EDF Hartlepool cores were not ranged as part of this analysis.

Uncertainties are determined by repeating the FT, sampling from the background distributions separately each time. This produces a range of possible FTs, which fluctuate due to background uncertainties. These fluctuations can be seen in the FCT

Situation	Range [km]				
	Heysham 2	Torness	Sizewell B	Hinkley Point C	Gravelines
True Range	149	187	304	404	441
No Background, True Energy	148 ± 4	188 ± 5	306 ± 8	403 ± 11	440 ± 11
No Background, Reconstructed Energy	157 ± 4	195 ± 5	307 ± 8	397 ± 11	432 ± 11
Background Uncertainty, True Energy	156 ± 6	177 ± 10			
Background Uncertainty, Reconstructed Energy	155 ± 5	171 ± 9			

Table 7.14: Observed distance in km for the FT method. Both the true energy and reconstructed energy are considered, as is the inclusion of background uncertainties and the situation of zero background uncertainty. Situations with a slash are deemed impossible to range due to background uncertainties dominating.

for Heysham 2 in Figure 7.11, where the spectrum has been produced from signal and backgrounds one hundred times and the analysis repeated. This results in a range of possible amplitudes for every distance for both the FCT and FST. The range of amplitudes is then used to determine the uncertainty on the amplitudes from the FTs. The uncertainty on the observed distance is then determined by the range of distances that fall within the uncertainty of the amplitudes accepted by both the FCT and FST.

The FT for Heysham 2 with background uncertainties and with energy reconstruction applied is shown in Figure 7.12. The maximum for the FCT yields an accurate range, but with an uncertainty of ± 15 km. The FST is able to reduce this uncertainty significantly to ± 6 km, shown in Table 7.14.

Due to the low event rates for the distant reactors, it takes over 20 years of observation time to be able to range the Heysham 2 complex, and significantly longer for the more distant reactors.

7.2.5 Discussion

The results of both methods show the potential of using neutrino oscillation to determine the distance to an observed reactor, as well as the use of extending the sensitivity analysis to include a spectral analysis. The two analyses presented complement each other well, with the minimum chi-squared analysis allowing nearby reactors with a large signal contribution to be ranged, and the Fourier Transform (FT) method allowing the ranging of more distant reactors.

Despite showing potential, there are strong limitations to both methods. Whilst the chi-squared method can handle lower energy resolutions for mid-field reactors, the

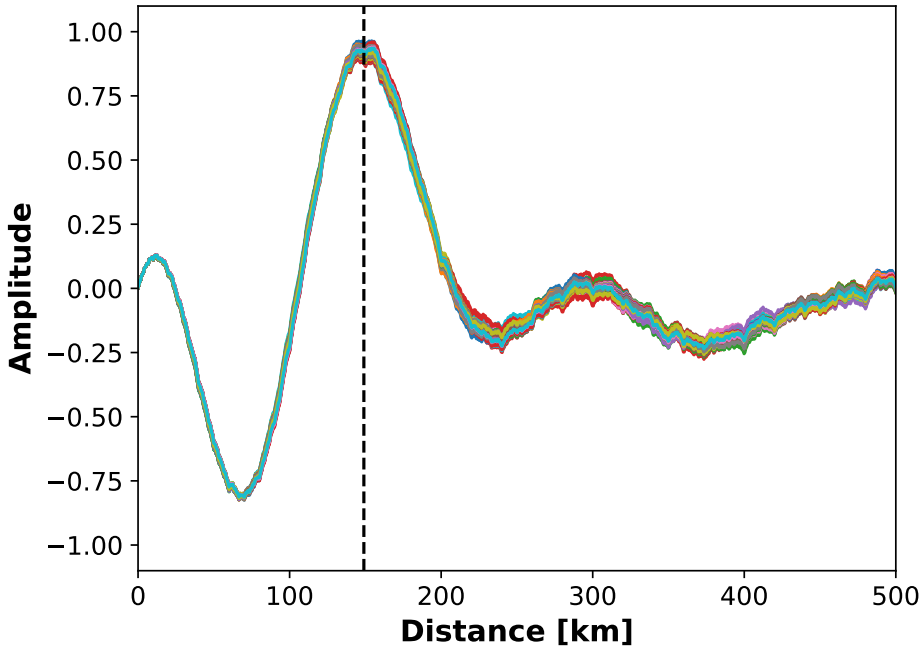

Figure 7.11: FCT analysis of Heysham 2 repeated 100 times to show the effect of fluctuations due to background uncertainties. Reconstructed energy is used here. The vertical dashed line at 149 km is the true distance to Heysham 2 from Boulby.

energy threshold and detector efficiency strongly limits the utilization of lower energy events. This causes the discrepancy between the true and observed range for the Hartlepool reactors.

The FT method is able to range reactors in more complex scenarios. However, the event rate for these distant reactors results in this taking a long time, in excess of 20 years, and therefore being impractical.

A relaxing of the level of measurement precision may allow a ranging analysis to occur more quickly, allowing it to have more utility. The results quoted are the best results where the most precise values are obtained based on the data reduction and rate-only analysis previously performed. However, if instead of a precise measurement, a determination of whether the observed spectrum is consistent with expectation for the expected reactor operation is acceptable, a quicker result may be obtained. In this case, rather than matching an exact model, showing the spectrum does not match the expected shape or FT would be a positive result, particularly if it is in combination with an observation of excess signal from the rate-only analysis. The FT analysis could also be applied to remove signals from known reactors from the data. If their distance

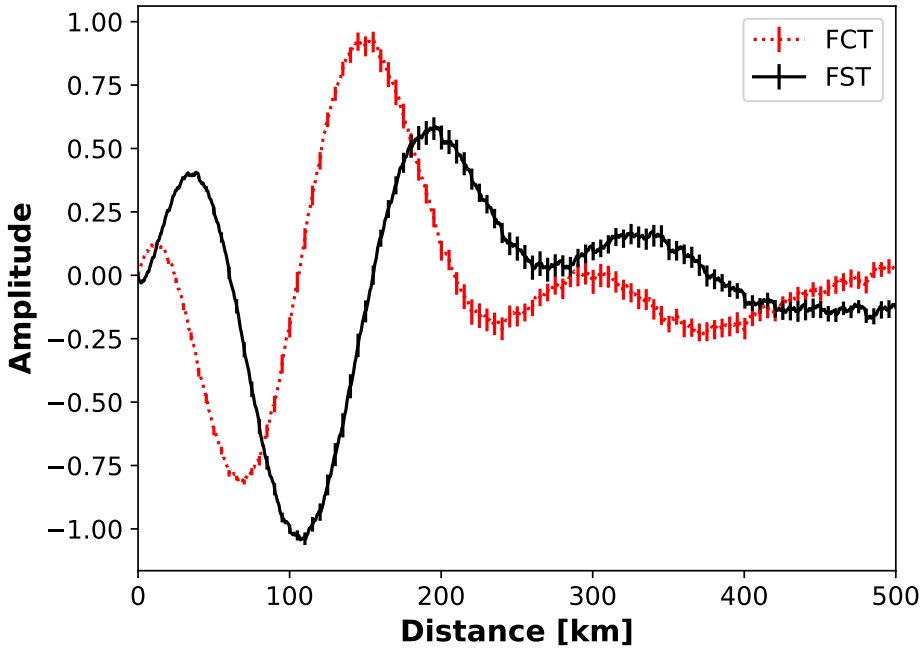

Figure 7.12: The Fourier transform, in sine (black solid) and cosine (red dotted), for Heysham 2 with background uncertainties and energy resolution effects.

can be extracted using a FT, the component of the observed spectrum due to known reactor operations could be subtracted.

This detector configuration is not able to make the best use of spectral analysis. A potential solution is using gadolinium-loaded liquid scintillator. This would lower the energy threshold, boost detector efficiency at low energies and improve energy resolution. In principle, this could allow the FT method to work at much shorter ranges by resolving the θ_{13} oscillations or allow the chi-squared method to range Hartlepool with much more accuracy. The FT analysis could give an accurate range to a mid-field reactor in months by using the better energy performance of a liquid scintillator combined with the increased signal rates it would yield.

7.3 Conclusions

The performance of four NEO detector configurations for reactor antineutrino detection and monitoring has been analysed. The detector designs are chosen as maximal and minimal options to fit inside a 25 m cavern constructed at STFC's Boulby Underground Laboratory in North Yorkshire, UK. Two designs have been considered, both right

cylinders, a 16 m height and diameter and a 22 m height and diameter tank. Two fill media have also been considered, water and WbLS, both of which are doped with the neutron capture agent gadolinium to harness the coincident-pair signal of IBD. Both tank designs have a 15 % photocoverage, the previously determined minimum viable coverage for useful sensitivity.

Full MC simulations were performed for all signals and backgrounds, with a complete reconstruction-data reduction-analysis chain developed to determine the optimal sensitivity to several real reactor signals in the UK and France. The data reduction, LEARN, is a novel path combining likelihoods and machine learning for background rejection, and is a different approach to the previous cuts-based analyses used for reactor monitoring prototypes [5, 350].

Comparisons have been made to the results obtained by the best-performing cuts-based analysis Cobraa for the purpose of cross-checking and validating results. From the comparisons in subsubsection 7.1.3.1, it can be seen that the 16 m detector is suited to observing the nearby signal from Hartlepool, but lacks any significant sensitivity to signals at large distances. The inability to detect anything other than very dominant signals in a reasonable time-frame precludes this detector from any real world use case, limiting it to being a research and prototype design.

The larger detector offers significantly more sensitivity, being able to observe a four-core signal in around 6 months, and the single-site signal from Heysham 2 at 149 km in 19 months. Cobraa showed that this detector has some sensitivity with Gd-H_2O, with dwell times for anomaly detection taking $\sim$50 % longer than with the inclusion of WbLS. The 22 m Gd-WbLS detector is able to reach 2σ anomaly significance in 205 days for Heysham 2 using LEARN version 1, shown by Figure 7.13. This may be deemed sufficient in some cases when paired with other monitoring techniques.

The general agreement in the results between the two independent reconstruction-analysis chains creates trust in the results. There are some differences in the results, however. The percentage differences in the Hartlepool results can be somewhat neglected. The short dwell times and quoting results to the nearest day yields larger percentage differences in the 16 m detector. The other large difference comes from the Heysham 1 & 2 and Heysham 2 & Torness results. LEARN consistently finds higher dwell times for the Heysham 1 & 2 complex than for Heysham 2 & Torness, but Cobraa sees the reverse trend. This difference arises due to the differing principles on which the data reductions are constructed. LEARN suppresses particular background compo-

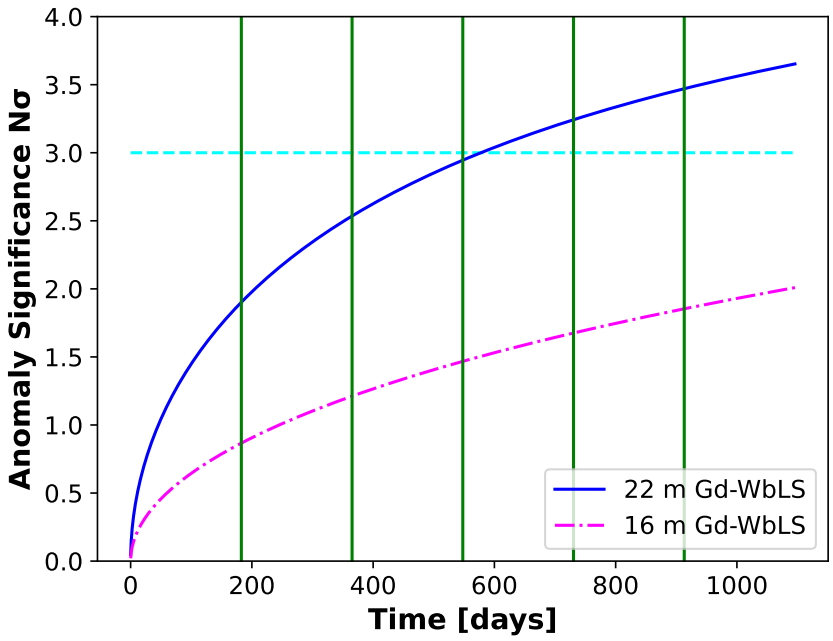

Figure 7.13: Sensitivity of the two detector sizes with Gd-WbLS to Heysham 2 using LEARN version 1 as a function of observation time. The vertical solid green lines represent six-month intervals, the horizontal dashed cyan line is the 3σ significance threshold for observation.

nents before optimisation of energy cuts for minimum dwell time; Cobraa optimises all cuts for minimum dwell time during data reduction. This results in LEARN typically favouring higher signal rates whereas Cobraa typically favours lower background rates. In the case of the combined Heysham complex, there is a higher signal and background when compared to the Heysham 2 & Torness scenario. As there is already a higher signal, and the Heysham spectrum peaks at higher energy, Cobraa is able to apply more aggressive cuts to reject backgrounds. In the case of Heysham 2 & Torness, the signal is lower but so is the background due to the assumption that the AGR-1 cores at Heysham 1 are decommissioned. This gives LEARN a lower background to contend with and allows it to boost the accepted signal rate. As a result, LEARN is more successful in analysing this scenario. Being able to explain and justify these differences, and noting small differences elsewhere, breeds confidence in the analysis chains.

Despite the good agreement and the possible acceptance of a 2σ anomaly measurement when combined with other safeguarding methods, taking several months to

make an observation leaves a significant amount of time for reactor misuse and the redirection of nuclear materials. A larger detector would improve these dwell times and extend the range of detection, but this would create significant added costs. Due to this, the Nu Tools report [145] commissioned by the Office of Defense Nuclear Non-proliferation (DNN) to provide an assessment of the utility of neutrino detectors for non-proliferation stated

> "Non-Cooperative Reactor Monitoring or Discovery: Implementation constraints related to required detector size, dwell time, distance, and backgrounds preclude consideration of neutrino detectors for non-cooperative reactor monitoring or discovery."

However, Nu Tools does not preclude cooperative monitoring and leaves space for future applications, with the recommendation that support for

> "neutrino detector system development for areas of potential utility, principally for future nuclear deals and advanced reactors"

should be maintained. This allows reactor exclusion in the mid-field to remain a potential use case, with proposed Small Modular Reactors (SMRs) being considered near the existing Hartlepool complex providing a potential test case in the future.

To demonstrate that this is possible, further sensitivity needed to be found. This is where the improvements to LEARN become relevant. As only one section of the path was changed from the version validated with Cobraa, it is assumed that this analysis is still validated. Significant improvements in sensitivity are seen, with dwell times coming down by a factor of more than $\sim$2. The 22 m Gd-WbLS detector is able to reach 2σ for Heysham 2 in 3 months, and the 16 m detector can do it 13 months (Figure 7.14). These significant improvements extend the range of the detector monitoring from 10's of km to potentially 100's of km under the future nuclear deals and advanced reactor scenarios that Nu Tools states neutrino monitoring is relevant for. The larger detector is able to measure the combined PWR signal to 3σ in under a year.

This improvement comes before the option of sideband analyses, in which reactor-off periods can be used to make background measurements to input into the data reduction. This would potentially allow even greater sensitivity to more distant reactors. However, reactor-off times differ depending on design. AGRs only have short shutdown periods for refuelling, so it is difficult to make reactor-off measurements. It also risks any clandestine operation being mixed in as a background, making it harder to detect.

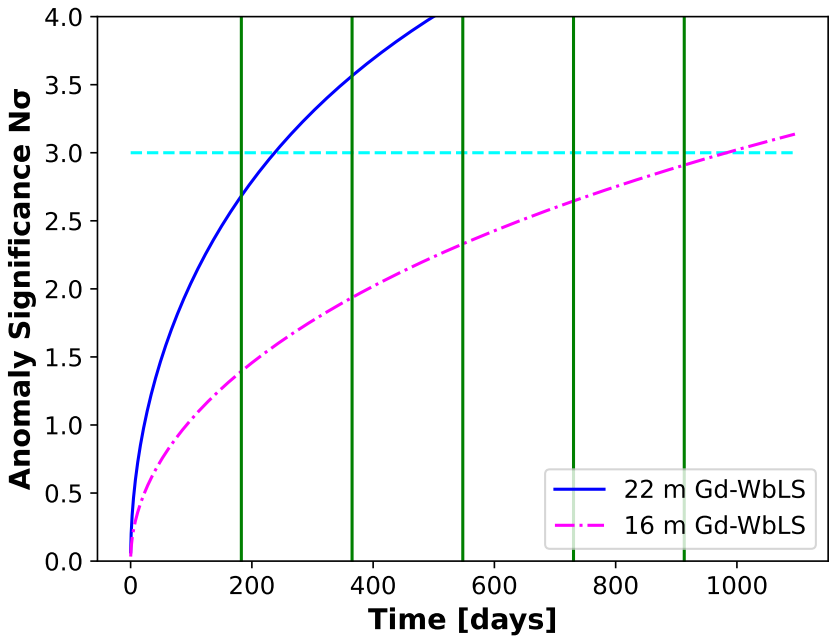

Figure 7.14: Sensitivity of the two detector sizes with Gd-WbLS to Heysham 2 using LEARN version 2 as a function of observation time. The vertical solid green lines represent six-month intervals, the horizontal dashed cyan line is the 3σ significance threshold for observation.

They may, however, allow better understanding of detector systematics and modelling uncertainties. The current analyses include modelling uncertainties as part of the significance, but no detector systematic uncertainties. This makes the impact of sideband analyses hard to understand completely until detector systematics are fully modelled.

Further improvement may be available in the LEARN chain if the entire data reduction is optimised for dwell time. Currently, the likelihood and machine learning steps are optimised to suppress an individual background. By combining steps, and optimising earlier, it may be possible that further improvement in either background reduction or signal maximisation can be found.

The rate-only analysis has been extended to include spectral analyses to harness neutrino oscillations to determine the distance to an observed reactor. The analyses show potential to range real reactor signals, but are significantly limited by the detector design. A minimum chi-squared analysis is able to range nearby reactors which produce a dominant signal well within the lifetime of this kind of detector, with the

EDF Hartlepool reactor ranged to 50 % of its true distance. A FT analysis is able to handle reactors at much larger standoff distances, up to 180 km, when background uncertainties are included. However, this would take a very large amount of time due to the low event rate, even with the improved data reduction.

With both analyses, the fundamental issue is the detector's performance. An order of magnitude increase in signal rate is needed to range the Heysham 2 cores at 149 km within a reasonable detector lifetime, and the energy thresholds and detector efficiency limit the ranging of more local reactors. Using gadolinium-doped liquid scintillator could offer a solution as it would improve energy resolution, lower the threshold and improve low energy efficiency.

Due to performance issues, the gadolinium-doped WbLS detection medium is not appropriate to use in precisely determining the distance to operating reactors. However, the analyses developed could be used with a more sensitive detector for this purpose.

One thing that has not been attempted at present, but could offer improvement, is combining the rate-only analysis with the spectral analyses for background reduction. The spectral analyses rely on the background having already been reduced, and are standalone analyses attached onto the end of the rate-only analysis. Combining the two could allow a quicker indication of whether the spectrum is consistent with expectation based on known backgrounds and reactor operation. Knowledge of the expected spectra and measurements of any signal above background could allow the spectral shape of the excess to be used. If the excess signal rate is large enough, it may allow ranging of the reactor in a shorter time. This could be improved further if combined with background-specific analysis, allowing background spectra to be subtracted from observations more easily. This could also be extended to use the FT analysis to remove known reactors from the observed spectrum if their standoff distance is extracted. Test beds, such as the planned BUTTON experiment at Boulby or WATCHBOY [362], may be required to make measurements of the background in advance of detector construction.

These improvements may allow much cheaper and smaller detectors to be viable for reactor exclusion at the 10's of km range, which would pave the way for real world applications of neutrino detectors in non-proliferation.

In Nu Tools, far-field monitoring is defined as a deployment at over 2 km from the reactor; in the study presented here, the Hartlepool cores at 26 km are considered a mid-field standoff, the reactors further away at over 149 km are considered far-field. Nu Tools states that long range monitoring is precluded by practicalities relating to the

construction of sufficiently large detectors to observe weak neutrino signals. However, the results obtained show that a 16 m detector with a Gd-H_2O fill, the smallest and most basic detector tested, could make an anomaly detection of Hartlepool in a week. This makes less intrusive monitoring at distance more of a possibility.

Although current safeguarding is generally seen as sufficient, particularly for power reactors, advanced reactor types present potential gaps in the techniques used. Research reactors already have documented cases of misuse surrounding them [144], such as diversion of material or production of neutron generators, so advanced reactors could create the same issues on a larger scale before safeguarding is able to catch up with reactor development.

Neutrino detectors could fill this safeguarding gap. It is expected that the neutrino emission rates follow similar trends for advanced reactors as the current designs, so neutrino detector design would remain unchanged. It was noted that the fact a "single system design could have broad applicability" was of interest in the non-proliferation community, and that non-proliferation experts generally expressed a need for "alternate technical methods" to ensure adequate safeguarding and where conventional methods such as item accountancy may no longer apply. Neutrino detectors are seen to "display potential" for this, with spectral measurements providing more information about core operation.

Cost is seen as a major barrier to the use of neutrino detectors for non-proliferation. Advanced reactors and their construction may allow detectors to become cost competitive if adopted early in the development cycle, with a "safeguards-by-design" principle being seen as attractive. The additional verification provided by neutrino detection would make the costs more viable if included at an early stage.

These conclusions from the Nu Tools study provide justification for the consideration of neutrino detectors for non-proliferation. The current technology may not be seen as cost-effective for the current reactor designs, but may become beneficial in the future. As such, the final recommendation from Nu Tools is to

> "conduct modeling and simulation studies that will evaluate potential performance of neutrino detectors in specific use cases".

The work presented so far acts as a significant step in determining the viability of neutrino detection for non-proliferation following this recommendation. The dwell times at distances Nu Tools considered far-field are significantly lower than previous analyses and information available at the time, and the spectral analyses show significant

potential to harness further information. These analysis improvements and extensions may alter the conclusions of future studies, and bring the neutrino detector into more immediate consideration for a role in non-proliferation and safeguarding. Further improvement is still required, particularly to reduce the limiting factors of detector size, construction and cost, to make neutrino monitoring completely viable, but the LEARN chain and additional spectral analyses show significant improvement on previous work, and still have areas available for improvement in the future.

Chapter 8

Future Work and Conclusions

Nuclear reactors have been a source of power generation for decades, but they also create contention due in part to their potential for weapons-grade material proliferation. Current treaties and safeguards, as administered by the IAEA, cover almost all current situations and risks. However, it is acknowledged that an evolving reactor landscape, in which advanced reactor types and new nuclear deals are developed, could lead to a gap in the safeguarding against the proliferation of weapons [145].

Nuclear reactors emit electron antineutrinos during the fission process. These antineutrinos have been observed and used for research since the very start of experimental neutrino physics, and have yielded a large amount of information about the neutrino. They have even been used to gain information about the reactor core from which they are emitted. By combining neutrino research with nuclear reactor power generation, the potential for applying neutrino detectors to reactor monitoring arises. Antineutrino monitoring would in principle reduce intrusion to reactor sites and be independent of the reactor-type being monitored, but its utility is unproven.

This thesis presents potential designs for a prototype far-field reactor antineutrino monitoring detector, a novel reconstruction-data reduction-analysis chain and the performance results of the detector designs. The characterisation of the technology required to construct this type of detector is also presented alongside a test bed facility for hardware testing.

8.1 Current Status of WATCHMAN and AIT-NEO

The EDF reactor cores in northern England and Scotland are vital to a reactor monitoring prototype to be viable at Boulby. However, the announcement of the acceleration of plans to decommission the AGR cores [363] effectively precluded Boulby as a site to host a detector such as NEO as part of AIT. This marked the end of the AIT-NEO project as planned for Boulby, and drew a close to the planning of construction.

This did not mark the end of the concept as a whole though. The simulation studies still provide a benchmark on the utility of applying neutrino detectors to reactor monitoring, and efforts on the development of neutrino technology for non-proliferation continue.

8.2 Boulby Underground Laboratory Development

Although the AIT facility will not be constructed at Boulby to host NEO, plans to expand Boulby with a new facility to host future experiments continue. The existing laboratory hosts BUTTON-30, a 30 T water-based test bed detector currently under construction, which will continue with some of the technology development initially planned for AIT.

A second laboratory at the same depth of the existing laboratory is being excavated, with this being a staging site for the construction of a larger experiment in a future deeper laboratory. Plans for a future phase of BUTTON with a 1 kT volume to be hosted at this second laboratory are under development.

A new, deeper laboratory is planned, with the hope of hosting a next generation dark matter detector such as XLZD. In many ways, this meshes with Boulby's past as a world-class facility capable of hosting the most advanced dark matter detectors better than a reactor monitoring prototype would.

8.3 Conclusion

Several key areas have been investigated as part of the study into the feasibility of a far-field reactor antineutrino monitor, and whilst the project in the form presented here may not be continuing, the work itself has not been fruitless.

In chapter 3, the design, operation, and stability of the 2-tonne PocketWATCH test

bed for hardware characterisation is presented. This facility is unique in the region, with full temperature control and constant water purification. In depth studies of the water quality show that it transmits light in the relevant wavelengths for Cherenkov radiation, and is also gadolinium-compatible. This allows it to host equipment in the conditions that would be experienced in SK or EGADS, as well as HK. PocketWATCH has measures to allow photosensors to be operated in single-photon mode, something which has been utilised in PMT characterisation and light injection testing.

As part of the development of detector technologies, Hamamatsu R7081 PMTs have been tested in detail. QA tests are described in section 4.5, which follow a standard procedure similar to many previous experiments. A subset of these PMTs were subjected a new testing regime, in which they were submerged in the PocketWATCH tank and characterised. A focus on the contributions to dark rate showed that the dark rate is medium-independent, but depends on several environmental conditions such as light exposure prior to testing. The main source of dark rate is thermionic emission from the photocathode, with the major background being photons produced in the detector. This testing is relevant to many particle detectors, as understanding the photosensors used is necessary to design and operate an experiement.

The main concepts and questions in this work relating to reactor antineutrino monitoring are answered by simulation studies of the NEO detector. The implementation of MC simulations is detailed in chapter 5, with a novel data reduction presented in chapter 6. The data reduction comprises likelihood and machine learning techniques, offering a departure from the previous cuts-based methods. The data reduction provides a significant improvement over previous studies, and shows potential for reactor antineutrino monitoring when combined with the sensitivity metrics defined in section 7.1. A further pair of spectral analyses make use of neutrino oscillations to determine the distance to observed nuclear reactors.

The key questions relate to the utility of a reactor neutrino detector for non-proliferation. Previous concepts for non-proliferation, in which far-field detectors could be used as a non-cooperative monitoring tool, have been ruled out for infrastructure and cost reasons [145]. However, advanced reactors and new nuclear deals lead to scenarios in which neutrino detectors are of use. Potential gaps in safeguarding arising in these scenarios could be mitigated by the early adoption of neutrino detectors. Antineutrinos are unshieldable and do not depend on external conditions, only the conditions of the core. They also allow a much less intrusive monitoring option than current safeguards,

and could provide a scientific facility and training programme to a host nation.

To be of use, a detector must be sensitive enough to observe a reactor. The cross-checked analysis in subsubsection 7.1.3.1 shows that a 22 m detector with a Gd-WbLS fill would have some sensitivity to reactors up to 150 km away, with a smaller 16 m detector sufficing for mid-field monitoring. These results suggest significant improvement is required in the analysis or detector to be used for reactor monitoring.

Improvement in the data reduction techniques yielded much more sensitivity, with these results in subsubsection 7.1.3.2. With the level of performance here, a larger detector could be used for cooperative monitoring at distances of 150 km and a smaller detector still shows useful sensitivity. The requirement for WbLS is also reduced by the data reduction improvements, allowing much simpler and cheaper detectors to be viable. The analysis developed for reactor observation can be extended to a spectral analysis. Using the effect of neutrino oscillations on the energy spectrum, the distance to an observed reactor can be determined. Although pure liquid scintillators offer the best performance here, using WbLS allows spectra to be used to improve the analysis of signal and background rates.

The work presented here shows that there exists potential to monitor reactors via their antineutrino emission. By demonstrating a large improvement in sensitivity due to analysis improvements, smaller and cheaper detector designs can be considered. Previously, difficulties implementing a neutrino detector for reactor monitoring relating to cost, detector size and complexity had precluded their use. However, the significant improvements found allow these detectors to be considered in the future by demonstrating the utility of simpler and cheaper designs.

The analyses developed have use beyond reactor monitoring. For many experiments, reactor neutrinos are a significant background. Being able to understand and suppress them can improve the sensitivity of these experiments. Other experiments use IBD as a signal, such as in the detection of supernova antineutrinos. Here, the data reduction and analysis presented can be used to extract the alternative signal. Overall, the data reduction and analysis chain offers an improvement over previously used cuts-based analyses by using novel methods. Further improvement is still possible by optimising the analysis as a whole, compared to the current step-by-step implementation.

Bibliography

[1] M. Thiesse et al., "PocketWATCH: design and operation of a multi-use test bed for water Cherenkov detector components in pure and gadolinium loaded water", J. Instrum. **19**, T05005 (2024).

[2] S. Wilson et al., "Characterisation of the temperature-dependent dark rate of Hamamatsu R7081-100 10" photomultiplier tubes", J. Instrum. **18**, P08017 (2023).

[3] O. A. Akindele et al., "Acceptance tests of Hamamatsu R7081 photomultiplier tubes", J. Instrum. **18**, P08015 (2023).

[4] S. T. Wilson et al., "Remote reactor ranging via antineutrino oscillations", `10.48550/ARXIV.2303.16661` (2024).

[5] L. Kneale et al., "Sensitivity of an antineutrino monitor for remote nuclear reactor discovery", Phys. Rev. Appl. **20**, 034073 (2023).

[6] J. Chadwick, "Intensitätsverteilung im magnetischen Spectrum der β-Strahlen von radium B + C", Verhandl. Dtsc. Phys. Ges. **16**, 383 (1914).

[7] P. Hernández, "Neutrino physics", CERN Yellow Reports, Vol 5 (2016): Proceedings of the 2015 CERN–Latin-American School of High-Energy Physics **5**, `10.5170/CERN-2016-005` (2016).

[8] N. Bohr, "Faraday lecture. Chemistry and the quantum theory of atomic constitution", J. Chem. Soc., 349 (1932).

[9] W. Pauli, "Dear radioactive ladies and gentlemen - letter to Lise Meitner", `cds.cern.ch/record/83282` (December 1930).

[10] W. Pauli, "Dear radioactive ladies and gentlemen", Phys. Today **31N9**, 27 (1978).

[11] J. J. Thomson, "XL. Cathode rays", Lond. Edinb. Dubl. Phil. Mag., 5th ser. **44**, 293–316 (1897).

[12] E. Rutherford, "LIV. Collision of α particles with light atoms. IV. An anomalous effect in nitrogen", Lond. Edinb. Dubl. Phil. Mag., 6th ser. **37**, 581–587 (1919).

[13] E. Fermi, "Versuch einer Theorie der β-Strahlen. I", Z. Phys. **88**, 161–177 (1934).

[14] E. Fermi, "Tentativo di una teoria dei raggi β", Nuovo Cim. **11**, 1–19 (1934).

[15] F. E. Close, *Neutrino* (Oxford University Press, Oxford; New York, 2010).

[16] W. J. Henderson, "The upper limits of the continuous β-ray spectra of thorium C and C″", Proc. R. Soc. A: Math. Phys. Eng. Sci. **147**, 572–582 (1934).

[17] J. Chadwick, "The existence of a neutron", Proc. R. Soc. A: Math. Phys. Eng. Sci. **136**, 692–708 (1932).

[18] L. Bonolis, "Bruno Pontecorvo: from slow neutrons to oscillating neutrinos", Am. J. Phys. **73**, 487–499 (2005).

[19] H. Bethe and R. Peierls, "The "neutrino"", Nature **133**, 532–532 (1934).

[20] F. Reines, "The early days of experimental neutrino physics", Sci. **203**, 11–16 (1979).

[21] "The Reines-Cowan experiments: detecting the poltergeist", Los Alamos Sci. **25** (1997).

[22] H. R. Crane, "The energy and momentum relations in the beta-decay, and the search for the neutrino", Rev. Mod. Phys. **20**, 278–295 (1948).

[23] F. Reines and C. L. Cowan, "A proposed experiment to detect the free neutrino", Phys. Rev. **90**, 492–493 (1953).

[24] C. L. Cowan et al., "Large liquid scintillation detectors", Phys. Rev. **90**, 493–494 (1953).

[25] F. Reines and C. L. Cowan, "Detection of the free neutrino", Phys. Rev. **92**, 830–831 (1953).

[26] C. L. Cowan et al., "Detection of the free neutrino: a confirmation", Sci. **124**, 103–104 (1956).

[27] F. Reines and C. L. Cowan, "Free antineutrino absorption cross section. I. Measurement of the free antineutrino absorption cross section by protons", Phys. Rev. **113**, 273–279 (1959).

[28] C. S. Wu et al., "Experimental test of parity conservation in beta decay", Phys. Rev. **105**, 1413–1415 (1957).

[29] T. D. Lee and C. N. Yang, "Question of parity conservation in weak interactions", Phys. Rev. **104**, 254–258 (1956).

[30] E. C. G. Sudarshan and R. E. Marshak, "Chirality invariance and the universal fermi interaction", Phys. Rev. **109**, 1860–1862 (1958).

[31] J. J. Sakurai, "Mass reversal and weak interactions", Nuovo Cim. **7**, 10.1007/BF02781569 (1958).

[32] R. P. Feynman and M. Gell-Mann, "Theory of the fermi interaction", Phys. Rev. **109**, 193–198 (1958).

[33] M. Goldhaber, L. Grodzins, and A. W. Sunyar, "Helicity of neutrinos", Phys. Rev. **109**, 1015–1017 (1958).

[34] J. C. Street and E. C. Stevenson, "New evidence for the existence of a particle of mass intermediate between the proton and electron", Phys. Rev. **52**, 1003–1004 (1937).

[35] E. P. Hincks and B. Pontecorvo, "Search for gamma-radiation in the 2.2-microsecond meson decay process", Phys. Rev. **73**, 257–258 (1948).

[36] B. Pontecorvo, "Electron and muon neutrinos", Zh. Eksp. Teor. Fiz. **37**, 1751–1757 (1959).

[37] M. Schwartz, "Feasibility of using high-energy neutrinos to study the weak interactions", Phys. Rev. Lett. **4**, 306–307 (1960).

[38] G. Danby et al., "Observation of high-energy neutrino reactions and the existence of two kinds of neutrinos", Phys. Rev. Lett. **9**, 36–44 (1962).

[39] M. L. Perl et al., "Evidence for anomalous lepton production in e^+-e^- annihilation", Phys. Rev. Lett. **35**, 1489–1492 (1975).

[40] R. L. Workman et al. (Particle Data Group), "Review of particle physics", Prog. Theor. Exp. Phys. **2022**, 10.1093/ptep/ptac097 (2022).

[41] M. Akrawy et al., "Measurement of the Z^0 mass and width with the opal detector at LEP", Phys. Lett. B **231**, 530–538 (1989).

[42] P. Aarnio et al., "Measurement of the mass and width of the Z^0-particle from multihadronic final states produced in e^+e^- annihilations", Phys. Lett. B **231**, 539–547 (1989).

[43] B. Adeva et al., "A determination of the properties of the neutral intermediate vector boson Z^0", Phys. Lett. B **231**, 509–518 (1989).

[44] D. DeCamp et al., "Determination of the number of light neutrino species", Phys. Lett. B **231**, 519–529 (1989).

[45] G. S. Abrams et al., "Measurements of Z-boson resonance parameters in e^+-e^- annihilation", Phys. Rev. Lett. **63**, 2173–2176 (1989).

[46] M. Grünewald et al., "Precision electroweak measurements on the Z resonance", Phys. Rep. **427**, 257–454 (2006).

[47] K. Kodama et al., "Observation of tau neutrino interactions", Phys. Lett. B **504**, 218–224 (2001).

[48] E. Fermi et al., "Artificial radioactivity produced by neutron bombardment", Proc. R. Soc. A: Math. Phys. Eng. Sci. **146** (1934).

[49] E. Fermi et al., "Artificial radioactivity produced by neutron bombardment. II", Proc. R. Soc. A: Math. Phys. Eng. Sci. **149** (1935).

[50] B. Pontecorvo, "Isomeric forms of radio rhodium", Nature **141**, 785–786 (1938).

[51] F. E. Close, *Half-life, The divided life of Bruno Pontecorvo, physicist or spy* (Basic Books, 2015).

[52] B. Pontecorvo, "Neutron well logging – a new geological method based on nuclear physics", Oil Gas J. **40** (1941).

[53] B. Pontecorvo and G. Swift, *Geophysical prospecting*, US Patent 2,353,619, 1941.

[54] B. Pontecorvo, *Method and apparatus for geophysical exploration*, US Patent 2,349,753, 1942.

[55] B. Pontecorvo, *Well surveying*, US Patent 2,398,324, 1943.

[56] B. Pontecorvo, *Method of geophysical prospecting*, US Patent 2,508,772, 1945.

[57] S. M. Bilenky, "Bruno Pontecorvo and modern neutrino physics", Nuovo Cim. C **37**, 3–15 (2014).

[58] B. Pontecorvo, "Inverse β process", Report PD-205, Chalk River Laboratory (1946).

[59] R. Davis, "Attempt to detect the antineutrinos from a nuclear reactor by the $Cl^{37}(\bar{\nu}, e^-)A^{37}$ reaction", Phys. Rev. **97**, 766–769 (1955).

[60] R. Davis, D. S. Harmer, and K. C. Hoffman, "Search for neutrinos from the sun", Phys. Rev. Lett. **20**, 1205–1209 (1968).

[61] G. C. Hanna, D. H. W. Kirkwood, and B. Pontecorvo, "High multiplication proportional counters for energy measurements", Phys. Rev. **75**, 985–986 (1949).

[62] M. Conversi, E. Pancini, and O. Piccioni, "On the disintegration of negative mesons", Phys. Rev. **71**, 209–210 (1947).

[63] E. P. Hincks and B. Pontecorvo, "The absorption of charged particles from the 2.2-μsec. meson decay", Phys. Rev. **74**, 697–698 (1948).

[64] B. Pontecorvo, "Nuclear capture of mesons and the meson decay", Phys. Rev. **72**, 246–247 (1947).

[65] M. Gell-Mann and A. Pais, "Behavior of neutral particles under charge conjugation", Phys. Rev. **97**, 1387–1389 (1955).

[66] B. Pontecorvo, "Mesonium and anti-mesonium", Sov. Phys. JETP **6**, 429 (1957).

[67] B. Pontecorvo, "Inverse beta processes and nonconservation of lepton charge", Zh. Eksp. Teor. Fiz. **34**, 247 (1957).

[68] V. Gribov and B. Pontecorvo, "Neutrino astronomy and lepton charge", Phys. Lett. B **28**, 493–496 (1969).

[69] Z. Maki, M. Nakagawa, and S. Sakata, "Remarks on the unified model of elementary particles", Prog. Theor. Phys. **28**, 870–880 (1962).

[70] R. Davis, "Solar neutrinos. II. experimental", Phys. Rev. Lett. **12**, 303–305 (1964).

[71] J. N. Bahcall, "Solar neutrinos", Phys. Rev. Lett. **17**, 398–401 (1966).

[72] H. A. Bethe, "Energy production in stars", Phys. Rev. **55**, 434–456 (1939).

[73] J. N. Bahcall, A. M. Serenelli, and S. Basu, "New solar opacities, abundances, helioseismology, and neutrino fluxes", Astrophys. J. **621**, L85–L88 (2005).

[74] B. T. Cleveland et al., "Measurement of the solar electron neutrino flux with the Homestake chlorine detector", Astrophys. J. **496**, 505–526 (1998).

[75] J. N. Bahcall, M. H. Pinsonneault, and G. J. Wasserburg, "Solar models with helium and heavy-element diffusion", Rev. Mod. Phys. **67**, 781–808 (1995).

[76] V. A. Kuzmin, "Detection of solar neutrinos by means of the $Ga^{71}(\nu, e^-)Ge^{71}$ reaction", Zh. Eksp. Teor. Fiz. **49** (1965).

[77] J. N. Bahcall et al., "Proposed solar-neutrino experiment using ^{71}Ga", Phys. Rev. Lett. **40**, 1351–1354 (1978).

[78] M. Cribier et al., "Results of the whole GALLEX experiment", Nucl. Phys. B Proc. Suppl. **70**, 284–291 (1999).

[79] J. N. Abdurashitov et al., "Solar neutrino flux measurements by the Soviet-American gallium experiment (SAGE) for half the 22-year solar cycle", J. Exp. Theor. Phys. **95**, 181–193 (2002).

[80] K. S. Hirata et al., "Observation of ^{8}B solar neutrinos in the Kamiokande-II detector", Phys. Rev. Lett. **63**, 16–19 (1989).

[81] D. Casper et al., "Measurement of atmospheric neutrino composition with the IMB-3 detector", Phys. Rev. Lett. **66**, 2561–2564 (1991).

[82] K. Hirata et al., "Observation of a small atmospheric ν_μ/ν_e ratio in Kamiokande", Phys. Lett. B **280**, 146–152 (1992).

[83] Y. Fukuda et al., "Atmospheric ratio in the multi-GeV energy range", Phys. Lett. B **335**, 237–245 (1994).

[84] Y. Fukuda et al. (Super-Kamiokande Collaboration), "Evidence for oscillation of atmospheric neutrinos", Phys. Rev. Lett. **81**, 1562–1567 (1998).

[85] J. Boger et al., "The Sudbury Neutrino Observatory", Nucl. Instrum. Methods Phys. Res. A: Accel. Spectrom. Detect. Assoc. Equip. **449**, 172–207 (2000).

[86] Q. R. Ahmad et al. (SNO Collaboration), "Measurement of the rate of $\nu_e + d \rightarrow p + p + e^-$ interactions produced by ^{8}B solar neutrinos at the Sudbury Neutrino Observatory", Phys. Rev. Lett. **87**, 071301 (2001).

[87] Q. R. Ahmad et al. (SNO Collaboration), "Direct evidence for neutrino flavor transformation from neutral-current interactions in the Sudbury Neutrino Observatory", Phys. Rev. Lett. **89**, 011301 (2002).

[88] S. Fukuda et al. (Super-Kamiokande Collaboration), "Solar ^{8}B and hep neutrino measurements from 1258 days of Super-Kamiokande data", Phys. Rev. Lett. **86**, 5651–5655 (2001).

[89] R. N. Mohapatra et al., "Theory of neutrinos: a white paper", Rep. Prog. Phys. **70**, 1757–1867 (2007).

[90] S. P. Mikheyev and A. Y. Smirnov, "Resonance Amplification of Oscillations in Matter and Spectroscopy of Solar Neutrinos", Sov. J. Nucl. Phys. **42**, 913–917 (1985).

[91] L. Wolfenstein, "Neutrino oscillations in matter", Phys. Rev. D **17**, 2369–2374 (1978).

[92] A. Piepke, "KamLAND: a reactor neutrino experiment testing the solar neutrino anomaly", Nucl. Phys. B Proc. Suppl. **91**, 99–104 (2001).

[93] S. Abe et al. (The KamLAND Collaboration), "Precision measurement of neutrino oscillation parameters with KamLAND", Phys. Rev. Lett. **100**, 221803 (2008).

[94] P. F. de Salas et al., "2020 global reassessment of the neutrino oscillation picture", J. High Energy Phys. **2021**, 10.1007/jhep02(2021)071 (2021).

[95] F. Kaether et al., "Reanalysis of the Gallex solar neutrino flux and source experiments", Phys. Lett. B **685**, 47–54 (2010).

[96] J. N. Abdurashitov et al. (SAGE Collaboration), "Measurement of the solar neutrino capture rate with gallium metal. III. Results for the 2002–2007 data-taking period", Phys. Rev. C **80**, 015807 (2009).

[97] G. Bellini et al. (Borexino Collaboration), "Precision measurement of the ^{7}Be solar neutrino interaction rate in Borexino", Phys. Rev. Lett. **107**, 141302 (2011).

[98] J. Hosaka et al. (Super-Kamiokande Collaboration), "Solar neutrino measurements in Super-Kamiokande-I", Phys. Rev. D **73**, 112001 (2006).

[99] J. P. Cravens et al. (Super-Kamiokande Collaboration), "Solar neutrino measurements in Super-Kamiokande-II", Phys. Rev. D **78**, 032002 (2008).

[100] K. Abe et al. (Super-Kamiokande Collaboration), "Solar neutrino results in Super-Kamiokande-III", Phys. Rev. D **83**, 052010 (2011).

[101] B. Aharmim et al. (SNO Collaboration), "Combined analysis of all three phases of solar neutrino data from the Sudbury Neutrino Observatory", Phys. Rev. C **88**, 025501 (2013).

[102] Y. Takeuchi (Super-Kamiokande Collaboration), "Recent results and future prospects of Super-Kamiokande", Nucl. Instrum. Methods Phys. Res. A: Accel. Spectrom. Detect. Assoc. Equip. **952**, 161634 (2020).

[103] D. Adey et al. (Daya Bay Collaboration), "Measurement of the electron antineutrino oscillation with 1958 days of operation at Daya Bay", Phys. Rev. Lett. **121**, 241805 (2018).

[104] G. Bak et al. (RENO Collaboration), "Measurement of reactor antineutrino oscillation amplitude and frequency at RENO", Phys. Rev. Lett. **121**, 201801 (2018).

[105] Y. Abe et al. (Double Chooz Collaboration), "Indication of reactor $\bar{\nu}_e$ disappearance in the Double Chooz experiment", Phys. Rev. Lett. **108**, 131801 (2012).

[106] F. P. An et al., "Observation of electron-antineutrino disappearance at Daya Bay", Phys. Rev. Lett. **108**, 171803 (2012).

[107] H. Nunokawa, S. Parke, and R. Z. Funchal, "Another possible way to determine the neutrino mass hierarchy", Phys. Rev. D **72**, 013009 (2005).

[108] K. Abe et al. (Super-Kamiokande Collaboration), "Atmospheric neutrino oscillation analysis with external constraints in Super-Kamiokande I-IV", Phys. Rev. D **97**, 072001 (2018).

[109] M. Aartsen et al., "The IceCube neutrino observatory: instrumentation and online systems", J. Instrum. **12**, P03012–P03012 (2017).

[110] M. G. Aartsen et al. (IceCube Collaboration), "Measurement of atmospheric neutrino oscillations at 6-56 GeV with IceCube DeepCore", Phys. Rev. Lett. **120**, 071801 (2018).

[111] M. Ageron et al., "ANTARES: the first undersea neutrino telescope", Nucl. Instrum. Methods Phys. Res. A: Accel. Spectrom. Detect. Assoc. Equip. **656**, 11–38 (2011).

[112] A. Albert et al. (ANTARES Collaboration), "Measuring the atmospheric neutrino oscillation parameters and constraining the 3+1 neutrino model with ten years of ANTARES data", J. High Energy Phys. **2019**, `10.1007/jhep06(2019)113` (2019).

[113] Z. Li et al. (Super-Kamiokande Collaboration), "Measurement of the tau neutrino cross section in atmospheric neutrino oscillations with Super-Kamiokande", Phys. Rev. D **98**, 052006 (2018).

[114] M. G. Aartsen et al. (IceCube Collaboration), "Measurement of atmospheric tau neutrino appearance with IceCube DeepCore", Phys. Rev. D **99**, 032007 (2019).

[115] K. Abe et al., "The T2K experiment", Nucl. Instrum. Methods Phys. Res. A: Accel. Spectrom. Detect. Assoc. Equip. **659**, 106–135 (2011).

[116] A. Habig, "The NOvA experiment", Nucl. Phys. B Proc. Suppl. **229-232**, 460 (2012).

[117] K. Abe et al. (T2K Collaboration), "Constraint on the matter-antimatter symmetry-violating phase in neutrino oscillations", Nature **580**, 339–344 (2020).

[118] I. Esteban et al., "The fate of hints: updated global analysis of three-flavor neutrino oscillations", J. High Energy Phys. **2020**, 10.1007/jhep09(2020)178 (2020).

[119] M. G. Aartsen et al., "PINGU: a vision for neutrino and particle physics at the south pole", J. Phys. G: Nucl. Part. Phys. **44**, 054006 (2017).

[120] S. Aiello et al., "Determining the neutrino mass ordering and oscillation parameters with KM3NeT/ORCA", Eur. Phys. J. C **82**, 10.1140/epjc/s10052-021-09893-0 (2022).

[121] F. Di Lodovico, "The Hyper-Kamiokande experiment", J. Phys.: Conf. Ser. **888**, 012020 (2017).

[122] B. Abi et al., "Volume I. introduction to DUNE", J. Instrum. **15**, T08008–T08008 (2020).

[123] JUNO Collaboration, "JUNO physics and detector", Prog. Part. Nucl. Phys. **123**, 103927 (2022).

[124] F. An et al., "Neutrino physics with JUNO", J. Phys. G: Nucl. Part. Phys. **43**, 030401 (2016).

[125] D. Kvasnicka and U.S. Department of Energy, *The history of nuclear energy* (U.S. Government, 2011).

[126] International Atomic Energy Agency, *Energy, electricity and nuclear power estimates for the period up to 2050*, Reference Data Series 1 (IAEA, Vienna, 2020).

[127] International Atomic Energy Agency, *Safe handling and storage of plutonium*, Safety Reports Series 9 (IAEA, Vienna, 1998).

[128] A. L. Nichols, D. L. Aldama, and M. Verpelli, *Handbook of nuclear data for safeguards: database extensions* (IAEA, Vienna, 2008).

[129] World Nuclear Association, *Image Library: Reactor Diagrams*, Accessed 22 June 2023.

[130] International Atomic Energy Agency, *Management of high enriched uranium for peaceful purposes: status and trends*, TECDOC Series 1452 (IAEA, Vienna, 2005).

[131] S. Bogetic et al., "Anti-neutrino flux from the EdF Hartlepool nuclear power plant", `10.48550/ARXIV.2301.07153` (2023).

[132] H. M. Kristensen and R. S. Norris, "Global nuclear weapons inventories, 1945-2013", Bull. At. Sci. **69**, 75–81 (2013).

[133] H. M. Kristensen and R. S. Norris, "Worldwide deployments of nuclear weapons, 2017", Bull. At. Sci. **73**, 289–297 (2017).

[134] American Nuclear Society, *Plutonium handbook, A guide to the technology*, edited by O. J. Wick (Gordon & B, 1967).

[135] C. M. Lederer, J. M. Hollander, and I. Perlman, *Table of isotopes*, 6th ed. (Wiley, New York, 1967).

[136] A. Bernstein, "Viewpoint: getting burnt by weapons plutonium: security implications of U.S. disposition options", Nonproliferation Rev. **4**, 72–81 (1997).

[137] R. J. Gilbert and E. P. Kahn, *International comparisons of electricity regulation* (Cambridge University Press, 2007).

[138] United Nations, *Treaty on the Non-Proliferation of Nuclear Weapons*, 1970.

[139] International Atomic Energy Agency, *Model protocol additional to the agreements(s) between the state(s) and the international atomic energy agency for the application of safeguards*, 1997.

[140] International Atomic Energy Agency, *IAEA safeguards glossary*, International Nuclear Verification Series 3 (Rev. 1) (IAEA, Vienna, 2022).

[141] G. Zuccaro-Labellarte and R. Fagerholm, "Safeguards at research reactors: current practices, future directions", International Atomic Energy Agency Bulletin (Austria); **38** (1996).

[142] International Atomic Energy Agency, *Research reactor database*, Accessed 23 June 2023.

[143] International Atomic Energy Agency, *Safeguards techniques and equipment*, International Nuclear Verification Series 1 (Rev. 2) (IAEA, Vienna, 2011).

[144] B. D. Reid, G. A. Anzelon, and K. Budlong-Sylvester, "Strengthening IAEA safeguards for research reactors", 10.2172/1330299 (2016).

[145] O. A. Akindele et al., "Nu tools: exploring practical roles for neutrinos in nuclear energy and security", 10.2172/1826602 (2021).

[146] L. A. Mikaelian, "Neutrino laboratory in the atomic plant", in Proceedings of the International Conference on Neutrino Physics and Neutrino Astrophysics, Neutrino '77 (1978).

[147] A. A. Borovoi and L. A. Mikaélyan, "Possibilities of practical applications of neutrinos", At. Energy **44**, 589–592 (1978).

[148] V. A. Korovkin, S. A. Kodanev, A. D. Yarichin, et al., "Measurement of nuclear fuel burnup in a reactor according to neutrino emission", At. Energy **56**, 214–218 (1984).

[149] V. A. Korovkin, S. A. Kodanev, N. S. Panashchenko, et al., "Measurement of power generation of a power reactor by the method of neutrino detection", At. Energy **65**, 169–173 (1988).

[150] Y. V. Klimov et al., "Neutrino method remote measurement of reactor power and power output", At. Energy **76**, 123–127 (1994).

[151] P. Huber, "Determination of antineutrino spectra from nuclear reactors", Phys. Rev. C **84**, 024617 (2011).

[152] T. A. Mueller et al., "Improved predictions of reactor antineutrino spectra", Phys. Rev. C **83**, 054615 (2011).

[153] E. Christensen, P. Huber, and P. Jaffke, "Antineutrino reactor safeguards: a case study of the DPRK 1994 nuclear crisis", Sci. Glob. Secur. **23**, 20–47 (2015).

[154] E. Christensen, P. Huber, and P. Jaffke, "Antineutrino reactor safeguards - a case study", 10.48550/ARXIV.1312.1959 (2014).

[155] N. S. Bowden et al., "Observation of the isotopic evolution of pressurized water reactor fuel using an antineutrino detector", J. App. Phys. **105**, 064902 (2009).

[156] F. von Feilitzsch, A. Hahn, and K. Schreckenbach, "Experimental beta-spectra from ^{239}Pu and ^{235}U thermal neutron fission products and their correlated antineutrino spectra", Phys. Lett. B **118**, 162–166 (1982).

[157] K. Schreckenbach et al., "Determination of the antineutrino spectrum from ^{235}U thermal neutron fission products up to 9.5 MeV", Phys. Lett. B **160**, 325–330 (1985).

[158] A. Hahn et al., "Antineutrino spectra from ^{241}Pu and ^{239}Pu thermal neutron fission products", Phys. Lett. B **218**, 365–368 (1989).

[159] N. Haag et al., "Experimental determination of the antineutrino spectrum of the fission products of ^{238}U", Phys. Rev. Lett. **112**, 122501 (2014).

[160] G. Mention et al., "Reactor antineutrino anomaly", Phys. Rev. D **83**, 073006 (2011).

[161] H. Almazán et al. (STEREO Collaboration), "Improved sterile neutrino constraints from the STEREO experiment with 179 days of reactor-on data", Phys. Rev. D **102**, 052002 (2020).

[162] F. P. An et al. (Daya Bay Collaboration), "Evolution of the reactor antineutrino flux and spectrum at Daya Bay", Phys. Rev. Lett. **118**, 251801 (2017).

[163] G. Bak et al. (RENO Collaboration), "Fuel-composition dependent reactor antineutrino yield at RENO", Phys. Rev. Lett. **122**, 232501 (2019).

[164] The Double Chooz Collaboration, "Double chooz θ_{13} measurement via total neutron capture detection", Nat. Phys. **16**, 558–564 (2020).

[165] Y. J. Ko et al. (NEOS Collaboration), "Sterile neutrino search at the NEOS experiment", Phys. Rev. Lett. **118**, 121802 (2017).

[166] J. M. Berryman and P. Huber, "Reevaluating reactor antineutrino anomalies with updated flux predictions", Phys. Rev. D **101**, 015008 (2020).

[167] V. I. Kopeikin, Y. N. Panin, and A. A. Sabelnikov, "Measurement of the ratio of cumulative spectra of beta particles from ^{235}U and ^{239}Pu fission products for solving problems of reactor-antineutrino physics", Phys. At. Nucl. **84**, 1–10 (2021).

[168] V. Kopeikin, M. Skorokhvatov, and O. Titov, "Reevaluating reactor antineutrino spectra with new measurements of the ratio between ^{235}U and ^{239}Pu β spectra", Phys. Rev. D **104**, L071301 (2021).

[169] M. Estienne et al., "Updated summation model: an improved agreement with the Daya Bay antineutrino fluxes", Phys. Rev. Lett. **123**, 022502 (2019).

[170] A. Letourneau et al., "Origin of the reactor antineutrino anomalies in light of a new summation model with parametrized β^- transitions", Phys. Rev. Lett. **130**, 021801 (2023).

[171] L. Hayen et al., "First-forbidden transitions in the reactor anomaly", Phys. Rev. C **100**, 054323 (2019).

[172] J. Cao and K.-B. Luk, "An overview of the Daya Bay reactor neutrino experiment", Nucl. Phys. B **908**, 62–73 (2016).

[173] H. de Kerret et al., "The Double Chooz antineutrino detectors", Eur. Phys. J. C **82**, 10.1140/epjc/s10052-022-10726-x (2022).

[174] S.-B. Kim and the RENO Collaboration, "RENO: reactor experiment for neutrino oscillation at Yonggwang", Journal of Physics: Conference Series **120**, 052025 (2008).

[175] M. R. Anderson et al. (The SNO+ Collaboration), "Measurement of neutron-proton capture in the SNO+ water phase", Phys. Rev. C **102**, 014002 (2020).

[176] A. Allega et al. (The SNO+ Collaboration), "Evidence of antineutrinos from distant reactors using pure water at SNO+", Phys. Rev. Lett. **130**, 091801 (2023).

[177] G. Ricciardi, N. Vignaroli, and F. Vassani, "An accurate evaluation of electron (anti-)neutrino scattering on nucleons", J. High. Energ. Phys **2022**, 212 (2022).

[178] A. Strumia and F. Vissani, "Precise quasielastic neutrino/nucleon cross-section", Phys. Lett. B **564**, 42–54 (2003).

[179] S. Dye and A. Barna, "Global antineutrino modeling for a web application", 10.48550/ARXIV.1510.05633 (2015).

[180] P. Vogel and J. F. Beacom, "Angular distribution of neutron inverse beta decay, $\bar{\nu}_e + \mathrm{p} \to \mathrm{e}^+ + \mathrm{n}$", Phys. Rev. D **60**, 053003 (1999).

[181] O. Smirnov, "Experimental aspects of geoneutrino detection: status and perspectives", Prog. Part. Nucl. Phys. **109**, 103712 (2019).

[182] P. A. Cherenkov, "Visible luminescence of pure liquids under the influence of γ-radiation", Dokl. Akad. Nauk SSSR **2**, 451–454 (1934).

[183] I. M. Frank and I. E. Tamm, "Coherent visible radiation of fast electrons passing through matter", Compt. Rend. Acad. Sci. URSS **14**, 109–114 (1937).

[184] P. A. Cherenkov, "Visible radiation produced by electrons moving in a medium with velocities exceeding that of light", Phys. Rev. **52**, 378–379 (1937).

[185] S. Schoppmann, "Review of novel approaches to organic liquid scintillators in neutrino physics", Symmetry **15**, 10.3390/sym15010011 (2023).

[186] J. Birks, *The Theory and Practice of Scintillation Counting* (Pergamon Press: Oxford, UK, 1964).

[187] J. P. Doering, "Electronic energy levels of benzene below 7 eV", J. Chem. Phys. **67**, 4065–4070 (1977).

[188] J. Franck and E. G. Dymond, "Elementary processes of photochemical reactions", Trans. Faraday Soc. **21**, 536–542 (1926).

[189] E. Condon, "A theory of intensity distribution in band systems", Phys. Rev. **28**, 1182–1201 (1926).

[190] G. F. Knoll, *Radiation Detection and Measurement*, 3rd edition (John Wiley and Sons, New York, 2000).

[191] C. Buck and M. Yeh, "Metal-loaded organic scintillators for neutrino physics", J. Phys. G Nucl. Part. Phys. **43**, 093001 (2016).

[192] T. Förster, "Zwischenmolekulare energiewanderung und fluoreszenz", Ann. Phys. **437**, 55–75 (1948).

[193] M. Anderson et al., "Development, characterisation, and deployment of the SNO+ liquid scintillator", J. Instrum. **16**, P05009 (2021).

[194] P. Lombardi et al., "Decay time and pulse shape discrimination of liquid scintillators based on novel solvents", Nucl. Instrum. Methods Phys. Res. A: Accel. Spectrom. Detect. Assoc. Equip. **701**, 133–144 (2013).

[195] C. Buck et al., "Production and properties of the liquid scintillators used in the STEREO reactor neutrino experiment", J. Instrum. **14**, P01027 (2019).

[196] H.-L. Xiao et al., "Study of absorption and re-emission processes in a ternary liquid scintillation system", Chin. Phys. C **34**, 1724 (2010).

[197] W. Beriguete et al., "Production of a gadolinium-loaded liquid scintillator for the Daya Bay reactor neutrino experiment", Nucl. Instrum. Methods Phys. Res. A: Accel. Spectrom. Detect. Assoc. Equip. **763**, 82–88 (2014).

[198] J. S. Park et al., "Production and optical properties of Gd-loaded liquid scintillator for the RENO neutrino detector", Nucl. Instrum. Meth. A **707**, 45–53 (2013).

[199] B. R. Kim et al. (NEOS), "Development and mass production of a mixture of LAB- and DIN-based gadolinium-loaded liquid scintillator for the NEOS short-baseline neutrino experiment", J. Radioanal. Nucl. Chem. **310**, 311–316 (2016).

[200] A. Abusleme et al., "Optimization of the JUNO liquid scintillator composition using a Daya Bay antineutrino detector", Nucl. Instrum. Methods Phys. Res. A: Accel. Spectrom. Detect. Assoc. Equip. **988**, 164823 (2021).

[201] H. Steiger, "Tao—the Taishan antineutrino observatory", Instrum. **6**, 50 (2022).

[202] G. Bellini, "The impact of Borexino on the solar and neutrino physics", Nucl. Phys. B **908**, 178–198 (2016).

[203] F. Masetti, F. Elisei, and U. Mazzucato, "Optical study of a large-scale liquid-scintillator detector", J. Lumin. **68**, 15–25 (1996).

[204] S. Mufson et al., "Liquid scintillator production for the NOvA experiment", Nucl. Instrum. Methods Phys. Res. A: Accel. Spectrom. Detect. Assoc. Equip. **799**, 1–9 (2015).

[205] F. Suekane, "KamLAND", Prog. Part. Nucl. **57**, 106–126 (2006).

[206] A. G. Piepke, S. Moser, and V. M. Novikov, "Development of a gd loaded liquid scintillator for electron anti-neutrino spectroscopy", Nucl. Instrum. Methods Phys. Res. A: Accel. Spectrom. Detect. Assoc. Equip. **432**, 392–398 (1999).

[207] M. Abbes et al., "The Bugey 3 neutrino detector", Nucl. Instrum. Methods Phys. Res. A: Accel. Spectrom. Detect. Assoc. Equip. **374**, 164–187 (1996).

[208] The KamLAND-Zen collaboration et al., "The nylon balloon for xenon loaded liquid scintillator in KamLAND-Zen 800 neutrinoless double-beta decay search experiment", J. Instrum. **16**, P08023 (2021).

[209] G. Boireau et al. (Nucifer Collaboration), "Online monitoring of the Osiris reactor with the Nucifer neutrino detector", Phys. Rev. D **93**, 112006 (2016).

[210] C. Aberle et al., "Large scale gd-beta-diketonate based organic liquid scintillator production for antineutrino detection", J. Instrum. **7**, P06008 (2012).

[211] T. M. Undagoitia et al., "Spectroscopy of electron-induced fluorescence in organic liquid scintillators", Eur. Phys. J. D **57**, 105–110 (2010).

[212] J. E. Bertie and Z. Lan, "Infrared intensities of liquids XX: The intensity of the OH stretching band of liquid water revisited, and the best current values of the optical constants of H_2O(l) at 25 °C between 15,000 and 1 cm^{-1}", Appl. Spectrosc. **50**, 1047–1057 (1996).

[213] L. Rayleigh, "On the transmission of light through an atmosphere containing small particles in suspension, and on the origin of the blue of the sky", Philos. Mag. J. Sci. **47**, 375–384 (1899).

[214] G. Mie, "Beiträge zur optik trüber medien, speziell kolloidaler metallösungen", Ann. Phys. **330**, 377–445 (1908).

[215] C. V. Raman, "A new radiation", Ind. J. Phys. **2**, 387–398 (1928).

[216] J. B. Birks, "Scintillations from organic crystals: specific fluorescence and relative response to different radiations", Proc. Phys. Soc. A **64**, 874–877 (1951).

[217] T. A. Laplace et al., "Modeling ionization quenching in organic scintillators", Mater. Adv. **3**, 5871–5881 (2022).

[218] C. N. Chou, "The nature of the saturation effect of fluorescent scintillators", Phys. Rev. **87**, 904–905 (1952).

[219] H. Bagán et al., "Classical vs. evolved quenching parameters and procedures in scintillation measurements: the importance of ionization quenching", Nucl. Instrum. Methods Phys. Res. A: Accel. Spectrom. Detect. Assoc. Equip. **592**, 361–368 (2008).

[220] K. Abe et al., "Calibration of the Super-Kamiokande detector", Nucl. Instrum. Methods Phys. Res. A: Accel. Spectrom. Detect. Assoc. Equip. **737**, 253–272 (2014).

[221] L. Gao et al., "Attenuation length measurements of a liquid scintillator with LabVIEW and reliability evaluation of the device", Chin. Phys. C **37**, 076001 (2013).

[222] M. Wurm et al., "Optical scattering lengths in large liquid-scintillator neutrino detectors", Rev. Sci. Instrum. **81**, 053301 (2010).

[223] R. E. Meads et al., "The capture cross section of thermal neutrons in water", Proc. Phys. Soc. A **69**, 469 (1956).

[224] B. Hamermesh, G. R. Ringo, and S. Wexler, "The thermal neutron capture cross section of hydrogen", Phys. Rev. **90**, 603–606 (1953).

[225] B. D'Mellow et al., "The replacement of cadmium as a thermal neutron filter", Nucl. Instrum. Methods Phys. Res. A: Accel. Spectrom. Detect. Assoc. Equip. **577**, 690–695 (2007).

[226] R. Breukers, C. Bartle, and A. Edgar, "Transparent lithium loaded plastic scintillators for thermal neutron detection", Nucl. Instrum. Methods Phys. Res. A: Accel. Spectrom. Detect. Assoc. Equip. **701**, 58–61 (2013).

[227] P. Das et al., "Gamma-ray spectrum from thermal neutron capture on gadolinium-157", Prog. Theor. Exp. Phys. **2019**, 023D01 (2019).

[228] G. Leinweber et al., "Neutron capture and total cross-section measurements and resonance parameters of gadolinium", Nucl. Sci. Eng. **154**, 261–279 (2006).

[229] T. Tanaka et al., "Gamma-ray spectra from thermal neutron capture on gadolinium-155 and natural gadolinium", Prog. Theor. Exp. Phys. **2020**, 43–45 (2020).

[230] A. Renshaw, "Research and development for a gadolinium doped water Cherenkov detector", Phys. Procedia **27**, 1249–1256 (2012).

[231] J. F. Beacom and M. R. Vagins, "Antineutrino spectroscopy with large water Cherenkov detectors", Phys. Rev. Lett. **93**, 171101 (2004).

[232] M. Vagins, "New ideas in neutrino detection", PRAMANA - J. Phys. **67**, 691–698 (2006).

[233] L. Marti et al., "Evaluation of gadolinium's action on water Cherenkov detector systems with EGADS", Nucl. Instrum. Methods Phys. Res. A: Accel. Spectrom. Detect. Assoc. Equip. **959**, 163549 (2020).

[234] G. Pronost, "Looking for Gd neutron captures from SN ν with EGADS detector", in Proceedings of 35th International Cosmic Ray Conference — PoS(ICRC2017), ICRC2017 (August 2017).

[235] H. Zhang et al. (Super-Kamiokande Collaboration), "Supernova relic neutrino search with neutron tagging at Super-Kamiokande-IV", Astropart Phys. **60**, 41–46 (2015).

[236] K. Abe et al. (Super-Kamiokande Collaboration), "First gadolinium loading to Super-Kamiokande", Nucl. Instrum. Methods Phys. Res. A: Accel. Spectrom. Detect. Assoc. Equip. **1027**, 166248 (2022).

[237] M. Yeh et al., "A new water-based liquid scintillator and potential applications", Nucl. Instrum. Methods Phys. Res. A: Accel. Spectrom. Detect. Assoc. Equip. **660**, 51–56 (2011).

[238] L. Bignell et al., "Characterization and modeling of a water-based liquid scintillator", J. Instrum. **10**, P12009 (2015).

[239] D. R. Onken et al., "Time response of water-based liquid scintillator from X-ray excitation", Mater. Adv. **1**, 71–76 (2020).

[240] J. W. Choi et al., "Development of water-based liquid scintillator based on hydrophilic-lipophilic balance index", Phys. Scr. **97**, 045304 (2022).

[241] X. Xiang et al., "Design, construction, and operation of a 1-ton water-based liquid scintillator detector at Brookhaven National Laboratory", 10.48550/ARXIV.2403.1323 (2024).

[242] J. Caravaca et al., "Experiment to demonstrate separation of Cherenkov and scintillation signals", Phys. Rev. C **95**, 055801 (2017).

[243] M. Askins et al., "THEIA: an advanced optical neutrino detector", Eur. Phys. J. C **80**, 416 (2020).

[244] B. J. Land et al., "MeV-scale performance of water-based and pure liquid scintillator detectors", Phys. Rev. D **103**, 052004 (2021).

[245] R. Bonventre and G. D. O. Gann, "Sensitivity of a low threshold directional detector to CNO-cycle solar neutrinos", Eur. Phys. J. C **78**, 10.1140/epjc/s10052-018-5925-7 (2018).

[246] Y. Suzuki, "The Super-Kamiokande experiment", Eur. Phys. J. C **79**, 10.1140/epjc/s10052-019-6796-2 (2019).

[247] J. Caravaca et al., "Characterization of water-based liquid scintillator for Cherenkov and scintillation separation", Eur. Phys. J. C **80**, 867 (2020).

[248] V. Fischer and E. Tiras, "Water-based liquid scintillator detector as a new technology testbed for neutrino studies in Turkey", Nucl. Instrum. Methods Phys. Res. A: Accel. Spectrom. Detect. Assoc. Equip. **969**, 163931 (2020).

[249] E. J. Callaghan et al., "Measurement of proton light yield of water-based liquid scintillator", Eur. Phys. J. C **83**, https://doi.org/10.1140/epjc/s10052-023-11242-2 (2022).

[250] C. Aberle et al., "Measuring directionality in double-beta decay and neutrino interactions with kiloton-scale scintillation detectors", J. Instrum. **9**, P06012 (2014).

[251] A. Lyashenko et al., "Performance of Large Area Picosecond Photo-Detectors (LAPPD™)", Nucl. Instrum. Methods Phys. Res. A: Accel. Spectrom. Detect. Assoc. Equip. **958**, 162834 (2020).

[252] M. Minot et al., "Large Area Picosecond Photodetector (LAPPD™) - Pilot production and development status", Nucl. Instrum. Methods Phys. Res. A: Accel. Spectrom. Detect. Assoc. Equip. **936**, 527–531 (2019).

[253] T. Kaptanoglu et al., "Cherenkov and scintillation separation in water-based liquid scintillator using an LAPPD™", Eur. Phys. J. C **82**, 10.1140/epjc/s10052-022-10087-5 (2022).

[254] J. Caravaca et al., "Cherenkov and scintillation light separation in organic liquid scintillators", Eur. Phys. J. C **77**, 10.1140/epjc/s10052-017-5380-x (2017).

[255] G. D. Orebi Gann et al., "Snowmass2021 - letter of interest, The RAT(-PAC) simulation and analysis code base", in (2020).

[256] S. D. Biller, E. J. Leming, and J. L. Paton, "Slow fluors for effective separation of Cherenkov light in liquid scintillators", Nucl. Instrum. Methods Phys. Res. A: Accel. Spectrom. Detect. Assoc. Equip. **972**, 164106 (2020).

[257] T. Kaptanoglu, M. Luo, and J. Klein, "Cherenkov and scintillation light separation using wavelength in LAB based liquid scintillator", J. Instrum. **14**, T05001–T05001 (2019).

[258] T. Kaptanoglu et al., "Spectral photon sorting for large-scale Cherenkov and scintillation detectors", Phys. Rev. D **101**, 072002 (2020).

[259] M. J. Ford et al., "Pulse-shape discrimination in water-based scintillators", Nucl. Instrum. Methods Phys. Res. A: Accel. Spectrom. Detect. Assoc. Equip. **1036**, 166854 (2022).

[260] T. Anderson et al., "Eos: conceptual design for a demonstrator of hybrid optical detector technology", J. Instrum. **18**, P02009 (2023).

[261] J. Ashenfelter et al., "Lithium-loaded liquid scintillator production for the PROSPECT experiment", J. Instrum. **14**, P03026–P03026 (2019).

[262] WATCHMAN Collaboration, "The AIT-NEO project: results from the NEO performance trade study", Unpublished (2021).

[263] S. Fukuda et al., "The Super-Kamiokande detector", Nucl. Instrum. Methods Phys. Res. A: Accel. Spectrom. Detect. Assoc. Equip. **501**, 418–462 (2003).

[264] M. Pathak et al., "Narrowband ultraviolet B emission from gadolinium activated $Y_3Ga_5O_{12}$ nano-garnets", Mater. Res. Bull. **97**, 512–516 (2018).

[265] P. B. Weatherly, "Probing the strength of non-standard interactions between solar neutrinos and up or down quarks in matter using recoil electron spectra measured by Super-Kamiokande", Ph.D. thesis (University of California, Irvine, 2019).

[266] S. Locke, "New methods to reduce cosmogenic backgrounds of Super-Kamiokande in the solar neutrino energy regime", Ph.D. thesis (University of California, Irvine, 2020).

[267] H. Sekiya, "Low energy neutrinos in Super-Kamiokande", J. Phys.: Conf. Ser. **718**, 062052 (2016).

[268] M. Mori et al., "Searching for supernova bursts in Super-Kamiokande IV", Astrophys. J. **938**, 35 (2022).

[269] B. L. Paredes et al., "Response of photomultiplier tubes to xenon scintillation light", Astropart. Phys. **102**, 56–66 (2018).

[270] V. Albanese et al., "The SNO+ experiment", J. Instrum. **16**, P08059 (2021).

[271] S. Mukhopadhyay, R. Maurer, and P. Guss, "Use of a position-sensitive multi-anode photomultiplier tube for finding gamma-ray source direction", in SPIE proc. Vol. 9213, edited by A. Burger et al. (September 2014).

[272] J. Greer, *Neutron-gamma detection in novel borehole detectors*, IoP Joint APP and HEPP Annual Conference, 2023.

[273] Hamamatsu Photonics, *Photomultiplier Tubes: Basics and Applications, 4th edition* (2017).

[274] A. G. Wright, *The photomultiplier handbook* (Oxford University Press, August 2017).

[275] J. S. Milnes and J. Howorth, "Picosecond time response characteristics of microchannel plate PMT detectors", in SPIE proc. Vol. 5580, edited by D. L. Paisley et al. (March 2005).

[276] J. Bortfeldt et al., "Timing performance of a micro-channel-plate photomultiplier tube", Nucl. Instrum. Methods Phys. Res. A: Accel. Spectrom. Detect. Assoc. Equip. **960**, 163592 (2020).

[277] Hamamatsu Photonics, *Large photocathode area photomultiplier tubes*, `https://www.hamamatsu.com/content/dam/hamamatsu-photonics/sites/documents/99_SALES_LIBRARY/etd/LARGE_AREA_PMT_TPMH1376E.pdf`, Accessed: 2023-06-14.

[278] V. A. Li et al., "Scalability of gadolinium-doped-water Cherenkov detectors for nuclear nonproliferation", Phys. Rev. Appl. **18**, [physics.ins-det/2204.08618v2], 034059 (2022).

[279] Hamamatsu Photonics (private communication), 2018.

[280] E. H. Bellamy et al., "Absolute calibration and monitoring of a spectrometric channel using a photomultiplier", Nucl. Instrum. Methods Phys. Res. A: Accel. Spectrom. Detect. Assoc. Equip. **339**, 468–476 (1994).

[281] C. Bauer et al., "Qualification tests of 474 photomultiplier tubes for the inner detector of the Double Chooz experiment", J. Instrum. **6**, P06008 (2011).

[282] Hamamatsu Photonics, *Water-proof Type Photomultiplier Assembly R7081-100-10-WA-S80: Tentative Data Sheet*, December 2017.

[283] Y. Zhang et al., "Study of 20-inch PMTs dark count generated large pulses", J. Instrum. **17**, P10048 (2022).

[284] T. Kaptanoglu, "Characterization of the Hamamatsu 8" R5912-MOD photomultiplier tube", Nucl. Instrum. Methods Phys. Res. A: Accel. Spectrom. Detect. Assoc. Equip. **889**, 69–77 (2018).

[285] B. Herold and O. Kalekin, "PMT characterisation for the KM3NeT project", Nucl. Instrum. Methods Phys. Res. A: Accel. Spectrom. Detect. Assoc. Equip. **626-627**, S151–S153 (2011).

[286] J. Brack et al., "Characterization of the Hamamatsu R11780 12 in. photomultiplier tube", Nucl. Instrum. Methods Phys. Res. A: Accel. Spectrom. Detect. Assoc. Equip. **712**, 162–173 (2013).

[287] J. Aguilar et al., "Study of large hemispherical photomultiplier tubes for the ANTARES neutrino telescope", Nucl. Instrum. Methods Phys. Res. A: Accel. Spectrom. Detect. Assoc. Equip. **555**, 132–141 (2005).

[288] R. Abbasi et al., "Calibration and characterization of the IceCube photomultiplier tube", Nucl. Instrum. Methods Phys. Res. A: Accel. Spectrom. Detect. Assoc. Equip. **618**, 139–152 (2010).

[289] C. Wright, *Monitoring Tools for the LUX-ZEPLIN Outer Detector*, IoP Joint APP and HEPP Annual Conference, 2023.

[290] H. Gadey, S. Chatzidakis, and A. T. Farsoni, "Monte Carlo characterization of the cosmic ray muon flux in shallow subsurface geological repositories intended for disposal of radioactive materials", Appl. Radiat. Isot. **163**, 109209 (2020).

[291] H. R. Krall, "Extraneous light emission from photomultipliers", IEEE Trans. Nucl. Sci. **14**, 455–459 (1967).

[292] G. Haefeli, "Contribution to the development of the acquisition electronics for the LHCb experiment", PhD thesis (Ecole Polytechnique, Lausanne, 2004).

[293] O. W. Richardson, "Electron emission from metals as a function of temperature", Phys. Rev. **23**, 153–155 (1924).

[294] P. B. Coates, "Thermionic emission from photocathodes", J. Phys. D: Appl. Phys **5**, 1489 (1972).

[295] International Atomic Energy Agency, *Depleted uranium*, `https://www.iaea.org/topics/spent-fuel-management/depleted-uranium`, accessed 19th May 2023.

[296] C. Yanagisawa and T. Kato, *Report on the Super-Kamiokande accident*, 2001.

[297] D. Cyranoski, "Imploding detectors shatter plans for Japan's neutrino experiments", Nature **414**, 381–382 (2001).

[298] K. Eguchi et al. (KamLAND Collaboration), "First results from KamLAND: evidence for reactor antineutrino disappearance", Phys. Rev. Lett. **90**, 021802 (2003).

[299] F. P. An et al., "Antineutrino energy spectrum unfolding based on the Daya Bay measurement and its applications", Chin. Phys. C **45**, 073001 (2021).

[300] M. Weekes, "Cosmic-ray muons for imaging: Monte Carlo simulation studies into assaying nuclear waste packages, deep geological repositories, and carbon reservoirs", Ph.D. thesis (University of Sheffield, March 2023).

[301] J. Autran et al., "Characterization of atmospheric muons at sea level using a cosmic ray telescope", Nucl. Instrum. Methods Phys. Res. A: Accel. Spectrom. Detect. Assoc. Equip. **903**, 77–84 (2018).

[302] Y. Fukuda et al., "Measurements of the solar neutrino flux from Super-Kamiokande's first 300 days", Phys. Rev. Lett. **81**, 1158–1162 (1998).

[303] M. Robinson et al., "Measurements of muon flux at 1070m vertical depth in the Boulby underground laboratory", Nucl. Instrum. Methods Phys. Res. A: Accel. Spectrom. Detect. Assoc. Equip. **511**, 347–353 (2003).

[304] C. Galbiati and J. F. Beacom, "Measuring the cosmic ray muon-induced fast neutron spectrum by (n, p) isotope production reactions in underground detectors", Phys. Rev. C **72**, 025807 (2005).

[305] D.-M. Mei and A. Hime, "Muon-induced background study for underground laboratories", Phys. Rev. D **73**, 053004 (2006).

[306] E.-I. Esch et al., "The cosmic ray muon flux at WIPP", Nucl. Instrum. Methods Phys. Res. A: Accel. Spectrom. Detect. Assoc. Equip. **538**, 516–525 (2005).

[307] S. Kamat, "Extending the sensitivity to the detection of WIMP dark matter with an improved understanding of the limiting neutron backgrounds", Ph.D. thesis (Case Western Reserve University, January 2005).

[308] C. Waltham (SNO Collaboration), "Downward muon flux at the Sudbury Neutrino Observatory", Proceedings of the XIX International Conference on Neutrino Physics & Astrophysics, Sudbury, Canada (2000).

[309] H. Wulandari et al., "Neutron background studies for the cresst dark matter experiment", `10.48550/ARXIV.HEP-EX/0401032` (2004).

[310] M. Cribier et al., "The muon induced background in the GALLEX experiment", Astropart. Phys. **6**, 129–141 (1997).

[311] C. Berger et al. (Fréjus Collaboration), "Experimental study of muon bundles observed in the Fréjus detector", Phys. Rev. D **40**, 2163–2171 (1989).

[312] Boulby Underground Laboratory, *Schematic of Boulby Underground Laboratory*, 2023.

[313] P. Scovell, "An update from the Boulby Underground Laboratory", in DMUK (April 2019).

[314] I. Lawson and B. Cleveland, "Low background counting at SNOLAB", in AIP conf. proc. Vol. 1338 (2011).

[315] G. Pronost et al., "Development of new radon monitoring systems in the Kamioka mine", Prog. Theor. Exp. Phys. **2018**, 10.1093/ptep/pty091 (2018).

[316] Y. Nakano et al., "Measurement of radon concentration in Super-Kamiokande's buffer gas", Nucl. Instrum. Methods Phys. Res. A: Accel. Spectrom. Detect. Assoc. Equip. **867**, 108–114 (2017).

[317] Google, *Google Maps satellite image showing location of nuclear power stations in the UK and northern France*, 2022.

[318] International Atomic Energy Agency, *Power Reactor Information System (PRIS)*, 2022.

[319] J. B. Goode, D. Harbottle, and B. C. Hanson, "Vacuum drying of advanced gas reactor fuel", Prog. Nucl. Energy **109**, 145–158 (2018).

[320] EDF Energy, *Nuclear Lifetime Management*, 2022.

[321] EDF Energy, *Sizewell B starts review to extend operation by 20 years*, 2022.

[322] ASN, *ASN issues a position statement on the conditions for continued operation of the 900 MWe reactors beyond 40 years*, 2021.

[323] EDF Energy, *About Hinkley Point C*, 2022.

[324] Institute of Mechanical Engineers, *Nuclear power stations*, 2022.

[325] WATCHMAN Collaboration, "Alternative reactor sensitivity study: risk mitigation for the NEO project", Unpublished (2021).

[326] A. Scarff, "Tank - design", Technical report, University of Sheffield, Unpublished (2021).

[327] S. Seibert, *RAT-PAC*, 2014.

[328] L. Lönnblad, "CLHEP—a project for designing a C++ class library for high energy physics", Comput. Phys. Commun. **84**, 307–316 (1994).

[329] J. Allison et al., "Recent developments in GEANT4", Nucl. Instrum. Methods Phys. Res. A: Accel. Spectrom. Detect. Assoc. Equip. **835**, 186–225 (2016).

[330] S. Agostinelli et al., "GEANT4 — a simulation toolkit", Nucl. Instrum. Methods Phys. Res. A: Accel. Spectrom. Detect. Assoc. Equip. **506**, 250–303 (2003).

[331] G. Horton-Smith, *GLG4sim*, 2005.

[332] R. Brun and F. Rademakers, "ROOT — an object oriented data analysis framework v6.18/02", Nucl. Instrum. Methods Phys. Res. A: Accel. Spectrom. Detect. Assoc. Equip. **389**, 81–86 (1997).

[333] Brookhaven National Laboratory and Lawrence Berkeley National Laboratory (private communication), 2021.

[334] F. Bečvář, "Simulation of γ cascades in complex nuclei with emphasis on assessment of uncertainties of cascade-related quantities", Nucl. Instrum. Methods Phys. Res. A: Accel. Spectrom. Detect. Assoc. Equip. **417**, 434–449 (1998).

[335] A. Bernstein et al., *Conceptual design overview of the Advanced Instrumentation Testbed (AIT) and the WATer CHerenkov Monitor of ANtineutrinos (WATCHMAN)*, tech. rep. (March 2019).

[336] O. A. Akindele et al., "Exclusion and verification of remote nuclear reactors with a 1-kiloton gd-doped water detector", Phys. Rev. Appl. **19**, 034060 (2023).

[337] S. Haselschwardt et al., "A liquid scintillation detector for radioassay of gadolinium-loaded liquid scintillator for the LZ outer detector", Nucl. Instrum. Methods Phys. Res. A: Accel. Spectrom. Detect. Assoc. Equip. **937**, 148–163 (2019).

[338] Hamamatsu Photonics (private communication), 2020.

[339] T. Zhang et al., "Low background stainless steel for the pressure vessel in the PandaX-II dark matter experiment", J. Instrum. **11**, T09004 (2016).

[340] Y. Zhang et al. (Super-Kamiokande Collaboration), "First measurement of radioactive isotope production through cosmic-ray muon spallation in Super-Kamiokande IV", Phys. Rev. D **93**, 012004 (2016).

[341] H. Araújo et al., "Radioactivity backgrounds in ZEPLIN–III", Astropart. Phys. **35**, 495–502 (2012).

[342] S. W. Li and J. F. Beacom, "First calculation of cosmic-ray muon spallation backgrounds for MeV astrophysical neutrino signals in Super-Kamiokande", Phys. Rev. C **89**, 045801 (2014).

[343] S. Chu, L. Ekström, and R. Firestone, *The Lund/LBNL Nuclear Data Search: Table of Radioactive Isotopes*, 1999.

[344] TUNL Nuclear Data Evaluation Project, *Energy Level Diagrams*, 2021.

[345] C. Jollet and A. Meregaglia, "^{9}Li and ^{8}He decays in GEANT4", Nucl. Instrum. Methods Phys. Res. A: Accel. Spectrom. Detect. Assoc. Equip. **949**, 162904 (2020).

[346] Y.-F. Wang et al., "Predicting neutron production from cosmic-ray muons", Phys. Rev. D **64**, 013012 (2001).

[347] A. Tang et al., "Muon simulations for Super-Kamiokande, KamLAND, and CHOOZ", Phys. Rev. D **74**, 053007 (2006).

[348] F. Sutanto et al., "Measurement of muon-induced high-energy neutrons from rock in an underground Gd-doped water detector", Phys. Rev. C **102**, 034616 (2020).

[349] J. Battat et al., "Radon in the DRIFT-II directional dark matter TPC: emanation, detection and mitigation", J. Instrum. **9**, P11004–P11004 (2014).

[350] L. Kneale, "Coincidence-based reconstruction and analysis for remote reactor monitoring with antineutrinos", Ph.D. thesis (University of Sheffield, October 2021).

[351] M. Shinoki et al. (Super-Kamiokande Collaboration), "Measurement of the cosmogenic neutron yield in Super-Kamiokande with gadolinium loaded water", Phys. Rev. D **107**, 092009 (2023).

[352] E. Tziaferi et al., "First measurement of low intensity fast neutron background from rock at the Boulby Underground Laboratory", Astropart Phys. **27**, 326–338 (2007).

[353] M. Carson et al., "Neutron background in large-scale xenon detectors for dark matter searches", Astropart. Phys. **21**, 667–687 (2004).

[354] M. Smy (Super-Kamiokande Collaboration), "Low Energy Event Reconstruction and Selection in Super-Kamiokande-III", in Proceedings of 30th International Cosmic Ray Conference, Vol. 5, ICRC2007 (July 2007), pp. 1279–1282.

[355] L. Kneale, M. Smy, and M. Malek, "Coincidence-based reconstruction for reactor antineutrino detection in gadolinium-doped Cherenkov detectors", Nucl. Instrum. Methods Phys. Res. A: Accel. Spectrom. Detect. Assoc. Equip. **1053**, 168375 (2023).

[356] M. Nakahata et al., "Calibration of Super-Kamiokande using an electron LINAC", Nucl. Instrum. Methods Phys. Res. A: Accel. Spectrom. Detect. Assoc. Equip. **421**, 113–129 (1999).

[357] K. Abe et al. (Super-Kamiokande Collaboration), "Solar neutrino measurements in Super-Kamiokande-IV", Phys. Rev. D **94**, 052010 (2016).

[358] O. Y. Smirnov et al., "Measurement of neutrino flux from the primary proton–proton fusion process in the Sun with Borexino detector", Phys. Part. Nucl. **47**, 995–1002 (2016).

[359] F. Pedregosa et al., "Scikit-learn: machine learning in Python", J. Mach. Learn. Res. **12**, 2825–2830 (2011).

[360] F. Sutanto, O. Akindele, M. Bergevin, et al., "Progress report: study on the effect of varying veto thickness on the sensitivity of Gd-H_2O filled tank", Technical report, Lawrence Livermore National Laboratory, Unpublished (2021).

[361] G. Cowan, "Discovery sensitivity for a counting experiment with background uncertainty", Technical report, Royal Holloway, University of London (2012).

[362] S. Dazeley et al., "A search for cosmogenic production of β-neutron emitting radionuclides in water", Nucl. Instrum. Methods Phys. Res. A: Accel. Spectrom. Detect. Assoc. Equip. **821**, 151–159 (2016).

[363] *As noted in Hansard*, `https://hansard.parliament.uk/commons/2021-06-23/debates/21062318000007/NuclearPowerStationDecommissioning`.